2021

Towards Remote Gait Analysis: Combining Physics and Probabilistic Models for Estimating Human Joint Mechanics

Reed Donovan Gurchiek
University of Vermont

TOWARDS REMOTE GAIT ANALYSIS: COMBINING PHYSICS AND PROBABILISTIC MODELS FOR ESTIMATING HUMAN JOINT MECHANICS

A Dissertation Presented

by

Reed Donovan Gurchiek

to

The Faculty of the Graduate College

of

The University of Vermont

In Partial Fulfillment of the Requirements
for the Degree of Doctor of Philosophy
Specializing in Mechanical Engineering

May, 2021

Defense Date: January 12, 2021
Dissertation Examination Committee:

Ryan S. McGinnis, Ph.D., Advisor
Michael J. Toth, Ph.D., Chairperson
Bruce D. Beynnon, Ph.D.
Niccolo Fiorentino, Ph.D.
Cynthia J. Forehand, Ph.D., Dean of the Graduate College

Abstract

The connected health movement and remote patient monitoring promise to revolutionize patient care in multiple clinical contexts. In orthopedics, continuous monitoring of human joint and muscle tissue loading in free-living conditions will enable novel insight concerning musculoskeletal disease etiology. These developments are necessary for comprehensive patient characterization, progression monitoring, and personalized therapy. This vision has motivated many recent advances in wearable sensor-based algorithm development that aim to perform biomechanical analyses traditionally restricted to confined laboratory spaces. However, these techniques have not translated to practical deployment for remote monitoring. Several barriers to translation have been identified including complex sensor arrays. Thus, the aim of this work was to lay the foundation for remote gait analysis and techniques for estimating clinically relevant biomechanics with a reduced sensor array.

The first step in this process was to develop an open-source platform that generalized the processing pipeline for automated remote biomechanical analysis. The clinical utility of the platform was demonstrated for monitoring patient gait following knee surgery using continuous recordings of thigh-worn accelerometer data and rectus femoris electromyograms (EMG) during free-living conditions. Individual walking bouts were identified from which strides were extracted and characterized for patient evaluation. A novel, multifactorial asymmetry index was proposed based on temporal, EMG, and kinematic descriptors of gait that was able to differentiate between patients at different stages of recovery and that was more sensitive to recovery time than were indices of cumulative physical activity.

The remainder of the work focused on algorithms for estimating joint moment and simulating muscle contraction dynamics using a reduced sensor array. A hybrid technique was proposed that combined both physics and probabilistic models in a complementary fashion. Specifically, the notion of a muscle synergy function was introduced that describes the mapping between excitations from a subset of muscles and excitations from other synergistic muscles. A novel model of these synergy functions was developed that enabled estimation of unmeasured muscle excitations using a measured subset. Data from thigh- and shank-worn inertial sensors were used to estimate segment kinematics and muscle-tendon unit (MTU) lengths using physics-based techniques and a model of the musculoskeletal geometry. These estimates of muscle excitation and MTU length were used as inputs for EMG-driven simulation of muscle contraction. Estimates of muscle force, power, and work as well as net joint moment from the proposed hybrid technique were compared to estimates from laboratory-based techniques. This presents the first sensor-only (four EMG and two inertial sensors) simulation of muscle contraction dynamics and joint moment estimation using machine learning only for estimating unmeasured muscle excitations.

This work provides the basis for automated remote biomechanical analysis with reduced sensor arrays; from raw sensor recordings to estimates of muscle moment, force, and power. The proposed hybrid technique requires data from only four EMG and two inertial sensors and work has begun to seamlessly integrate these sensors into a knee brace for monitoring patients following knee surgery. Future work should build on these developments including further validation and design of methods utilizing remotely and longitudinally observed biomechanics for prognosis and optimizing patient-specific interventions.

Citations

Material from this dissertation has been published in the following form:

Gurchiek, RD, Choquette, RH, Beynnon, BD, Slauterbeck, JR, Tourville, TW, Toth, MJ, McGinnis, RS.. (2019). Open-source remote gait analysis: A post-surgery patient monitoring application. Scientific Reports, 9(1): 17966.

Gurchiek, RD, Cheney, N, McGinnis, RS.. (2019). Estimating biomechanical time-series with wearable sensors: A systematic review of machine learning techniques. Sensors, 19(23): 5227.

Gurchiek, RD, Garabed, CP, McGinnis, RS.. (2020). Gait event detection using a thigh-worn accelerometer. Gait and Posture, 80: 214-216.

Gurchiek, RD, Ursiny, AT, McGinnis, RS.. (2020). A Gaussian process model of muscle synergy functions for estimating unmeasured muscle excitations using a measured subset. IEEE Transactions on Neural Systems and Rehabilitation Engineering, 28(11): 2478-2487.

Material from this dissertation has been submitted for publication in the following form:

Gurchiek, RD, Beynnon, BD, Agresta, CE, Choquette, RH, McGinnis, RS.. (2020). Wearable sensors for remote patient monitoring in orthopedics: A narrative review. Minerva Ortopedica e Traumatologica.

Acknowledgements

I sincerely thank all of my dissertation committee members: to Dr. Michael Toth for your insight concerning the contribution of muscle atrophy to pathological gait mechanics; to Dr. Bruce Beynnon for your insight concerning musculoskeletal diseases in general and innovation in management of those conditions; and to Dr. Niccolo Fiorentino for our many discussions concerning neuromusculoskeletal modeling, simulating muscle contraction dynamics, and human motion analysis in general. I send a special thanks to my advisor, Dr. Ryan McGinnis. Your guidance has been paramount to my training and development as an engineer and scientist and concerns every aspect of this project. In particular, your drive to make these techniques practical and to promote real change with wearables-based applications has had a profound effect. The fundamental ideas behind many of the developments in this work began with our discussions even before my time at UVM. It has been most satisfying to pursue those ideas and see them come to fruition.

I thank Rebecca Choquette for your assistance in data collection in patients recovering from knee surgery. Also, to Dr. Timothy Tourville: discussions with you concerning novel applications for wearables in rehabilitation has always been enlightening.

I thank all of the many undergraduate and graduate students who helped with this work in data collection, data analysis, and conceptual discussions: Anna Ursiny, Nicole Donahue, Cole Garabed, Brett Meyer, Dakota Allen, Lukas Adamowicz, Lindsey Tulipani, Samantha Fox, Abigail Teixeira, James Doherty, Curtis Ianni, and Tori Weissman.

Finally, I owe a big thanks to my wife, Zoë, and son, Kadrian. You have made sacrifices for this endeavor and have been a major source of support. I could not have done this without you.

Table of Contents

Page

List of Tables

Table Page

List of Figures

Chapter 1: Wearable Sensors for Remote Patient Monitoring in Orthopedics: A Narrative Review

A modified version of this chapter has been submitted for publication as: Gurchiek, RD, Beynnon, BD, Agresta, CE, Choquette, RH, McGinnis, RS (2020). Wearable sensors for remote patient monitoring in orthopedics: A narrative review. Minerva Ortopedica e Traumatologica..

1.1. Introduction

1.1.1. Prevalence of musculoskeletal disorders

Over the past three decades, musculoskeletal disorders rank among the top 10 factors underlying the increased health burden across the globe [1]. Notably, among working age males and females (20-50 years old), musculoskeletal disorders are one of the three greatest contributors to years lived with a disability and the majority of these conditions concern the lower body (lumbar region and below) [2]. In particular, hip and knee osteoarthritis (OA) are a leading cause of disability affecting over 300 million people worldwide [2], [3]. These have detrimental economic effects both in terms of human capital [2] and healthcare spending. For example, in the USA, orthopedic surgeries were the most common inpatient operating room procedures in 2012 [4] and in 2016 the largest expenditures were in musculoskeletal disorders (over $350 billion) with the majority in the 20-64 year old category [5]. Thus, a clear need has been recognized for innovative approaches in the management and monitoring of patients with orthopedic conditions [6].

1.1.2. Remote patient monitoring framework

Remote patient monitoring via mobile health technologies (Figure 1) promise major contributions to these innovation efforts and across multiple clinical contexts [7]–[9]. The development of digital biomarkers has become a major thrust area [10] and may play an important role in optimizing patient care in orthopedic medicine. This connected health movement is largely driven by advances in sensor hardware, wearability, and methods for estimating clinically relevant biomechanical and physiological variables [11]–[16]. Analyses previously restricted to confined laboratory spaces can now theoretically be performed

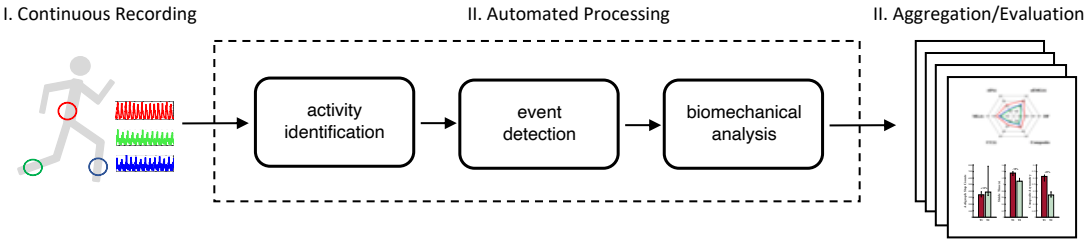

Figure 1: Schematic overview of remote monitoring framework. Wearable sensors continuously record data that are automatically processed for estimation of clinically relevant biomechanical variables. These data are aggregated and used for patient characterization at single time-points and across multiple days for trends analysis.

remotely. This includes estimation of spatiotemporal descriptors of gait [17], gait speed [18]–[20], joint and/or single segment kinematics [21]–[23], inverse dynamics (e.g., joint moments, ground reaction forces) [14], [24]–[27], and indices of motor control (e.g., muscle synergy analysis [28], activation patterns [29]). We say "theoretically" because the potential to actually deploy these techniques for remote observation is merely suggested given that they require only wearable sensor data and given sufficient estimation performance based on validation studies. However, it is not clear to what extent these methods have actually been deployed for this purpose.

Biomechanical outcomes at a joint-, limb-, and/or muscle-specific level are useful for diagnosis and, importantly, for identifying causal factors related to disease onset and progression [30]–[32]. The potential to continuously monitor tissue loads and characterize the biomechanics of free-living movement, at this level of detail, indicate several improvements to the current standard of care. Compared to laboratory-based analysis, remote observations would enable increased observation frequency and ecologically valid evaluation. Concerning ecological validity, in-lab observations may not accurately reflect those in free-living conditions and especially for gait speed-dependent variables [33]–[35]. Concerning increased observation frequency, continuous monitoring and longitudinal data are needed to understand patient-specific responses to joint and tissue loads, prescribed or otherwise [30]. Remote gait analysis, in particular, is important in this context because of the relationship between ambulatory loads and tissue health [31], [36].

Increased observation frequency (e.g., analysis of every daily walking bout) facilitates novel investigation into several disease-related phenomena that are currently not well understood. For example, in the context of anterior cruciate ligament reconstruction surgery (ACLR), uncertainty surrounds the cause and effect relationship between post-surgery biomechanics and early onset knee OA as well as how to prescribe optimal loading in rehabilitation [37]. Further, healthy articular cartilage appears to adapt favorably to mechanical loading and yet unfavorably for aged or diseased tissue [32], [38]. In the context of OA, this transition is thought to occur near the onset of the disease but a more exact characterization remains unknown [38]. These are likely related to the accumulation and type of load (e.g., compressive or shear) [39] and thus continuous monitoring may help elucidate these and other cumulative load-dependent processes. Further, longitudinal observations enable prognosis concerning anticipated trajectories of clinical outcomes based on personalized prediction models [40], [41]. These trajectories should be characterized as soon as possible as early identification is critical in musculoskeletal disease [30], [38], [42]. For example, in the context of ACLR, pathomechanics manifest early [37], [43], [44] but their effects can be mitigated given the efficacy of gait retraining [45], [46] and because adopted gait patterns are learned over a long period of time [47]. These trajectories and intervention responses are patient-specific and based on dense datasets which augment clinical decision-making and personalized treatment plans [48].

Beyond performing the same evaluations characteristic of traditional human motion capture in laboratory environments, some insight is unique to remote analysis being completely outside the scope of infrequent laboratory observations. This includes, for example, analyzing the variation in gait mechanics across multiple time scales (e.g., stride-by-stride, hour-by-hour, day-by-day), quantification of cumulative tissue loads, evaluating the retention of movement patterns in a gait retraining context [45], [46], [49], and the assessment of physical activity (PA). Concerning the latter, indices of cumulative PA (e.g., daily step count) are common for patient characterization in orthopedics. However, analyzing free-living gait at a stride-by-stride level is advantageous in terms of both granularity and, for particular mechanical variables (e.g., joint moment), sensitivity to disease etiology [50], [51]. Novel measures have been proposed unique to wearable sensor data that classify health status (e.g., fall risk [52], OA risk [41]) or predict changes in cartilage microstructure [53] as well as surrogate measures that correlate with traditional biomechancial

variables of clinical importance [54], [55]. Controlled, laboratory-based evaluations are the gold standard and are necessary to probe specific mechanical properties related to musculoskeletal disease. However, it is clear that remote observations should be incorporated to augment this process for comprehensive evaluation.

1.1.4. Review aim

Despite this promising potential, the extent to which these techniques have actually been utilized for remote monitoring of patients with musculoskeletal disorders remains unclear. Jung et al. (2020) recently reviewed 58 studies utilizing wearable sensors for remote monitoring in multiple subject populations, but none were specifically related to orthopedic conditions [56]. They also summarize previous reviews similarly concerned with a general cohort [57] as well as in specific clinical contexts (e.g., multiple sclerosis [8], Parkinson's disease [58]), but not for musculoskeletal disorders.

In an orthopedic context, Arnold et al. (2016) reviewed eight studies concerning changes in PA following total hip or knee arthroplasty (THA or TKA, respectively) [59]. Similarly, Withers et al. (2017) reviewed 17 studies concerning changes in PA following THA [60], but only four of these used a wearable sensor. Johns et al. (2020) reviewed 12 studies concerning changes in PA following interventions for ankle OA, but only one used a wearable sensor [61]. These reviews were less concerned with the methodological aspects of remote monitoring, but rather regarding clinical insight based on one type of wearables-based outcome; namely, the effect of select interventions on changes in PA. Small et al. (2019) limited their review to 45 studies that used inertial sensors to evaluate patients following knee arthroplasty in both free-living and laboratory environments. Their categorization of wearables-based assessments included (1) functional and gait parameters, (2) physical activity, and (3) joint instability. However, remote monitoring was not analyzed as a distinct category, although 28 of their reviewed studies monitored patients in free-living conditions using a wearable sensor.

To the author's knowledge, no previous reviews have addressed specifically the remote analysis of individual strides as an approach separate from indices of cumulative PA. Thus, the current review aimed to characterize the extent to which wearable sensors have been used for remote analysis at a stride-by-stride level (or some other task-specific segmentation) as opposed to indices of cumulative PA.

1.2. Search strategy

The PubMed database was searched on September 15, 2020 for relevant articles using search terms related to the use of wearable sensors for remote monitoring of gait in orthopedic populations. Only journal articles (no conference proceedings) written in English were considered. Articles were removed if they did not clearly use a wearable sensor for evaluation and/or if they did not passively evaluate free-living activity. Passive evaluation was defined as the evaluation of unprescribed movement. For example, performing a prescribed 10 m walk test or prescribed in-home rehabilitation exercises were considered active, not passive, evaluations. Studies characterizing only active evaluations were not included for review even though the environment might have been remote. The references in each identified article were searched for additional studies to include. All relevant articles in the aforementioned previously published reviews [59]–[62] were also included.

The following data were extracted from each reviewed article: clinical context (e.g., OA, ACLR); impaired or surgical joint or region; and the type, number, and location of wearable sensors. Further, the primary outcome from this review concerned a categorization of the variables estimated from the remote analyses. Specifically, all outcome variables were categorized as a either a measure of cumulative PA or as pertaining to a stride-level analysis. For example, common measures of cumulative PA include daily step count, percentage of time spent walking, and energy expenditure whereas stride-by-stride variables may include gait speed, stride frequency, or sit-to-stand time. Some activity monitors output step count in one-minute epochs from which stride frequency (strides/minute) can be calculated as an indicator of activity intensity. However, stride frequency computed as the number of strides counted in one minute is not necessarily equivalent to the average stride frequency computed for each individual stride in the same minute [63]. Thus, cadences based on step counts stored in one-minute bins were not considered stride-level variables. In most cases, evaluative outcomes were processed using proprietary software. Others described custom algorithms that processed raw data for identifying walking bouts (e.g., in 5 second epochs) and gait events (e.g., foot contact). For the latter case, some of these studies also reported stride frequency, but without explicitly stating that stride frequency was computed per stride. In these instances, it was assumed that the

variables were computed stride-by-stride as these algorithms, gait event detection in particular, are sufficient to do so and because the raw sensor data were processed.

1.3. Results

A total of 90 studies were identified that met all inclusion and exclusion criteria. Note that these data were compiled after the study presented in Chapter 3 was published; thus, it was included for review. A general increasing trend was observed in the number of studies monitoring patients remotely (Figure 2). Across all studies, most patients suffered from musculoskeletal diseases of the knee (70 studies) followed by the hip (24 studies), spine (5 studies), and ankle (2 studies) (Figure 3). The most popular locations for wearable sensors were the waist (40 studies), thigh (28 studies), and shank (17 studies) while less than 10% of studies used sensors located on the chest/trunk, wrist, upper arm, and foot (Figure 3). Accelerometers were the most common type of sensor (84 studies). Electromyography (EMG) sensors were used in three studies and smartphones were used in two studies. Magneto-inertial measurement units (MIMU; accelerometer, gyroscope, magnetometer) were also used in two studies [64], [65]. However, the processing algorithm was described as "acceleration-based" and the associated reference describing the development of the algorithm apparently required only accelerometer data [66]. Thus, it is not clear how the gyroscope and magnetometer data were used, if at all.

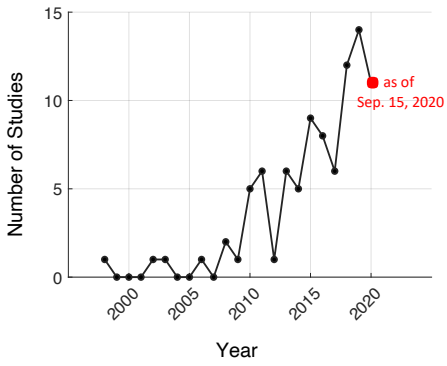

Figure 2: Publications per year of studies that utilized wearable sensors for remote monitoring in patients with orthopedic conditions.

Most studies quantified cumulative PA (87 studies, 97%) compared to only ten studies (11%) that characterized movement on a stride-by-stride level (Figure 3). One study used stride-level data, including chair rise time, as inputs to a regularized linear model for estimating timed-up-and-go (TUG) time (trained on in-lab observations) [67]. All other studies evaluating stride-level outcomes report an aggregate measure (e.g., mean) of all identified strides [34], [68]–[72] or a select few [73]–[75] for walking gait as well as sit-to-stand time for identified sit-to-stand events in two studies [73], [74]. Stride-level variables were mostly temporal (e.g., stride frequency, duty factor) in addition to gait speed [34], knee flexion angle [75], and between-leg asymmetries based on rectus femoris muscle activity (EMG) and thigh kinematics [70]. Table 1 summarizes each study pertaining to the inquiries of the current review.

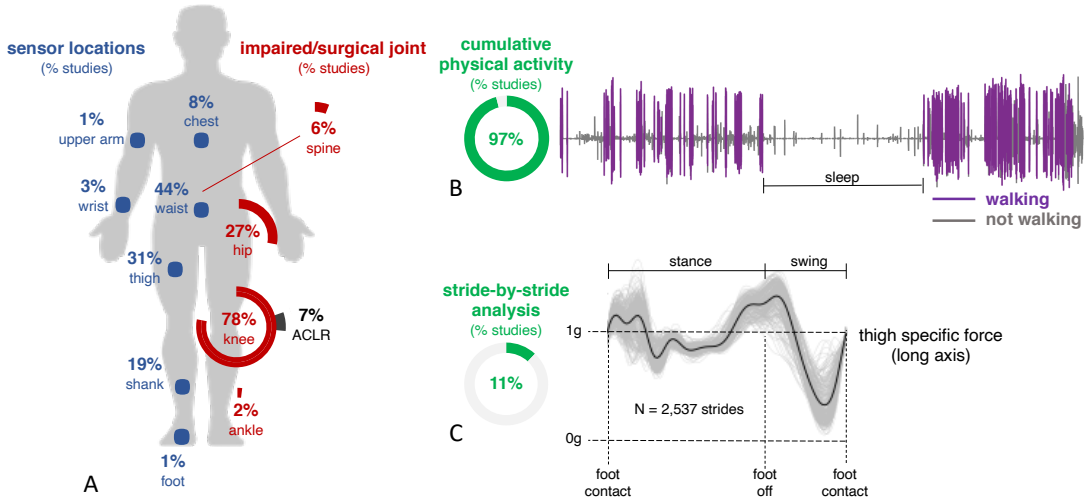

Figure 3: Summary of the studies included for review including wearable sensor location (A, blue), the joint/region of interest (A, red) and the percentage of studies that characterized free-living movement using either indices of cumulative PA (B) and/or stride-level variables (C).

Table 1: Summary of studies included in review

Author (year) [reference]	Clinical Context	Sensors type (#): location	PA	Stride-Level
Oldham and Howe (1998) [76]	KOA, pre-TKA	EMG (2): VL, RF	Y	N
Walker et al. (2002) [77]	KOA, TKA	ACC (1): trunk	Y	N
Talbot et al. (2003) [78]	KOA	ACC (2): waist	Y	N
Franklin et al. (2006) [79]	TKA	ACC (1): ankle	Y	N
Brandes et al. (2008) [80]	KOA, pre-TKA	ACC (2): waist, ankle	Y	N
de Groot et al. (2008) [81]	KOA, HOA, TKA, THA	ACC (3): sternum, both thighs	Y	N
Howe and Rafferty (2009) [82]	KOA	EMG (2): VL, VM ACC (1): thigh	Y	N
Foucher et al. (2010) [34]	post-THA	ACC (1): ankle	N	gait speed
Schulte et al. (2010) [83]	LSS, SS	ACC (1): ankle	Y	N
Tsuji et al. (2010) [84]	KOA, TKA	ACC (1): waist	Y	N
Vissers et al. (2010) [85]	KOA, TKA	ACC (3): sternum, both thighs	Y	N
Winter et al. (2010) [86]	KOA, HOA, LSS, pre-TKA, pre-THA, pre-SS	ACC (1): ankle	Y	N
Assal et al. (2011) [87]	AOA, TAA	ACC (1): ankle	Y	N
Brandes et al. (2011) [88]	KOA, TKA	ACC (4): ankle, thigh, waist x2	Y	N
Hayes et al. (2011) [89]	TKA	ACC (5): chest, both thighs, both feet	Y	N
Robbins et al. (2011) [90]	KOA	ACC (1): waist	Y	N
Tonelli et al. (2011) [91]	KOA, pre-TKA	ACC (1): thigh	Y	N
Vissers et al. (2011) [73]	HOA, THA	ACC (3): sternum, both thighs	Y	stride frequency chair rise time
Holsgaard-Larsen and Roos (2012) [92]	KOA, HOA, pre-TKA, pre-THA	ACC (1): upper arm	Y	N
Chmelo et al. (2013) [93]	KOA	ACC (1): waist	Y	N

Doré et al. (2013) [94]	KOA, other knee abnormalities	ACC (1): unclear	Y	N
Fujita et al. (2013) [95]	HOA, THA	ACC (1): waist	Y	N
Lin et al. (2013) [96]	HOA, THA	ACC (1): waist	Y	N
Maly et al. (2013) [97]	KOA	ACC (1): waist	Y	N
Vissers et al. (2013) [74]	KOA, HOA, TKA, THA	ACC (4): sternum x2, both thighs	Y	stride frequency chair rise time
Bolszak et al. (2014) [98]	post-TKA	ACC (1): waist	Y	N
Dessery et al. (2014) [99]	KOA	ACC (1): waist	Y	N
Harding et al. (2014) [100]	KOA, HOA, TKA, THA	ACC (1): waist	Y	N
Lützner et al. (2014) [101]	TKA	ACC (1): shank	Y	N
White et al. (2014) [102]	KOA	ACC (1): ankle	Y	N
Davenport et al. (2015) [103]	post-hip surgery (hip fracture)	ACC (1): thigh	Y	N
Kahn and Schwarzkopf (2015) [104]	KOA, TKA	ACC (1): waist	Y	N
Kretzschmar et al. (2015) [105]	KOA	ACC (1): waist	Y	N
Lee et al. (2015) [106]	KOA	ACC (1): waist	Y	N
Lo et al. (2015) [107]	KOA	ACC (1): waist	Y	N
Maly et al. (2015) [108]	KOA	ACC (1): waist	Y	N
Øiestad et al. (2015) [109]	KOA	ACC (1): ankle	Y	N
Song et al. (2015) [110]	KOA	ACC (1): waist	Y	N
Verlaan et al. (2015) [68]	KOA	ACC (1): thigh	Y	stride frequency
Fukutani et al. (2016) [111]	KOA	ACC (1): thigh	Y	N
Kahn and Schwarzkopf (2016) [112]	KOA, TKA	ACC (1): waist	Y	N
Liu et al. (2016) [113]	KOA	ACC (1): waist	Y	N
Lützner et al. (2016) [114]	KOA, TKA	ACC (1): shank	Y	N

Mobbs et al. (2016) [115]	SS (multiple indications)	ACC (1): waist	Y	N
Taniguchi et al. (2016) [116]	post-TKA	ACC (1): unclear	Y	N
Toogood et al. (2016) [117]	post-THA	ACC (1): ankle	Y	N
White et al. (2016) [118]	KOA	ACC (1): ankle	Y	N
Bell et al. (2017) [119]	post-ACLR	ACC (1): waist	Y	N
Brisson et al. (2017) [120]	KOA	ACC (1): waist	Y	N
Cooper et al. (2017) [121]	KOA, TKA	ACC (1): thigh	Y	N
Engdal et al. (2017) [122]	post-THA	ACC (1): thigh	Y	N
Mehta et al. (2017) [123]	hip arthroscopy (femoroacetabular impingement)	phone (1): unclear	Y	N
Schotanus et al. (2017) [69]	KOA, TKA	ACC (1): thigh	Y	stride frequency
Agarwal et al. (2018) [124]	KOA	ACC (1): waist	Y	N
Daugaard et al. (2018) [125]	KOA, post-TKA	ACC (1): thigh	Y	N
Fenten et al. (2018) [126]	post-TKA	ACC (1): thigh	Y	N
Fenton et al. (2018) [127]	KOA	ACC (1): ankle or waist	Y	N
Halilaj et al. (2018) [53]	KOA	ACC (1): waist	Y	N
Hayashi et al. (2018) [128]	post-TKA, post-THA	ACC (1): waist	Y	N
Hjorth et al. (2018) [129]	post-THA, post-RHA	ACC (1): thigh	Y	N
Losina et al. (2018) [130]	KOA, TKA	ACC (1): unclear	Y	N
Master et al. (2018) [131]	KOA	ACC (1): waist	Y	N
Pellegrini et al. (2018) [132]	TKA	ACC (1): waist	Y	N
Sliepen et al. (2018) [133]	KOA	ACC (1): thigh	Y	N
Twiggs et al. (2018) [134]	KOA, TKA	ACC (1): wrist	Y	N

Allen et al. (2019) [135]	KOA	ACC (1): waist	Y	N
Chapman et al. (2019) [75]	TKA	ACC (2): thigh, shank	N	knee flexion angle
Frimpong et al. (2019) [136]	KOA, TKA	ACC (1): waist	Y	N
Gilmore et al. (2019) [137]	post-SS (multiple indications)	ACC (1): thigh	Y	N
Gurchiek et al. (2019) [70]	post-ACLR	EMG (2): both RF ACC (2): both thighs	Y	stride frequency asymmetry
Hjorth et al. (2019) [71]	post-THA, post-RHA	ACC (1): thigh	Y	stride frequency
Jeong et al. (2019) [138]	KOA	ACC (1): wrist	Y	N
Kuenze et al. (2019) [139]	post-ACLR	ACC (1): waist	Y	N
Kuenze et al. (2019) [140]	post-ACLR	ACC (1): waist	Y	N
Luna et al. (2019) [141]	KOA, HOA, TKA, THA	ACC (1): wrist	Y	N
Ramkumar et al. (2019) [142]	KOA, TKA	phone (1): unclear	Y	N
Saporito et al. (2019) [67]	post-THA	ACC (1): trunk	N	multiple
Shofer et al. (2019) [143]	AOA, TAA, ankle arthrodesis	ACC (1): ankle	Y	N
Vaughn et al. (2019) [144]	TKA, THA	ACC (1): waist or thigh	Y	N
Baez et al. (2020) [145]	post-ACLR	ACC (1): waist	Y	N
Brisson et al. (2020) [146]	KOA	ACC (1): waist	Y	N
Christiansen et al. (2020) [147]	post-TKA	ACC (1): waist	Y	N
Jelsma et al. (2020) [65]	post-RHA	MIMU (1): thigh	Y	N
Jelsma et al. (2020) [64]	post-THA, post-RHA	MIMU (1): thigh	Y	N
Keppler et al. (2020) [148]	hip surgery (hip fracture)	ACC (1): waist	Y	N
Lisee et al. (2020) [149]	post-ACLR	ACC (1): waist	Y	N
Sakakima et al. (2020) [150]	multiple (spine, hip, knee)	ACC (1): waist	Y	N
Taylor et al. (2020) [151]	post-hip surgery (hip fracture), hip fracture	ACC (1): thigh	Y	N

Vangeneugden et al. (2020) [72]	KOA	ACC (1): thigh	Y	stride frequency
Voinier et al. (2020) [152]	KOA	ACC (1): ankle	Y	N

KOA: knee OA, TKA: before (pre-) and after (post-) TKA, HOA: hip OA, THA: before (pre-) and after (post-) THA, LSS: lumbar spinal stenosis, SS: spinal surgery, AOA: ankle OA, TAA: before (pre-) and after (post-) total ankle arthroplasty, RHA: before (pre-) and after (post-) resurfacing hip arthroplasty, VL: vastus lateralis, RF: rectus femoris, VM: vastus medialis, ACC: accelerometer (or pedometer)

1.4. Discussion

The main finding of this review was that despite a plethora of research dedicated to wearable sensor-based biomechanical analysis and the potential to improve patient care by deploying these techniques remotely, these developments have not translated to remote deployment. Only ten studies characterized free-living gait on a stride-by-stride level extracting variables often computed in laboratory-based gait analysis. Moreover, only three of these ten studies computed non-temporal descriptors of gait. The first was Foucher et al. (2010) [34] who found that gait speed increased from three weeks to twelve months post-THA when observed remotely; a finding that was reflected in laboratory observations (for which patients were told to walk at a "normal comfortable" speed). However, conclusions regarding comparisons to healthy controls differed between laboratory and remote observations at the later time point. Specifically, laboratory-based observations suggested slower gait in patients at 12 months post-THA compared to healthy controls, while remote observations suggested no difference. The second was Chapman et al. (2019) [75] who found that knee flexion range of motion during the stance phase of gait recovers faster than for the swing phase of gait in patients rehabilitating from TKA. The knee flexion angle estimate was based on estimates of the angular deviation of the thigh and shank segment long axes relative to the direction of gravity using accelerometer outputs from thigh- and shank-fixed sensors. This method is similar to what has been deployed for attitude estimation in less dynamic conditions; for example, to evaluate knee flexion range of motion [153] or for drift correction in integration-based approaches [16], [154]. To the author's knowledge, this is the first and only in-lab validation (and subsequent remote deployment) for knee flexion angle estimation using an accelerometer-only technique during dynamic activity like gait. The third was Gurchiek et al. (2019) [70] who found that stride-level descriptors of gait biomechanics were more sensitive to recovery time than were

indices of PA (step count, time spent walking) in patients rehabilitating from ACLR (Chapter 3). They proposed a multifactorial asymmetry measure that considered between-leg differences in duty factor, between-leg differences in phase-specific (stance or swing) mean muscle excitation, and between-leg similarity in like time-series (thigh acceleration and rectus femoris muscle excitation). Moreover, they illustrate the fluctuation of this asymmetry measure throughout the entire wear time. Analysis of within-day gait variability is unique to remote monitoring and has been explored by others for temporal gait variables [72] and PA [72], [136], [137].

Contrary to the scarce use of wearables-based biomechanical analysis at a stride-by-stride level, the results of this review confirm the popular belief that indices of PA are the most common metric used for remote monitoring in orthopedics. These metrics were used to investigate multiple scientific inquiries including evaluating the effect of select interventions on the recovery and progression of PA over time [64], [69], [77]–[79], [81], [83], [84], [87], [88], [95], [96], [99]–[101], [104], [114], [115], [117], [121], [123], [128], [130], [132], [134], [136], [137], [141]–[143], [147], [148], [151] and to compare PA between impaired and unimpaired populations [68], [76], [77], [80], [82], [86], [92], [95], [101], [119], [125], [139], [149], [150]. Another popular comparison was between wearables-based estimates of PA and subjective, questionnaire-based assessments wherein discrepancies were most often found [77], [119], [139], [143], [144] or weak correlations [89]. Others suggest the extent to which objective and subjective PA assessments yield similar conclusions may depend on sex [98] and/or the specific metric used [98], [136].

Indices of cumulative PA alone often represent a targeted outcome in interventions [81], [84] as they are vital for cardiovascular health [155] and weight loss [156] which positively affects tissue health in obese populations [157], [158]. Beyond the distinct clinical insight unique to indices of PA, the relationship between these measures and other targeted outcomes is also relevant, for example, as a potential surrogate measure and for understanding what underlies variance in PA (pain, muscle strength, etc.). Regarding PA as a potential surrogate measure, analysis of this relationship ultimately concerns the extent to which conclusions drawn about a patient are similar when characterized using PA compared to other outcomes. Across the studies included in the current review, this analysis was by way of correlation/regression analysis

or by examining whether or not two groups that differed according to one measure also differed according to PA-based metrics (e.g., comparing groups between two time points or comparing unimpaired and impaired groups). For example, studies from the current review identified positive relationships between PA and gait speed [102], [106], [127]. Mixed results were observed for other outcomes including, for example, pain in TKA [77], [81], [100], [112], THA [96], [100], knee OA [90], [91], [93], [111], [113], [146], and spine surgery [115], [137]; muscle strength in knee OA [78], [93], [138] and ACLR [139]; ground reaction force during gait in knee and hip OA [80], time since surgery following ACLR [70], [119], spine surgery [83], [115], and TKA/THA [95], [128], [141] which may be patient-specific [128], [141]; and joint range of motion in knee OA [91] and TKA [116], [136]. While some of this variation may be due to differences in the clinical context and/or the specific PA metric, these findings suggest caution should be taken concerning PA as a biomarker for recovery, as an indication of gait quality (and vice versa), and for prognosis.

Concerning prognosis, some have found no relationship between PA and cartilage tissue health [109], [118] or inconclusive results [105] while others have identified relationships [53], [94], [120], [152]. This discrepancy between studies that have and have not identified associations between PA and tissue morphology/degradation appears related to the consideration of additional factors that provide context for interpreting the cumulative PA metric. For example, Halilaj et al. (2018) showed that while indices of PA alone were not associated with region-specific tissue degradation, canonical correlation analysis identified a novel activity index and microstructural index that were significantly correlated ($r = 0.96$, $p = 0.004$) [53]. Moreover, bivariate correlations between the activity index and activity intensities indicated that both under-loading and over-loading can be detrimental to tissue health. Others have made similar observations wherein PA contextualized by BMI [152] or pain [107] explain variance in tissue health. Further, the theoretical cumulative knee adductor load (CKAL, product of the daily step count and the average knee adduction moment impulse measured in-lab) has been found to better discriminate between healthy individuals and patients with knee OA than the peak knee adduction moment alone [97]. However, conflicting results suggest that CKAL and other load-contextualized PA metrics do not explain any additional variance in cartilage morphology across samples of patients with clinical knee OA [108], [120]. The CKAL metric assumes that the average knee adduction moment trajectory across a number of strides measured in a single, laboratory-

based gait analysis is representative of every stride taken during daily life. This is likely not a valid assumption given that joint moment is gait speed-dependent (and nonlinearly in some cases) [159], in-lab "normal" gait speeds are not representative of out-of-lab observations [33]–[35], and because gait biomechanics vary stride-by-stride and throughout the day [70]. These motivate the characterization of cumulative tissue loads on a stride-by-stride basis that may pave the way to a better understanding of optimal loading and how to prescribe it.

Several factors may underlie the observed scarcity of studies implementing wearables-based remote biomechanical analysis. These include the requirement of additional analyses, algorithm processing time, lack of open-source algorithms and validation datasets, insufficient algorithm validation, a disconnect between algorithm developers and clinicians who wish to deploy those algorithms, and convenience of the wearable sensor system. For example, remote patient monitoring requires activity identification and gait event detection [70] (Figure 1) which may not be necessary for algorithm validation since data are labeled and other instrumentation can detect gait events (e.g., force plates). Open-source algorithms streamline use by teams not involved in the algorithm development both for deployment and further validation for which open-source datasets are important. Some algorithms may be insufficiently validated based on the validation sample (e.g., sample size [13], lack of validation on impaired populations [12]) or inadequate statistical error analysis [13]. In addition to these factors, Loncar-Turukalo et al. (2019) identified technology acceptance, comfortability, and the lack of research on battery technology and energy efficient solutions as potential barriers to the connected health movement [11]. Arguably, comfortability and the convenience of the wearable sensor system are the biggest hurdles preventing remote biomechanical analysis in practice. Many methods require complex sensor arrays across multiple body segments that are unattractive, inconvenient, and may discourage use [160], [161]. This has motivated the pursuit of reduced-sensor arrays [162], [163] and that seamlessly integrate into accessories commonly worn by patients (e.g., shoe [164], knee brace [165]).

Accelerometers were the most common wearable sensor used across all studies. Gyroscopes have greater power requirements compared to accelerometers which may have discouraged the use of IMU-based joint angle estimation algorithms. Advances in battery technology has been identified as a research gap in

remote monitoring [11] and may help overcome this barrier. Only three studies monitored muscle activity remotely using wearable EMG sensors [70], [76], [82]. This represents a relatively unexplored area in general that should be explored given the clinical relevance of muscle activation patterns and their relation to other biomechancial variables of interest. For example, EMG data are the most common input to machine learning models for estimating biomechanical time-series (Chapter 4) [12]. Novel models of muscle coordination have been developed that enable estimation of unmeasured muscle excitations from a measured subset thus reducing the number of required sensors (Chapter 5) [162]. However, interpretation of EMG recordings in applications requiring normalization by the maximal voluntary contraction is complicated in remote analysis since the properties of the skin-electrode interface varies throughout the day (e.g., sweat, temperature) and affects the normalization constant. Thus, compensatory methods should be the focus of future research.

A general increasing trend with respect to time was observed in the overall number of studies monitoring patients remotely in orthopedics (Figure 2). This finding has been observed in related reviews [11], [12] and reflects the increasing popularity in wearables-based human motion analysis. Impairments of the knee joint were studied the most across all articles included in this review which is consistently observed in reviews concerning rehabilitation in OA [166], [167]. However, considering only studies concerned with knee/hip OA or TKA/THA, the knee joint comprised 77% of studies in this review which is comparable to the same ratio for estimates of the global prevalence of knee and hip OA (87%) [2]. Despite the great number of studies focused on the knee joint, only 7% were concerned with monitoring patients post-ACLR. This should be the focus of future work as remote monitoring could be especially relevant for this population in the early rehabilitation stages.

1.5. Conclusion

Indices of cumulative PA are the most common metric for remote monitoring in orthopedics. Remote biomechanical analysis at a stride-by-stride level is relatively under-utilized considering the vast increase in research devoted to wearables-based algorithm development. Analyses of cumulative PA have provided unique, clinically relevant insight that should be incorporated into patient evaluations. Likewise,

analysis of individual strides has led to the development of novel digital biomarkers for monitoring rehabilitation progression. Future deployment of algorithms for continuous monitoring of joint and tissue loads may help clarify uncertainty surrounding their relationship with tissue degradation and implications for optimal loading.

1.6. Dissertation outline

This literature review highlights the need for practically deployable remote gait analysis techniques. In particular, open-source algorithms that automatically process raw data from a reduced sensor array for estimating clinically relevant biomechanical variables are needed. Thus, the aim of this dissertation was to lay the foundation for these techniques. Throughout this work, a focus was placed on exploring methods for monitoring knee joint loads using a reduced sensor array. Chapter 2 describes the validation of an algorithm for identifying gait events using a single, thigh-worn accelerometer. Chapter 3 describes the use of this algorithm as a part of an open-source platform that generalizes the processing pipeline for remote biomechanical analysis and its application for monitoring patients recovering from knee surgery. With the general analytical framework established, Chapters 4-6 then focus specifically on the development of methods for biomechancial analysis using a reduced sensor array. Chapter 4 is a review of machine learning techniques that have been proposed as solutions to the reduced sensor array estimation problem. The findings of that review motivated a potential hybrid technique combining both physics and probabilistic models comprised generally of two steps: (1) estimate a complete set of muscle excitations using only a measured subset (thus reducing the number of required sensors) and (2) use the complete set of muscle excitations from step (1) along with inertial sensor-based estimates of the system kinematics to drive the muscle contraction dynamics using EMG-driven techniques. In this way, clinically relevant biomechanics can be estimated (e.g., muscle force, moment, power). Chapter 5 describes the development and validation of a Gaussian process model of muscle synergy functions as a solution to step (1). Chapter 6 then describes the development and validation of the hybrid technique in step (2) utilizing the Gaussian process model developed in Chapter 5. Chapter 7 concludes with a summary of developments and implications for future work.

Chapter 2: Gait Event Detection Using a Thigh-Worn Accelerometer

A modified version of this chapter was published as: Gurchiek, RD, Garabed, CP, McGinnis, RS (2020). Gait event detection using a thigh-worn accelerometer. Gait and Posture, 80: 214-216.

2.1. Introduction

Recent developments in remote gait analysis promise improved monitoring of patients with both neurological and musculoskeletal conditions [8], [33], [70], [168], [169]. Gait event detection is doubly important for remote analyses as it provides the information needed to compute spatiotemporal gait variables, which alone are clinically informative, and it enables more complex analyses that require accurate gait phase segmentation (e.g., see Chapter 3 [70]). For example, knowledge of gait phase can aid in the use of simplifying assumptions such as zero foot velocity during stance for pedestrian tracking [170] or zero distal contact forces during the swing phase of gait for inverse dynamics-based estimates of joint moment [27].

Several gait event detection methods have been proposed and differ according to algorithm used and the number, type, and location of wearable sensors [171]. Methods utilizing a single, thigh-worn accelerometer are practically deployable as they present minimal burden to the patient and have demonstrated clinical utility [70], [172]. Aminian et al. (1999) validated an algorithm using a thigh-worn accelerometer for estimating spatiotemporal variables for preferred walking speeds which relied on constant low-pass filter cutoff frequencies. A modified version of the Aminian algorithm with adaptable cutoff frequencies was used for monitoring patients' gait following knee surgery (Chapter 3) [70]. It is important to note that accurate estimates of spatiotemporal gait variables do not infer accurate estimation of the actual foot contact or foot off events. These errors should be characterized so that gait phase-dependent task constraints can be applied appropriately. However, errors in thigh-worn accelerometer-based estimates of foot contact and foot off events have not been reported in previous studies [172]–[174]. Therefore, the purpose of this study was to quantify the error in estimating foot contact and foot off events during gait using a similar version of the

algorithm proposed in Chapter 3 [70]. We also report spatiotemporal gait variable estimation performance for comparison to previous studies.

2.2. Methods

2.2.1. Experimental design

Thirty-two healthy subjects (16 female, 21 ± 3 years old, height (data available from 31 subjects): 1.74 ± 0.09 m) walked for one-minute at various self-selected walking speeds on a pressure treadmill (h/p/cosmos quasar, Nussdorf-Traunstein, Germany, 100 Hz) with a three-axis accelerometer (Opal, APDM, Inc., Portland, OR, USA) on the left and right lateral thigh. The range of walking speeds (0.56 – 1.78 m/s) and stride times (0.91 – 1.57 s) analyzed well encompass those observed for young and elderly healthy populations [33], [175] as well as for patients with neurological and musculoskeletal impairment [70], [168]. Ground truth foot contact and foot off instances were identified from the vertical ground reaction force measurements provided by the treadmill using a 20 N threshold. Accelerometer data were downsampled from the original sampling frequency (128 Hz) to 31.25 Hz to mimic sampling frequencies used for remote monitoring [70]. All subjects provided written consent to participate and study activities were approved by the local Institutional Review Board.

2.2.2. Event detection algorithm

The first step is to estimate the direction of the thigh longitudinal axis in the sensor frame. During a standing calibration trial, the thigh is assumed vertical such that the longitudinal axis of the thigh is aligned with the gravity vector but pointing up. Because the subject is still during this calibration trial, the average value of the measured accelerometer data during this period approximates the world frame vertical axis (i.e., the thigh longitudinal axis by assumption) represented in the sensor frame. The algorithm takes as input the raw accelerometer data projected onto this thigh longitudinal axis during walking.

Next, the power spectral density (PSD) of the thigh accelerations during the whole walking bout is estimated. The dominant frequency between 0.5 and 4 Hz is used to approximate the step frequency (Figure

4a). Next, we approximate the stride frequency as the largest frequency less than the approximate step frequency that is associated with a peak in the PSD (Figure 4a). The acceleration signal is then low-pass filtered at the approximate step and stride frequencies as well as five times the approximate stride frequency. Low-pass filtering with a cutoff equal to five times the approximate stride frequency is intended to retain only those signal characteristics associated with the true thigh kinematics while removing those characteristics due to noise (e.g., soft-tissue artefact). Scaling with stride frequency in this way enables the algorithm to adapt to variable gait speeds (more signal content is retained for larger stride frequencies) and the choice of five as the scalar is based on cutoff frequencies used to remove soft-tissue artefact in surface electromyography signal processing [176].

These three signals are then used to identify foot contact and foot off events. The acceleration signal low-pass filtered at the approximate step frequency is characterized by two peaks per stride cycle and one of them is associated with foot off (arrow 3 in Figure 4b). The peak associated with foot off is most often the larger one, but not always. To identify the correct peak in the step frequency filtered signal, we take advantage of the fact that the thigh acceleration low-pass filtered at the approximate stride frequency has only one minimum per stride which precedes foot contact and is associated with mid-swing. Thus, the proposed algorithm works by first identifying all local minima in the stride frequency filtered signal (arrow 1 in Figure 4b) providing a rough estimate of the instant of mid-swing prior to each foot contact. In some rare cases, we found the stride frequency filtered signal will have two minima per stride. These cases are identified by computing the time difference between all identified minima. If any two minima differ by less than a user-specified parameter (minimum stride time), then the algorithm has to decide which is the correct one (i.e., the one that precedes the true foot contact). To make this decision, we take advantage of the fact that the signal immediately following the true pre-contact minima is expected to be more variable (due to high frequency characteristics associated with impact) than the signal in the interval following the false one (which precedes swing phase). We compute the sample variance of the signal (high-pass filtered at 10 Hz) for two intervals: (i) the interval beginning with the first minimum and ending with the second and (ii) the interval following the second minimum with length equal to that in (i). The minimum preceding the interval with largest variance is then identified as the true pre-contact minimum. For each of these identified pre-

contact minima, we find the next positive going 1 g crossing in the signal low-pass filtered at five times the approximate stride frequency (determined via linear interpolation where necessary). This event is the estimate of foot contact. Finally, we identify the last peak in the step frequency filtered signal preceding each pre-contact minima in the stride frequency filtered signal. This event is the estimate of foot off.

The proposed algorithm is different than that proposed in [172] in that adaptable cutoff frequencies were used and in the definition of the signal feature associated with foot contact. In [172], foot contact was associated with a peak in the raw acceleration signal that occurs near the positive going 1 g crossing signal feature in the proposed algorithm. We did not find that this peak was reliably identifiable for all subjects. We found that the positive going 1 g crossing was more reliably identifiable and it provided a consistent starting point for stride cycles which is important in computing time-series asymmetries for clinical evaluation (see Chapter 3) [70].

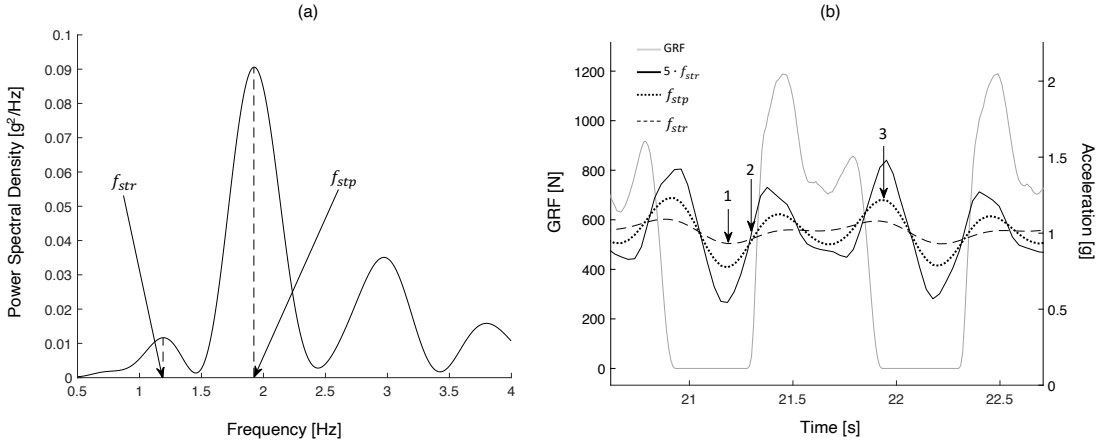

Figure 4: Gait event detection algorithm. First, step (f_{stp}) and stride (f_{str}) frequencies are approximated from the power spectral density of the raw accelerometer signal (a). Foot contact and foot off events are then determined algorithmically by associating consistently identifiable features in the processed accelerometer signals (b, arrows 1-3) with ground truth data obtained from the measured vertical ground reaction forces (b, GRF, solid grey line, left vertical axis). The minimum in the f_{str}-filtered signal (b, dashed black line) preceding foot contact (b, arrow 1) are identified first. The estimate of foot contact is then associated with the positive going 1 g crossing (b, arrow 2) in the 5 Hz-filtered signal (b, solid black line) following this minimum. Finally, the foot off event is associated with the second peak (b, arrow 3) in the f_{stp}-filtered signal (b, dotted black line) following foot contact.

2.2.3. Statistical analysis

Estimation performance was quantified across all strides using the absolute error (AE) and root mean square error (RMSE) between the reference measurements and accelerometer-based estimates of foot contact and foot off events as well as stride time, stance time, and swing time. The bout-average stride, stance, and swing time estimates were further evaluated using Pearson's correlation coefficient and Bland-Altman analysis for repeated measures [177], [178].

2.3. Results

Across all strides (N = 3,898), the estimation error was 39 $\pm$ 28 ms AE (47 ms RMSE) for foot contact; 28 $\pm$ 28 ms AE (40 ms RMSE) for foot off; 11 $\pm$ 14 ms AE (17 ms RMSE) for stride time; 46 $\pm$ 31 ms AE (55 ms RMSE) for stance time; and 45 $\pm$ 30 ms AE (54 ms RMSE) for swing time. The correlation between the estimated and measured bout-average stride, stance, and swing times were 1.00, 0.92, and 0.80, respectively. The bias and 95% limits of agreement (lower limit, upper limit) for the bout-average stride, stance, and swing time estimates were 0 (-2, 3) ms, 13 (-85, 110) ms, and -12 (-109, 85) ms, respectively (Figure 5). The (5^{th}, 95^{th}) percentiles (mean $\pm$ 1.65 SD) of the foot contact and foot off estimation errors were (-91, 51) ms and (-70, 60) ms (Figure 6).

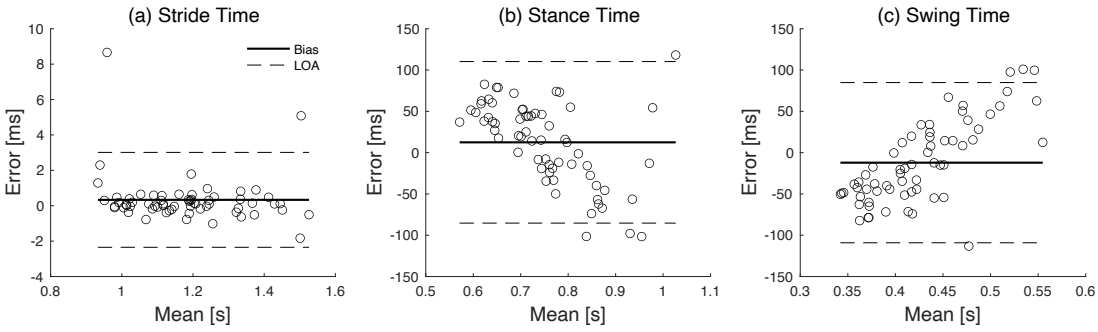

Figure 5: Bland-Altman plots of the estimation error (vertical axis) between the measured and estimated bout-average stride time (a), stance time (b), and swing time (c) against the mean of the measured and estimated values (horizontal axis). The solid black line in each figure is the bias (mean error) and the dashed black lines denote the 95% limits of agreement (LOA).

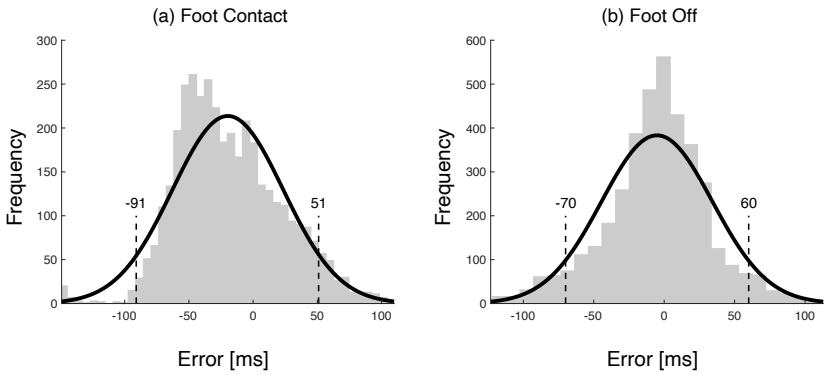

Figure 6: Error distributions for estimates of foot contact (a, left) and foot off (b, right) events. The solid black line is a normal distribution fit to the discrete histogram data (grey bars). Errors are computed as the algorithm estimated timestamp minus the reference measurement timestamp such that a negative error means the algorithm estimate was early and a positive error means the algorithm estimate was late. The dashed black lines in each figure indicate the 5th (lesser number) and 95th (greater number) percentiles.

2.4. Discussion

The RMSE in estimating foot contact and foot off events (47 ms and 40 ms) present improvements over that reported for a shank accelerometer (80 ms and 68 ms) [17]. Methods using a sacral accelerometer appear more accurate for foot contact estimation (28 ms RMSE), but with comparable foot off estimation errors (40 ms RMSE) [17]. Based on the error distributions in estimating these gait events (5th and 95th percentiles), biomechanical analyses enforcing task constraints dependent on the stance (swing) phase of gait should force the assumption only for data at least 91 ms after (51 ms before) the estimated foot contact event and 60 ms before (70 ms after) the estimated foot off event. This knowledge provides the intervals of time during which one may apply stance phase- (e.g., zero velocity updates) and/or swing phase- (e.g., zero distal contact force) based assumptions with 95% confidence. The largest of these (91 ms) amounts to less than three samples for the 31.25 Hz sampling frequency. In a post-hoc analysis we found nearly identical results in foot contact and foot off estimation error with data sampled at 128 Hz (40 ms and 28 ms AE, respectively) and thus inaccuracies in the proposed algorithm cannot be attributed to the relatively low sampling frequency. Bland-Altman analysis revealed an apparent relationship between stance and swing time errors and their

magnitudes (Figure 5). Similar results have been observed previously [17] and warrants further investigation. Nevertheless, spatiotemporal gait variables were estimated with strong correlations ($r \geq 0.80$) and low absolute errors (11 to 46 ms) comparable to other methods [17]. These results were observed for a large sample size relative to previous studies of similar aim [17], [172], [173] and for a broad range of gait speeds and stride times which are representative of a multitude of subject populations [33], [70], [175], supporting the use of this approach for remote gait analysis.

Chapter 3: Open-Source Remote Gait Analysis: A Post-Surgery Patient Monitoring Application

A modified version of this chapter was published as: Gurchiek, RD, Choquette, RH, Beynnon, BD, Slauterbeck, JR, Tourville, TW, Toth, MJ, McGinnis, RS (2019). Open-source remote gait analysis: A post-surgery patient monitoring application. Scientific Reports, 9(1): 17966.

3.1. Introduction

The digital medicine revolution is driven by advances in wearable sensor technology and the algorithms for analyzing and interpreting their data. These mobile health technologies enable improved remote patient monitoring, personalized intervention, and could be used to provide improved continuity across care transitions. While transitional care has been recognized as a national priority [179], and has been shown to improve outcomes, increase the efficient use of health care resources, and decrease health care costs [180], [181], current interventions are resource and personnel intensive [182]. Digital medicine innovations that harness existing cyber infrastructures, wearable sensors, and mobile devices may improve the efficiency and effectiveness of transitional care interventions. This approach could be transformative for a broad range of clinical domains, including for neurological [183], musculoskeletal [184], and mental health [9], [185] conditions.

Concerning current techniques for remote patient monitoring, physical activity is the most targeted health behavior, with a large commercial market. However, these measures are too general for most clinical applications as they provide minimal biomechanical or physiological insight at a joint- or limb-specific level. For both neurological and musculoskeletal disorders, physical activity (e.g., step count) is often the primary outcome measure from free-living wearable sensor data (Chapter 1) [119], [186]. In these clinical populations, traditional gait analysis provides far more valuable information concerning neuromusculoskeletal health and, in the aftermath of various clinical interventions, recovery of physical function [47]. However, these traditional assessments are constrained to specialized motion analysis laboratories which may not accurately reflect an individual's free-living gait [33]. This motivates the pursuit of remote gait analysis techniques able to capture more clinically relevant biomechanics including

quantitation of motor control indices (e.g., muscle activation patterns [187]) and musculoskeletal dynamics [188].

To answer this unmet need, several groups have started to explore methods for tracking free-living gait biomechanics [29], [33], [168], [189]–[193]. The general framework for remote gait analysis shared by these efforts has three steps: (1) identification of walking bouts, (2) stride detection, and (3) analysis. This approach has been used to detect and characterize bradykinesia in Parkinson's disease patients [189] and demonstrate that in-lab observations of gait speed [33] and gait asymmetry [168], [192] differ from daily-life. The components of this framework reflect recent advances in wearable sensor-based activity identification [194], event detection [195], and biomechanical analysis [20], [26], [27], [196]–[198]. The development and application of these solutions are multi-disciplinary efforts requiring research teams with expertise in medicine, data science, and engineering. Open-source solutions may allow analysis of wearable sensor data collected in free-living conditions by teams without expertise in signal processing or machine learning. This reduces barriers to applying digital health solutions for remote patient monitoring.

To this end, we present an open-source analytical platform which captures this general framework (Figure 7) and could be applied for remote biomechanical analysis of any task (see *https://github.com/M-SenseResearchGroup/RemoteBMX*). It has been designed with a modular structure to enable flexibility and to encourage improvements and customization from members of the scientific community. For example, customization could allow for the analysis of other tasks (e.g., stair ascent, running), the extraction of alternative clinical information, or the utilization of different wearable sensors. These modifications are dependent on the patient population being monitored. To demonstrate how the platform may be tailored for a specific patient population, it was deployed as a rehabilitation monitoring application in patients recovering from reconstructive surgery of the anterior cruciate ligament (ACLR). ACLR is the most effective treatment for ACL rupture [199]. However, approximately 50% of patients who undergo ACLR will go on to develop post-traumatic osteoarthritis (PTOA) [200]. Previous research suggests that altered gait biomechanics following ACLR are responsible for this phenomenon [31], [200]. Pathological gait is often characterized by

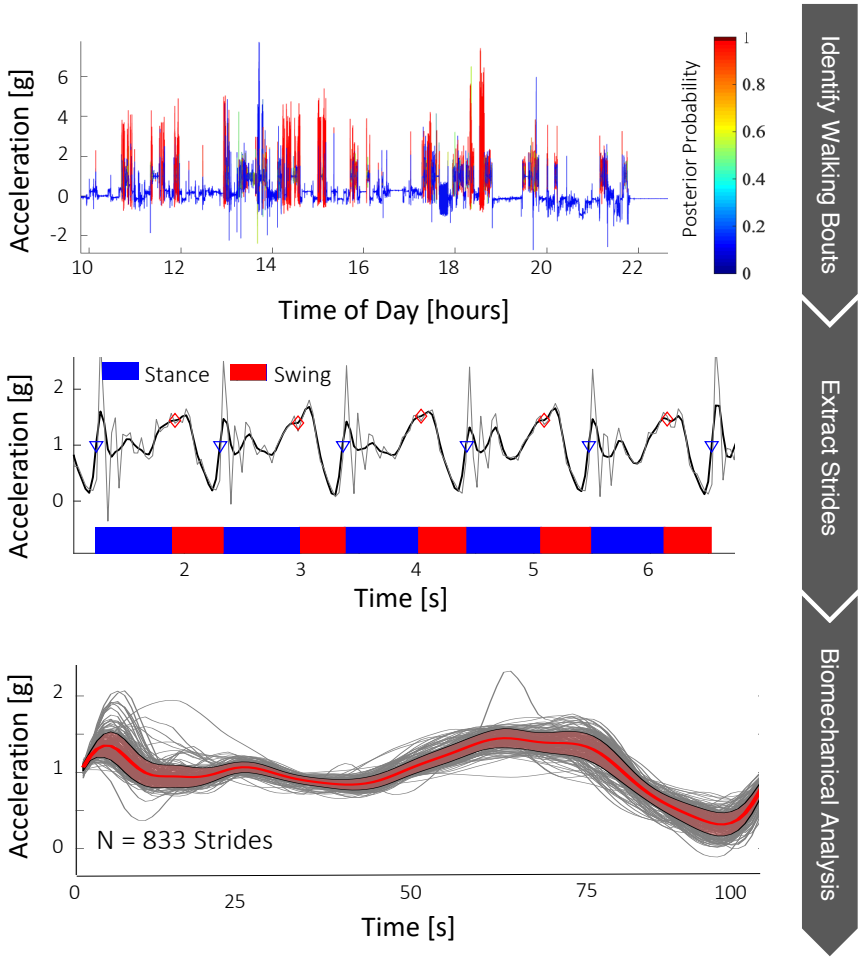

Figure 7: Graphical summary of the proposed remote gait analysis. The proposed approach is comprised of three basic steps: (1) walking bout identification, (2) stride extraction and gait phase segmentation, and (3) biomechanical analysis of individual strides.

inter-limb asymmetries which manifest early in the post-surgical period [43], [44], [201], and develop into compensatory gait patterns over time [47], [202]. It is imperative that these maladaptations are identified early so that corrective rehabilitative interventions can be pursued [45]. Thus, this application presents an ideal candidate for which to demonstrate the clinical utility of the proposed platform.

Platform modifications were context-specific and driven by the current understanding of the clinical problem. In the context of ACLR, inter-limb gait asymmetry has been identified as a biomarker for recovery [44], [201], [203]. These asymmetries represent altered gait kinematics that are linked to PTOA-related knee

joint contact forces in this population [47], [204], [205]. Quadriceps muscle dysfunction is common following ACLR [187], [203], [206], [207] and may be responsible for the development of pathological gait. Thus, direct observation of asymmetric gait kinematics and quadriceps muscle activity in the early post-operative period could identify pathological gait and signal the need for remedial actions to prevent developing PTOA. However, algorithms for extracting this information from wearable sensor data captured in free-living conditions do not yet exist.

To this end, patients recovering from ACLR present an ideal population for which to specify and test the use of the proposed platform. Our analysis was tailored for monitoring gait asymmetries relating to spatiotemporal variables, and kinematic and muscle activation time-series. Our novel analysis quantifies asymmetry in the following gait measures: duty factor (DF); mean surface electromyography (sEMG) amplitude of the rectus femoris during the stance and swing phase of gait; muscle activation time-series; as well as cranial-caudal (CC), medio-lateral (ML), and antero-posterior (AP) thigh acceleration time-series. A composite asymmetry score was also defined as the average of these seven asymmetries. We show the ability of these asymmetry indices to discriminate between patients at different time points in the recovery process and compared to healthy controls. Step count estimates from a commercially available activity monitor worn by some of the patients also enables a comparison of the proposed analysis to current techniques for monitoring recovery.

3.2. Methods

3.2.1. Study design

Our system was deployed to evaluate gait in three groups of subjects: (1) subjects less than six weeks after ACLR (T1: 3 male, 3 female, recovery time (mean $\pm$ SD) = 2.1 $\pm$ 1.6 weeks, age = 26 $\pm$ 11 yo, height = 1.74 $\pm$ 0.11 m, mass = 70.52 $\pm$ 16.21 kg), (2) subjects at least six weeks after ACLR (T2: 2 male, 4 female, recovery time = 17.2 $\pm$ 2.0 weeks, age = 26 $\pm$ 6 yo, height = 1.70 $\pm$ 0.13 m, mass = 77.82 $\pm$ 15.44 kg), and (3) healthy controls (C: 8 male, 8 female, age = 23 $\pm$ 5 yo, height = 1.74 $\pm$ 0.11 m, mass = 70.51 $\pm$ 13.17 kg). Each subject wore a single sensor (BioStamp, MC10 Inc., Lexington, MA) on the muscle belly of

the rectus femoris of each thigh, which recorded tri-axial accelerometer (sampling frequency: 31.25 Hz, range: ± 16 g) and surface electromyography (sEMG) (sampling frequency: 250 Hz) data during daily life for one day. Daily step counts from a waist worn activity monitor (Actigraph, Pensacola, FL) were also available for nine ACLR patients (T1: N = 4, T2: N = 5). These enable a comparison between the proposed analysis and current standards (e.g step counts [119]) in their respective sensitivity to patient recovery. This study was approved by the University of Vermont Institutional Review Board. All study activities were in accordance with the relevant guidelines and informed consent was obtained from all participants.

3.2.2. Remote gait analysis platform

The general approach to biomechanical analysis of any task in daily life using the proposed platform takes on the following form: (1) activity identification, (2) event detection, and (3) analysis. The specifications for the current ACLR patient monitoring application were described graphically in Figure 7. This framework easily allows future users to make application-specific modifications to analyze different tasks (e.g., crutching, stair ascent) or analyze differently the same tasks presented in the current study. For monitoring ACLR patients, the proposed analysis requires, at a minimum, raw accelerometer data to operate. Herein, we also consider sEMG data to provide a more complete picture of free-living gait biomechanics in this population.

3.2.3. Identification of walking bouts

A support vector machine (SVM) binary classifier (Gaussian kernel) was used to identify walking bouts. The model was trained using annotated tri-axial accelerometer data from the healthy control group recorded during various activities including multi-speed walking and running over ground and on a treadmill, stair ascent and descent, crutching, sitting, standing, and lying down. Annotated walking, crutching, lying down, sitting, and standing data were also available from three ACLR patients. Data from each activity were partitioned into four-second, non-overlapping windows. This yielded a total of 3,102 observations (1,318 walk; 1,784 not walk) for training the walking classifier.

The constant thigh relative sensor attitude was determined for each leg by considering accelerometer data during a standing calibration trial (as in [26]) and used to project raw accelerometer data

onto the thigh-fixed cranial-caudal axis (referred to as CC_i, $i \in \{R, L\}$, R: right, L: left, directed proximally). The first principal component of acceleration in the transverse plane during each four-second window was assumed to coincide with the antero-posterior axis of the thigh (referred to as AP_i, points anteriorly, see [153]), from which the medio-lateral axis (referred to as ML_i, points laterally) can also be determined. Accelerometer data were projected onto these three anatomical axes and used to extract a total of 152 time and frequency domain features. Performance of the classifier was evaluated using leave-one-subject-out (LOSO) cross-validation where, for each iteration, data from one subject was removed for testing and a classifier was trained on the remaining data using only those features from the training set with a Davies-Bouldin index [208] (*DBI*) less than two. From the LOSO validation, the classifier achieved 98.32% accuracy, 97.04% sensitivity, 99.27% specificity, and the area under the ROC curve (AUC) was 1.00. The classifier made no misclassification errors (100% accuracy) on the 132 observations from the three ACLR patients during the LOSO validation, which supports its use to identify gait in this population.

Following this performance characterization, annotated data from all sixteen healthy controls and the three ACLR subjects were used to train the classifier deployed for the proposed analysis. Davies-Bouldin feature selection ($DBI < 2$) indicated six features to use as input to the classifier: (i) average 25th quantile of CC_R and CC_L, (ii) average correlation between CC_R with AP_L and CC_L with AP_R, (iii) correlation between CC_R with CC_L, (iv) average skewness of AP_R and AP_L, (v) average percentage of signal power contained below 0.25 Hz for AP_R and AP_L, and (vi) average median value of AP_R and AP_L.

These six features were extracted from each four-second window of raw accelerometer data collected during daily life from all subjects and were used as input to the SVM classifier to label each window as "walking" or "not walking." This enabled an estimate of the total amount of time spent walking which we used as an indicator of gross physical activity. Windows labeled as walking were aggregated into walking bouts if (1) at least two consecutive windows (8 seconds) were classified as walking, and (2) the posterior probability of the window's walking classification was at least 0.8. This threshold was determined as the point that minimized the distance between the classifier's ROC curve and the point (0, 1) on the true positive rate-false positive rate plane. A very small subset (451 observations or approximately 0.19%) of bouts

containing clipped sEMG (e.g., due to sensor delamination from skin) and/or accelerometer signals were removed.

All aspects of the walking classifier presented herein (feature extraction, training, validation, etc.) were performed using the MATLAB R2018a Statistics and Machine Learning Toolbox (Version 11.3) and our open-source platform specifically designed for wearable sensor-based activity identification. This platform streamlines the development of activity classifiers by enabling the building of population-specific feature sets, the extraction of novel features, feature manipulation (e.g., PCA, DBI), training and testing of various classification models, and automated leave-one-subject-out cross-validation with detailed error analysis. For more details see *https://github.com/M-SenseResearchGroup/ActivityIdentification*.

3.2.4. Stride extraction and gait phase segmentation

Foot contact and foot off events were identified as described in Chapter 2. The implementation used in this analysis slightly differs from the description in Chapter 2 in the identification of the true pre-contact minima and in that the signal used for foot contact estimation (positive going 1 g crossing) is based on a constant 5 Hz cutoff frequency as opposed to the adaptable cutoff frequency described in Chapter 2 (five times the approximate stride frequency). Constraints were placed on the stride time (0.91 s – 1.57 s) and duty factor (DF, percentage of stride cycle spent in stance) (0.44 – 0.73) of identified strides to avoid accidental analysis of non-walking data [175]. To be considered for further analysis, an eight-second walking bout had to include at least two strides.

3.2.5. Biomechanical analysis

Accelerometer and sEMG signals from each extracted stride were used to compute discrete biomechanical variables to evaluate gait. We quantify asymmetries in gait kinematics and muscle activity between legs during each stride using accelerometer data in each anatomical direction low-pass filtered with a cutoff frequency of 6 Hz (as per [209]) and the envelope of the sEMG data (computed as per [209]). These four time-series (sEMG, CC, AP, ML) were normalized by stride time so that each sample corresponds to a percentage of the gait cycle.

Eight indices of asymmetry (referred to as asymmetries) were computed for each eight-second walking bout. Three of these asymmetries ($a_k, k \in \{1,2,3\}$) were the relative difference between discrete biomechanical variables of each leg as per

$$a_k = \left| \frac{I_k - H_k}{H_k} \right| \tag{3.1}$$

where I_k and H_k are the values of discrete variable k for the injured and healthy leg respectively. The three discrete variables for this analysis were mean sEMG during stance, mean sEMG during swing, and DF. The other four asymmetries (a_m) are defined as per

$$a_m = 0.5(1 - r_m). \tag{3.2}$$

where $m \in \{\text{sEMG}, \text{CC}, \text{AP}, \text{ML}\}$, and r_m is the correlation coefficient of the ensemble means of like time-series between the injured and healthy legs. The final index of asymmetry was a composite asymmetry score equal to the mean of the aforementioned asymmetries.

3.2.6. Statistical analysis

Outlier asymmetries were identified for each patient and removed after the biomechanical analysis as a final check to remove potentially errant data. A one-way analysis of variance (ANOVA) was used to compare the daily average of gait asymmetries and stride times between the three groups. Normality was checked using the Kolmogorov-Smirnov test. If the assumption of normality was violated, group distributions were compared using the Kruskal-Wallis test. If a significant difference was detected, post-hoc pairwise comparisons were made using Tukey's honest significant difference criterion. Effect sizes (Cohen's *d*) were computed where the ANOVA revealed significant differences and were interpreted qualitatively as weak ($d < 0.25$), small ($0.25 \leq d < 0.5$), medium ($0.5 \leq d < 1.0$), and large ($d \geq 1.0$) [210]. The agreement between our estimate of gross physical activity (total time spent walking) and the Actigraph step counts estimate was evaluated using Pearson's correlation.

To compare the sensitivity of physical activity with that of our composite asymmetry score and estimated stride times to time spent in recovery, we also determine the correlation between recovery time

with composite asymmetry, stride time, Actigraph step counts, and estimated time spent walking for each ACLR patient using Spearman's rank correlation. The level of significance was set to 0.05 for all statistical tests.

3.3. Results

Subjects were categorized as either T1 (less than 6 weeks post-surgery), T2 (greater than 6 weeks post-surgery) or C (healthy controls). Data were collected for 20.24 ± 6.28 hours on average for each subject (except one T1 patient for whom no walking bouts met the criteria for analysis) and a total of 41,893 strides were analyzed (T1: 1,743 strides, T2: 9,616 strides, C: 20,939 strides). Estimated total time spent walking (hours) was strongly correlated ($r = 0.71, p = 0.03$) with Actigraph step counts (Figure 8) but showed a stronger correlation with recovery time ($r = 0.63, p = 0.08$) than Actigraph step counts ($r = 0.25,\ p = 0.52$), although neither was statistically significant. The composite asymmetry score ($r = -0.87,\ p < 0.01$) and stride time ($r = -0.91,\ p < 0.01$) were both strongly associated with recovery time (Figure 9).

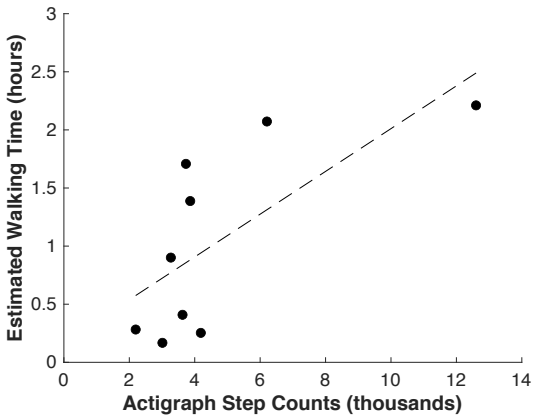

Figure 8: Scatter plot of the total time spent walking from the proposed method vs step counts estimated by Actigraph activity monitors.

Stride times and most gait asymmetry measures decreased across groups (i.e., T1 > T2 > C). Pairwise significant differences were found between C and T1 as well as T1 and T2 for stride times and all asymmetries (all with large effect sizes) except mean normalized sEMG which was trending towards significance (stance: $p = 0.05$, swing $p = 0.12$) (Table 2). All time-series (sEMG, CC, AP, ML), duty factor, and composite asymmetries were significantly different ($p < 0.01$) between C and T1, but only the CC acceleration time-series, duty factor, and composite asymmetries were significantly different between T1 and T2 (Table 2). There were no differences between C and T2 for any asymmetries.

The proposed framework enables the investigation of gait biomechanics continuously throughout the day. To demonstrate the utility of this application, composite asymmetry scores averaged over each 15-minute bin are illustrated in Figure 10 for one patient with longitudinal observations at about 2 weeks post-surgery (red dashed line) and again 17 weeks later (blue dashed line). The solid lines illustrate the average trend of the other groups for comparison (T1: red, T2: blue, C: black).

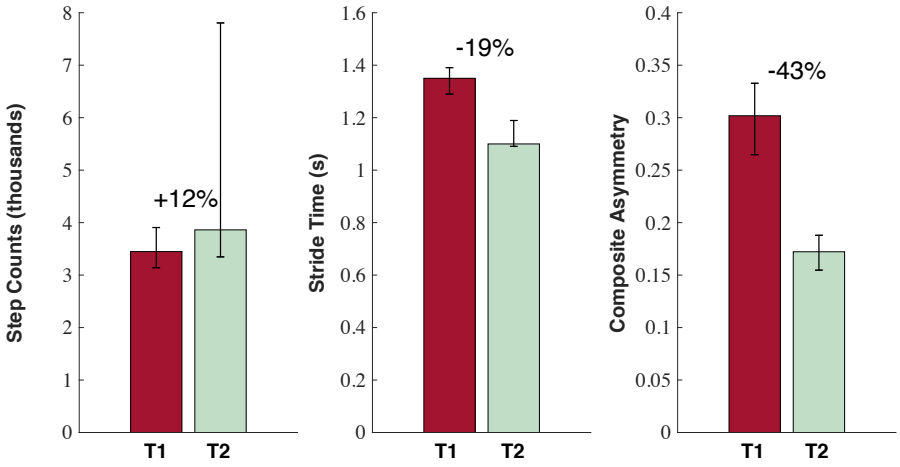

Figure 9: Percent difference in the median Actigraph step counts (a), strides times (b), and composite asymmetry scores (c) between the T1 (red) and T2 (green) groups. Error bars denote the 25th and 75th quantiles.

Table 2: Comparison of daily average stride times and asymmetries

	Mean (SD)			Pairwise Comparisons		
Variable	T1	T2	C	C-T1	C-T2	T1-T2
ST	1.34 (0.08)	1.14 (0.07)	1.10 (0.05)	**4.08****	0.34	**2.70****
DF	0.13 (0.05)	0.04 (0.02)	0.03 (0.01)	**4.20****	0.61	**2.48****
EMG St	0.22 (0.12)	0.13 (0.03)	0.15 (0.04)		ANOVA $p = 0.05$	
EMG Sw	0.41 (0.14)	0.27 (0.04)	0.29 (0.12)		ANOVA $p = 0.12$	
EMG(t)	0.41 (0.10)	0.29 (0.11)	0.25 (0.07)	**2.10****	0.52	0.07
AP(t)	0.32 (0.13)	0.10 (0.05)	0.07 (0.04)	**3.57****	0.49	0.08
ML(t)	0.38 (0.13)	0.28 (0.04)	0.24 (0.06)	**1.74****	0.51	0.08
CC(t)	0.20 (0.08)	0.06 (0.04)	0.03 (0.02)	**4.19****	0.26	**2.20****
Comp.	0.29 (0.05)	0.17 (0.03)	0.15 (0.03)	**3.78****	0.65	**2.96****

ST: Stride Time; units seconds. Duty Factor (DF), EMG Stance (EMG St), and EMG Swing (EMG Sw) asymmetry scores are the percent difference between the healthy and injured leg (i.e., 0.5 indicates that the between leg difference is 50% that of the healthy leg). EMG(t), AP(t), ML(t), and CC(t) are pattern asymmetries for the sEMG time-series and the antero-posterior, medio-lateral, and cranial-caudal thigh acceleration time-series respectively. Composite asymmetry score (Comp.) is the average value of the other seven asymmetry scores. **Bold** numbers in the pairwise comparisons are effect sizes ($^{*}p \leq 0.05$, $^{**}p \leq 0.01$) and non-bold numbers are the p values for non-significant pairwise differences.

3.4. Discussion

Herein, we present a new computational platform that enables multi-modal gait analysis in free-living conditions based on data from commercially available wearable devices. We demonstrate the utility of this platform in a sample of patients recovering from ACLR. Results suggest that platform-derived gait measures agree with gold standard actigraphy but better discriminate between patients' gait at different time points in the recovery process. Similarly, platform-derived measures are able to detect gait differences between patients at different stages of recovery, and with large effect sizes. We further discuss the implications of these results and how this new platform could be deployed for remote gait analysis in a variety of clinical populations.

Currently, actigraphy technologies are broadly used for characterizing free-living physical activity and gait [119], [186]. The statistically significant association we observe (Figure 8; $r = 0.71, p = 0.03$) between actigraphy-derived daily step counts and platform-derived walking time suggest that the proposed analysis platform is valid for capturing free-living physical activity. Similar findings of agreement between different indices of physical activity have been reported elsewhere [119]. Although the correlation between recovery time and the platform-derived measure of walking time ($r = 0.63, p = 0.08$) appears stronger than that for actigraphy-derived step counts ($r = 0.25, p = 0.52$), neither was statistically significant, which also agrees with previous work [119]. This finding is intuitive as there are a variety of extraneous variables that affect daily physical activity and have nothing to do with rehabilitation progress (e.g., weather, day of the week). These results suggest a fundamental limitation of physical activity indices for monitoring rehabilitation progression. The vast majority of research investigating pathological biomechanics characteristic of gait following ACLR suggests the existence of more sensitive metrics including quadriceps activation [211], ground reaction force [44], and joint work [201]. However, these metrics currently require laboratory-based methodologies that are not widely transferable to clinical use.

The proposed platform answers this unmet need by capturing more subtle biomechanical changes in gait associated with recovery under free-living conditions. Our results demonstrate that platform-derived stride times are more strongly associated with recovery time ($r = -0.91,\ p < 0.01$) than both actigraphy-derived step counts ($r = 0.25,\ p = 0.52$) and platform-derived estimates of total walking time ($r = 0.63, p = 0.08$). These results are supported by previous work where decreased walking speeds have been associated with decreased joint health following ACLR [212] (stride times are associated with walking speed [175]). These results provide additional evidence in support of the utility of platform-derived measures of free-living gait biomechanics.

Stride time, walking speed, and other spatiotemporal parameters are informative biomechanical measures related to recovery in this population, and more broadly are important indicators of mobility impairment [20], [33], [197], [212]. Nevertheless, a need has been recognized for more sensitive biomarkers. For example, it has been shown that spatiotemporal *symmetry* may manifest even in the presence of a true

gait abnormality [213]. Further, research suggests the pursuit of metrics that characterize the *full waveform pattern* of mechanical variables throughout the gait cycle [214]. In light of these results, the proposed platform has been designed to capture additional measures that may be more indicative of, and sensitive to, rehabilitation progress. Figure 9 and Table 2 report results from our efforts to define a novel gait asymmetry analysis that incorporates temporal (duty factor), kinematical (ML, AP, CC acceleration time-series), and neuromuscular (sEMG Swing, sEMG Stance, and sEMG time-series) measures. The effect sizes of the differences between groups were largest for the asymmetries relating to kinematic measures and duty factor. The mean normalized sEMG during stance and swing asymmetries were the only variables for which no significant difference was found, which may reflect increased within subject and group variance. The composite measure that captures asymmetries within each of these domains demonstrates significant differences between T1 and T2/C with large effect sizes ($d = 2.96$ and $d = 3.78$ respectively) suggesting that this measure may be useful for tracking biomechanical changes associated with rehabilitation progress.

To this end, we further examine the association of these measures of free-living gait biomechanics with time since surgery. Both stride time and our new composite asymmetry score present strong relationships with recovery time ($r = -0.91,\ p < 0.01$ and $r = -0.87,\ p < 0.01$ respectively) and are noticeably larger than that observed for any gross index of physical activity. Further, when comparing T1 and T2, the largest effect sizes were observed for the composite asymmetry ($d = 2.96$) which was also responsible for the largest percent difference between T1 and T2 (-43%) when compared to both stride time (-19%) and step counts ($+12\%$) (Figure 9). This suggests that these more detailed biomechanical measures may provide increased sensitivity to recovery time in this population and thus may be suitable candidates to pursue in developing novel *digital biomarkers* for tracking rehabilitation progress and gait asymmetries that have pathological consequences [44], [201]. The proposed asymmetry analysis also provides the clinician with insight into patient-specific adaptations and their particular mechanistic origin since it captures indices of both muscle activation and limb kinematics.

Having established the improved association between free-living measures of gait asymmetry and recovery time, we further examine how this new measure changes over the entire wear time for patients monitored in this study. Figure 10 reports the composite asymmetry score captured during every gait bout identified between 11 am and 8 pm for a single patient with longitudinal observations and with the group average trend for subjects in the T1, T2, and C groups for comparison. The difference between groups based on asymmetry magnitudes alone reflects the same general pattern observed in Table 2, namely a convergent trend toward decreased gait asymmetries with increased recovery time. However, Figure 10 provides additional insight whereby gait asymmetries appear more variable throughout the day for the early post-surgery time point when compared to the later time point and that of the control group. This supports the need for remote gait monitoring, as this variability would not be captured in a single gait assessment. Further investigation is necessary to understand the origins of this observation which may, for example, indicate an increased susceptibility to fatigue early in rehabilitation. The similar trends observed between the dashed

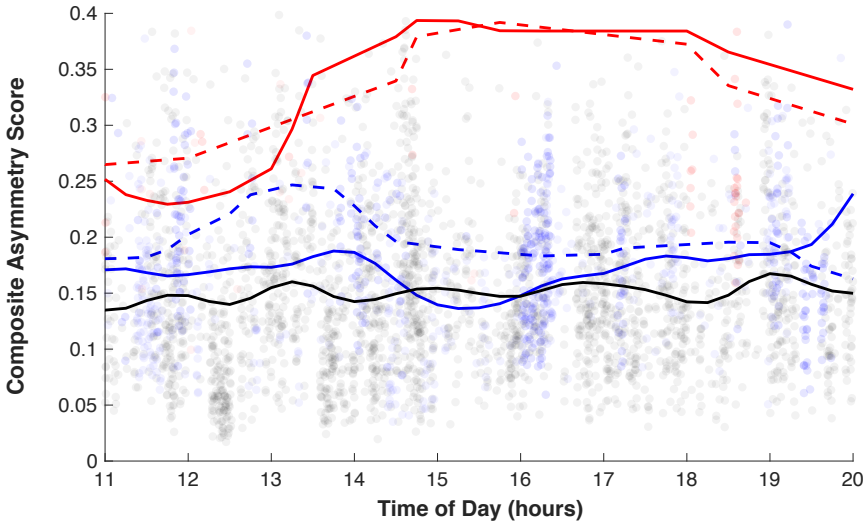

Figure 10: Composite asymmetry score throughout the day (averaged over every 15-minute bin) for a patient with longitudinal observations: 2.1 weeks post-surgery (red dashed line) and 19.1 weeks post-surgery (blue dashed line). The solid lines illustrate the average trends for the T1 (red), T2 (blue), and C (black) groups. The longitudinal patient's data was not included in the group means.

lines (single patient, different time points) and the solid lines (average of all other patients within respective group) of like colors suggests the results of our cross-sectional design may mirror what would be seen in a longitudinal study. Further investigation using a longitudinal design is necessary to confirm this conjecture.

Far fewer strides were identified and analyzed for patients in the T1 group (≈ 350 strides/day per patient) than for those in the T2 (≈ 1,600 strides/day per patient) and C (≈ 1,310 strides/day per patient) groups. One explanation is that the T1 patients simply walk less, which is also supported by the Actigraph step counts. Intuitively, this may reflect a natural tendency for an individual to avoid an activity like walking which loads the recently reconstructed knee. Despite the difference in the number of strides analyzed for the T1 group compared to T2/C, we see this as an acceptable limitation as the availability of gait biomechanics characterizing even 350 strides per day is already a substantial improvement over the current standard which often yields fewer observed strides and with limited ecological validity.

In the approach to remote patient monitoring proposed herein, we chose sensor locations that would minimize user burden while also providing the kinematic and muscle activity data key to the presented analysis. A minimum of one sensor per leg was required to extract inter-leg kinematic and muscle activation asymmetries. Future work could consider additional sensor locations in an effort to provide improved clinical utility. For example, if the muscle activity from a quadriceps antagonist (e.g., a knee flexor) were available it may provide insight into co-contraction indices and would perhaps make the knee extensor muscle activation time-series more interpretable. Inclusion of a sensor on the shank could allow for the extraction of knee joint kinematics [75], [153] that could add additional information indicative of recovery. However, current hardware constraints on the capacity of on-board memory and battery prevented use of gyroscope data and required a relatively low accelerometer sampling frequency (31.25 Hz) in order to enable sEMG data collection over the recording durations considered herein. While higher sampling frequencies and additional sensor modalities would be useful, accelerometer data recorded at 31.25 Hz is likely sufficient for capturing the segment kinematics of interest which is supported given the accelerometer signal power spectrum (see Figure 4) and the fact that traditional laboratory-based gait analysis often employs cutoff frequencies ≤ 8 Hz for low-pass filtering kinematic data [175], [209], [215].

The results presented herein demonstrate the clinical utility of the proposed analysis platform for remote monitoring of patients recovering from ACL reconstruction surgery. Our analysis describes an unprecedented evaluation of muscle activation concurrently with kinematical time-series during free-living gait. These constitute a novel asymmetry analysis which presents a substantial improvement over current techniques utilized for remote monitoring. Further investigation is necessary to fully realize the practical application of the proposed approach for continuous patient monitoring with a larger sample, longitudinal design, and more frequent observation (i.e., more than just two time points) during the recovery process. The underlying MATLAB code has been open-sourced and structured in a modular fashion so that users can easily add/edit functionality for their specific use case. For example, different activity classification models or stride segmentation algorithms that incorporate data from other wearable sensors located on different body segments could be inserted that are more precisely tuned for a given patient population. There are certainly algorithmic improvements and additions that could be made for the proposed remote gait analysis such as automatic anatomical calibration or estimation of other biomechanical variables. The modularity of the platform is intended to promote these improvements so that the platform may serve as a basis upon which to build a comprehensive approach for remote gait analysis. This contribution comes at a critical time in the use of wearable sensors for providing free-living patient monitoring capabilities. An open-source platform will promote cross-disciplinary efforts to further advance remote patient monitoring paradigms and digital medicine. Future research should investigate similar applications in other clinical contexts and begin the difficult task of understanding how to translate the detailed, big-data evaluations enabled by continuous monitoring paradigms into optimizing patient-specific interventions.

3.5. Post-hoc analysis of different data aggregation methods

The previous analysis demonstrated the clinical utility in characterizing stride-level variables for remote monitoring. Despite these promising results, it remains unclear whether the mean value is the best aggregation method to characterize the distribution of daily stride metrics. This question has increasing relevance for remote patient monitoring and, beyond gait analysis, digital health in general. Indeed, optimal

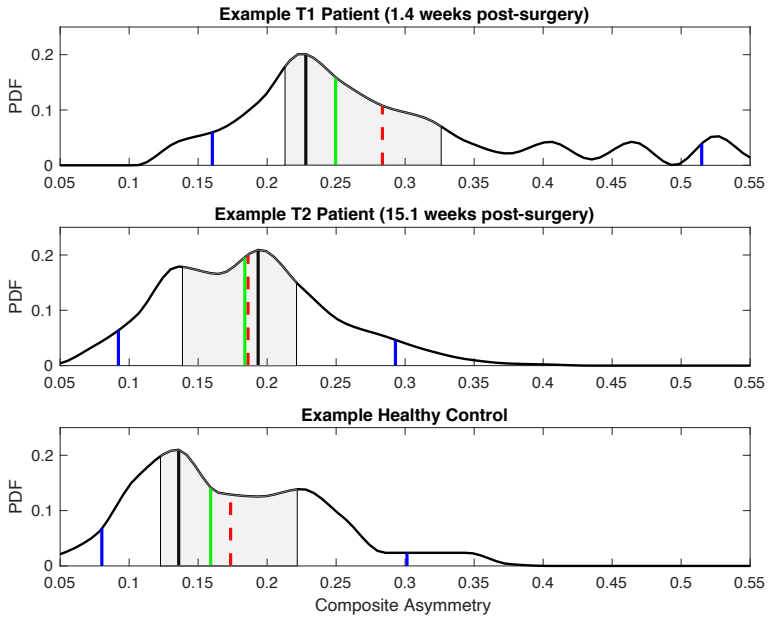

Figure 11: Approximate probability density functions (PDF) of composite asymmetry scores across all walking bouts during a single day for an ACLR patient for whom longitudinal data were available at both the T1 time point (1.4 weeks) (top) and the T2 time point (15.1 weeks) (middle). Data for an example healthy control is included in the bottom plot. The mean, median, mode, 95th percentile, and 5th percentile are indicated by the dashed red, solid green, thick solid black, rightmost solid blue, and leftmost solid blue vertical lines respectively. The shaded grey area indicates the interquartile range.

aggregation methods may be context specific (e.g., biomarker dependent and/or disease dependent). Thus, this post-hoc analysis investigated several data aggregation methods for characterizing the distribution of gait biomarkers for the same sample of patients recovering from ACLR regarding their sensitivity to recovery time.

The distribution of all composite asymmetry scores and stride times from the entire wear time for each subject were aggregated by six different methods: mean, median, mode, 95th percentile, 5th percentile, and IQR (Figure 11). The mode was calculated from approximate probability densities (Figure 11) for both asymmetry and stride time distributions. First, probability values were assigned for intervals of equal size. Then, a one-to-one correspondence was defined for these probability values with the mid-point of their respective interval. Probability values for asymmetries and stride times at a finer resolution were then

estimated by interpolation. The mode corresponds to the asymmetry or stride time associated with the largest peak in the approximate probability density function (Figure 11).

The primary finding of this post-hoc analysis was that the aggregation method yielding the greatest sensitivity to rehabilitation progress may be biomarker specific. For summarizing daily gait asymmetry, the 5th percentile was most sensitive to recovery time (ρ = -0.92) with both the mean and median also yielding strong relationships (ρ = -0.87 and ρ = -0.89 respectively) (Figure 12). However, the mode of stride times demonstrated the strongest association with recovery time (ρ = -0.93 vs. ρ = -0.83). The mean and median yielded similarly strong relationships (ρ = -0.91 for each). These findings were reinforced by the observed percent differences between groups. The 5th percentile yielded the largest differences in the composite asymmetry score when comparing both T2 relative to T1 (-47%) and C relative to T1 (-64%) whereas the mode yielded the largest differences for stride times when comparing T2 relative to T1 (-21%) and C relative to T1 (-23%). Taken together, these results indicate the need to consider multiple aggregation methods when summarizing the distribution of digital biomarkers captured during daily life.

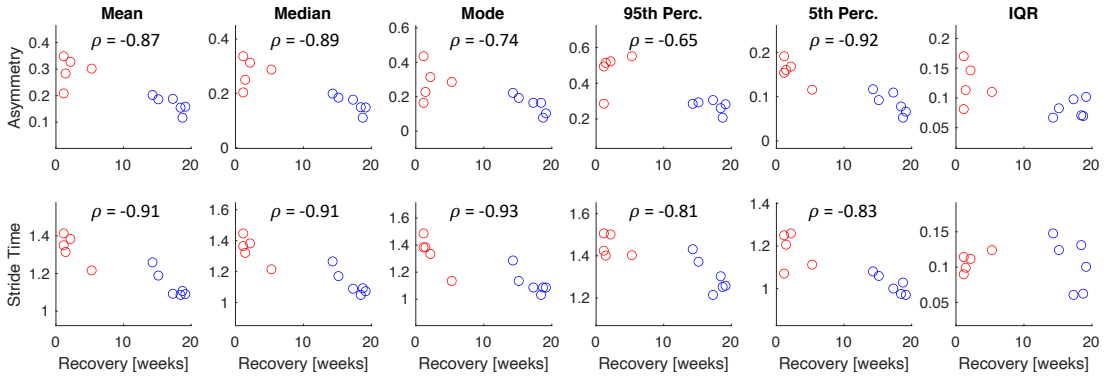

Figure 12: Scatter plots of daily asymmetry scores (top row) and stride times (bottom row) vs. recovery time post-surgery in weeks (T1: red, T2: blue) where daily distributions were aggregated as per the mean, median, mode, 95th percentile, 5th percentile, and interquartile range (IQR) (from the left column of plots to the right, respectively). The Spearman rank correlation coefficient (ρ) is included in each figure where the correlation was significant ($p < 0.05$). All stride time units are seconds. Composite asymmetry scores are unitless.

Lower values of the composite asymmetry score and stride time are associated with less impairment. As such, the 5th percentile can be interpreted as a confident lower bound on the observation of these measures and may indicate the best-case observation of each these biomarkers. Alternatively, the 95th percentile may be interpreted as a confident upper bound representing the worst-case scenario. In this study, the 95th percentile yielded significant relationships between recovery time with both stride times and composite asymmetry scores and significant differences between groups for all metrics. While these were not as pronounced as for the 5th percentile, both aggregation methods may be useful in a clinical evaluation for quantifying confidence bounds of biomarker distributions.

While the mean and median yielded similar results across all metrics analyzed, their differences reflect the multi-modal nature of the biomarker distributions (e.g., see Figure 11). Because of this multi-modal distribution, the IQR was computed as opposed to variance as an index of spread, albeit the IQR was least able to distinguish group differences. Even still, the IQR was significantly greater in the T1 group compared to both the T2 and C groups for the composite asymmetry scores (but not stride times) which may reflect a larger fluctuation of gait mechanics throughout the day. The source of this variation is unclear and could, for example, be related to a greater susceptibility to fatigue, smaller bouts of walking, or pain. Future investigations are necessary to fully understand this observation.

The inherent non-normality of the observed biomarker distributions further displaced the mode from other measures of central tendency, namely the median and mean (which would otherwise be expected to coincide). The mean is commonly used to summarize biomarker distributions and is justified by its discriminative ability as shown in this study. These results demonstrate similar discriminative ability with the median, which may be less susceptible to outliers and potentially a better choice for aggregating digital biomarkers observed during daily life.

Future work should consider developing aggregation methods that also capture temporal changes in these biomarkers to additionally capture physiologically relevant measures like fatigue. Moreover, these aggregation methods should be confirmed in a larger sample and with additional groups throughout recovery.

Chapter 4: Estimating Biomechanical Time-Series with Wearable Sensors: A Systematic Review of Machine Learning Techniques

A modified version of this chapter was published as: Gurchiek, RD, Cheney, N, McGinnis, RS (2019). Estimating biomechanical time-series with wearable sensors: A systematic review of machine learning techniques. Sensors, 19(23): 5227.

4.1. Introduction

Since the turn of the century, wearable sensors have experienced substantial technological advancements that have reduced their size and power requirements, improved their wearability, and increased the quality and types of data they capture. These improvements have allowed the application of wearable sensors to important clinical challenges impacting human health. These challenges include the development of novel digital biomarkers [10] that could be used for diagnosis, prognosis, and clinical decision making in a variety of neurological [7], [8], mental health [9], [185], and musculoskeletal [29], [153], [196], [213] disorders.

As described in Chapter 1, clinical evaluation using these biomarkers could be enhanced by also considering remote observation made during a patient's daily life (e.g., daily biomechanical variability is clinically informative in persons with multiple sclerosis [8]). Recent research suggests remote observations may differ than those made in the lab or clinic [33], [168], [192], and thus may provide additional information for informing clinical decision making. Additionally, remote observation could be used as an endpoint for assessing efficacy of interventions designed to target specific biomechanical indices (e.g., using biofeedback to reduce knee loading [216]). Taken together, these developments suggest that remote observation of patient biomechanics during daily life is emerging as an important tool for improving human health. Thanks to recent technological advancements, wearable sensors are ideally positioned to enable remote patient monitoring. However, wearable sensors do not necessarily provide direct measurement of the mechanisms underlying any particular clinical condition. Previous research on the mechanistic origins of various diseases (e.g., musculoskeletal [31], [200], [217], neurological [218]) motivate the incorporation of physically interpretable

biomarkers as a part of a comprehensive patient evaluation. These biomarkers, when observed continuously via remote patient monitoring, may then directly inform an optimal clinical intervention [45], [219], [220]. In this review we focus on the estimation of physically interpretable biomarkers for musculoskeletal and neurological disorders which take the form of biomechanical time-series representing joint, segment, and muscle kinetics and kinematics.

4.1.1. Physical models

The aforementioned biomechanical time-series may be determined from wearable sensor data using established mathematical relationships governed by physical models. For example, strapdown integration [154] of the angular rate signal from a segment attached gyroscope is a physics-based estimate of segment orientation where an accompanying accelerometer and magnetometer may provide the initial conditions and drift correction over time (e.g., see [196]). The development of sensor fusion techniques for removing integration drift in orientation estimates has been (and continues to be) a research focus [154], [221]. Inertial sensor estimates of segment kinematics are sufficient to estimate joint kinetics during open-chain tasks using an inverse-dynamics approach given estimates of segment inertial and geometric parameters [27]. However, additional sensors are needed for closed-kinetic chain tasks since then external contact forces must be considered (i.e., measured). Alternatively, wearable surface electromyography (sEMG) sensors may inform a solution for the net joint moment using Hill-type muscle models and thus also joint and/or segment kinematics for open-chain tasks via forward-dynamics [209], [222], [223]. However, as noted in [224], it is quickly realized that the number of sensors required to inform a physical model is inhibitive since the muscle activation of every muscle must be estimated thus limiting the use of these approaches for remote patient monitoring.

One solution is to simplify the physical model such that a reduced number of sensors can be used to measure all required independent variables. Many techniques for simplification have been proposed and are context dependent. For example, sacral accelerations have been assumed to represent those of the center of mass enabling a single inertial sensor estimate of ground reaction force [26]. For muscle force estimation, muscle contraction dynamics are often simplified to comply with a lumped-parameter Hill-type model as

opposed to a continuum model [225]–[228]. Further, it is common practice to assume unobserved muscle states (e.g., activation, tension) can be computed in terms of a single or multiple synergistic muscles whose states are available (e.g., via sEMG) [209], [224], [229]. Recently, Dorschky et al. (2019) present a physics-based technique for estimation wherein the states of a neuromusculoskeletal model (including the biomechanical time-series of interest) were optimized to agree with measured sensor data using trajectory optimization [25]. While the results were promising, the model was only two-dimensional, requires an inertial sensor on each of seven segments, and was further limited by computation time (mean CPU time was 50 $\pm$ 26 min across 60 optimizations where each optimization had 10 strides). The model simplifications and unwieldy sensor arrays required for physical modeling approaches motivate alternative methods for estimating biomechanical time-series, and especially for remote patient monitoring.

4.1.2. Regression techniques

Regression models that capture the relationship between wearable sensor inputs and biomechanical time-series outputs may provide an opportunity to further simplify the wearable sensor system required for remote patient monitoring. These models are developed from a large number of observations through a process that may be referred to as system identification [230], function approximation [231], or machine learning [232], depending on the field. It is important to note, however, that many of the physics-based techniques also regress model parameters from a large number of observations [228], wherein that process is often referred to as "calibration" and the parameters being regressed are physical constructs based on the derivation of the model from first principles (e.g., tendon slack length, muscle activation constants [209]). The current review will focus on the use of non-physical regression as a means for estimating joint, segment, and muscle kinetics and kinematics from wearable sensor data.

4.1.3. Relevant literature reviews

Techniques for estimating biomechanical time-series from wearable sensor data have been the focus of previous literature reviews. Faisal et al. (2019) recently provided a high-level overview of sensing technologies, applications of wearables in monitoring joint health, and analysis techniques [233]. Several reviews are available concerning the use of Hill-type muscle models for sEMG informed muscle force

estimation which can be used to estimate kinematics via forward-dynamics [223], [224], [228], [234]. Dowling (1997) mentions the potential use of neural networks in this context but does not review any relevant literature. Sabatini (2011) provides an overview of the use of inertial sensors for estimating segment and joint kinematics using physics-based techniques and sensor fusion algorithms [154]. Ancillao et al. (2018) review physics-based techniques for estimating ground reaction forces and moments using wearable inertial sensors [14]. While these previous reviews capture the current state of physics-based techniques well, there has not been a comprehensive review of regression techniques for estimating joint, segment, and muscle kinetics and kinematics from wearable sensor data. Schöllhorn (2004) provides a relevant review, but focuses only on neural networks and, as will be seen later, none of the articles they reviewed met the inclusion criteria outlined below and thus we also include studies using neural networks in this review [235]. Shull et al. (2014) review the applications of wearable sensors for clinical evaluation and for biofeedback, but they were only interested in gait, did not focus on the estimation technique, and none of the papers they reviewed used sEMG [236]. Caldas et al. (2017) review the application of adaptive algorithms for estimating gait phase, spatiotemporal features, and joint angles [237]. While joint angles are relevant to this review, Caldas et al. focus only on the use of inertial sensors and only mention three studies used to estimate joint angles; two of which are also included here. Finally, Ancillao et al. (2018) also reviewed machine learning techniques for estimating ground reaction forces and moments [14]. Thus, studies estimating only ground reaction forces and moments were excluded in this review.

The aim of this review was to characterize the use of regression algorithms to estimate biomechanical time-series from wearable sensor data. A secondary aim was to develop a classification method to group the prediction equations based on their technical similarities.

4.2. Methods

4.2.1. Search strategy

The PubMed and IEEE Xplore databases were searched for relevant articles in August 2019. Search terms were chosen to reflect the aims of the current review namely studies investigating (1) regression

of (2) human biomechanical time-series using (3) wearable sensor data (see Table 3 for search terms pertaining to items 1-3). After duplicates were removed, the title and abstract of each article was screened to determine if the full text would be reviewed.

4.2.2. Inclusion and exclusion criteria

Only peer-reviewed journal articles (no conference proceedings) written in English were considered. Articles were included in the review if they met all criteria within the following three categories:

(1) Sensor criteria: clear use of data for estimation from a sensor that is currently deployable as a wearable. Studies investigating model inputs dependent on *virtual* wearable sensor data derived from a non-wearable sensor were excluded. Studies using exoskeletons were excluded if the wearable sensor is only feasibly deployed using the exoskeleton.

(2) Prediction criteria: use of non-physical regression (not classification, regressed parameters must not be physical constructs). The estimated variable must have been a biomechanical time-series describing either the kinetics or kinematics of a joint, segment, or muscle. Studies were excluded if they estimated only grip or pinch forces unless the contact forces of each involved segment were estimated separately. Finally, studies estimating only ground reaction forces and moments were excluded as methods for this purpose have recently been reviewed [14].

(3) Validation criteria: all studies reviewed must have reported the objective (i.e., numerical) quantification of testing error using their estimation method. Studies were excluded if they report statistics for the training error only or if the only description of performance was given graphically. Studies utilizing inappropriate validation were excluded (e.g., one that could not be repeated or one using an invalid gold standard for validation).

These exclusion criteria were used for both the title/abstract screening and for full-text review. For many papers, the presence of one or several exclusion criteria was made clear via the title and/or the abstract. Therefore, these articles were removed after the title/abstract screening and were not full-text reviewed.

Table 3: Search terms and their relation to review relevant items

Review Relevant Item	Search Terms
Regression	regress* OR "machine learning" OR "artificial intelligence" OR "statistical learning" OR "supervised learning" OR "unsupervised learning" OR "neural network" OR perceptron OR "support vector" OR "gaussian process"
Biomechanical Time-Series	joint OR limb OR segment OR ankle OR knee OR hip OR wrist OR elbow OR shoulder OR muscle AND angle OR velocity OR acceleration OR moment OR torque OR force OR kinematic* OR kinetic* OR biomechanics OR mechanics OR dynamics
Wearable Sensors	wearable OR accelerometer OR gyroscope OR electromyo* OR EMG OR sEMG OR "inertial sensor" OR "inertial measurement unit" OR IMU OR insole OR goniometer

4.2.3. Data analysis

All studies that met the inclusion criteria were characterized by the sample size, subject demographics (sex, health status, age), wearable sensors (type, sampling frequency), biomechanical variable estimated, tasks for which the estimation was validated, model characteristics, and estimation performance. One aim of the current review was to summarize the various estimation techniques and their performance. A detailed description of the methods and error statistics used in each study is infeasible, so we grouped prediction equations post-hoc according to a grouping method which distinguishes the different techniques for comparison (see Section 4.3.4.). Further, we report summary statistics which summarize the overall performance (e.g., range of root mean square error across all observed tasks).

4.3. Results

A total of 46 articles met the inclusion criteria for full-text review out of 2,259 distinct articles identified via database search and from external sources (Figure 13). There was a clear increasing trend in the number of articles which met our review criteria published since the earliest identified in 1995 (Figure 14).

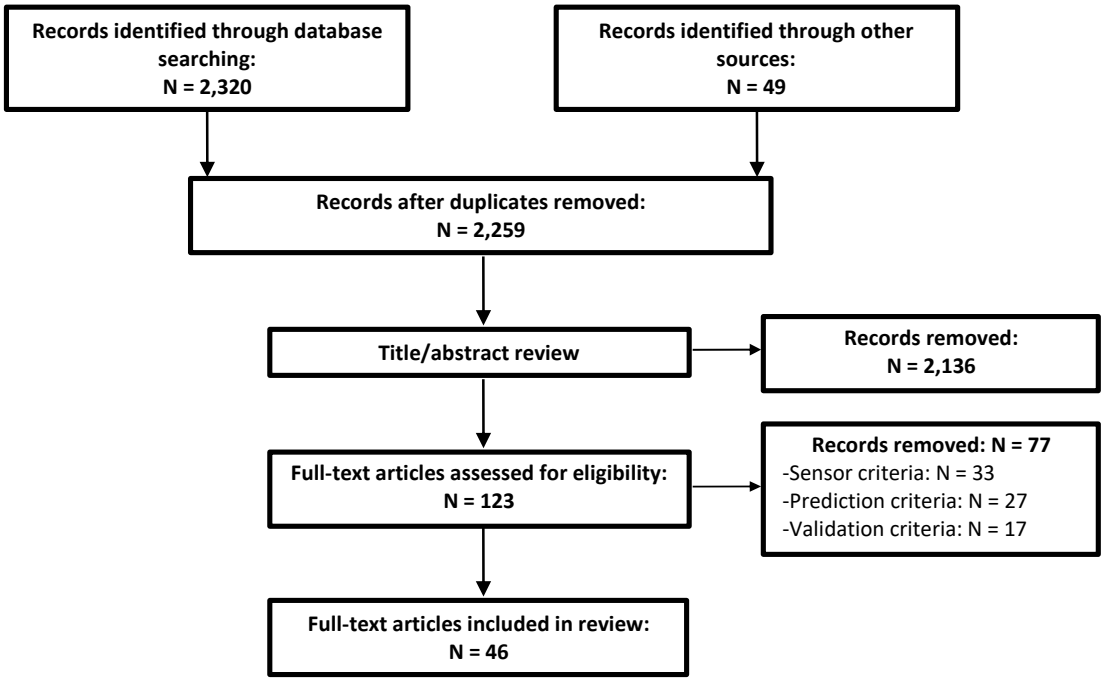

Figure 13: Flow chart of article selection process. Of the 123 full-text reviewed articles, 77 were removed on the basis of one or several exclusion criteria pertaining to the sensors used, the prediction approach, and/or the validation procedure. See section 4.2.2. for details concerning specific exclusion criteria.

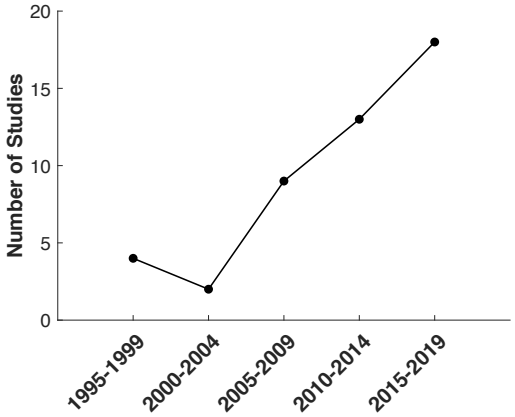

Figure 14: Number of articles included in the review for each five-year bin. The oldest paper included in our review was published in 1995.

4.3.1. Subject demographics

Across all participants used for validating the regression techniques, most were unimpaired males (64%) followed by unimpaired females (29%) and impaired individuals (7%). Three studies validated their algorithm on just one person while only 11 studies validated their algorithm on a sample size of greater than 10 participants. One study [238] did not report any information concerning the subject sample (other than that they were "normal" subjects) and the largest sample size for which an algorithm was validated was 33 (all unimpaired, 15 female) [239].

4.3.2. Wearable sensors

Surface electromyography sensors were the most popular wearable sensors used (32 studies) followed by inertial sensors (nine studies, four used magnetic/inertial measurement units, three used inertial measurement units, and two used accelerometers only) and high density sEMG (HD-sEMG) (five studies). One study used an electrogoniometer in addition to sEMG [240] and two studies used mechanomyography sensors in addition to sEMG [241], [242]. Two studies used force sensitive resistors to instrument insoles [243], [244] and one of these used an additional load cell over the Achilles' tendon [244]. The average sensor sampling rate across all studies using sEMG was 2,288.8 Hz (range: 500 – 16,000 Hz) and was 303.75 Hz

across the nine studies using inertial sensors (range: 50 – 1,500 Hz). Grid sizes for HD-sEMG included 128, 160, and 192 with an average sensor sampling rate of 1,838.4 Hz (range: 1.0 – 2.048 kHz).

4.3.3. Biomechanical variables

Across all studies, the most frequently estimated biomechanical time-series was joint kinematics (23 studies) followed by joint kinetics (16 studies), segment kinetics (seven studies), and segment kinematics (five studies) (Figure 15). Of the 16 studies estimating joint kinetics, only three estimated the intersegmental force. No studies estimated joint contact forces, individual muscle forces, or muscle kinematics. Most studies focused on joint/segment biomechanics in the sagittal plane (87%), followed by the frontal plane (46%), and transverse plane (33%) (Figure 15). Across all studies and considering the major upper and lower extremity

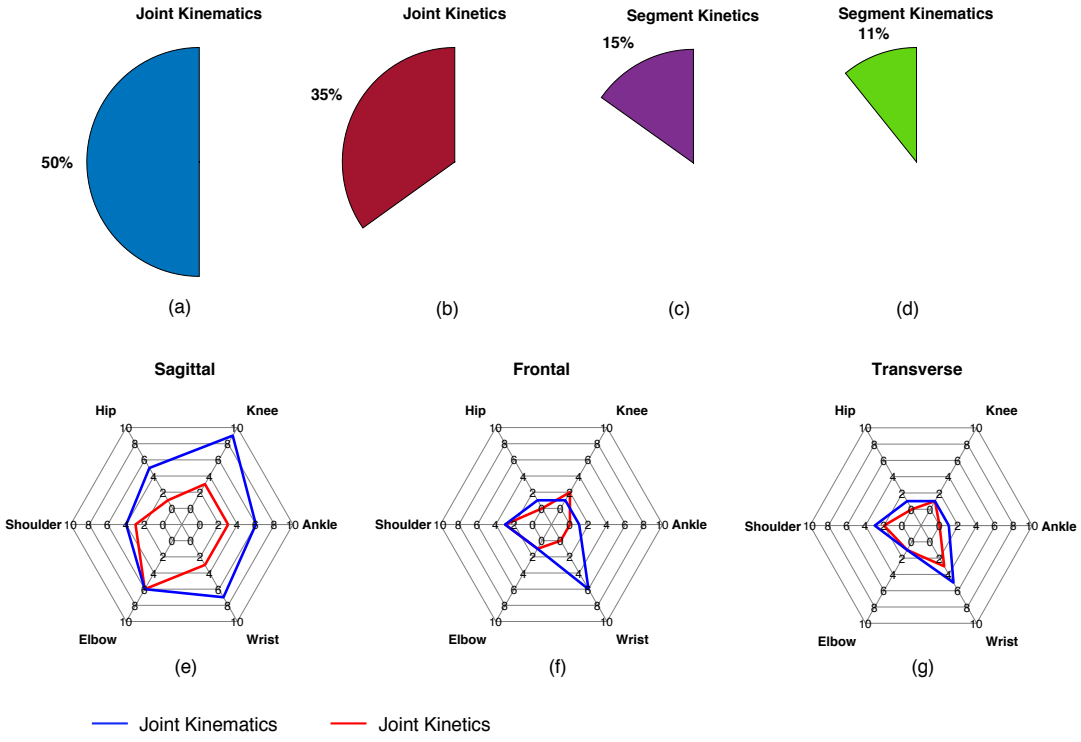

Figure 15: Description of the biomechanical variables estimated across all reviewed studies. The top row of figures illustrates the percentage of studies that estimated joint kinematics (a), joint kinetics (b), segment kinetics (c), and segment kinematics (d) and the bottom row of figures are radar plots illustrating the number of studies estimating the major upper and lower extremity joint kinematics (blue) and kinetics (red) in the sagittal (e), frontal (f), and transverse (g) planes. No studies estimated muscle forces or joint contact forces.

joints, the wrist joint received the most attention (28%), followed by the knee (26%), the elbow (24%), the ankle (20%), the shoulder (15%), and the hip (13%).

4.3.4. Classification of prediction equations

One aim of the current review was to develop a classification method *post-hoc* allowing a high-level comparison of the structure of the many different prediction equations used in the reviewed papers. Note that estimation performances were not compared statistically between methods from different studies as the nature of the model validation procedures were too often different enough such that a comparison of error statistics would not be appropriate. The rest of this section describes the classification we have developed for this comparison. We feel this method best groups the reviewed papers for an insightful comparison, but it is by no means unique. The description of all techniques used in the reviewed papers according to this classification is presented in Table 4 in addition to some other study characteristics for a succinct overview of all reviewed papers. It is recommended that the description of the classification system be read first to best understand the comparison in Table 4.

We use $\boldsymbol{x}(t) \in \mathbb{R}^d$ to denote the d-dimensional input used to estimate the m-dimensional output (biomechanical time-series) $\boldsymbol{y}(t) \in \mathbb{R}^m$ at time t. All reviewed papers presented regression algorithms to determine the parameters of a prediction equation $f: \mathbb{R}^d \rightarrow \mathbb{R}^m$ which defines the explicit mapping $\boldsymbol{x}(t) \rightarrow \boldsymbol{y}(t)$. In the context of this review, the i^{th} element $x_i(t)$ of the input $\boldsymbol{x}(t)$ may be a wearable sensor measurement after some pre-processing step (called an exogenous input) or a state variable being fed back. This state variable may be either an element $y_i(t - t_d)$ of a previous output $\boldsymbol{y}(t - t_d)$ (i.e., at time $t - t_d$, $t_d > 0$), or some other internal state (e.g., an output from a hidden neuron in a neural network). All prediction equations reviewed in this paper use exogenous inputs. In this review, we use the term *feedback* to refer to models which also use output and/or internal state variable feedback. For example, herein Elman networks [245], long-short term memory (LSTM) neural networks [246], [247], and non-linear/linear autoregressive (with exogenous inputs) models [242], [248] are all considered to have a feedback structure.

In general, an exogenous input $x_i(t)$ will be either the value of a sensor time-series s at time t, $s(t)$, or a discrete feature which describes s over some finite time interval. Note that $s(t)$ may be the raw

sensor signal itself or after some pre-processing step. For example, in this review, we classify the value of an sEMG envelope at some time instant as a time-series input, even though this value may depend on previous (or future) raw sEMG samples. Similar to system theory, we use the term *dynamic* to refer to models which use past exogenous inputs, for example $x_i(t - t_d)$ for $t_d > 0$, to estimate $\boldsymbol{y}(t)$ at time t. Note the difference between what we call a *dynamic* structure versus a *feedback* structure is that *dynamic* refers to the use of past *exogenous* inputs whereas *feedback* refers to the use of past *outputs* and/or *internal state variables* as a part of the input. We further classify discrete exogenous inputs as time-domain (TD) if computed in the time-domain (e.g., root mean square value) and frequency-domain (FD) if computed in the frequency-domain (e.g., Fourier coefficients). We also report which studies first decomposed the sEMG into motor unit action potentials (MUAPs) from which time domain (MUAP-TD) or frequency domain (MUAP-FD) discrete features were extracted.

Previous efforts to classify prediction equations have identified two classes, (1) a mixture of linear models and (2) a weighted sum of basis functions, into which a wide range of techniques can be classified [249]. We found that all prediction equations used in the studies reviewed herein can be viewed as a weighted sum of basis functions (where the weight of any one particular basis function is not restricted to be constant as in [249]). Given this general perspective, we identified a three-class classification for grouping the techniques used in each of the 46 reviewed papers: (i) polynomial mixtures ($\mathbb{P}^n$), (ii) neural networks (NN), and (iii) nonparametric regression (NP).

The $\mathbb{P}^n$ class is viewed as a special case where the basis functions are strictly n^{th}-order polynomials, $n \in \mathbb{N}$. Often, models are classified as either linear or non-linear, but here we consider both first-order polynomial mixtures ($n = 1$) and higher order polynomial mixtures ($n > 1$) as sub-classes of $\mathbb{P}^n$. This is because a first-order linear model may use features which are non-linear transformations of raw sensor signals. For example, consider a model using the sEMG amplitude at time t (denoted by $x(t)$) for estimation. Then the prediction equation $y(t) = a_1 x(t) + a_2 x^2(t)$, for coefficients $a_1, a_2 \in \mathbb{R}$, may be interpreted as a linear model with two features as inputs (namely sEMG amplitude and squared sEMG amplitude) or as a 2nd order polynomial with a single input (i.e., sEMG amplitude). To improve clarity, we report both the

polynomial model order and a description of the features used for estimation in Table 4. Prediction equations belonging to the $\mathbb{P}^n$ class in this review include those resulting from Gaussian mixture regression [250], lasso [251] and ridge [252] regression, and an ensemble of polynomials [252] among others.

The NN class is viewed as a special case where the basis functions are neural networks. This formulation allows for both radial basis function networks [253] and an ensemble of networks [254] as the final prediction equation.

The NP class refers to models which require access to all training data when making predictions (as defined in [231]). All NP prediction equations in this review are either linear smoothers [231], [255] or (kernelized) support vector regression (SVR). Linear smoothers express the estimated output for a test input as a linear combination of all training targets. These include the prediction equations resulting from Gaussian process regression [242], [256], kernel ridge regression [252], kernel smoothers [257], [258], and *k*-nearest neighbors regression [259].

4.3.2. Descriptive statistics of prediction equations

Neural networks were the most popular model (33 studies, 72%) followed by polynomial mixtures (14 studies, 30%) and nonparametric regression (seven studies, 15%). Of the 14 polynomial mixtures, 12 were first-order (linear models) of which nine used time-series inputs. Time-series inputs were used more often (72% of studies) than discrete features (33% of studies). Across the 15 studies using discrete features as inputs, 13 contained time-domain features, three contained frequency-domain features, and three studies estimated the decomposition of the raw sEMG signals into individual MUAPs before computing discrete features. Ten studies used a dynamic structure and nine studies used a feedback structure. Seven studies used principal component analysis as an unsupervised feature reduction method. Most studies present subject-specific models (80%). No final prediction equations developed in any studies were open-sourced, but one paper [260] provided open-source code for their MUAP decomposition algorithm. Table 4 provides an overview of the prediction equations used in each study as well as a summary statistic summarizing estimation performance.

Table 4: Overview of the 46 reviewed papers

Reference (year)	Sensors (f_s, max number)	Variable (location): plane(s)	Tasks	Inputs	Model	Performance Summary
Koike and Kawato [254] (1995)	sEMG (2 kHz, 10)	τ (elbow): S τ (shoulder): F	ISO, OC	TS	NN (FB, dyn)	CD: 0.89
Suryanarayanan et al. [238] (1996)	sEMG (2 kHz, 1)	θ (elbow): S	OC	TS	NN (dyn)	RMSE ≤ 15%
Shih and Patterson [261] (1997)	sEMG (900 Hz, 4)	τ (elbow): S τ (wrist): S τ (shoulder): S θ (elbow): S θ (wrist): S θ (shoulder): S	WCP	TS	NN	RMSE: 0.67 – 5.76 Nm, **0.64 – 5.62 Nm** RMSE: 4.78 – 13.76°, **4.73 – 14.33°**
van Dieën and Visser [262] (1999)	sEMG (600 Hz, 6)	τ (lumbo-sacral): S	ISO, LOC	TS	$\mathbb{P}^1$ (dyn)	RMSE: 26 - 54 Nm, *49 – 160 Nm*
Au and Kirsch [263] (2000)	sEMG (500 Hz, 6)	θ (shoulder): S, F, T θ (elbow): S $\dot{\theta}$ (shoulder): S, F, T $\dot{\theta}$ (elbow): S $\ddot{\theta}$ (shoulder): S, F, T $\ddot{\theta}$ (elbow): S	OC, LOC	TS	NN (dyn)	RMSE: 14.2 – 19.6° RMSE: 8 – 17.2° (impaired subjects)
Dipietro et al. [264] (2003)	sEMG (1 kHz, 5)	p (hand): T	OC	TS	NN (FB)	RMSE: 7.3 – 11.5%
Song and Tong [240] (2005)	sEMG (1 kHz, 3) goni (1 kHz, 2)	τ (elbow): S	LOC	TS	NN (FB)	nRMSE: 4.53 – 8.45% nRMSE: 10.56 – 16.20% (sEMG only)
Clancy et al. [230] (2006)	sEMG (4096 Hz, 8)	τ (elbow): S	ISO	TS	$\mathbb{P}^1$ (dyn)	MAE: 7.3%
Došen and Popovič [265] (2008)	2D ACC (200 Hz, 4)	θ (ankle): S θ (knee): S θ (hip): S $\ddot{p}$ (hip joint center): S	MSW	TS	NN (dyn)	RMSE: 1.19 – 3.60°, *1.18 – 2.62°* RMSE: 0.26 – 0.39 m/s^2, *0.29 – 0.46 m/s^2* CC (θ): 0.97 – 0.998, *0.97 – 0.998* CC ($\ddot{p}$): 0.96 – 0.99, *0.91 – 0.99*

Findlow et al. [257] (2008)	IMU (100 Hz, 4)	θ (ankle): S θ (knee): S θ (hip): S	Normal Walk	TS	NP (KS)	MAE: 1.69 – 2.30°, **4.91 – 9.06°** MAE: 1.78 – 5.32° (reduced sensor array) CC: 0.93 – 0.99, **0.70 – 0.89** CC: 0.87 – 0.99 (reduced sensor array)
Goulermas et al. [258] (2008)	IMU (--, 4)	θ (ankle): S θ (knee): S θ (hip): S	MSW	TS	NP (KS)	CC: 0.97, *0.96*, **0.83**
Hahn and O'Keefe [266] (2008)	sEMG (1 kHz, 7)	τ (ankle): S τ (knee): S τ (hip): S	Normal Walk	TS	NN	CD: 0.54 – 0.84 (sEMG only) CD: 0.77 – 0.92 (sEMG with demographics & anthropometrics)
Mijovic et al. [253] (2008)	2D ACC (50 Hz, 2)	$\ddot{\theta}$ (forearm): S	OC	TS	NN (RBF)	CD: 0.841 – 0.998, **0.75 – 0.99**, ***0.03 – 0.88***
Delis et al. [267] (2009)	sEMG (1744.25 Hz, 2)	θ (knee): S	Normal Walk	DISC (TD)	NN (SOM)	CC: 0.59 – 0.84
Jiang et al. [268] (2009)	sEMG (1 kHz, 8)	CF (hand)	ISO	DISC (TD)	1) NN 2) $\mathbb{P}^1$	1) CD: 0.86 2) CD: 0.78
Youn and Kim [241] (2010)	sEMG (1 kHz, 2) MMG (1 kHz, 2)	CF (hand)	ISO	DISC (TD)	NN	nRMSE $\leq$ *16% (MMG only)* nRMSE $\leq$ *13% (sEMG only)* nRMSE $\leq$ *10% (sEMG + MMG)*
Ziai and Menon [251] (2011)	sEMG (1 kHz, 8)	τ (wrist): S	ISO	TS	1) $\mathbb{P}^1$ 2) $\mathbb{P}^1$ (lasso) 3) $\mathbb{P}^1$ (LWPR) 4) NP (SVR) 5) NN (2L)	1) nRMSE: 2.88% 2) nRMSE: 2.83% 3) nRMSE: 3.03% 4) nRMSE: 2.85% 5) nRMSE: 2.82%
Nielsen et al. [269] (2011)	sEMG (1024 Hz, 7)	CF (hand)	ISO	DISC (TD)	NN	RMSE: 0.16 N RMSE: 0.10 N (impaired subjects) CD: 0.93 CD: 0.82 (impaired subjects)
de Vries et al. [270] (2012)	MIMU (50 Hz, 4) sEMG (1 kHz, 13)	ISF (SC): S, F, T ISF (AC): S, F, T ISF (shoulder): S, F, T ISF (elbow): S, F, T	LOC, ADL	TS	NN	nRMSE: *7 – 17%*
Jiang et al. [271] (2012)	sEMG (2048 Hz, 7)	θ (wrist): S, F, T	OC	DISC (TD)	NN	CD: 0.74 – 0.78
Muceli and Farina [272] (2012)	HD-sEMG 128 (2048 Hz, 2)	θ (wrist): S, F, T	OC	TS	NN	CD: 0.79 – 0.89

Clancy et al. [239] (2012)	sEMG (4096 Hz, 2)	τ (elbow): S	ISO	TS	$\mathbb{P}^1$, $\mathbb{P}^2$, $\mathbb{P}^3$, $\mathbb{P}^4$ (dyn)	nMAE: 4.65 – 6.38% nMAE: 5.55 – 7.97 % (reduced training set)
Howell et al. [243] (2013)	FSR (118 Hz, 12)	τ (ankle): S τ (knee): S, F	Normal Walk	TS	$\mathbb{P}^1$	nRMSE: 5.9 – 17.1% CC: 0.82 – 0.97
Kamavuako et al. [273] (2013)	sEMG (10 kHz, 6)	τ (wrist): S, T	ISO	DISC (TD)	NN	nRMSE: 6.1 – 13.5% CD: 0.87 – 0.91
Jiang et al. [274] (2013)	sEMG (2048 Hz, 7)	θ (wrist): S, F, T	OC	DISC (TD)	NN	CD: 0.63 – 0.86, *0.34 – 0.74* CD: 0.61 – 0.77, *0.46 – 0.59* (impaired subjects)
Farmer et al. [248] (2014)	sEMG (1 kHz, 4)	θ (ankle): S	Normal Walk	TS	NN (FB, dyn)	RMSE: 1.2 – 5.4°
Ngeo et al. [256] (2014)	sEMG (2 kHz, 8)	θ (MCPs): S	OC	TS DISC (TD)	1) NN (dyn) 2) NP (GPR, dyn)	1) CC: 0.71 (TS inputs only) 2) CC: 0.84 (TS inputs only)
Hahne et al. [252] (2014)	HD-sEMG 192 (2048 Hz, 1)	θ (wrist): S, F	OC	DISC (TD)	1) $\mathbb{P}^1$ (ridge) 2) $\mathbb{P}^1$ 3) NN 4) NP (KRR)	4) CD: 0.8 (reduced sensor array) CD: 0.8 – 0.9 (range across all models)
Jacobs and Ferris [244] (2015)	FSR (1 kHz, 8) Load Cell (1 kHz, 1)	τ (ankle): S	MSW, Calf Raises	TS	NN	nRMSE: 7.04 – 13.78% nRMSE: 8.72 – 16.52% (FSR only) nRMSE: 20.47 – 46.02% (Load Cell only)
de Vries et al. [275] (2016)	MIMU (50 Hz, 4) sEMG (1 kHz, 13)	ISF (shoulder): S, F, T	LOC, ADL	TS	NN	nSEM: *4 – 1 %* nSEM: *3 – 21%* (reduced sensor array)
Wouda et al. [259] (2016)	MIMU (240 Hz, 5)	θ (ankle): S, F, T θ (knee): S, F, T θ (hip): S, F, T θ (shoulder): S, F, T θ (elbow): S, F, T θ (wrist): S, F, T θ (spine): S, F, T	OC, ADL, MSW, MSR, sport	TS	1) NN 2) NP (*k*-NN)	1) Mean Error: ***7°*** 2) Mean Error: ***8°***
Michieletto et al. [250] (2016)	sEMG (1 kHz, 8)	θ (knee): S	Seated Kick	TS	$\mathbb{P}^1$ (GMR)	Custom error statistic (see paper)
Xiloyannis et al. [242] (2017)	sEMG (--, 5) MMG (--, 5)	$\dot{\theta}$ (MCPs): S	OC, ADL, ISO	TS	1) $\mathbb{P}^1$ (FB) 2) NP (GPR, FB)	1) CC: *0.54* 2) CC: 0.79, *0.62*, 0.67 (sEMG only)

Zhang et al. [276] (2017)	sEMG (1 kHz, 8)	θ (shoulder): S, F, T θ (elbow): S	OC	DISC (TD)	NN	CD: 0.90 – 0.91, *0.86 – 0.87*
Ding et al. [277] (2017)	sEMG (2 kHz, 8)	θ (elbow): S θ (humerus): S, F, T	OC, ADL	TS	1) NN 2) NN (FB) 3) NN (FB, UKF)	1) RMSE: *11 - 14°*, CC: *0.88 – 0.90* 2) RMSE: *11 - 15°*, CC: *0.87 – 0.89* 3) RMSE: *7 – 9°*, CC: *0.95 – 0.96*
Clancy et al. [278] (2017)	sEMG (2048 Hz, 16)	CF (hand): S, F τ (wrist): T	ISO	TS	$\mathbb{P}^1$	RMSE: 6.7 – 10.6%, *11.0 – 15.7* (4 sensors)
Xia et al. [246] (2018)	sEMG (2 kHz, 5)	p (hand): S, F, T	OC	DISC (FD) DISC (TD)	1) NN (CNN) 2) NN (C-LSTM, FB)	1) CD: 0.78 2) CD: 0.90
Wouda et al. [279] (2018)	MIMU (240 Hz, 3)	θ (knee): S	MSR	TS	NN	RMSE: *2.27 – 8.41°*, **6.29 – 25.05°** CC: *0.98 – 0.99*, **0.77 – 0.99**
Sun et al. [260] (2018)	sEMG (16 kHz, 1)	CF (forearm)	ISO	DISC (MUAP-TD)	$\mathbb{P}^1$	CD: **0.72 – 0.89**
Chen et al. [280] (2018)	sEMG (1.2 kHz, 10)	θ (ankle): S θ (knee): S θ (hip): S	MSW	TS	NN (DBN)	RMSE: 2.45 – 3.96° CC: 0.95 – 0.97
Xu et al. [247] (2018)	HD-sEMG 128 (1 kHz, 1)	CF (forearm)	ISO	TS	1) NN (CNN) 2) NN (LSTM, FB) 3) NN (C-LSTM, FB)	1) nRMSE: *7.33 – 10.93%* 2) nRMSE: *6.16 – 9.33%* 3) nRMSE: *5.95 – 9.74%*
Wang et al. [245] (2019)	sEMG (1.6 kHz, 5)	θ (knee): S	LOC	DISC (FD)	NN (FB)	nRMSE: 3.55 – 5.13%
Dai and Hu [281] (2019)	HD-sEMG 160 (2048 Hz, 1)	θ (MCPs): S	OC	TS, DISC (MUAP-FD)	$\mathbb{P}^2$	CD: 0.66 – 0.81 (TS inputs) CD: 0.69 – 0.86 (MUAP-FD inputs)
Dai et al. [282] (2019)	sEMG (2048 Hz, 16)	CF (hand): S, F τ (wrist): T	ISO	TS	$\mathbb{P}^1$ (dyn)	RMSE: 7.3 – 9.2%, *11.5 – 13.0%* (4 sensors)
Kapelner et al. [283] (2019)	HD-sEMG 192 (2048 Hz, 3)	θ (wrist): S, F, T	OC	DISC (TD, MUAP-TD)	$\mathbb{P}^1$	CD: 0.77 (MUAP-TD inputs) CD: 0.70 (TD inputs)

Stetter et al. [232] (2019)	IMU (1.5 kHz, 2)	ISF (knee): S, F, T	MSW, MSR, sport	TS	NN (2L)	nRMSE: **14.2 – 45.9%** CC: **0.25 – 0.94**

Sensors: f_s: sampling frequency (-- indicates f_s not reported), ACC: accelerometer; IMU: inertial measurement unit (accelerometer + gyroscope); MIMU: IMU with magnetometer, HD-sEMG *N*: high density grid of *N* surface electromyography electrodes, FSR: force sensitive resistors (instrumented insole); MMG: mechanomyography; goni: electrogoniometer

Variables: τ: net joint (muscle) moment; $\theta, \dot{\theta}, \ddot{\theta}$: joint/segment angular position, velocity, acceleration; $p, \dot{p}, \ddot{p}$: segment position, velocity, acceleration; ISF: joint intersegmental force; CF: joint/segment contact force, AC: acromio-clavicular joint, SC: sterno-clavicular joint, MCPs: one or several of the metacarpophalangeal joints

Tasks: ISO: isometric; OC, LOC: open-chain, loaded open-chain; MSW: multi-speed walking; ADL: activities of daily living (brushing teeth, drinking, etc.); MSR: multi-speed running; sport: sport related movements (e.g., jumping, kicking, throwing)

Inputs: TS: time-series; DISC: discrete; TD, FD: time-domain, frequency domain; MUAP: sEMG data were first decomposed into motor unit action potentials from which discrete features were extracted

Model: FB: model exhibits output and/or internal state variable feedback (includes *autoregression*); dyn: dynamic (dependent on previous inputs); $\mathbb{P}^n$: mixture of n-th order polynomials; GMR: Gaussian mixture regression; NN: neural network; RBFN: radial basis function network; SOM: self-organizing map; DBN: deep belief network; NP: nonparametric regression; KS: kernel smoother; GPR: Gaussian process regression; SVR: support vector regression; KRR: kernel ridge regression; *k*-NN: *k* nearest neighbors regression; UKF: unscented Kalman filter; CNN: convolutional neural network, LSTM: long-short term memory network, C-LSTM: CNN in series with LSTM; 2L: two hidden layers

Performance Summary: RMSE: root mean square error; nRMSE: normalized RMSE (e.g., RMSE in physical units normalized by maximum); MAE: mean absolute error; nMAE: normalized mean absolute error (see nRMSE); nSEM: normalized standard error of measurement; CC: correlation coefficient; CD: coefficient of determination; *italic performance metrics indicate results for task extrapolation (e.g., trained on normal walking data, tested on fast walking data*), **bold performance metrics indicate results for subject extrapolation (all data in the test set were associated with different subjects than were data in the training set)**

4.4. Discussion

Remote monitoring of patient segment, muscle, and joint kinematic and kinetic time-series has been established as an important component of digital health. Practical limitations in the number of sensors that can be deployed simultaneously to a given user motivate the pursuit of regression-based approaches. Thus, the primary aim of this review is to summarize relevant developments in the use of regression for estimating these biomechanical time-series. This review is timely given the increase in relevant studies since the turn of the century (Figure 14) and the limitations of other systematic reviews in the area. While many different techniques were observed since the first relevant method published in 1995, there are some common themes consistent across studies which we discuss below. Additionally, we discuss challenges concerning the practical implementation of the reviewed methods and common characteristics of the techniques that provided the best performance to provide possible directions for future work. In particular, we discuss how incorporating domain knowledge often improved performance and the implications for hybrid estimation (i.e., using both physics-based and machine learning techniques in concert). Note that our identification of techniques that may improve performance was not based on a comparison of methods between the studies reviewed herein. Instead, we draw conclusions concerning techniques that led to improved performance only where those conclusions were inferred within individual studies that report an appropriate statistical comparison.

4.4.1. Overview of regression techniques

Neural networks were the most popular regression model. Most incorporated a 3-layer feed forward neural network (non-recurrent, single hidden layer) [241], [244], [251]–[253], [256], [259], [261], [263], [265]–[276], [279] and differed based on the choice of activation function and/or number of hidden neurons. The number of hidden neurons in the NN models reviewed was usually optimized over a set of predefined values [240], [241], [245], [248], [252], [256], [259], [263], [264], [266], [268], [269], [271], [272], [277] but sometimes not [232], [244], [261], [265], [270], [275]. Two papers considered an ensemble of networks. Koike and Kawato (1995) trained two task-specific NNs (one for postural activities and the

other for dynamic) and a gating network which provided the weights for linearly combining the joint torque estimates from the two task-specific NNs [254]. Ding et al. (2017) utilized an unscented Kalman filter for combining two NNs to estimate elbow joint angle and upper arm orientation [277] wherein a recurrent NN trained using sEMG data with reduced information redundancy (using a custom reduction approach) was used to model the time-update equation and a second NN trained to estimate a redundant sEMG time-series was used as the measurement-update equation. Convolutional and long-short term memory NN (CNN and LSTM, respectively) were first used in 2018. Xia et al. (2018) found that an LSTM in series with a CNN (C-LSTM) outperformed a CNN alone for estimating hand position during general open-chain tasks [246]. Likewise, Xu et al. (2018) found that C-LSTM outperformed LSTM alone which outperformed CNN alone (nRMSE: 8.67%, 9.07%, and 12.13%, respectively) for estimating contact forces at the distal forearm and was one of the few studies to use a leave-one-subject-out validation approach [247].

Polynomial mixtures were the next most popular model and of these, first order polynomials were most common. Consideration of simple linear models is motivated by an observed relationship between sEMG amplitude and muscle force, especially at lower force levels. However, to increase muscle force, additional motor units are recruited and/or stimulation frequency increases which along with heterogenous activation within a muscle and load sharing between muscles makes this relationship non-linear [224], [228]. Some reviewed papers compared linear models ($\mathbb{P}^1$) to both neural networks [251], [252], [268] and nonparametric regression [242], [251], [252]. Although between model comparisons varied and two of these four studies only considered isometric tasks [251], [268], the NN and NP performances were no different than those from linear models. Comparisons have also been made between first order and higher order polynomial mixtures. It was shown in [262] that linear models performed equally as well as second order models for estimating lumbo-sacral joint torque using sEMG and Clancy et al. (2006) show that superior sEMG amplitude estimation techniques (e.g., whitening, multi-channel) can improve linear models [230]. Alternatively, Clancy et al. (2012) show that 2nd or 3rd order polynomials outperformed 1st and 4th order models (with regularization and optimal dynamic orders) for estimating isometric elbow joint torque using sEMG inputs [239]. A few studies considered an ensemble of polynomials. Michieletto et al. (2016) used Gaussian mixture regression, which can be shown to be a linear mixture [249], to estimate knee

flexion/extension angle using sEMG inputs [250]. Hahne et al. (2014) used degree-of-freedom-specific linear models to estimate wrist joint angle and linearly combined their estimates using weights determined by a logistic regression model trained to classify the degree-of-freedom of the movement (the weights were the posterior class probabilities) [252].

Nonparametric regression was used least frequently. This may be due to the amount of data necessary to compute an estimate given the nonparametric models used in the reviewed studies (although reduction methods exist [231]). While this may be prohibitive for real-time applications (e.g., for prosthetic control [252]) it may still be a feasible method for remote patient monitoring applications where data can be stored locally during the day and processed at a later time. Linear smoothers were the most popular nonparametric regression. The first study to use nonparametric regression in the proposed context was in 2008 where the Nadaraya-Watson estimator, a kernel smoothing technique, was used to estimate lower extremity joint angles using IMU data [257]. Goulermas et al. (2008) built upon this model by incorporating an additional term in the Gaussian kernel intended to accentuate or attenuate a training target's contribution to the final estimate according to a custom pattern similarity index [258]. Several papers noted the advantage of nonparametric regression for small training sets. For example, Ngeo et al. (2014) show Gaussian process regression outperformed a neural network in estimating finger joint angles using sEMG data, especially for smaller data sets [256]. Similarly, Hahne et al. (2014) found that kernel ridge regression outperformed a neural network for both a reduced training set and when reducing the number of sEMG channels of a high-density array (from 192 to 12 – 16) [252].

4.4.2. Concerns for practical implementation

Remote patient monitoring and myoelectric prosthetic control were the two most common applications used to motivate the many different techniques reviewed which indicates that eventual users of these systems are expected to present with clinical impairment. However, our results show that most studies do not validate their estimation techniques on impaired individuals. Evaluating algorithm performance on unimpaired populations is certainly useful for algorithm development as it reduces extraneous variables and simplifies study recruitment and retention efforts. Nevertheless, these algorithms need to be deployed to

impaired populations and, while some studies present improved or equal performance for impaired individuals, many show that performance decreases. Thus, caution should be taken when considering how well a technique will work when deployed for a population on which it has not been validated. This clearly applies for a model trained on healthy participants but deployed to participants with impairment (though in some cases the drop in performance is minimal [20]). However, one also cannot assume that a model trained and tested on impaired participants will have identical performance characteristics as the same model trained and tested on healthy participants.

In addition to generalizing performance across populations, more research is needed to better understand how these regression models generalize across individuals and tasks. The majority of studies (80%) developed subject-specific models and only 33% of studies explored task extrapolation. The latter may be less of a barrier to implementation since in practice task identification will likely be a part of the pipeline for automated analysis [70], in which case highly accurate activity classification models are required [284]. Thus, task specific models could be selected following task identification. However, given the approaches reviewed herein, subject-specific models require every user to be observed in-lab for model training. Further, the observation sets for model training must be broad enough in scope (e.g., multi-speed, multi-load) so that they can be confidently applied for estimation in unconstrained environments. These requirements substantially limit the scalability of these solutions for remote patient monitoring. Subject-general models may be one of the more difficult challenges to overcome in the future as they appear to frequently result in performance decreases [253], [257], [258], [279]. Intuitively, this may indicate that current regression models are learning person-specific patterns as opposed to generalizable phenomena. This may be a result of the small sample sizes used for model training in many of the reviewed studies. To fully realize the potential of regression techniques for estimating biomechanical time-series, future work should incorporate observations from impaired populations in their training and validation sets and larger sample sizes to foster learning of generalizable phenomena.

The clinical utility of the reviewed estimation techniques is largely driven by the estimated biomechanical variables. This review found no relevant studies which estimated muscle or joint contact

forces. This is likely due to the fact that direct measurement of these variables is substantially more invasive than joint or segment mechanics. Nevertheless, indirect muscle and joint contact force estimates enabled by traditional laboratory-based gait analysis can be informative clinically [219], [220]. Thus, models trained using these indirect estimates as training targets may be useful for estimating muscle and joint contact forces in remote environments. Further, future research should investigate the estimation of frontal and transverse plane joint mechanics. Specifically, frontal plane joint moment may be especially useful in monitoring patients at risk of developing knee osteoarthritis and remote observation of these mechanics may provide clinical endpoints to evaluate intervention efficacy or inform rehabilitation decision making [46], [216]. There is room for improvement in this area as only one study [243] reports the estimation of non-sagittal plane moment of any lower extremity joint (frontal plane knee joint moment during walking), and performance was inferior to sagittal plane estimates achieving normalized root mean squared error of 16.4 $\pm$ 5.7% (vs. 10.7 $\pm$ 5.3% for sagittal plane moments) in healthy subjects.

Deployment of many of the reviewed techniques is further complicated by hardware limitations. Of particular concern are the battery capacity and memory constraints of current wearables. Of the more popular wearable sensors, gyroscopes are notorious for limiting long-term capture due to their power requirements and would thus limit immediate application of several methods reviewed [232], [257]–[259], [270], [275], [279]. Alternatively, accelerometers and sEMG are able to provide continuous recording for at least 24-hours with current battery technology. The use of sEMG for remote monitoring is less common than accelerometry and has been used primarily for quantifying indices of physical activity [285]–[288]. Recent efforts have estimated muscle activation time-series during walking using methods similar to those used to estimate muscle force using Hill-type muscle models [29], [70], [193]. This pre-processing step was used by several reviewed papers suggesting they may be practically deployed. However, the sEMG sampling frequency used in many of the reviewed studies (500 Hz to 16 kHz) was much higher than what has been used for remote monitoring (10 – 250 Hz). It is currently unknown to what extent estimation performance is influenced by sEMG sampling frequency. Future research should explore these limitations in search of hardware and algorithmic solutions that are practically deployable for remote patient monitoring.

An additional practical concern is the number of wearable sensors required for the reviewed algorithms. Several studies considered the effect of reducing the number of sensors on estimation performance. Clancy et al. (2017) present a backward stepwise selection method for reducing the number of necessary sensors [278]. They show that additional sensors beyond four (up to 16) provided no statistically significant advantage for estimating degree of freedom specific wrist joint kinetics. This reduction method was later used by Dai et al. (2019) for a similar application where the reduction approach generally outperformed pre-selected sensor locations [282]. Dai and Hu (2019) present a method for reducing a high-density grid of 160 sEMG electrodes down to an 8x8 grid, however, the 8x8 subset was finger specific (for estimating finger kinematics) [281]. Future work in the development of regression approaches for estimating biomechanical time-series should incorporate analysis of the effect of reducing instrumentation complexity (i.e., reducing the number and types of sensors required) on estimation performance.

Finally, only one study provided open-source code for any part of their methodology [260]. The code was for performing the MUAP decomposition of the raw sEMG signals and not the actual regression model. Providing open-source code for subject-general models will allow non-specialized research teams without expertise in engineering or computer science to utilize these methods for clinical purposes. Further, it will allow 3rd party validation; a necessary component prior to practical deployment and to promote confidence from the public in the clinical utility of these tools. Open-source data as well as open-source code in future studies would help speed the pace of development of these techniques.

4.4.3. Incorporating domain knowledge

While we excluded physics-based techniques from the current review, several papers incorporated domain knowledge into their approach (e.g., muscle and neural physiology, rigid body dynamics) which was often reported to improve performance. For example, Koike and Kawato (1995) incorporated feedback of joint angular position and velocity specifically on the basis of the well-known force-length and force-velocity property of muscle [254]. Further, pre-processing of the raw sEMG signals to optimally estimate sEMG amplitude was often motivated by an understanding of muscle activation dynamics. State-of-the art estimation incorporates signal whitening and the use of multiple channels (multiple sensors per muscle)

[228], [230], [289]. These techniques have been shown to improve estimation performance compared to other methods [230], [239]. Most papers used the standard high-pass filter, rectify, low-pass filter processing to estimate sEMG amplitudes and a broad range of low-pass filter cutoff frequencies were used [200], [240], [242], [247], [248], [250], [251], [256], [261]–[263], [266], [270], [280], [282]. In addition to enveloping techniques, some incorporate the fact that the observed sEMG is the superposition of many MUAPs. Three studies (all since 2018) computed discrete features as model inputs after first performing MUAP decomposition (Table 4). Given their results, Dai and Hu (2019) recommend the MUAP decomposition over standard enveloping techniques [281]. Sun et al. (2018) identified shape-based clusters (K-means, $5 \leq K \leq 20$) of MUAPs extracted from the biceps brachii sEMG and suggest the different clusters represent different motor units [260]. The final estimation can be seen as a scaling of a single feature related to the number of activated motor units which they use to represent firing rate (see eq. (10) in [260]). Thus, the pre-processing of the raw sEMG signal, to estimate both sEMG amplitude and MUAPs, based on its physiological origin [228], [289] may have contributed to improved estimation performance.

An electromechanical delay (delayed increase in muscle force following neural excitation) is also known to characterize muscle contraction dynamics [228]. This phenomenon may provide a physiological justification for the improvements in performance associated with the use of a dynamic model structure allowing previous sEMG values to have lasting effects on the estimated output. Total delay was sometimes optimized using a grid search (625 – 875 ms [263], 50 – 150 ms [248]) and sometimes not (130 ms [262], 0.5 ms [238], 488.3 ms [282]). Clancy et al. (2006) found that performance increased with greater total time delay up to about 10 or 15 samples (i.e., 244.1 or 366.2 ms) [230]. Likewise, Clancy et al. (2012) tried between 1 and 30 sample delays and found that lesser time delays (namely total delay < 5 samples or 122.1 ms) resulted in poorer performance [239]. Overly large delays also resulted in poor performance, especially for high polynomial orders which they attribute to overfitting. The best total delays (439.5 ms – 683.ms) were dependent on polynomial order and the regularization method. Ngeo et al. (2014) modeled the sEMG to activation dynamics using the method described in [290] and optimized the electromechanical delay. Optimal values were person-specific (between 39.6 – 75 ms) and they show that incorporating electromechanical delay into their activation model improved performance compared to neglecting it [256]. Some of the optimal

delays reported in the reviewed studies are larger than what is reported elsewhere in the literature (30 – 150 ms) [228]. One explanation may be that in addition to the delayed effect of neural excitation, more information concerning the sEMG time-history could help a regression algorithm capture some sub-task related neural control pattern which may be inferred from a sufficiently large (i.e., > 150 ms) window of time. The muscle synergy hypothesis may provide a physiological basis for expecting said pattern to exist [291]. This concept was mentioned in several reviewed papers and thus we pay it special attention next.

4.4.4. Reference to muscle synergies

Several papers referred to the muscle synergy hypothesis in the development of their models and in the discussion of its performance. The muscle synergy hypothesis provides a potential explanation of how the central nervous system accomodates redundancy in motor control [292]. The theory suggests that the activation time-series of a given muscle is a linear combination of a small set of basis waveforms. Non-negative matrix factorization (NNMF) is an algorithm commonly used in muscle synergy analysis to optimally determine the basis functions and the coefficients for linear combination given a set of muscle sEMG or activation time-series [291]–[293]. Jiang et al. (2009) used these techniques directly in their estimation and show that for estimating contact forces at the hand, their method using NNMF is nearly unsupervised in that target force values are not needed and is only supervised in the sense that the degree of freedom must be known for model training [268].

Others have referred to muscle synergies as a possible explanation for the observed accuracy of some regression techniques [230], [263], [264], [276]. The synergy hypothesis indicates that the activity of all muscles contributing to a given joint torque may be approximated given a common and observable subset of sEMG observations. While the estimation of muscle activation time-series was not included in the current review, we note that Bianco et al. (2018) explored the possibility of estimating unmeasured muscle activations from sEMG time-series measured from eight different muscles using the traditional linear combination of basis waveforms formulation of muscle synergies [294]. To the authors' knowledge, no studies have regressed unmeasured muscle activations using a reduced number of wearable sensors. In this formulation, the function being identified in the regression would effectively model the synergistic

relationship between muscles. Such an approach might enable estimated activations to inform a complete set of Hill-type muscle models crossing the joint of interest to estimate muscle force. Wang and Buchannan (2002) tried a similar approach wherein a neural network was trained to learn the muscle activation dynamics (intramuscular EMG to muscle activation model) using estimated torque error to drive parameter adaptation in the learning process [295]. However, they estimated activations only for those muscles with measured intramuscular EMG. Thus, advances in modeling the observed synergistic behavior of muscle activations may prove useful for improving estimation of biomechanical time-series with a minimal number of wearable sensors. These observations motivated the developments described in Chapter 5.

The muscle synergy hypothesis suggests that an observed set of muscle activation or sEMG time-series carries redundant information and can be explained by a lower dimensional structure (e.g., less than the number of sensors available). Regularization is a common technique in machine learning used to reduce model complexity and prevent overfitting, usually at the expense of training error. Reducing the number of inputs by removing redundant information also reduces model complexity and the muscle synergy hypothesis may provide a physiological basis for this phenomenon. Clancy et al. (2012) compared ridge regression to their pseudo-inverse based regularization wherein the reciprocals of singular values below some threshold were replaced with zero [239]. The best ridge regression results were similar to the pseudo-inverse regularization. However, optimal fits were less sensitive to changes in pseudo-inverse tolerances near the optimum than they were to changes in the ridge penalty hyperparameter suggesting the pseudo-inverse technique may be easier to tune. This technique, also used in [278] and [282], along with self-organizing maps [267] and principal component analysis [247], [252], [269], [272], [276], [280], [283] are examples of unsupervised feature reduction techniques. Chen et al. (2018) found that using a deep belief network to reduce 10 inputs to three outperformed the PCA approach for the same dimensionality reduction task [280]. This might be considered a supervised dimensionality reduction (as would lasso regression [251]) as the determination of the weights in the hidden neurons of the deep belief network are optimized so that the final output best approximates the training set targets. Thus, although feature reduction is common in machine learning for improving generalizability, it may be further justified on a physiological basis given the assumption that a lower dimensional structure of the inputs exists.

4.4.5. Towards a hybrid approach

A general conclusion from these observations is that clever incorporation of domain knowledge in regression techniques may improve performance. In the papers we reviewed, this was mostly by way of sensor signal pre-processing, feature engineering, and model structure (e.g., feedback or dynamic). Incorporation of domain knowledge in regression has been suggested for other biomechanics applications [19], and as shown in [231], a good understanding of system dynamics can directly inform kernel structure in Gaussian process regression. For these reasons, hybrid methods using both physics-based and machine learning techniques in concert are being proposed in other fields including climate sciences [296], GPS-inertial navigation [297], and general chaotic processes [298]. As noted in a recent editorial [299] concerning climate modeling, "The hybrid approach makes the most of well-understood physical principles such as fluid dynamics, incorporating deep learning where physical processes cannot yet be adequately resolved." The general approach observed in many of these techniques are generalizable and applicable beyond specific scientific disciplines and thus may prove beneficial for remote patient monitoring. One approach might be to regress an unobserved internal state for which the physical relationship with observed measurements is either not well understood or not fully informed (e.g., not enough sensors) and then to drive a physical model using the estimated internal state variable. For example, this was done in [295] where the authors' chose to model muscle activation dynamics using a neural network since they determined these dynamics to be the least well understood. A second approach might be the fusion of a regression estimate and a physical model estimate. Along these lines, if uncertainties are modeled, the parameters of the regression (or the physical model) may be adapted in real-time. Gui et al. (2019) use a similar approach to remove the need to calibrate an EMG-torque model [300]. In the proposed context this could be especially useful as it may be interpreted as real-time subject specification from a general model. Further, it may enable the adaptation of a model to time-varying signal characteristics (e.g., due to electrode displacement, changes in skin conductivity, specific spatial position of inertial sensors) which may negatively impact estimation [251]. Future developments in hybrid methods that take advantage of the strengths of both physical models and machine learning may help realize the maximum potential of remote patient monitoring.

4.5. Conclusion

Regression techniques present an alternative approach to physical models for estimating biomechanical time-series using wearable sensor data. These methods could be transformative for personalizing healthcare interventions as they allow the monitoring of a patient's biomechanics continuously and in unconstrained environments. The aim of this review was to summarize relevant regression techniques in this context to imply directions for future research concerning practical implementation and improving estimation performance. Several reviewed studies found that incorporating some form of domain knowledge resulted in better estimation accuracy. Advances in this area along with open-source algorithms, validation in impaired populations, and consideration of practical hardware limitations (e.g., battery capacity and memory) may expedite future developments to make clinical implementation a reality. In summary, future work should consider the following:

- Development of methods using hardware specifications that can be implemented remotely and for a full 24-hour capture
- Development of subject-general models or real-time calibration
- Development of hybrid machine learning and physics-based estimation
- Open-source algorithms
- Development of regression models for estimating muscle forces and joint contact forces
- Validation of models on impaired populations

Chapter 5: A Gaussian Process Model of Muscle Synergy Functions for Estimating Unmeasured Muscle Excitations Using a Measured Subset

A modified version of this chapter was published as: Gurchiek, RD, Ursiny, AT, McGinnis, RS (2020). A Gaussian process model of muscle synergy functions for estimating unmeasured muscle excitations using a measured subset. IEEE Transactions on Neural Systems and Rehabilitation Engineering, 28(11): 2478-2487.

5.1. Introduction

Recent developments in remote gait analysis point toward the need to incorporate free-living observation of joint mechanics into comprehensive patient evaluations [70], [160], [301]. These measurements could capture patient-specific responses to prescribed interventions with an observation frequency not possible using laboratory-based approaches. Moreover, these measurements of clinically relevant biomechanics could be used to inform patient-specific modifications to rehabilitation programs and to evaluate their efficacy [46], [216] across a broad range of clinical populations [8], [37].

Analysis of muscle excitations during gait are integral to delivering on this vision. In this paper, muscle excitation (a.k.a. sEMG amplitude [228], [302]) refers to the time-varying excited state of muscle and is related to motor unit recruitment and firing rate [302]. Muscle excitation is distinguished from muscle activation which is defined functionally for scaling active muscle force in sEMG-driven muscle force estimation [228] and has been related to the calcium dynamics promoting muscle force production [224], [303]. Muscle excitations alone provide clinical insight into motor control. To this end, are used to quantify control complexity in patients with neurological disorders via synergy analysis [28], [304] and, in a remote gait analysis application, for monitoring rehabilitation progress following knee surgery (Chapter 3) [70]. Further, excitations drive muscle activation dynamics which are used to estimate muscle forces [209], [224], [290]. Remote estimation of muscle forces provides an avenue for advancing the current state of remote monitoring techniques (mostly limited to spatiotemporal variables [8], [301]) to incorporate additional clinically relevant biomechanical variables. For example, muscle work could be utilized in an adaptive rehabilitation context for its relation to work-induced muscle hypertrophy [305]. Further, muscle forces are

necessary to estimate muscle contributions to joint contact force and net joint moments using force plate-free techniques [209], [290] (a requirement for remote monitoring) both of which provide invaluable insight in many orthopedic conditions [31], [37].

Wearable sEMG sensors provide the hardware solution to realize the aforementioned remote analyses, but one of the primary limitations to practical deployment is the number of sensors necessary [224]. For joint contact force and net joint moment estimates, a sensor would be required on every muscle. Such a complex wearable system greatly impedes users' daily life; an increased burden that may discourage use [160]. Non-sEMG data have been used to estimate muscle forces and/or excitations (with or without sEMG data) using both regression [306]–[309] and optimization-based solutions to the muscle redundancy problem following inverse-dynamics [310]. However, wearable sensor solutions in this context also require many sensors [25], [311] limiting use in remote gait analysis.

Regression techniques have been proposed as a means to reduce the number of necessary wearable sensors for estimating biomechanical time-series (Chapter 4) [12]. These have proven successful for estimating joint moments, which as discussed earlier, serve as the starting point for optimization-based muscle force solutions. However, as mentioned in Chapter 4 [12], a hybrid approach may enable a more generalized solution wherein machine learning is used to augment estimation where the physics are least well understood [299]. For example, consider that a model using only sEMG inputs trained to estimate joint angle during open-chain tasks must learn (1) the mapping from a subset of measured excitations to a complete set, (2) muscle activation dynamics, (3) muscle contraction dynamics, (4) rigid body dynamics, and (5) forward integration of the kinematic equations. In this example, steps (2)-(5) and their associated physics have been well studied whereas the mapping described in step (1) is least well understood. Thus, the proposed hybrid solution would be to approximate the behavior of step (1) using machine learning wherein a complete set of muscle excitations would be informed by a measured subset. This complete set of excitations could then drive the dynamics of steps (2)-(5) using sEMG-driven techniques which are well described in the biomechanics literature [209], [290]. The success of regression models motivates the existence of the mapping in step (1) (which we refer to as synergy functions) and is further supported by recent results

suggesting a subset of muscles may carry the information necessary for reconstructing unmeasured excitations [294].

In this study, we propose to model synergy functions as a Gaussian process (GP) and develop an approximation to their behavior that allows estimation of unmeasured excitations from a measured subset. Gaussian process regression is suitable in this context as it has been shown advantageous for small datasets [256] and because it provides the variance of the estimate which may prove beneficial in sensor fusion frameworks considered in future applications. Further, a GP model permits a connection to probabilistic theories of motor control [312]. The novel developments in this study (building on our preliminary work [313]) include the Gaussian process model of muscle synergy functions and the estimation of unmeasured muscle excitations using only a subset of sEMG data.

5.2. Gaussian process model of muscle synergy functions

The main assumption made in this development is the existence of a function, $f_m: \mathbb{R}^d \rightarrow \mathbb{R}$, which maps the excitation $y_m(t) \in \mathbb{R}$ of muscle m (called the output muscle) at time t from an input vector $\boldsymbol{x}(t) \in \mathbb{R}^d$ (Figure 16). Specifically, $\boldsymbol{x}(t)$ is composed of excitations from a subset of p muscles (called the input muscle set) during a finite time interval, $[t_1 \quad t_n]$, such that $t_1 \leq t \leq t_n$ (called the input window). The d-dimensional input $\boldsymbol{x}(t)$ is partitioned as per

$$\boldsymbol{x}(t) = [\boldsymbol{v}_1(t) \quad \boldsymbol{v}_2(t) \quad \cdots \quad \boldsymbol{v}_p(t)] \tag{5.1}$$

where $\boldsymbol{v}_i(t)$ is n-dimensional,

$$\boldsymbol{v}_i(t) = [v_{i,1} \quad v_{i,2} \quad \cdots \quad v_{i,n}] \tag{5.2}$$

and $v_{i,j}$ is the j^{th} sample of the excitation time-series of the i^{th} input muscle such that $v_{i,1} = v_i(t_1)$ and $v_{i,n} = v_i(t_n)$. Thus, the dimension of the input, $d = pn$, is dependent on the number of input muscles, the size of the input window $(t_n - t_1)$, and the sEMG sampling frequency. The idea employed here is that the subset of input muscles and the output muscle are controlled in a coordinated fashion (i.e., synergistically) to achieve some sub-task during the time interval $[t_1 \quad t_n]$ (e.g., propulsion of the center of mass during walking) and

that this relationship can be inferred just from the excitations of the input muscles. Due to the nature of this mapping, we refer to f_m as a synergy function.

Our approach is to approximate f_m using Gaussian process regression [231]. To this end, we model the synergy function f_m as a GP indexed on the input muscle excitations. This implies [314] that the scalar $f_m(\boldsymbol{x})$ is a random variable with Gaussian distribution as per $f_m(\boldsymbol{x}) \sim \mathcal{N}\big(\mu_m(\boldsymbol{x}), \sigma_m^2(\boldsymbol{x})\big)$ and is jointly Gaussian with $f_m(\boldsymbol{x}')$ (a synergy function output associated with an arbitrary input vector $\boldsymbol{x}'$) with covariance given by

$$\mathrm{cov}\big(f_m(\boldsymbol{x}), f_m(\boldsymbol{x}')\big) = k_m(\boldsymbol{x}, \boldsymbol{x}') \tag{5.3}$$

where $k_m(\boldsymbol{x}, \boldsymbol{x}')$ is a muscle-specific covariance function defining the covariance between $f_m(\boldsymbol{x})$ and $f_m(\boldsymbol{x}')$. Thus, for consistency, the variance of $f_m(\boldsymbol{x})$, denoted as $\sigma_m^2(\boldsymbol{x})$, is $k_m(\boldsymbol{x}, \boldsymbol{x})$ and the mean is defined by a muscle-specific mean function $\mu_m(\boldsymbol{x})$.

To learn the behavior of the synergy function f_m, we observe the synergistic relationship between the input muscle excitations and those of the output muscle given a set of N measured input-output pairs, $\big(y_{m,i}, \boldsymbol{x}_i\big)$, called the training set. It is assumed that the measured output muscle excitations $y_{m,i}$ in the training set are additively corrupted with muscle-specific, independent and identically distributed, zero-mean Gaussian noise, $w_{m,i} \sim \mathcal{N}(0, \epsilon_m^2)$, so that

$$y_{m,i} = f_m(\boldsymbol{x}_i) + w_{m,i}. \tag{5.4}$$

The N measured output muscle excitations in the training set are used to form a column vector $\boldsymbol{y}_m$ (a random vector),

$$\boldsymbol{y}_m = [y_{m,1} \quad y_{m,2} \quad \cdots \quad y_{m,N}]^T \tag{5.5}$$

which is characterized by a joint multivariate Gaussian distribution, $\boldsymbol{y}_m \sim \mathcal{N}(\boldsymbol{\mu}_m, \Sigma_m)$, expressed in terms of its mean vector $\boldsymbol{\mu}_m$ and $N \times N$ covariance matrix Σ_m. Since $w_{m,i}$ is zero-mean, the mean vector $\boldsymbol{\mu}_m$ is (element-wise expectation in eq. (5.5))

$$\boldsymbol{\mu}_m = [\mu_m(\boldsymbol{x}_1) \quad \mu_m(\boldsymbol{x}_2) \quad \cdots \quad \mu_m(\boldsymbol{x}_N)]^T \tag{5.6}$$

and due to the independence assumption, the element in row r and column c of Σ_m is

$$[\Sigma_m]_{r,c} = k_m(\boldsymbol{x}_r, \boldsymbol{x}_c) + \epsilon_m^2[\mathrm{I}]_{r,c} \tag{5.7}$$

where $[\mathrm{I}]_{r,c}$ is the element in row r and column c of the $N \times N$ identity matrix I [231], [315].

Given an unseen input, $\boldsymbol{x}_*$ (not in the training set), the corresponding synergy function value, $f_m^* = f_m(\boldsymbol{x}_*)$, must also be jointly Gaussian with $\boldsymbol{y}_m$ (per the GP model) and thus

$$\begin{bmatrix} \boldsymbol{y}_m \\ f_m^* \end{bmatrix} \sim \mathcal{N}\left(\begin{bmatrix} \boldsymbol{\mu}_m \\ \mu_m(\boldsymbol{x}_*) \end{bmatrix}, \begin{bmatrix} \Sigma_m & \boldsymbol{k}_m(\boldsymbol{X}, \boldsymbol{x}_*) \\ \boldsymbol{k}_m^T(\boldsymbol{X}, \boldsymbol{x}_*) & k_m(\boldsymbol{x}_*, \boldsymbol{x}_*) \end{bmatrix} \right) \tag{5.8}$$

where we have used $\boldsymbol{k}_m^T(\boldsymbol{X}, \boldsymbol{x}_*)$ to denote the N-element row vector of covariances between f_m^* and each muscle excitation in the training set $\boldsymbol{y}_m$ such that

$$\boldsymbol{k}_m^T(\boldsymbol{X}, \boldsymbol{x}_*) = [k_m(\boldsymbol{x}_1, \boldsymbol{x}_*) \quad \cdots \quad k_m(\boldsymbol{x}_N, \boldsymbol{x}_*)]. \tag{5.9}$$

and the symbol $\boldsymbol{X}$ is used to denote all input vectors in the training set. Finally, the conditional distribution of the synergy function value f_m^* is given by conditioning the joint Gaussian prior in eq. (5.8) on the observed training data, $\boldsymbol{y}_m$. This conditional distribution is Gaussian with mean [231], [315]

$$\bar{f}_m^* = \mu_m(\boldsymbol{x}_*) + \boldsymbol{k}_m^T(\boldsymbol{X}, \boldsymbol{x}_*)\Sigma_m^{-1}(\boldsymbol{y}_m - \boldsymbol{\mu}_m) \tag{5.10}$$

and variance

$$(\sigma_m^*)^2 = k_m(\boldsymbol{x}_*, \boldsymbol{x}_*) - \boldsymbol{k}_m^T(\boldsymbol{X}, \boldsymbol{x}_*)\Sigma_m^{-1}\boldsymbol{k}_m(\boldsymbol{X}, \boldsymbol{x}_*). \tag{5.11}$$

Therefore, in the proposed estimation procedure, given a subset of (unseen) measured muscle excitations organized as a model input, $\boldsymbol{x}_*$, our estimate of y_m^* is $\bar{f}_m^*$ in eq. (5.10) and can be written as

$$y_m^* = \mu_m(\boldsymbol{x}_*) + \beta_{m,1}k_m(\boldsymbol{x}_1, \boldsymbol{x}_*) + \cdots + \beta_{m,N}k_m(\boldsymbol{x}_N, \boldsymbol{x}_*) \tag{5.12}$$

where the coefficient $\beta_{m,i}$ (specific to output muscle m) is the i^{th} element of the column vector $\boldsymbol{\beta}_m$ given by

$$\boldsymbol{\beta}_m = \Sigma_m^{-1}(\boldsymbol{y}_m - \boldsymbol{\mu}_m) \tag{5.13}$$

and it is clear that the output y_m^* is a scalar. The variance of the estimate is the sum of the variance, $(\sigma_m^*)^2$,

of the conditional distribution of f_m^* in eq. (5.11) and the noise variance ϵ_m^2 in eq. (5.4) as per

$$\text{var}(y_m^*) = (\sigma_m^*)^2 + \epsilon_m^2. \tag{5.14}$$

When deploying this method in practice, the $\beta_{m,i}$ are already known as they depend on training data only and as seen in eq. (5.13) require inversion of the covariance matrix Σ_m. This inversion can be thought of as training the model and is required in eq. (5.11) to describe the uncertainty of the estimate, y_m^*, in eq. (5.14). Further, the mean function and covariance function may depend on one or more hyperparameters (including the noise variance ϵ_m^2) which are optimized by minimization of the negative log marginal likelihood over the training data using conjugate gradient descent. Hyperparameters for the models used in this work are introduced when the mean and covariance functions are specified. All aspects of training the GP models were done using the GPML toolbox [316], [317] in MATLAB R2019b. A custom package was developed that streamlines the development of different model structures (e.g., input muscle sets, input window size) for training, testing, and evaluation.

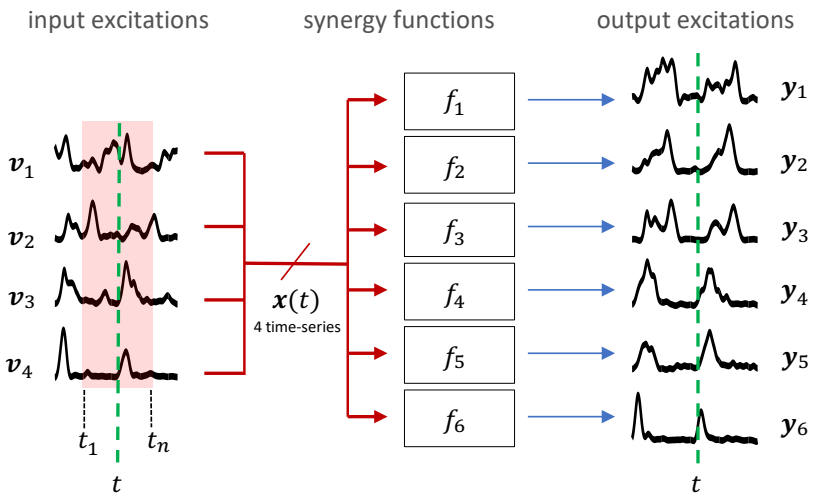

Figure 16: Visual overview of the proposed estimation procedure. In this example, four muscle excitation time-series are available from measured sEMG data (input muscles: v_i) and are used to estimate the excitation time-series of six other muscles (output muscles: y_i). To estimate the muscle excitation at time t (green dashed line) for a given output muscle, a finite time interval $[t_1\ t_n]$ (black dashed lines), called the input window (shaded red area), of each input muscle is input to the corresponding synergy function (f_i).

5.3. Experimental validation

Sixteen unimpaired subjects walked for one-minute at a self-selected normal walking speed on a level treadmill (h/p/cosmos quasar) while sEMG data (BioStamp nPoint, MC10, Inc., sampling frequency: 1000 Hz) were continuously recorded from 10 muscles of the right leg: tibialis anterior (TA), peroneus longus (PL), lateral gastrocnemius (LG), medial gastrocnemius (MG), soleus (SOL), vastus medialis (VM), rectus femoris (RF), vastus lateralis (VL), biceps femoris (BF), and semitendinosus (ST). Electrode placement was according to SENIAM recommendations [318]. Muscle excitations were computed from raw sEMG data using methods common for estimating muscle force [209]. Specifically, sEMG data were digitally high-pass filtered at 30 Hz, rectified, low-pass filtered at 6 Hz, and normalized by the maximum value across the walking trial and several muscle-specific maximum voluntary contraction trials (MVC). All muscle excitation time-series were resampled to 250 Hz to explore application of the proposed approach for sampling frequencies used in remote monitoring [70]. Following a visual sEMG data quality check, all data for seven subjects were removed as there was no clear signal during walking for at least one muscle. Thus, all data used in this study were from the other nine subjects (five males, height: 1.8 ± 0.1 m, mass: 72.3 ± 12.4 kg, age: 21 ± 1 years). The average walking speed across all subjects was 0.84 ± 0.13 m/s and the average stride time was 1.31 ± 0.22 s. All subjects provided written consent to participate and all activities were approved by the University of Vermont Institutional Review Board (#18-0518).

The proposed GP model for estimating muscle excitations is modifiable in many ways. In this study, we explore the effects of different model characteristics at three levels: (1) input muscle sets, (2) structure of the input window, and (3) stationarity of the covariance function. All models explored were subject-specific models, i.e., all data used to train and test a given model were from the same subject. Models were trained on 15 seconds of data from the first half of the one-minute walking trial. Models were evaluated using 15 seconds of data from the second half of the trial, and thus these data were not "seen" by the model during the training process. A constant mean function was assumed for all GP models dependent on a single hyperparameter c_m,

$$\mu_m(\boldsymbol{x}) = c_m. \tag{5.15}$$

5.3.1. Input muscle sets

The impact of input muscle set on estimation performance was explored using an exhaustive approach. We trained models using every possible combination of four, three, and two input muscles (out of the 10 we instrumented) yielding 210, 120, and 45 combinations, respectively. For each input set, GP models were trained to estimate the excitations of each of the muscles not in the input set. For this analysis, we used a scaled, squared exponential covariance function with isotropic length scale given by

$$k_m(\boldsymbol{x}, \boldsymbol{x}') = \theta_1 \exp\left(-\frac{\boldsymbol{r}^T\boldsymbol{r}}{2\theta_2^2}\right) \tag{5.16}$$

where $\boldsymbol{r} = \boldsymbol{x} - \boldsymbol{x}'$ and the hyperparameters are the scalar θ_1 and the characteristic length scale θ_2. The window size $(t_n - t_1)$ was set to 1.0 s and the window relative output time $(t_n - t)$ was set to 0.5 s. The maximum number of function evaluations for hyperparameter optimization was set to 50.

5.3.2. Model selection

Only one input muscle set for each of the four-, three-, and two-muscle input sets was used to further examine the effect of window structure (section 5.3.3.) and the stationarity of the covariance function (section 5.3.4.). Using an exhaustive search approach, one would normally score the performance of each input set according to some performance metric and choose the one with the best score. However, several different metrics are common for evaluating estimation of biomechanical time-series including Pearson's correlation coefficient (*r*), percentage of variance accounted for (VAF), root mean square error (RMSE), and mean absolute error (MAE) [12]. In an attempt to select the best input set with consideration of each of these metrics we utilized a z-score averaging method. To this end, each metric was computed for each muscle-specific synergy function corresponding to each muscle in the output set for each investigated input set. These were evaluated by comparing the estimated excitations with the true measured excitations in the test set. Performance metrics for a given input set were first averaged across all output muscles and then across all subjects yielding four metrics (*r*, VAF, RMSE, MAE) for each input muscle set. Four additional metrics per input muscle set were computed wherein the same procedure was repeated except that muscles were weighted in the averaging across muscles according to their relative physiological cross-sectional area (PCSA, data

taken from [319]). This was done to bias the selection of muscles with the greatest capacity to produce muscle force (on average). In practice, the excitations of the long head of the BF and of the ST are often assumed equivalent to that of the short head of the BF and the semimembranosus, respectively [209]. Therefore, for the PCSA-weighted average, the BF weighting was based on the sum of the PCSA of the long and short heads of the BF and the ST weighting was based on the sum of the PCSA of the ST and the semimembranosus. Thus, eight performance metrics were available for each input muscle set. The values for each metric were converted to z-scores (demeaned and normalized by the standard deviation across all models). RMSE and MAE z-scores were negated so that larger values indicated better performance for all metrics. Finally, the average of these z-scores served as the single performance metric by which the models were ranked. This was done separately for the four-, three-, and two-muscle input sets under consideration.

5.3.3. Input window structures

Window structure was modified according to the input window size ($t_n - t_1$) and the window relative output time ($t_n - t$). Fourteen input window structures were explored, namely, every combination of seven input window sizes (1.75, 1.50, 1.25, 1.00, 0.75, 0.50, and 0.25 seconds) and two window relative output times: 0.0 s such that $t = t_n$ and half the window size such that $t = 0.5(t_1 + t_n)$. Each window structure was explored separately for the best four-, three-, and two-muscle input sets determined from section 5.3.1. The same mean function, covariance function, and optimization settings were used in this analysis. The best input window structure was chosen using the z-score averaging method in section 5.3.2.

5.3.4. Covariance function stationarity

This analysis concerns the stationarity of the covariance function for the proposed estimation problem. The squared exponential covariance function in eq. (5.16) is stationary (i.e., it is a function only of $\boldsymbol{r} = \boldsymbol{x} - \boldsymbol{x}'$ which is unchanged given a translation of the origin). As an example non-stationary covariance function, we use the neural network covariance function given by [231], [320]

$$k_m(\boldsymbol{x}, \boldsymbol{x}') = \theta_1^2 \arcsin\left(\frac{\tilde{\boldsymbol{x}}^T \tilde{\boldsymbol{x}}'}{\sqrt{(\theta_2^2 + \tilde{\boldsymbol{x}}^T \tilde{\boldsymbol{x}})(\theta_2^2 + \tilde{\boldsymbol{x}}'^T \tilde{\boldsymbol{x}}')}}\right) \tag{5.17}$$

where $\tilde{\boldsymbol{x}}^T = [\boldsymbol{x}^T \ 1]$ and θ_i are hyperparameters. It was shown in [320], that eq. (5.17) is the covariance function for a neural network with an error function activation in the hidden layer as the number of hidden units tends to infinity. Six models were trained, one for each of the best four-, three-, and two-muscle input sets described previously and for both the squared exponential and neural network covariance functions. The best window structure determined from the analysis described in section 5.3.3. was used for each model. Since there were only six models to train and this was the last level of model characteristics explored, we allowed the hyperparameter optimization to continue until convergence.

5.3.5. Muscle activation dynamics

One potential use of this method may be to estimate muscle force using a reduced sEMG array wherein excitations are input to a muscle activation model. To evaluate the error in estimating muscle activations in this way, we used estimated and measured excitations as inputs to a critically damped, linear, second-order activation model with unity gain and 3 Hz natural frequency [321]. Only the four-muscle input set with squared exponential covariance function was used for this analysis.

5.3.6. Comparison to NNMF-based methods

To the authors' knowledge, no previous study has presented similar results in estimating muscle excitations from a measured subset to which ours could be compared. However, Bianco et al. (2018) showed that synergy excitations computed from a subset of measured muscles could reconstruct unmeasured excitations if the synergy weights for the unmeasured muscles were known [294]. Following this approach, three synergy vectors and the corresponding excitations were determined for the best four-muscle input set using an iterative procedure utilizing both the multiplicative update and alternating least squares algorithms for non-negative matrix factorization (NNMF). This was done using test set data for each subject. Synergy weights for the output muscles were determined using linear least squares regression as in [294].

5.3.7. Statistical analysis

All models were evaluated using the performance metrics described in section 5.3.2.: *r*, VAF, RMSE, and MAE. RMSE and MAE values are expressed as a percentage of MVC. These quantify estimation

performance by comparing estimated muscle excitations to measured excitations in the test set (all unseen data). Metrics were computed for each output muscle separately and averaged across subjects. Average correlations were corrected using Fisher's z transformation [322] and interpreted qualitatively as weak ($r \leq 0.35$), moderate ($0.35 < r \leq 0.67$), strong ($0.67 < r \leq 0.90$), and very strong ($r \geq 0.90$) [323]. Per the analysis described in section 5.3.5., activations driven by the estimated excitations were compared to those driven by the measured excitations using *r*, VAF, RMSE, and MAE. The reconstruction accuracy of the NNMF approach was compared to the estimation accuracy of the proposed method using VAF.

5.4. Results

According to the z-score averaging method and following the analysis described in section 5.3.1., the best four-muscle input set was BF, PL, SOL, VL ($r = 0.76$, VAF = 86%, RMSE = 3.6%, MAE = 2.4%) and strong correlations ($r > 0.67$) were observed for 200 out of the 210 sets. The best three-muscle input set was BF, PL, SOL ($r = 0.73$, VAF = 84%, RMSE = 3.4%, and MAE = 2.2%) and strong correlations were observed for 80 out of the 120 sets. The best two-muscle input set was LG, SOL ($r = 0.67$, VAF = 74%, RMSE = 4.1%, and MAE = 2.7%) and strong correlations were observed for only two out of the 45 sets (the other was PL, MG). These muscle sets were used for the remaining analyses. Heatmaps illustrating the pair-wise predictability for unique muscle pairs as well as for individual muscles are shown in Figures 17-19.

The window relative output time corresponding to half the window size, $t = 0.5(t_1 + t_n)$, performed better than $t = t_n$ for all models. Generally, larger window sizes performed better up to what appears to be a point of diminishing returns (Figure 20). For both the four- and three-muscle input sets, the 1.75 and 1.50 s window sizes had a z-score of 0.53. For the two-muscle input set, the 1.75 s window size (z-score = 0.52) was only slightly better than the 1.50 s window size (z-score = 0.51). Thus, in the remaining analyses, a 1.50 s window size with 0.75 s window relative output time was used.

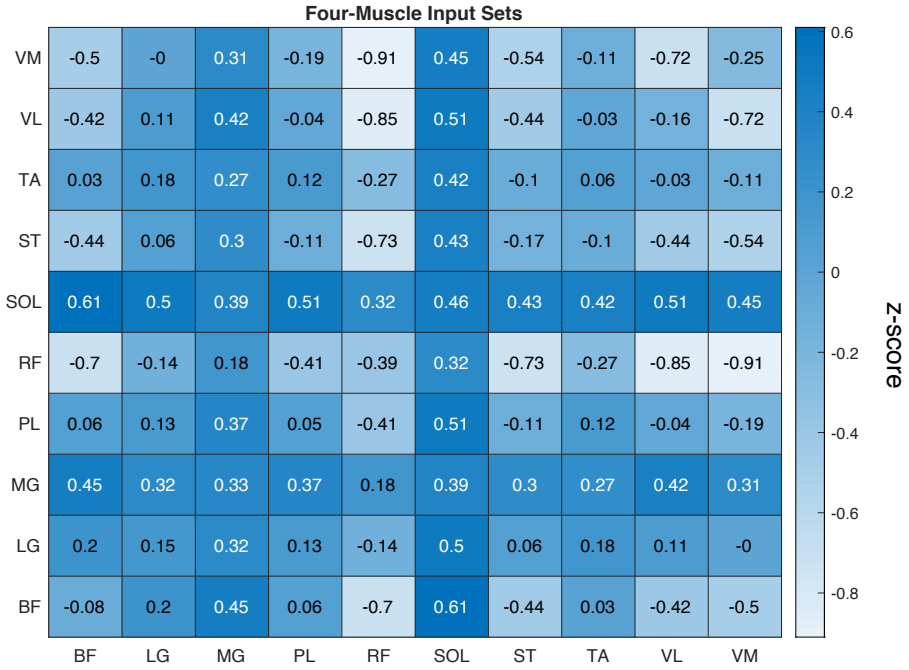

Figure 17: Average z-score (used to rank input muscle sets as described in manuscript) of all four-muscle input sets containing each unique pair of input muscles. The z-score corresponding to a muscle paired with itself indicates the average z-score across all four-muscle input sets that contained that muscle. For example, the average z-score for four-muscle input sets that included BF and SOL was 0.61 and the average z-score for four-muscle input sets that included SOL was 0.46. Each unique pair of muscles were present in 28 of the 210 total four-muscle input sets and each unique muscle was present in 84 of the total 210 sets.

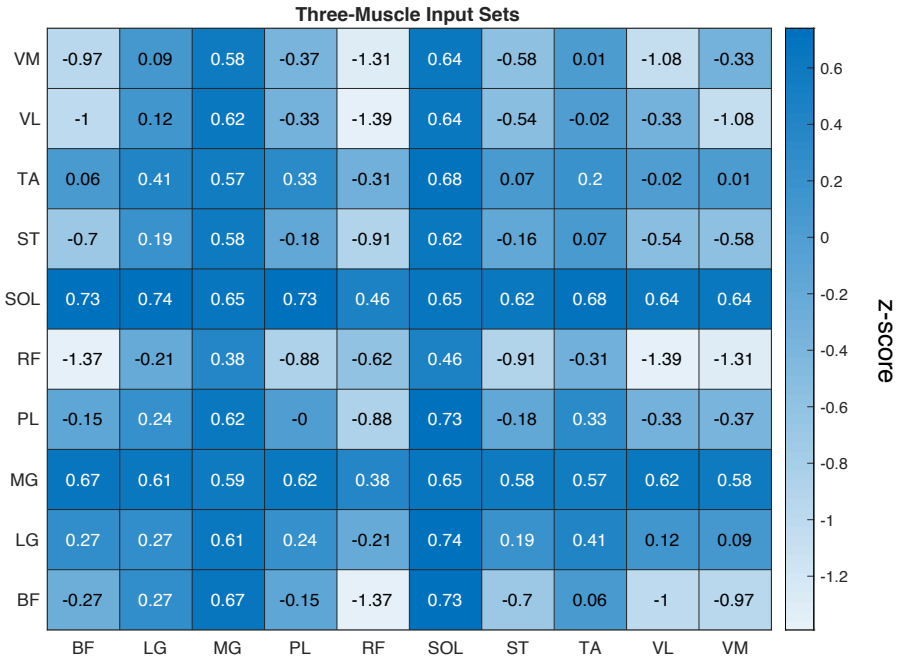

Figure 18: Average z-score (used to rank input muscle sets as described in manuscript) of all three-muscle input sets containing each unique pair of input muscles. The z-score corresponding to a muscle paired with itself indicates the average z-score across all three-muscle input sets that contained that muscle. For example, the average z-score for three-muscle input sets that included BF and SOL was 0.73 and the average z-score for three-muscle input sets that included SOL was 0.65. Each unique pair of muscles were present in 8 of the 120 total three-muscle input sets and each unique muscle was present in 36 of the total 120 sets.

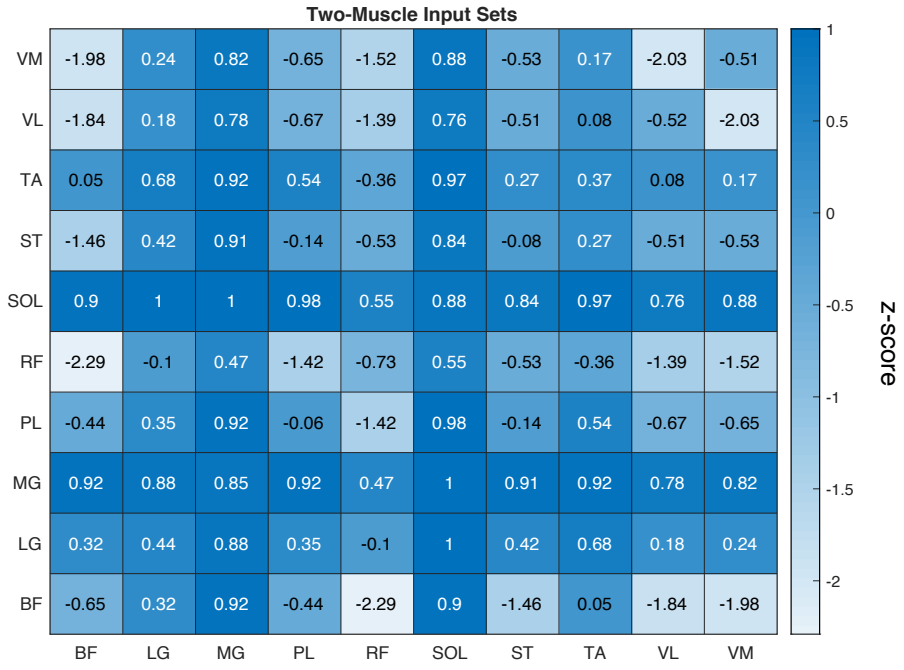

Figure 19: Average z-score (used to rank input muscle sets as described in manuscript) of all two-muscle input sets containing each unique pair of input muscles. The z-score corresponding to a muscle paired with itself indicates the average z-score across all two-muscle input sets that contained that muscle. For example, the average z-score for two-muscle input sets that included BF and SOL was 0.9 and the average z-score for two-muscle input sets that included SOL was 0.88. Each unique pair of muscles were present in only 1 of the 45 total two-muscle input sets and each unique muscle was present in 9 of the total 45 sets.

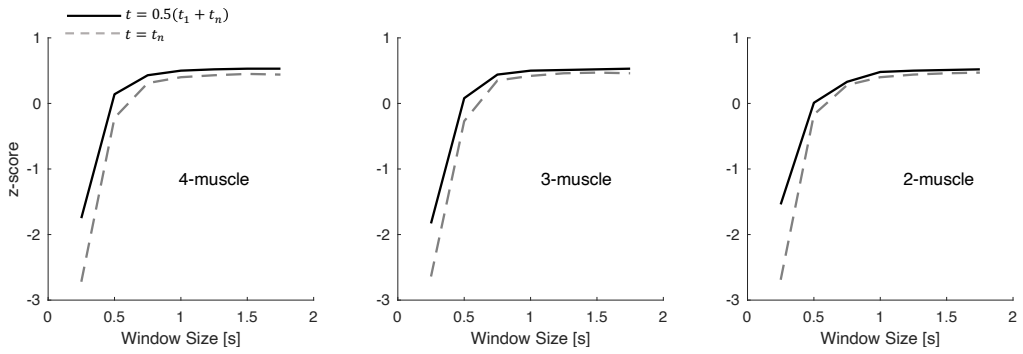

Figure 20: Relationship between window size (in seconds) and z-scores used to rank window structures for window relative output times $t = t_n$ (dashed grey line) and $t = 0.5(t_1 + t_n)$ (solid black line) using the best four-muscle input set (BF, PL, SOL, VL: leftmost plot), the best three-muscle input set (BF, PL, SOL: middle plot), and the best two-muscle input set (LG, SOL: rightmost plot).

The estimation performance for models using the squared exponential and neural network covariance functions are presented in Table 5. Although their performances were similar, the subject-averaged statistics shown in Table 5 suggest the stationary covariance function (squared exponential) performed better across all output muscles and input muscle sets except that the two-muscle input model with neural network covariance resulted in a slightly greater correlation ($r = 0.68$) for the VL model compared to $r = 0.67$ for the squared exponential covariance. For the four-muscle input set, all correlations were strong and on average accounted for ≥ 85% VAF. Likewise, all correlations were strong for the three-muscle input set except for the RF ($r = 0.66$). The two-muscle input set performed surprisingly well with strong correlations across all muscles except moderate correlations observed for the BF ($r = 0.65$) and RF ($r = 0.63$). Further, the BF model accounted for only 55% VAF which was noticeably less compared to other muscles. The next lowest VAF for the two-muscle input set was 75% for ST while all models for the three-muscle input set explained more than 80% VAF. Figure 21 depicts a graphical comparison of estimated and measured excitations.

Comparison of muscle activations informed by measured and estimated excitations are presented in Table 6 (four-muscle input set). Strong to very strong correlations were observed across all muscles and on average, activations driven by the estimated excitations were able to explain more than 90% VAF in the

true activation time-series except for the ST (VAF = 89%) with MAE < 4.0%. Figure 22 depicts a graphical comparison of estimated and true activations for every output muscle and for every subject.

The NNMF-based reconstruction performance quantified by VAF was 74 ± 15% for MG, 82 ± 9% for LG, 66 ± 13% for TA, 67 ± 15% for ST, 89 ± 9% for VM, and 80 ± 15% for RF which was less than that observed for all output muscle models using the four-muscle input set except for the VM (NNMF: VM VAF = 89%, GP: VM VAF = 87%).

Table 5: Muscle excitation estimation performance

		Stationary Covariance				Non-Stationary Covariance			
Input	Output	*r*	VAF	RMSE	MAE	*r*	VAF	RMSE	MAE
4 Muscles (BF,PL,SOL,VL)	MG	0.89	88 (5)	7.2 (2.2)	4.7 (1.6)	0.89	87 (5)	7.4 (2.3)	5.0 (1.7)
	LG	0.81	85 (10)	4.9 (1.9)	3.2 (1.2)	0.80	83 (13)	5.1 (2.0)	3.5 (1.5)
	TA	0.81	88 (5)	4.0 (2.1)	2.8 (1.4)	0.79	85 (7)	4.3 (2.2)	3.2 (1.7)
	ST	0.82	82 (8)	2.4 (1.4)	1.5 (0.8)	0.81	80 (10)	2.5 (1.3)	1.6 (0.8)
	VM	0.78	87 (10)	2.1 (1.3)	1.3 (0.7)	0.77	85 (11)	2.2 (1.4)	1.4 (0.8)
	RF	0.68	88 (8)	0.8 (0.3)	0.5 (0.2)	0.69	87 (10)	0.8 (0.3)	0.5 (0.2)
3 Muscles (BF,PL,SOL)	MG	0.89	87 (5)	7.2 (2.2)	4.8 (1.6)	0.89	87 (5)	7.5 (2.3)	5.1 (1.7)
	LG	0.80	84 (10)	5.1 (2.1)	3.3 (1.2)	0.79	82 (12)	5.3 (2.3)	3.6 (1.6)
	TA	0.80	87 (5)	4.1 (2.1)	2.8 (1.4)	0.79	85 (6)	4.4 (2.2)	3.2 (1.7)
	ST	0.81	81 (8)	2.4 (1.4)	1.5 (0.8)	0.80	80 (8)	2.5 (1.3)	1.6 (0.8)
	VM	0.76	83 (15)	2.3 (1.5)	1.4 (0.8)	0.73	79 (19)	2.5 (1.6)	1.6 (0.9)
	VL	0.73	84 (11)	1.5 (1.2)	0.9 (0.7)	0.70	80 (16)	1.7 (1.4)	1.1 (0.9)
	RF	0.66	86 (7)	0.8 (0.3)	0.5 (0.2)	0.64	84 (10)	0.9 (0.4)	0.6 (0.2)
2 Muscles (LG,SOL)	MG	0.91	90 (3)	6.5 (1.7)	4.3 (1.3)	0.91	90 (4)	6.5 (1.7)	4.4 (1.3)
	PL	0.76	80 (8)	6.5 (2.3)	4.2 (1.4)	0.76	78 (8)	6.7 (2.3)	4.5 (1.5)
	TA	0.80	87 (3)	4.1 (1.9)	2.9 (1.3)	0.78	85 (5)	4.4 (2.1)	3.2 (1.6)
	ST	0.76	75 (10)	2.7 (1.5)	1.8 (0.9)	0.74	73 (12)	2.8 (1.5)	2.0 (1.0)
	BF	0.65	55 (29)	4.8 (2.3)	2.9 (1.4)	0.61	46 (33)	5.2 (2.3)	3.4 (1.5)
	VM	0.71	82 (15)	2.4 (1.5)	1.5 (0.8)	0.69	79 (18)	2.5 (1.6)	1.6 (0.9)
	VL	0.67	81 (12)	1.5 (1.1)	1.0 (0.7)	0.68	81 (12)	1.5 (1.1)	1.0 (0.7)
	RF	0.63	84 (11)	0.9 (0.4)	0.6 (0.3)	0.63	83 (10)	0.9 (0.3)	0.6 (0.2)

Measured and estimated excitations were compared for the best four, three, and two muscle input sets, the best input window structure, and for a stationary (squared exponential) and non-stationary (neural network) covariance function using only data from the test set. Performance metrics include correlation coefficient (*r*); percentage of variance accounted for (VAF); root mean square error (RMSE) in units percentage of MVC; mean absolute error (MAE) in units percentage of MVC. The reported VAF, RMSE, and MAE values are the average across all subjects for each muscle with the standard deviation in parentheses. The *r* values are the average correlation coefficients across all subjects using Fisher's *z* transformation as described by Silver and Dunlap (1987).

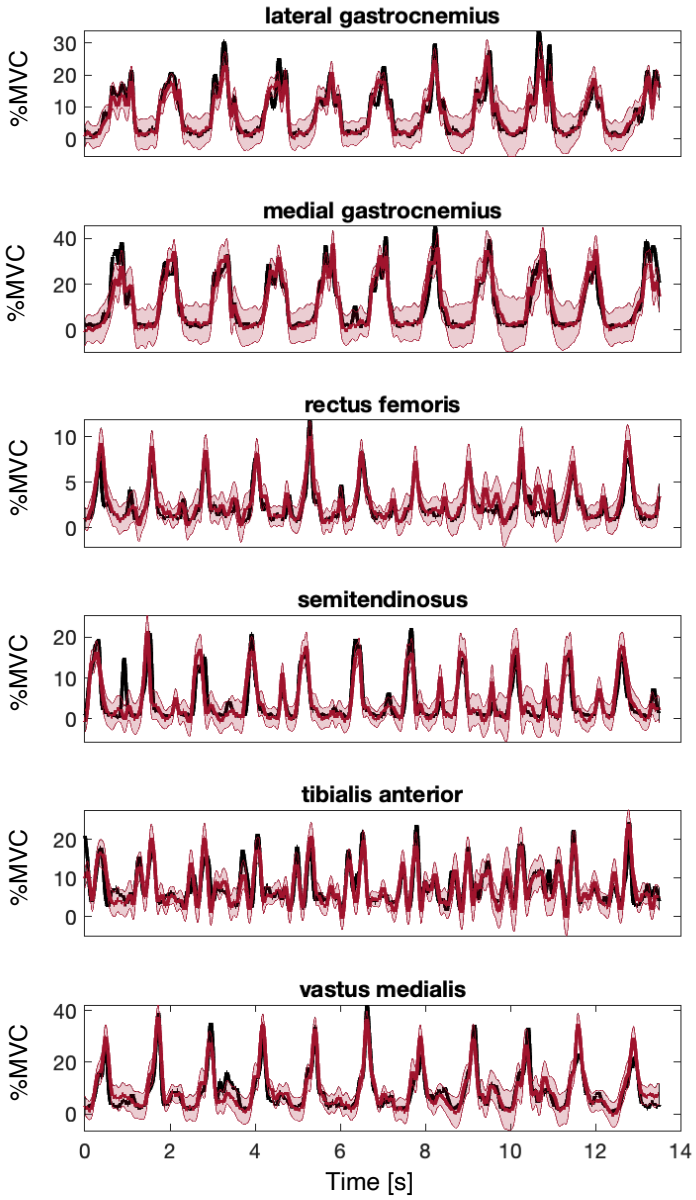

Figure 21: Graphical comparison of the estimated excitation time-series (red line) and the measured excitation time-series (black line) for data from the test set of a typical subject. The shaded area represents the mean $\pm$ two standard deviations, i.e., the square root of the variance in eq. (5.14).

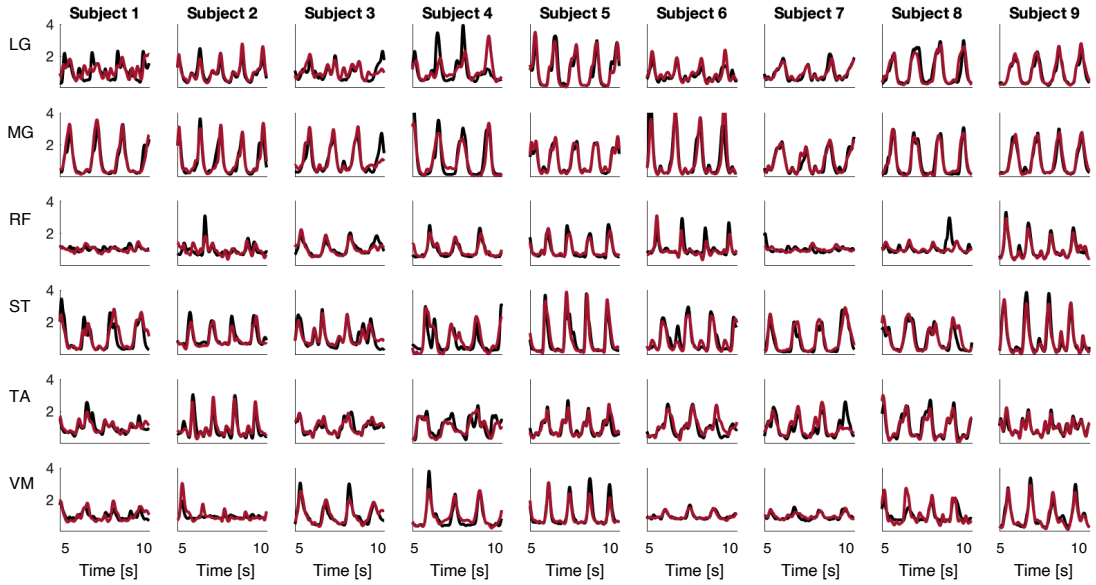

Figure 22: Graphical comparison of muscle activation time-series from estimated (red lines) and measured (black lines) muscle excitation time-series per the analysis described in section 5.3.5. Shown here are the middle five seconds of each activation time-series determined using a second-order, linear activation model driven by corresponding excitations from the test set. Columns correspond to individual subjects and rows correspond to individual output muscles. Activation units have been normalized by the average activation throughout the full 15 seconds of test set data.

5.5. Discussion

In this paper, we have demonstrated the ability to accurately estimate unmeasured muscle excitations using a subset of measured sEMG data. The feasibility of this approach has previously only been suggested based on conclusions from a recent review of regression techniques for biomechanical time-series [12] and was indirectly supported in [294]. Based on these previous results, we introduced the notion of muscle synergy functions (Figure 16) and developed from first principles the Gaussian process regression-based approximation to their behavior (section 5.2.).

An exhaustive search was used to study optimal input muscle sets. The set selection approach considered both the raw estimation performance metrics and weighted performance metrics according to the relative muscle PCSA. The former is important in clinical applications where excitations are used to quantify

motor control complexity [28], [304] and to monitor progression following knee surgery [70]. Incorporating the additional PCSA-weighted average of performance metrics was done to purposely bias the muscle set selection such that the muscles with the greatest force producing capacity were estimated more accurately (on average). This choice was motivated by the potential use of this technique for estimating muscle force in remote gait analysis. This could be transformative for this area of research, providing insight into biomechanical variables more sensitive to disease etiology and that are ideal for personalizing rehabilitation (e.g., joint contact forces) [37]. Different selection criteria may be justified in other applications (e.g., muscle weights based on their relative contribution to the net joint moment during walking) and may lead to a different choice of an input muscle set. For example, to instrument a knee brace, one may wish to only consider muscles nearest the knee joint. In other applications where sensor placement is performed by the patient it may be beneficial to develop models using muscles which are easiest to locate for non-specialists. Our results suggest other input muscle sets not further analyzed beyond the analysis described in section 5.3.1. may be equally viable candidates. For example, 200/210 four-muscle and 80/120 three-muscle input sets achieved strong correlations in the estimation performance.

The soleus was the only muscle consistently chosen across the four-, three-, and two-muscle input sets. This may be due to the PCSA-weighted averaging method as the soleus is the largest muscle and thus was given the largest weight (24%). The best four-muscle input set (BF, PL, SOL, VL) included a muscle that crossed the knee joint anteriorly and posteriorly and the posterior ankle but with no dorsiflexor. The only dorsiflexor measured in this study was the TA, however, in our analysis the TA was consistently well estimated suggesting its behavior is well-inferred from the other input muscles during walking.

A general increasing trend was observed between estimation performance and input window size. In section 5.2., we postulated that the input window size may serve to identify a neural control strategy to accomplish some sub-task during walking similar to how identified synergy vectors have been associated with certain phases of the gait cycle [291]. The average stride time of individuals in this study was 1.31 s and thus, using the 1.50 s window size and 0.75 s window relative output time, the synergy functions were able to “see” approximately the previous and future half gait cycle of input excitations to infer output excitations.

From this perspective, it may be that optimal window size is stride time (or gait speed) dependent. This should be investigated further in future research.

It is important to note that the final estimator in eqs. (5.10) and (5.12) truly captures the synergistic relationship between input and output muscles as it has no indication of time. Thus, the approximated synergy functions are not directly time dependent. Further, any gait phase dependent periodicity inherent in the sEMG signal during walking is not directly modeled (e.g., by including gait-phase as an input). For this reason, the GP model may be sensitive to step-by-step variation in both sEMG magnitude and frequency (Figure 21). Although this is visually apparent for the TA in Figure 21 (from a single subject), we did not directly test this phenomenon which may be done in future work by deliberately imposing step-by-step variation in the experimental design. A future approach may incorporate time dependency by segmenting input excitations by stride, normalizing by stride time, and including the percentage gait cycle as an input.

In addition to time independency, the proposed model is also independent of any kinematic behavior which may be incorporated by including inertial sensor data (e.g., angular rate, acceleration) as additional inputs [306]. Under the current approach, it may be that including a broad enough range of activities in the training set (e.g., stair ascension, cycling) could allow learning more generalizable phenomena enabling less strict activity identification specificity in the remote gait analysis pipeline (e.g., a locomotion activity classifier is less strict than a walking activity classifier) [70]. Future work should explore this further along with task and sub-task (e.g., variable gait speeds) extrapolation.

The proposed synergy function models can be modified in many ways beyond input muscle sets and input window structure, especially regarding the GP model (e.g., mean and covariance function). It would have been infeasible to exhaustively explore all covariance functions. Rather we explored a stationary and non-stationary covariance function in eqs (5.16) and (5.17) respectively and found (negligible) superior performance using the squared exponential covariance. The squared exponential covariance utilized in this work was isotropic in that the characteristic length scale, θ_2 in eq. (5.16), was the same for all inputs. An alternate approach to be explored in future work may be including length scales specific to each input muscle which can ultimately weight the relevance of specific input muscles for particular output muscles. For

example, the VL may be especially relevant for estimating VM output excitations, but this remains to be seen. Along these lines, a linear mean function may further improve estimation accuracy, $\mu_m(\boldsymbol{x}) = \boldsymbol{\rho}^T \boldsymbol{x}$, wherein input muscles which are anatomically and/or functionally similar to the particular output muscle can be preferentially weighted according to the associated element in $\boldsymbol{\rho}$ (the hyperparameters). Finally, although all estimated output muscle excitations were in the interval [0 1] (a physiological constraint) the conditional distribution characterized in eqs. (5.10) and (5.11) suggests non-zero probability densities for excitations outside this interval. For this reason, a beta likelihood function may be more appropriate [317] and should be explored in future work.

We explored the potential of driving muscle activation dynamics given the estimated muscle excitations. Our results suggest this is a valid approach with MAE less than 4.0% across all output muscles, strong correlations, and an ability to explain between 89-93% VAF (Table 6). For all output muscles, activation estimation performance metrics were greater than for excitation estimation. Activation dynamics essentially act to smooth input excitations which may underlie this observation. Thus, results may be further improved if a lesser low-pass filter cutoff frequency were chosen in the sEMG pre-processing. We chose 6 Hz as this is common for muscle force estimation, but others have used less [324]. This should be explored in future research as well as quantifying the muscle force estimation error given the activation estimation proposed here.

While there is no other study using a comparable approach (i.e., using only sEMG inputs) to compare our results, a comparison to a reconstruction approach using the more familiar NNMF-based synergy analysis is instructive. The proposed approach explained more percentage VAF across all output muscles except a negligible difference for the VM. The NNMF-based reconstruction VAF for some muscles was less than that reported for the three-synergy configuration in [294]. One explanation is that synergies were extracted from only four muscles in this study compared to eight in [294] and the optimal subset for the NNMF reconstruction may be different than for the GP model. Further, the results in [294] were for only two subjects compared to nine in this study. When comparing the NNMF reconstruction and GP estimation, it is important to note that the NNMF technique has an unfair advantage in that the synergy model was informed

Table 6: Muscle activation estimation performance

Muscle	*r*	VAF	RMSE	MAE
MG	0.93	93 (4)	5.2 (1.8)	3.5 (1.2)
LG	0.86	91 (6)	3.5 (1.3)	2.4 (0.9)
TA	0.83	92 (5)	3.1 (1.8)	2.1 (1.3)
ST	0.88	89 (6)	1.7 (1.1)	1.1 (0.6)
VM	0.84	92 (5)	1.5 (1.0)	1.0 (0.6)
RF	0.74	93 (5)	0.5 (0.2)	0.4 (0.1)

Measured and estimated excitations from the test set for the four-muscle input set (BF,PL,SOL,VL) were used to estimate muscle activations. Performance metrics include correlation coefficient (*r*); percentage of variance accounted for (VAF); root mean square error (RMSE) in units percent MVC; mean absolute error (MAE) in units percent MVC. The reported VAF, RMSE, and MAE values are the average across all subjects for each muscle with the standard deviation in parentheses. The *r* values are the average correlation coefficients using Fisher's z transformation as described by Silver and Dunlap (1987).

partly by the data it sought to reconstruct. For this reason, as noted in [294], the NNMF approach does not solve the problem of estimating unmeasured excitations using a measured subset; it only provides insight into the feasibility of doing so. This is in contrast to the proposed approach wherein the GP model was informed by a completely different dataset than it was tested on.

A major limitation in using Gaussian process regression (or any non-parametric regressor) is computation time. For the four-muscle input set, the average total model training time (six total synergy models, one for each output muscle) was 31 minutes per subject. For the same configuration, the average computation time to estimate 1.0 s of data was 0.2 s. This is less of a burden for remote patient monitoring applications as current pipelines generate clinical reports offline after a full 24-hour recording [70]. The estimation of muscle excitations in eq. (5.12) requires inversion of the large $(N \times N)$ covariance matrix Σ_m. This inversion can be performed before deployment and thus speed up the estimation. The matrix Σ_m^{-1} is also required for computing the estimation variance in eqs. (5.11) and (5.14). Modeling these variances are a benefit of the GP approach as they provide an indication of the uncertainty of the muscle excitation estimate which may be useful if excitations are allowed to be adjusted in a sensor fusion framework given other measurements of the musculoskeletal system dynamics.

The aim of this paper was to lay the foundation for future development in this area and thus we only investigated subject-specific models of unimpaired persons for normal walking speeds. Thus, our results are interpretable only in the context of estimating muscle excitations for gait speeds similar to those represented in the training set and specifically for the range of gait speeds and stride times analyzed in this study. Importantly, the range of stride times in this study cover the majority of those observed remotely in impaired and unimpaired gait [29], [70]. Our models being subject-specific may not be an immediate barrier to remote estimation of muscle forces as sEMG-driven muscle force estimation techniques also require a calibration session [209], [290]. Future research should explore application in impaired populations and subject-general models (the feasibility of which has been supported recently [325]).

The muscles modeled in the current study are sufficient for sEMG-driven techniques currently used to estimate knee and ankle joint moments [209], [290]. However, other applications (e.g., estimating joint contact force) may require the estimation of deep-located muscle excitations which would otherwise require invasive measurement techniques. Our results motivate future investigations in this area. Note, however, that to implement the proposed method to estimate deep-located muscle excitations, data from those muscles must be available in the training set (as per eqs. (5.10) and (5.12)) and would still require invasive techniques for model training.

All data from seven subjects were removed because of low-quality sEMG data for at least one muscle. Noise contamination in the sEMG signal is a well-known phenomenon [228], [318] and presents an issue that would need to be addressed for practical deployment of the proposed technique. For example, if an input excitation were of poor signal quality when applying this method in practice, a potential solution might be to use a pre-trained model which depends on input excitations from all other instrumented muscles (not noise contaminated). Compensatory methods of this sort and automated identification of poor sEMG signal quality should be investigated in future research.

5.6. Conclusion

This study describes a Gaussian process model of the synergistic relationship between muscles. Importantly, this model enables estimation of unmeasured muscle excitations from a measured subset which makes it a practical solution for remote patient monitoring. Estimated excitations were shown able to drive activation dynamics with high accuracy. These results motivate future research into remote estimation of muscle force (e.g., given inertial sensor-driven estimates of muscle-tendon unit kinematics) for incorporation into a comprehensive remote patient monitoring framework.

Chapter 6: Hybrid Machine Learning and Physics-Based Simulation of Muscle Contraction Dynamics Using a Reduced Sensor Array

6.1. Introduction

Remote patient monitoring, enabled by advances in wearable sensor technology and estimation techniques, promises improved management of musculoskeletal disease. To date, most of these analyses are based on estimates of physical activity (Chapter 1). More recent developments quantify stride-by-stride gait biomechanics at a segment-, joint-, and muscle-specific level and have shown that these variables may be more relevant for monitoring patient health (Chapter 3) [70], [75]. However, the most clinically relevant biomechanical variables have not been observed outside of controlled, laboratory environments. Ideally, clinicians would have access to the cumulative loads experienced by muscle and other articular tissue across every step taken by the patient in daily life. Patient characterization at this level may enable personalized rehabilitation and optimal evaluation of intervention efficacy. Further, remote monitoring may provide novel insight into musculoskeletal disease etiology. For example, a well-known phenomenon in osteoarthritis concerns the positive effects of load on healthy tissue and yet detrimental effects on diseased tissue [38]. This transition is thought to occur near the onset of the disease, but a more exact characterization is currently absent. Monitoring cumulative tissue loads in a patient's natural loading environment presents an avenue through which to elucidate these and other cumulative load-dependent phenomena.

To realize these ideas, efforts must be made to characterize joint kinetics and muscle contraction dynamics in remote environments. The biomechanical variables associated with these analyses (e.g., joint moment, muscle power) provide far more clinical relevance than what is typically evaluated remotely (e.g., physical activity, spatiotemporal gait parameters). While both frontal plane and sagittal plane knee joint moment should be considered for management of musculoskeletal disease [50], [51], [120], [326]–[328], knee flexion moment in particular, is thought to play an especially important role in early knee osteoarthritis [50], [327] and for monitoring patients following reconstructive surgery of the anterior cruciate ligament (ACLR) [188], [329]–[333]. Concerning muscle contraction dynamics, muscle power is a well-known critical

determinant of physical function [334]. Moreover, the phenomena of work- [305] and load- [335] induced muscle hypertrophy motivate the estimation of cumulative muscle work and force which may provide a basis for optimal exercise prescription and understanding subsequent patient-specific responses. Muscle-specific work and power objectively quantify exercise or movement intensity and continuous observation may help elucidate exercise-dose response relationships in orthopedic populations [336]. These analyses may be especially relevant in monitoring patients post-ACLR for which both the knee extensor and flexor musculature is compromised [187], [203], [337] due in part to muscle atrophy [338], [339] and muscle activation deficits [203], [340]. In this context, early intervention is critical [44], [201], and continuous, remote monitoring is necessary to best inform personalized rehabilitation which has been shown effective at targeting specific biomechanical outcomes [46], [341].

Methods do exist for estimating these clinically relevant biomechanics and that use only data from wearable sensors [24], [25]. However, these methods require complex sensor arrays that may discourage use [342]. Regression techniques have been proposed as a means to reduce the number of required sensors [12], but possibly at the expense of generalizability. Hybrid solutions have been suggested wherein machine learning is used only where the physics are least well understood or insufficiently informed [12], [162], [299]. In this work, an approach of this sort was developed wherein Gaussian process (GP) synergy functions (Chapter 5) [162] were used to estimate a complete set of muscle excitations using only a measured subset thus reducing the number of required electromyography (EMG) sensors. These excitations were used along with estimates of muscle-tendon unit (MTU) kinematics from inertial measurement unit (IMU) data in an EMG-driven simulation to characterize the joint and muscle dynamics (Figure 23).

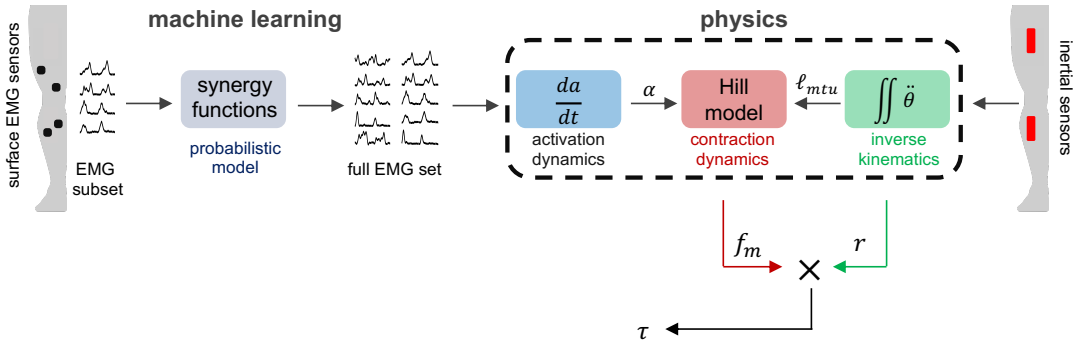

Figure 23: Overview of the proposed hybrid technique. Muscle excitations measured from a subset of muscles (far left) are used to estimate a full set of excitations using GP synergy functions (purple block) while IMU data (far right) are used to estimate MTU length (l_{mtu}) and moment arm (r) via inverse kinematics (green block). Muscle excitation is input to the muscle activation (α) dynamics (blue block) which along with MTU length is input to the muscle contraction dynamics (red block). These dynamics are simulated using EMG-driven techniques. Muscle force (f_m) is output from the contraction dynamics block and generates a muscle moment (τ) acting through the MTU moment arm.

6.2. Overview of the proposed approach

The primary aim of this development was to estimate knee flexion moment (KFM) and ankle flexion moment (AFM) as well as force, power, cumulative concentric work, and cumulative eccentric work for individual muscles during the stance phase of gait using a reduced sensor array. Specifically, these variables were estimated using data from only two IMUs (one on the shank and one on the thigh) and four EMG sensors (placed over the vastus medialis, peroneus longus, and lateral and medial gastrocnemii) via EMG-driven simulation of muscle contraction dynamics (Figure 23). These sensor locations were chosen because they are all close enough to the knee joint that they could be seamlessly built into a knee brace which may enable practical deployment of this technique for patients following knee surgery (Chapter 7).

In the next section, the general physics governing muscle contraction dynamics are developed as well as the relationships between all biomechanical variables of interest. It will be shown that the estimation of these biomechanical variables requires three inputs including the length of each MTU, the moment arm of

each MTU associated with the flexion degree of freedom (DOF) for the knee and ankle joints, and the excitation of each muscle. The subsequent sections then describe the computational methods used to estimate these inputs and for simulating the muscle contraction dynamics; both for implementing the proposed technique in practice using the reduced sensor array and for validation using optical motion capture (OMC), force plate data, and a full set of EMG (as opposed to the four EMG subset).

The required MTU length and moment arm inputs are a function only of the segment kinematics given a calibrated model of the subject-specific musculoskeletal geometry. The required full set of muscle excitations (a.k.a. EMG amplitude [228], [302] which relate to motor unit recruitment and motor unit firing rate [302]) are estimated using pre-trained, subject- and muscle-specific GP synergy function models. Further, the muscle contraction dynamics described in the next section depend on several subject- and MTU-specific parameters that need to be identified.

Therefore, the proposed technique requires generally two steps for practical deployment: (1) model calibration and (2) remote estimation. Step (1), model calibration, requires a visit to a motion capture laboratory to perform the aforementioned calibration of the musculoskeletal geometry and GP synergy function models as well as the MTU parameter identification. The latter requires estimation of KFM and AFM via inverse dynamics analysis (ground truth) and via gold standard EMG-driven simulation of the muscle contraction dynamics (i.e., with a full set of EMG data and OMC-based inverse kinematics). Step (2), remote estimation, involves four sub-steps: (i) a daily calibration which in practice would happen every time a new set of sensors were placed on the person including sensor-to-segment alignment and maximal voluntary contractions (MVC) for EMG normalization, (ii) estimation of segment kinematics (and thus MTU length and moment arm) using only the shank- and thigh-worn IMU data, (iii) estimation of all muscle excitations using only the four measured excitations from the EMG-instrumented muscles as inputs to muscle-specific GP synergy functions, and (iv) simulation of the muscle contraction dynamics. Each of these components including the theory of muscle contraction dynamics are described in the following sections as they were implemented for validating the proposed technique.

6.3. Muscle contraction dynamics: theoretical developments

This section describes the physics governing muscle contraction dynamics and, in particular, the equations needed to inform the biomechanical variables of interest: sagittal plane joint moment (KFM, AFM), muscle force, muscle power, and cumulative concentric and eccentric muscle work. The development here is deliberately generic wherein the sections that follow will specify the computational methods used in this work to simulate these dynamics in an EMG-driven approach.

The flexion moment for joint j (M_j, a.k.a. an internal moment or the net muscle moment) is equal to the sum of the flexion moments generated by each MTU, denoted as $\tau_{i,j}$ for MTU i, as per [343]

$$\mathrm{M}_j = \sum_{i=1}^{N_m} \tau_{i,j} \tag{6.1}$$

where N_m is the number of MTUs and the moment generated by MTU i is

$$\tau_{i,j} = f_{m_i} r_{i,j}. \tag{6.2}$$

In eq. (6.2), f_{m_i} is the contraction force produced by muscle i (along the MTU line of action) and $r_{i,j}$ is the moment arm for MTU i associated with the flexion DOF for joint j. The moment arm is related to the MTU length (ℓ_{mtu_i}) and flexion joint angle $\left(\theta_j\right)$ according to the principle of virtual work [217],

$$r_{i,j} = -\frac{\partial \ell_{mtu_i}}{\partial \theta_j}. \tag{6.3}$$

Note that the direction of f_{m_i} is such that a positive contraction force is in the same direction as a negative fiber or MTU length change (the direction of shortening) which explains the reason for the negative sign in eq. (6.3). The muscle force f_{m_i} is given assuming the phenomenological, lumped-parameter Hill muscle model (Figure 24) as per [344]

$$f_{m_i} = F_{0_i}\left(f_{v_i} f_{\ell_i} f_{A_i} + f_{p_i} + \beta_i \tilde{v}_{m_i}\right) \cos\phi_i \tag{6.4}$$

where F_{0_i} is the maximal isometric force produced by muscle i, f_{v_i} models the force-velocity property of muscle i [345], f_{ℓ_i} models the active force-length property of muscle i [346], f_{A_i} models the nonlinear

relationship between muscle activation and isometric muscle force [347], [348], f_{p_i} models the passive force-length property of muscle i [349], the product $\beta_i \tilde{v}_{m_i}$ models the effects of viscous damping within muscle fiber i where β_i is the damping coefficient and $\tilde{v}_{m_i}$ is the normalized fiber velocity [344], [350], and ϕ_i is the pennation angle of muscle fiber i. The maximal isometric force F_{0_i} is given by the product of the physiological cross-sectional area of the muscle $(C_i,)$ and the muscle stress at maximal isometric force (σ_i),

$$F_{0_i} = \sigma_i C_i. \tag{6.5}$$

The functions f_{v_i}, f_{ℓ_i}, f_{A_i}, and f_{p_i} collectively act to scale F_{0_i} which is projected along the MTU line of action via the scalar $\cos\phi_i$. The input to the activation nonlinearity function f_{A_i} is the activation signal (α_i, $0 \leq \alpha_i \leq 1$, the dynamics of which are driven by the muscle excitation signal (e_i) as per

$$\frac{d\alpha_i}{dt} = \dot{\alpha}_i\left(e_i, t_{d_i}, \boldsymbol{p}_i\right) \tag{6.6}$$

where $\dot{\alpha}_i$ is the activation dynamics function, t_{d_i} is an electromechanical time delay, and $\boldsymbol{p}_i$ represents a set of activation dynamics parameters (e.g., activation time constant). Normalized fiber length $\left(\tilde{\ell}_{m_i}\right)$ is input to both the active (f_{ℓ_i}) and passive (f_{p_i}) force-length functions where the normalization constant is the optimal fiber length (ℓ_{0_i}, the length at which the muscle produces maximum force during an isometric contraction) as per

$$\tilde{\ell}_{m_i} = \frac{\ell_{m_i}}{\ell_{0_i}} \tag{6.7}$$

and ℓ_{m_i} is the actual muscle fiber length. The output of the activation nonlinearity function f_{A_i} is also input to the active force-length function f_{ℓ_i} in order to model the dependency of the optimal fiber length on muscle activation only for normalization in eq. (6.7), which has been observed empirically [351]. This dependence has been modeled linearly as [209]

$$\bar{\ell}_{0_i}\left(f_{A_i}\right) = -\ell_{0_i}\lambda_i f_{A_i} + \ell_{0_i}(\lambda_i + 1) \tag{6.8}$$

where λ_i represents the percentage change in the optimal fiber length for a completely inactive muscle (i.e., $f_{A_i} = 0$). Note that the bar in $\bar{\ell}_{0_i}$ is used to indicate the activation-adjusted optimal fiber length and is used as the normalization constant in eq. (6.7) only for the active force-length function f_{ℓ_i}. The input to the force-velocity function f_{v_i} is normalized fiber velocity,

$$\tilde{v}_{m_i} = \frac{v_{m_i}}{v_{0_i}} \tag{6.9}$$

where v_{0_i} is the maximum fiber shortening velocity. Note that $v_{m_i} < 0$ indicates a shortening fiber during a concentric contraction, $v_{m_i} = 0$ indicates an isometric contraction, and $v_{m_i} > 0$ indicates a lengthening fiber during an eccentric contraction. The MTU geometry (Figure 24) is modeled such that [344]

$$\ell_{mtu_i} = \ell_{T_i} + \ell_{m_i} \cos \phi_i \tag{6.10}$$

where ℓ_{T_i} is the tendon length for MTU i. The geometry of the muscle fiber is modeled such that the fiber thickness (w_i) is constant,

$$w_i = \ell_{m_i} \sin \phi_i \,. \tag{6.11}$$

Let ϕ_{0_i} be the pennation angle when the muscle fiber length is optimal. Since eq. (6.11) must also be satisfied for $\ell_{m_i} = \ell_{0_i}$, the pennation angle corresponding to an arbitrary fiber length is

$$\phi_i = \operatorname{asin}\left(\frac{\ell_{0_i} \sin \phi_{0_i}}{\ell_{m_i}}\right). \tag{6.12}$$

Because the tendon and muscle are in series, the force in each element must be equivalent yielding the dynamic equilibrium equation [209], [344], [352]

$$\tilde{f}_{m_i} - \tilde{f}_{T_i} = 0 \tag{6.13}$$

where $\tilde{f}_{m_i}$ is the normalized muscle force (i.e., f_{m_i} in eq. (6.4) divided by F_{0_i}) and $\tilde{f}_{T_i}$ is the normalized tendon force function which models the nonlinear elastic behavior of the tendon. The force in the tendon is

$$f_{T_i} = F_{0_i} \tilde{f}_{T_i}. \tag{6.14}$$

The normalized tendon force $\tilde{f}_{T_i}$ is a function of tendon strain (ϵ_{T_i}) where

$$\epsilon_{T_i} = \frac{\ell_{T_i} - \ell_{S_i}}{\ell_{S_i}} \tag{6.15}$$

and ℓ_{S_i} is the tendon slack length. Muscle power (P_i) is given by the product of muscle force and velocity as per

$$P_i = -f_{m_i} \frac{ds_i}{dt} \tag{6.16}$$

where $s_i = \ell_{m_i} \cos \phi_i$ from eq. 6.10 and f_{m_i} has been negated since a positive contraction force is in the same direction as a shortening fiber ($s_i < 0$). Thus, $P_i > 0$ indicates the rate of work done by f_{m_i} during a concentric contraction whereas $P_i < 0$ indicates the rate of work done by f_{m_i} during an eccentric contraction. Cumulative concentric (W_{con_i}) and eccentric (W_{ecc_i}) muscle work during the stance phase of gait (i.e., during the time interval $t_{FC} \leq t \leq t_{FO}$ where t_{FC} indicates the instant of foot contact and t_{FO} indicates the instant of foot off) is given by the following time integrals:

$$W_{con_i} = \int_{t_{FC}}^{t_{FO}} f_{con_i} ds_i \tag{6.17}$$

and

$$W_{ecc_i} = \int_{t_{FC}}^{t_{FO}} f_{ecc_i} ds_i \tag{6.18}$$

where

$$f_{con_i} = \begin{cases} f_{m_i}, & ds_i < 0 \\ 0, & otherwise \end{cases} \tag{6.19}$$

and

$$f_{ecc_i} = \begin{cases} f_{m_i}, & ds_i > 0 \\ 0, & otherwise \end{cases}. \tag{6.20}$$

The fiber length ℓ_{m_i} and the muscle activation α_i are the state variables for the muscle contraction dynamics. The dynamics of α_i were described in eq. (6.6) whereas the time-derivative of the fiber length state variable (i.e., fiber velocity v_{m_i}) appears in $\tilde{f}_{m_i}$ in eq. (6.13) via the force-velocity function f_{v_i} in eq. (6.4). Thus, the dynamic equilibrium in eq. (6.13) represents an implicit formulation for the dynamics of the fiber length state variable. Therefore, the computation of the biomechanical variables of interest during the stance phase of gait including sagittal plane joint moment M_j in eq. (6.1), muscle force f_{m_i} in eq. (6.4) or likewise tendon force f_{T_i} in eq. (6.14) due to their equivalence in eq. (6.13), muscle power P_i in eq. (6.16), cumulative concentric work W_{con_i} in eq. (6.17), and cumulative eccentric work W_{ecc_i} in eq. (6.18) has been shown to be completely informed given the initial conditions $\ell_{m_i}(t_{FC})$ and $\alpha_i(t_{FC})$ and the following inputs: muscle excitation e_i for each muscle, MTU length ℓ_{mtu_i} for each MTU, and moment arm $r_{i,j}$ for each muscle and each joint (flexion DOF for knee and ankle).

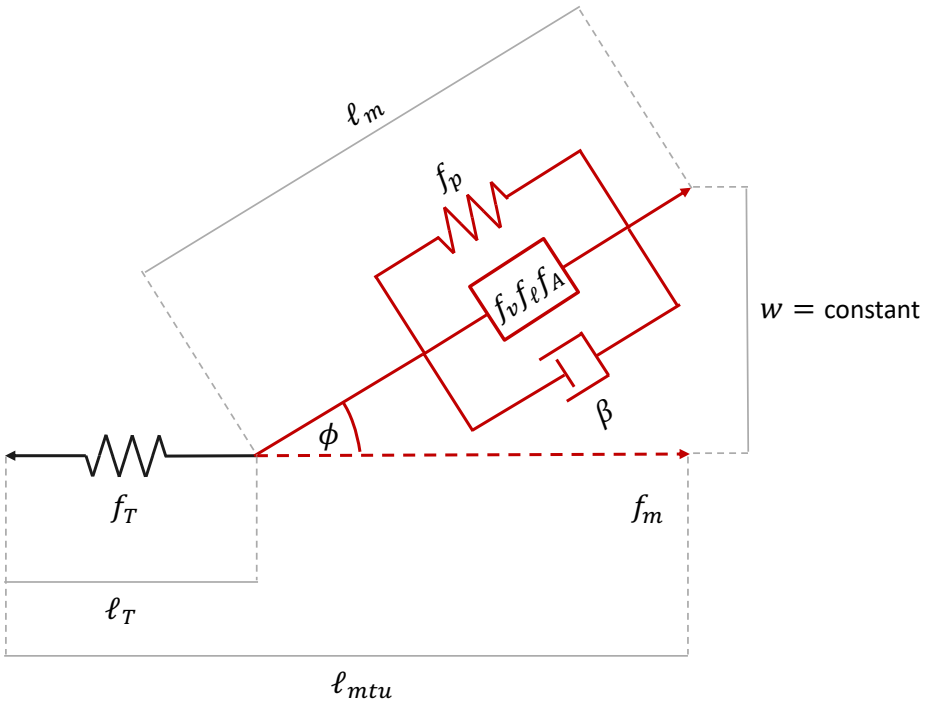

Figure 24: Geometry and block diagram for the Hill muscle model. All black elements are associated with the tendon, all red elements are associated with the muscle fiber, and all grey lines indicate various geometric measurements.

6.4. Proposed technique: model calibration

Practical deployment of the proposed sensor-driven technique requires an in-lab visit for model calibration. The following describes this process as it was implemented in this work including identification of the subject-specific musculoskeletal geometry, identification of MTU parameters related to muscle contraction dynamics, and training the GP synergy function models.

6.4.1. Calibration of the subject-specific musculoskeletal geometry

Generic musculoskeletal geometry

The musculoskeletal model consisted of five segments including a foot, shank, thigh, patella, and pelvis; three non-translating joints including a two DOF ankle joint, single DOF knee joint (tibiofemoral), and a three DOF hip joint; thirteen MTUs including the tibialis anterior (TA), peroneus longus (PL), soleus (SOL), medial gastrocnemius (LG), lateral gastrocnemius (LG) vastus medialis (VM), vastus intermedius (VI), vastus lateralis (VL), rectus femoris (RF), long head of the biceps femoris (BFL), short head of the biceps femoris (BFS), semitendinosus (ST), and semimembranosus (SM). These muscles are sufficient to estimate KFM and AFM as in previous work [324], [353], [354]. The MTU path points (origin, insertion, and via points) for each MTU were informed using the data reported by Horsman et al. (2007) as was the cylindrical geometry of the femoral condyle (position, cylindrical axis, radius) and the origin and insertion of the patellar ligament [355]. The patellar ligament was modeled as an inextensible element. The average position of origin and insertion points was used for multi-element muscles (e.g., superior and inferior elements of the VL).

Static and functional calibration

Two calibration trials were used to identify subject-specific parameters of the musculoskeletal geometry. A static calibration where the subject stood still in anatomical position was used as a reference configuration in which the relative positions of segment-fixed markers define each rigid body segment (Figure 25) with the exception of the patella (patellar kinematics were a function of the knee flexion angle only and thus no markers are placed on the patella).

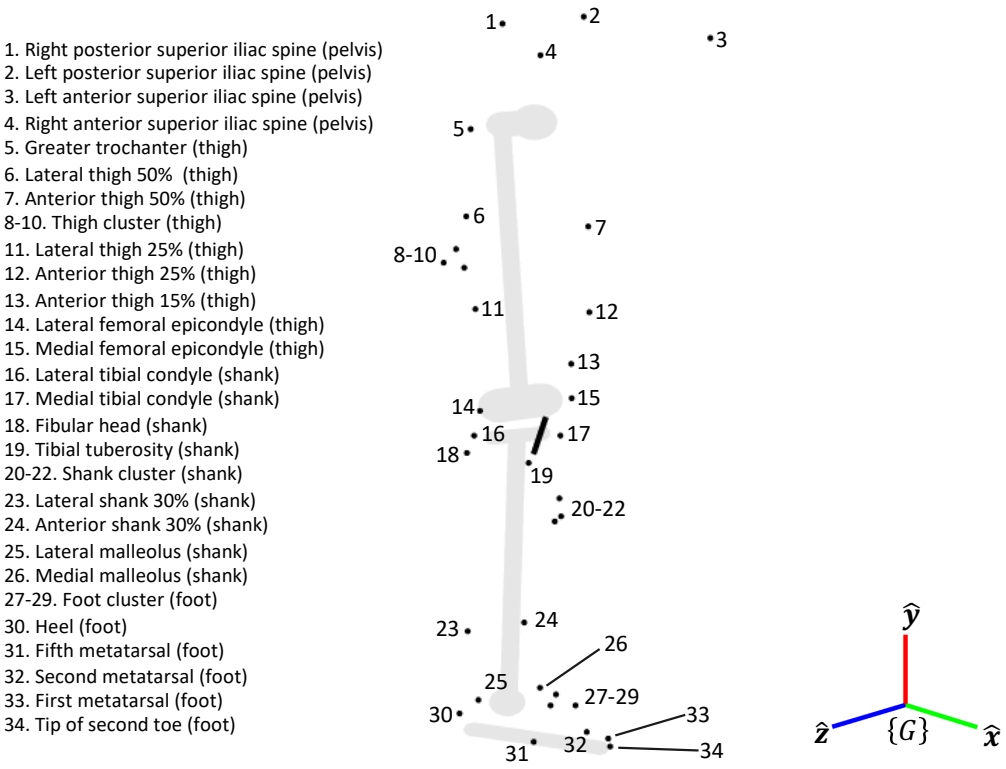

Figure 25: Marker set and rigid body model. The black dots indicate the position of the labeled marker as placed on the subject during the reference configuration (anatomical position). The thick black line near the knee joint models the patellar ligament. The coordinate system *{G}* at the bottom right of the figure indicates the global (inertial) frame wherein *x* indicates the direction in which the subject walked for all walking trials and *y* indicates the global vertical direction aligned with gravity.

A second functional calibration trial [23] was used in order to identify hip, knee, and ankle joint center positions as well as the knee joint flexion axis. During the functional calibration trial, the subject exercised multiple movements of each joint exciting all joint DOFs and was encouraged to utilize the full range of motion for each DOF. For the hip joint, the subject moved their leg in a star pattern (pure hip flexion, simultaneous hip flexion/abduction, pure hip abduction, simultaneous hip extension/abduction, and pure hip extension) and a circular pattern (as if stepping over a hurdle). For the knee joint, the subject performed five knee flexion and extension movements. For the ankle joint, the subject performed five ankle plantarflexion and dorsiflexion movements and three circular movements in both clockwise and counterclockwise directions.

The kinematics of each segment during the functional calibration trial were computed independently without regard for any mechanical constraints. To this end, segment orientation (quaternion representation) for each segment-fixed coordinate system (formed using any three non-colinear markers from the reference configuration) is determined using Davenport's solution to Wahba's problem wherein every unique two-marker combination for all segment-fixed markers during the static calibration trial were used as the reference vectors [356], [357]. Reference vectors were weighted by their length squared in the objective function of Wahba's problem. Segment positions were computed as described by Spoor and Veldpaus (1980) [358]. Segment kinematics were then used to estimate the hip and ankle joint centers using the pivot technique [359], [360] as well as the position and orientation of the knee joint flexion axis using the SARA method [361]. The knee joint center was defined as the point on the line defined by the SARA-identified knee joint flexion axis (position and orientation) which was closest to the midpoint of the medial and lateral femoral epicondyles.

Segment inertial properties

The identified hip, knee, and ankle joint centers and the knee joint flexion axis were used to define the position and orientation of segment-fixed coordinate systems for each segment in the reference configuration (static calibration trial). Segment-fixed coordinate systems were defined so as to coincide with the principal axes of inertia of their respective segment. The position of each segment (coordinate system origin) was coincident with the segment center of mass. All inertial parameters (mass, center of mass location, and radii of gyration) were taken from de Leva (1996) [362]. The basis vectors of the pelvis coordinate system were defined as per the ISB recommendations [363]. The long axis of the shank was defined by the unit vector pointing from the midpoint of the medial and lateral malleoli to the midpoint of the medial and lateral tibial condyles and the frontal plane was defined by the long axis of the shank and the SARA-identified knee flexion axis. The thigh coordinate system was assumed to coincide with that of the shank in the reference configuration. The long axis of the foot was defined by the unit vector pointing from the heel to the second metatarsal and the sagittal plane was defined by the long axis of the foot and the global vertical axis as the foot was assumed flat in the reference configuration. The local position of each MTU origin, insertion, and

via point (where applicable) were scaled based on an anthropometric measurement of each segment relative to the same measurement from the data reported in Horsman et al. (2007) including the distance between the midpoint of the anterior superior iliac spinae to the hip joint center for the pelvis, the longitudinal segment lengths for the thigh and shank, and the distance between the ankle joint center and the midpoint of the first and fifth metatarsals for the foot. The insertion of the RF, VM, VI, and VL were moved posteriorly 1.00 cm and the shank-fixed MTU path points of the SM and ST (insertion and via points) were moved inferiorly 3.00 cm in order to better align the knee flexion moment arms of these muscles with literature data [364], [365].

Joint coordinate systems

For an arbitrary system configuration, joint angles were generally defined as the angles associated with one, two, or three (depending on the number of joint DOFs) successive rotations that mapped a joint coordinate system fixed in the parent segment (proximal to the joint) to the same joint coordinate system fixed in the child segment (distal to the joint), i.e. a parent-to-child perspective, or vice versa, i.e. a child-to-parent perspective [366]. The orientation of the joint coordinate system with respect to the segment coordinate systems of the parent and child segments was determined during the reference configuration. The hip joint coordinate system was defined by the flexion axis which was coincident with the medio-lateral axis of the pelvis pointing to the right, the adduction axis which was coincident with the antero-posterior axis of the pelvis pointing anteriorly, and the internal rotation axis which was coincident with the cranio-caudal axis of the pelvis pointing cranially. The hip joint rotation sequence was first about the flexion axis, second about the adduction axis, and third about the internal rotation axis with a parent-to-child perspective. The knee joint coordinate system was defined by the flexion axis identified as per the SARA method pointing to the right and two other arbitrary unit vectors forming an orthogonal basis. The knee joint rotation sequence was about the flexion axis only with a child-to-parent perspective. The ankle joint coordinate system was defined by the dorsiflexion axis which was coincident with the knee joint flexion axis such that the ankle joint sagittal plane was aligned with that of the knee joint, the adduction axis which was defined by the direction of the line orthogonal to the dorsiflexion axis that intersects both the heel and a point on the line defined by the dorsiflexion axis and the ankle joint center (similar to the subtalar joint axis in previous work [217], [366]),

and a third unit vector orthogonal to both the dorsiflexion and adduction axes. The ankle joint rotation sequence was first about the dorsiflexion axis and second about the adduction axis with a parent-to-child perspective.

6.4.2. Identification of MTU parameters related to contraction dynamics

This calibration step is used to identify several MTU parameters related to the muscle contraction dynamics and requires a ground truth estimate of joint moment (inverse dynamics) as well as an OMC estimate of MTU kinematics (MTU length and moment arm) as inputs to the EMG-driven muscle contraction dynamics.

Inverse kinematics: optical motion capture

The problem of inverse kinematics is to determine the set of generalized coordinates which completely specify the rigid body system configuration for each discrete time instant given measured 3-D marker positions. In this work, the system configuration was described by a set of 28 generalized coordinates including three translational coordinates for each segment which specifies the position of each segment coordinate system origin represented in the global frame and four rotational coordinates for each segment which are the Euler parameters (unit length quaternion) describing the orientation of each segment coordinate system relative to the global frame. These generalized coordinates are defined such that the position of marker n represented in the global frame $\{G\}$ at the discrete time instant k ($\widehat{\boldsymbol{m}}_{n,k}^{G}$, a 3×1 column vector) is given by

$$\widehat{\boldsymbol{m}}_{n,k}^{G} = \boldsymbol{p}_{s_n,k}^{G} + R_{s_n,k}\boldsymbol{m}_{n}^{B} \tag{6.21}$$

where $\boldsymbol{m}_{n}^{B}$ is the constant 3×1 position vector of marker n represented in the segment-fixed coordinate system $\{B\}$ of segment s_n to which marker n is attached (determined from the reference configuration), $\boldsymbol{p}_{s_n,k}^{G}$ is the 3×1 column vector of the three translational coordinates of segment s_n, and $R_{s_n,k} \in SO(3)$ is a 3×3 rotation matrix parametrized by the four rotational coordinates ($\mathbf{q}_{s_n,k}$) of segment s_n [26], [367], [368]. The set of 28 generalized coordinates (denoted $\boldsymbol{x}_k$) at time instant k is determined following the approach described by Andersen et al. (2009) wherein the optimization problem was formulated as [369]

$$\min_{\boldsymbol{x}_k} \frac{1}{2} \sum_{n=1}^{N_{mkr_k}} \left(\boldsymbol{m}_{n,k}^{G} - \widehat{\boldsymbol{m}}_{n,k}^{G}\right)^T W_n \left(\boldsymbol{m}_{n,k}^{G} - \widehat{\boldsymbol{m}}_{n,k}^{G}\right) \tag{6.22}$$

subject to a set of 16 equality constraints

$$\begin{bmatrix} c_1(\boldsymbol{x}_k) \\ c_2(\boldsymbol{x}_k) \\ \vdots \\ c_{16}(\boldsymbol{x}_k) \end{bmatrix} = \begin{bmatrix} 0 \\ 0 \\ \vdots \\ 0 \end{bmatrix} \tag{6.23}$$

where N_{mkr_k} is the number of markers available from the OMC system at time instant k, $\boldsymbol{m}_{n,k}^{G}$ is the measured marker position for marker n, and W_n is a 3×3 marker-specific weighting matrix. Four of the constraint equations enforce the unit length constraint on the quaternions parametrizing segment orientation (one for each segment); nine of the constraint equations enforce the non-translating joint constraints for each of the hip, knee, and ankle joints (three for each joint); two of the constraint equations enforce the hinge joint constraint on the knee joint; and one constraint equation enforces the universal joint constraint on the ankle joint [368], [369]. The objective function in eq. (6.22) subject to the equality constraints in eq. (6.23) is minimized using the fmincon function in MATLAB R2019b (MathWorks, Natick, MA) with the interior-point optimization algorithm and analytic Jacobian and Hessian matrices of the objective and constraint equations with respect to $\boldsymbol{x}_k$. The constraint tolerance was set to 1e-6 and all markers were weighted equally (i.e., $W_n = I_3$, the 3×3 identity matrix, for all markers). The initial guess for $\boldsymbol{x}_1$ in the optimization was based on the unconstrained inverse kinematics solution described previously (Davenport's q method [356], [357]) and the initial guess for $\boldsymbol{x}_k$ when $k > 1$ was $\boldsymbol{x}_{k-1}$ [369].

Joint angles were computed given the orientation of the joint coordinate system fixed in the parent segment (from the reference configuration) relative to the same fixed in the child segment using an appropriate Euler angle decomposition [367]. The patellar ligament angle relative to the shank segment was determined by linear interpolation of the data reported by van Eijden et al. (1985) and the angle of the patella relative to the patellar ligament was modeled as a constant 20° [217], [370].

Given the segment position and orientation at each instant in time, the velocity and acceleration for segment s ($\dot{\boldsymbol{p}}_s^G$ and $\ddot{\boldsymbol{p}}_s^G$, respectively) as well as the quaternion time-derivative ($\dot{\mathbf{q}}_s$) were determined by

numerical differentiation using the 5-point central difference method. The quaternion time-derivative at time instant k is related to the orientation $\mathbf{q}_{s,k}$ and body-referenced angular velocity $\left(\boldsymbol{\omega}_{s,k}^{B}\right)$ as per [154], [368]

$$\dot{\mathbf{q}}_{s,k} = \frac{1}{2}\mathbf{q}_{s,k} \otimes \boldsymbol{\omega}_{s,k}^{B} \tag{6.24}$$

where the non-italic $\boldsymbol{\omega}_{s,k}^{B} \in \mathbb{H}$ denotes the pure quaternion (null scalar part) representing the cartesian vector $\boldsymbol{\omega}_{s,k}^{B} \in \mathbb{R}^3$ in quaternion space ($\mathbb{H}$) and $\otimes$ denotes the quaternion product [371]. Thus,

$$\boldsymbol{\omega}_{s,k}^{B} = 2\overline{\mathbf{q}}_{s,k} \otimes \dot{\mathbf{q}}_{s,k} \tag{6.25}$$

where $\overline{\mathbf{q}}_{s,k}$ denotes the quaternion conjugate (multiplicative inverse for unit quaternions) [371]. Then, the angular velocity $\boldsymbol{\omega}_{s,k}^{B}$ in cartesian space is simply the vector part of the pure quaternion $\boldsymbol{\omega}_{s,k}^{B}$ computed from eq. (6.25). Finally, the angular acceleration of segment s ($\dot{\boldsymbol{\omega}}_{s}^{B}$) represented in the segment-fixed coordinate system is computed via numerical differentiation of $\boldsymbol{\omega}_{s,k}^{B}$ as before. All segment linear and angular velocities and accelerations were low-pass filtered using a 4th order, zero-phase, Butterworth filter with a 6 Hz cutoff frequency where the filter order and cutoff frequency were adjusted for the backward pass [372].

MTU length and moment arm

The length of each MTU at each time instant was computed as the sum of the lengths of the line segments connecting the MTU path points (origin, via points, insertion) as per [217]

$$\ell_{mtu_i} = \sum_{v=1}^{N_{path_i}-1} \left[\left(\mathbf{z}_{i,v+1} - \mathbf{z}_{i,v}\right)^{T}\left(\mathbf{z}_{i,v+1} - \mathbf{z}_{i,v}\right)\right]^{1/2} \tag{6.26}$$

where N_{path_i} is the number of MTU path points (one for each via point and both the origin and insertion) and $\mathbf{z}_{i,v}$ is the global position of MTU path point v for MTU i. Note that $\mathbf{z}_{i,1}$ corresponds to the MTU origin and $\mathbf{z}_{i,N_{path_i}}$ corresponds to the MTU insertion for MTU i. The MTU paths of the MG and LG were modeled as the shortest curve connecting the origin and insertion points but that wrap posteriorly around the cylinder modeling the femoral condyle. The portion of this curve intersecting the surface of the cylinder is generally an elliptical arc. Thus, for the MG and LG, via points were created along this intersecting elliptical arc at

one-degree increments from which MTU length was computed using eq. (6.26). Moment arms for each MTU associated with the knee and ankle joint flexion DOF were estimated using a 3-point finite difference approximation to eq. (6.3).

Inverse dynamics

The intersegmental forces [343] and joint moments acting on each segment at the proximal and distal joints were computed using the recursive Newton-Euler equations [215]. The intersegmental force at the proximal joint acting on segment s represented in the segment coordinate system $\left(\boldsymbol{F}_{p_s}^B\right)$ was computed as per

$$\boldsymbol{F}_{p_s}^B = m_s\ddot{\boldsymbol{p}}_s^B - m_s\boldsymbol{g}^B - \boldsymbol{F}_{d_s}^B \tag{6.27}$$

where $\ddot{\boldsymbol{p}}_s^B = R_s\ddot{\boldsymbol{p}}_s^G$ is the linear acceleration of the center of mass of segment s represented in the segment coordinate system, $\boldsymbol{g}^B = R_s\boldsymbol{g}^G$ where $\boldsymbol{g}^G = [0 \quad -9.81 \quad 0]^T\ m/s^2$ is the gravitational acceleration vector, and $\boldsymbol{F}_{d_s}^B$ is the intersegmental force acting on segment s at the distal joint represented in the coordinate system of segment s. According to Newton's 3rd Law

$$\boldsymbol{F}_{d_s}^B = -R_s^T R_{s+1}\boldsymbol{F}_{p_{s+1}}^B \tag{6.28}$$

where the segments have been indexed such that the distal joint of segment s is the proximal joint of segment $s+1$. The joint moment acting on segment s at the proximal joint represented in the coordinate system of segment s $\left(\mathbf{M}_{p_s}^{\mathrm{B}}\right)$ was computed as per

$$\mathbf{M}_{p_s}^B = J_s\dot{\boldsymbol{\omega}}_s^B + \boldsymbol{\omega}_s^B \times J_s\boldsymbol{\omega}_s^B - \mathbf{M}_{d_s}^B - \boldsymbol{\rho}_{p_s}^B \times \boldsymbol{F}_{p_s}^B - \boldsymbol{\rho}_{d_s}^B \times \boldsymbol{F}_{d_s}^B \tag{6.29}$$

where J_s is the inertia matrix of segment s; $\mathbf{M}_{d_s}^B$ is the joint moment acting on segment s at the distal joint represented in the coordinate system of segment s; $\boldsymbol{\rho}_{p_s}^B$ and $\boldsymbol{\rho}_{d_s}^B$ are the position vectors pointing from the center of mass of segment s to the proximal and distal joint centers, respectively, represented in the coordinate system of segment s; and $\times$ denotes the vector cross-product. Again, note that

$$\mathbf{M}_{d_s}^B = -R_s^T R_{s+1}\mathbf{M}_{p_{s+1}}^B \tag{6.30}$$

where the segments have been indexed as in eq. (6.28). Only the KFM and AFM were needed in this work and thus the above equations were solved for the foot first followed by the shank. Note that the distal joint intersegmental force and distal joint moment for the foot segment correspond to the ground reaction force and moment measured by a force plate and the position of ground reaction force application is the force plate-measured center of pressure. The KFM and AFM were then computed by projecting $\mathbf{M}_{p_s}^{B}$ in eq. (6.29) onto the knee and ankle flexion axes, respectively, using an appropriate coordinate transformation. Note that since the knee flexion axis points to the right by definition, the moment projected onto this axis is actually an extension moment. Thus, it was negated so as to represent a flexion moment.

EMG-driven simulation of muscle contraction dynamics

The general dynamics of a muscle contraction were developed previously. This section describes the specification of the muscle model used in this work and the computational methods utilized for simulating the contraction dynamics. Ten EMG sensors were placed over the TA, PL, SOL, MG, LG, VM, VL, RF, BFL, and ST according to SENIAM standards [318]. Raw EMG data for these muscles were high-pass filtered at 30 Hz, full-wave rectified, low-pass filtered at 6 Hz, and normalized by the MVC excitation value defined as the largest excitation value across several walking, running, and muscle specific MVC trials [209]. The high-pass and low-pass filters were both 4$^{\text{th}}$ order, zero-phase, Butterworth filters with order and cutoff frequency adjusted for the backward pass [372]. This EMG envelope was the muscle excitation signal e_i driving muscle activation dynamics and a lower bound was set such that $0.01 \leq e_i \leq 1.00$ for all muscles [373]. The excitation of the BFS and SM was assumed equivalent to that of the BFL and ST, respectively, and the excitation of the VI was the average of VM and VL excitations, as done in previous work [353].

All MTU-specific parameters and functions described in the muscle contraction dynamics section (those indexed on i) need to be specified. The functions f_{v_i}, f_{ℓ_i}, f_{A_i}, f_{p_i}, $\tilde{f}_{T_i}$, and $\dot{\alpha}_i$ have taken on various forms in the literature for EMG-driven simulation. Arguably the most uncertainty surrounds the muscle activation parameters [295] including the activation dynamics function $\dot{\alpha}_i$ and the activation nonlinearity function f_{A_i} as the parameters of these functions are almost always included in the tunable parameter set [209], [290], [374]. Further, several models for f_{A_i} and $\dot{\alpha}_i$ with different behavior have been used in previous

research and it is not clear which is most appropriate. Thus, a novel development of this work is to utilize Bayesian optimization [375], [376] to optimize these functions in addition to several other MTU parameters. The optimization process is detailed in the next section and the remainder of this section specifies all MTU parameters not optimized in the Bayesian global optimization.

The following functions were used for all MTUs and thus the subscripted MTU index i has been dropped. The force-velocity function was taken from De Groote et al. (2016) as per [377]

$$f_v = a_1 \ln\left[\eta + (\eta^2 + 1)^{1/2}\right] + a_2 \tag{6.31}$$

where

$$\eta = a_3 \tilde{v}_m + a_4 \tag{6.32}$$

and $a_1 = -0.318$, $a_2 = 0.886$, $a_3 = -8.149$, and $a_4 = -0.374$. The active force-length function was modeled as the sum of three Gaussian density functions taken from De Groote et al. (2016) [377] as per

$$f_\ell = \sum_{k=1}^{3} b_{1,k} \exp\left[-\frac{0.5\left(\tilde{\ell}_m - b_{2,k}\right)^2}{b_{3,k} + b_{4,k}\tilde{\ell}_m}\right] \tag{6.33}$$

where $b_{1,1} = 0.815$, $b_{2,1} = 1.055$, $b_{3,1} = 0.162$, $b_{4,1} = 0.063$, $b_{1,2} = 0.433$, $b_{2,2} = 0.717$, $b_{3,2} = -0.030$, $b_{4,2} = 0.200$, $b_{1,3} = 0.100$, $b_{2,3} = 1.000$, $b_{3,3} = 0.354$, and $b_{4,3} = 0.000$. Recall that for eq. (6.33) only, $\tilde{\ell}_m = \ell_m / \bar{\ell}_0$ where $\bar{\ell}_0$ is the activation-adjusted optimal fiber length in eq. (6.8) and the percentage change in optimal fiber length for a completely inactive muscle was set to 15% [209] such that $\lambda = 0.15$ in eq. (6.8). The passive force-length function was taken from Thelen (2003) as per [378]

$$f_p = \frac{\exp\left[\frac{\kappa}{\epsilon_0^m}\left(\tilde{\ell}_m - 1\right)\right] - 1}{\exp(\kappa) - 1} \tag{6.34}$$

where the shape factor κ was set to 5.00 and the fiber strain due to the maximal isometric force ϵ_0^m was set to 0.55 (average of the old- and young-age values in [378]). The tendon force-strain function was modeled exponentially, similar to that used by De Groote et al. (2016) [377], as per,

$$\tilde{f}_T = \mu[\exp(E\epsilon_T) - 1] \tag{6.35}$$

where $\mu = \exp(-E\epsilon_0^T)$ and the slope of $\tilde{f}_T$ is equal to E when $\epsilon_T = \epsilon_0^T$. The slope E was set to 35.00 and ϵ_0^T was set to 0.04. The behavior of these functions specified in eqs. (6.31) – (6.35) is shown in Figures 26 and 27.

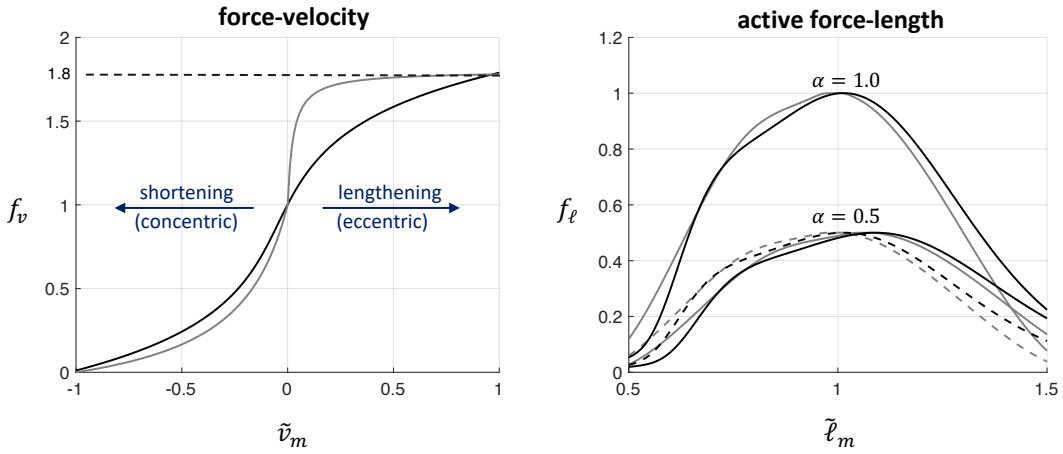

Figure 26: Force-velocity and active force-length functions. The solid black line in the force-velocity plot (left) was the function used in this study, eq. (6.31), and the solid grey line is a popular model in explicit integration approaches which uses Hill's hyperbolic force-velocity equation for negative (shortening) velocities (with the coefficient of shortening heat set to 0.25) and an approximation to the eccentric force generating behavior of lengthening muscle for positive velocities. Notice the discontinuity at zero velocity for the grey curve which is not suitable for implicit integration. While the curves appear more similar for negative velocities than for positive velocities, the eccentric behavior of the grey line is more similar to that of the black line after taking into the account the effects of viscous damping where larger damping coefficients are common in explicit integration approaches (e.g., β = 0.50 vs 0.01). The solid black line in the active force-length plot (right) was the function used in this study, eq. (6.33). The dashed lines show the effects of neglecting the increase in optimal fiber length as a function of decreased activation while the solid lines model those effects as in eq. (6.8). The grey line is a cubic spline interpolation of the force-length data tabulated in Gordon et al. (1966). The curves of lesser magnitude were for activation set to 0.5 while the others were for fully active muscle.

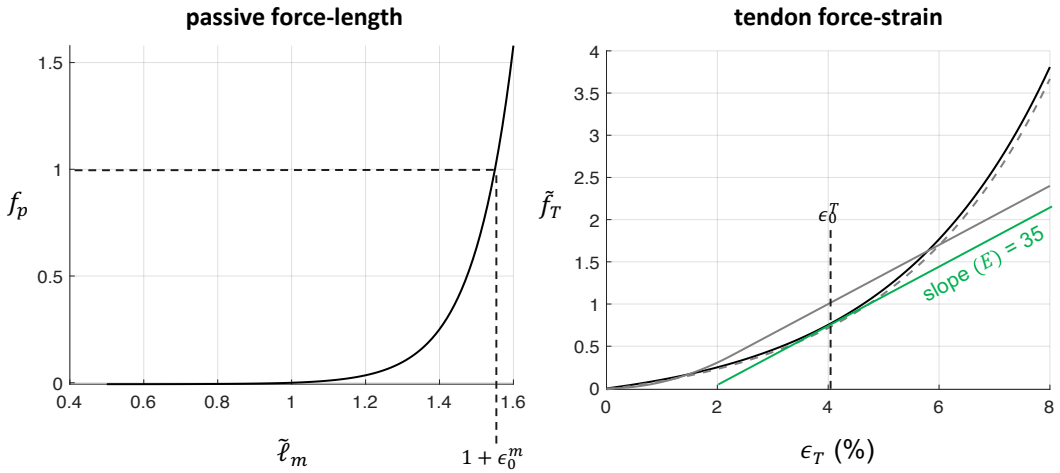

Figure 27: Passive muscle force-length and tendon force-strain functions. The passive force-length plot (left) shows the model, eq. (6.34), used in this study. The solid black line in the tendon force-strain plot (right) was the function used in this study, eq. (6.35). The solid grey line is a piecewise continuous model popular in explicit integration approaches where the tendon force-strain relationship is modeled nonlinearly in a region of low strains and linearly beyond this region. The function used in this study was modified from that used by De Groote et al. (2016), the grey dashed line, such that the slope of the tendon force with respect to strain was equivalent to the slope of the linear region of the piecewise model at the strain yielding maximal muscle isometric force (vertical black dashed line).

Fiber pennation angle ϕ_{0_i} was taken from Horsman et al. (2007) [355]. For all muscles, maximum shortening velocity v_0 was set to 15 optimal fiber lengths per second [373], the damping coefficient β was set to 0.01 [350], and the electromechanical time delay t_d was set to 40 ms [209], [373]. The optimal fiber length ℓ_{0_i} and tendon slack length ℓ_{S_i} are often included in the tunable parameter set in the global optimization. However, since the present work includes more parameters related to activation dynamics than those previous studies, ℓ_{0_i} and ℓ_{S_i} were not tuned in the global optimization in order to avoid overfitting [290]. Instead, ℓ_{0_i} and ℓ_{S_i} were scaled similar to previous work [379] such that the range of muscle fiber lengths throughout the gait cycle would be within the range of previously published data if a rigid tendon model [344] were used. The range of normalized fiber length data were taken from Arnold and Delp (2011)

and Arnold et al. (2013) [373], [380]. The range of normalized MTU lengths (normalized by the MTU length in the reference configuration) were subject-specific and taken from walking trials during the in-lab calibration visit. Let ℓ_{mtu}^{ref} be the MTU length in the reference configuration; X_{mtu} and X_m be the maximum normalized MTU and fiber length during the gait cycle, respectively; and Y_{mtu} and Y_m be the minimum normalized MTU and fiber length during the gait cycle, respectively. Then by eq. (6.10) and the rigid tendon assumption one has

$$\begin{bmatrix} X_{mtu}\ell_{mtu}^{ref} \\ Y_{mtu}\ell_{mtu}^{ref} \end{bmatrix} = \begin{bmatrix} 1 & X_m \cos\phi_X \\ 1 & Y_m \cos\phi_Y \end{bmatrix} \begin{bmatrix} \ell_S \\ \ell_0 \end{bmatrix} \tag{6.36}$$

where $\phi_X = \text{asin}(X_m^{-1} \sin\phi_0)$ and likewise for ϕ_Y per eq. (6.12). The solution to the linear system eq. (6.36) yields the optimal fiber and tendon slack length for each MTU.

The activation dynamics were simulated using a Runge-Kutta formula with the ode45 function in MATLAB. The muscle contraction dynamics are notoriously stiff [352] and thus, rather than solving for v_m in eq. (6.13) and integrating explicitly, eq. (6.13) is integrated implicitly using the ode15i function in MATLAB and the analytic Jacobian of eq. (6.13) with respect to both the fiber length state variable ℓ_m and its time-derivative v_m. It was for this reason that eqs. (6.31) – (6.35) were chosen for the Hill model as they are all continuous at the second derivative as opposed to some models popular for integrating the dynamics explicitly (in particular for piecewise formulations of f_v and $\tilde{f}_T$ which are only continuous at the first derivative) [290], [350], [378]. The simulation was initialized using the MATLAB decic function to determine initial fiber length and velocity states that are consistent with the dynamic equilibrium in eq. (6.13). The decic function also requires an initial guess for fiber length and velocity which may not be dynamically consistent. In this case, fiber length and velocity were determined assuming a rigid tendon. Thus, tendon length was set equal to the tendon slack length such that fiber length was given from eq. (6.10) and fiber velocity was obtained from the MTU velocity (numerical differentiation of ℓ_{mtu}). The simulation was performed only for the stance phase of gait identified as the time interval for which the force plate-measured ground reaction force was greater than 20 N. The integrals in eqs. (6.17) and (6.18) were approximated using the trapezoidal method.

Bayesian optimization

Bayesian optimization was used to tune a scalar that scaled the maximal isometric force F_{0_i} and five muscle activation parameters including the activation dynamics function $\dot{\alpha}_i$, the activation time constant t_{act_i}, the activation to deactivation ratio $\zeta_i = t_{act_i}/t_{deact_i}$ where t_{deact_i} is the deactivation time constant, the activation nonlinearity function f_{A_i}, and an activation nonlinearity function parameter A_i. Muscles were grouped according to a strength group and an activation group wherein muscles belonging to the same group were assumed to have the same properties concerning the group-specific construct (i.e., strength or activation). The five strength groups were the knee extensors (VL, VM, VI, RF), knee flexors (BFL, BFS, ST, SM), gastrocnemii (MG, LG), uniarticular plantarflexors (SOL, PL), and dorsiflexors (TA). These groups were determined based on similar logic used in previous work (e.g., according to MTU structure and function) [209]. The activation groupings (novel to this work) were the same as the strength groupings except that all muscles within a group were required to have a similar proportion of type I (slow-oxidative) fibers determined from the tabulated data in Yamaguchi et al. (1990) [381]. The association between fiber type distribution and the activation-force relationship has been observed previously [348]. To this end, all muscles within each strength group with this proportion less than 60% were placed in a new group as well as those greater than or equal to 60%. This was the case only for the knee flexors where SM and ST were both 50% type I, while BFL and BFS were both 65% type I. Thus, the six activation groups were the knee extensors (VL, VM, VI, RF), lateral knee flexors (BFL, BFS), medial knee flexors (SM, ST), gastrocnemii (MG, LG), uniarticular plantarflexors (SOL, PL), and dorsiflexors (TA). This yields of total of 35 tunable parameters (one strength scalar for each of the five strength groups and five activation parameters for each of the six activation groups).

The range of the strength scalar was 0.5 – 2.0 and it scaled F_{0_i} initialized using eq. (6.5) where the physiological cross-sectional area C_i was taken from Horsman et al. (2007) [355] and the muscle stress at maximal isometric force σ_i was set to 0.3 MPa. Five activation dynamics functions were considered. The first was a 1st order, linear model (abbreviated L_1T_1) based on that used by Winters and Stark (1988) [382],

$$\dot{\alpha}_i = \bar{t}_{act_i}^{-1}(e_i - \alpha_i) \tag{6.37}$$

where $\bar{t}_{act_i}$ is the average of the activation and deactivation time constants. The second was a 1st order, nonlinear, piecewise-continuous model (abbreviated N_1T_2) based on that used by De Groote et al. (2016) [377],

$$\dot{\alpha}_i = \frac{1}{2}\left[\frac{(1+\tanh[0.1(e_i-\alpha_i)])}{t_{act_i}(0.5+1.5\alpha_i)} + \frac{(0.5+1.5\alpha_i)(1-\tanh[0.1(e_i-\alpha_i)])}{t_{deact_i}}\right](e_i-\alpha_i). \tag{6.38}$$

The third was a 1st order, bilinear model (abbreviated B_1T_2) based on that used by He et al. (1991) [383],

$$\dot{\alpha}_i = \left[\left(t_{act_i}^{-1} - t_{deact_i}^{-1}\right)e_i + t_{deact_i}^{-1}\right](e_i-\alpha_i). \tag{6.39}$$

The fourth was a 2nd order, linear model (abbreviated L_2T_1) based on the findings of Milner-Brown et al. (1973) [321],

$$\ddot{\alpha}_i = -2\Omega_i\dot{\alpha}_i - \Omega_i^2\alpha_i + \Omega_i^2 e_i \tag{6.40}$$

where the natural frequency Ω_i is equal to the average value of $t_{act_i}^{-1}$ and $t_{deact_i}^{-1}$. The fifth was a piecewise version of the model eq. (6.40) (abbreviated L_2T_2) where $\Omega_i = t_{act_i}^{-1}$ for $\dot{\alpha}_i \geq 0$ (during activation) and $\Omega_i = t_{deact_i}^{-1}$ for $\dot{\alpha}_i < 0$ (during deactivation). The range of the activation time constant was 10 – 60 ms and the range of the activation to deactivation ratio ζ_i was 0.25 – 1.0. All five activation dynamics were unity gain and the excitation signal in each model was delayed according to the electromechanical time delay (40 ms). Three activation nonlinearity functions were considered. The first was the exponential model used by Lloyd and Besier (2003) [209] (abbreviated Aexp) based on the findings of Potvin et al. (1996) [347],

$$f_{A_i} = \frac{\exp(A_i\alpha_i) - 1}{\exp(A_i) - 1}. \tag{6.41}$$

The second was the piecewise A-model [384] developed by Manal and Buchanan (2003) (abbreviated A), based on the findings of Woods and Bigland-Ritchie (1983) [348] which is dependent on a single parameter A_i'. The third was a modified version of the continuous approximation to the piecewise A-model used by Meyer et al. (2019) (abbreviated Ac) [374],

$$f_{A_i} = (1-A_i'')\alpha_i + A_i''\left(1 + \frac{\xi_1}{\xi_2 + \xi_3(\alpha_i+\xi_4)^{\xi_5}}\right) \tag{6.42}$$

where $\xi_1 = -7.623$, $\xi_2 = 4.108$ $\xi_3 = 29.280$, $\xi_4 = 0.884$, $\xi_5 = 17.227$. The parameter A_i'' in eq. (6.42) was a function of A_i such that the derivative of eq. (6.42) with respect to α_i evaluated at $\alpha_i = 0$ was equivalent to that of eq. (6.41). A similar adjustment was made to the single parameter A_i' of the piecewise A-model such that $A_i' = \frac{0.12}{0.35} A_i''$. These parameter adjustments were made so that the single tunable parameter A_i yielded similar behavior in all three activation nonlinearity functions for the range $-3 \leq A < 0$ [209]. The step response for each activation dynamics model and the behavior of these three activation nonlinearity functions is shown in Figure 28.

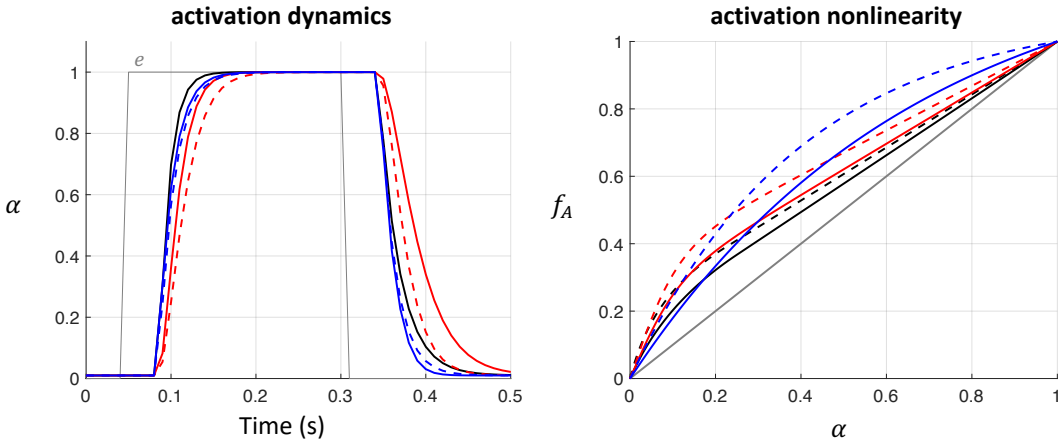

Figure 28: Activation dynamics and activation nonlinearity functions included in the tunable parameter set of the Bayesian global optimization. The step response for each activation dynamics model (with the electromechanical time delay t_d set to 40 ms, t_{act} = 12 ms and ζ = 0.5 such that t_{deact} = 24 ms) is shown in the left plot where the solid black line is the B_1T_2 model, the solid blue line is the N_1T_2 model, the dashed blue line is the L_1T_1 model, the solid red line is the L_2T_2 model, and the dashed red line is the L_2T_1 model. The behavior of the activation nonlinearity functions is shown on the right where solid lines correspond to A = -1.50 and dashed lines correspond to A = -2.50. The black lines correspond to the A model, the red lines correspond to the Ac model, the blue lines correspond to the Aexp model, and the grey line corresponds to the line of linearity.

The objective function in the global optimization was the average normalized mean squared error between the inverse dynamics and EMG-driven estimates of KFM and AFM across multiple calibration walking trials where normalization was by the variance of the inverse dynamics-based joint moment estimate. The MATLAB function bayesopt was used to optimize the 35 MTU parameters using the expected-improvement-plus acquisition function, 0.5 exploration ratio, 140 seed points (four times the number of parameters), 300 GP active set size, and the number of maximum objective function evaluations was set to 1225 (the number of parameters squared).

6.4.2. Gaussian process synergy model

The proposed sensor-driven technique uses data from four EMG-instrumented muscles to estimate the excitation of the other six muscles (would be unmeasured in practice). This estimation was performed by training an appropriate GP synergy function model [162] as described in Chapter 5. To this end, the input muscles were the four EMG-instrumented muscles: VM, MG, LG, and PL. The input window length was set to 1.5 seconds, the window relative output time was 0.75 seconds (the middle of the input window), the GP model covariance function was the isotropic squared exponential, and the GP model mean function was a constant (as in Chapter 5). All aspects of training the GP synergy function models were done using the GPML and syner-gp toolboxes [162], [316], [317].

6.5. Proposed technique: IMU and EMG-driven simulation of muscle contraction dynamics

This section describes the computational methods used for estimating the biomechanical variables of interest. Only the information from the calibrated model (musculoskeletal geometry, Bayesian optimized MTU parameters, and trained GP synergy model) and data from the reduced sensor array (two IMUs and four EMGs) are used in the following.

6.5.1. Sensor-to-segment calibration

The inverse kinematics solver requires only accelerometer and gyroscope data for thigh- and shank-fixed IMUs. The angular rate and specific force outputs from these sensors must be expressed in the segment

coordinate systems associated with the 28 generalized coordinates described previously. Thus, the TRIAD algorithm [357] was used to determine the orientation of the thigh- and shank-fixed IMU coordinate systems with respect to the thigh and shank segment coordinate systems, respectively. This required two reference vectors be measured in both the IMU and segment coordinate system. To this end, the gravity vector and knee joint flexion axis were used. The representation of the gravity vector in the segment frame was computed by rotating the global vertical axis to the segment frame during the reference configuration (static calibration trial) and the representation of the knee joint flexion axis in the segment frame was given as per the SARA method described previously. The representation of the gravity vector in the IMU frame was computed as the average direction of the specific force measured by the accelerometer during the static calibration trial. The representation of the knee joint flexion axis in the IMU frame is determined using a nonlinear least-squares method [198], [385]. In this approach, the objective function exploits a mechanical constraint imposed by modeling the knee as a hinge joint, namely that projections of the thigh and shank angular velocities measured by the segment-fixed gyroscopes onto the joint plane have the same magnitude [385]. This equality constraint is nonlinear in the unknown coordinates of the knee joint flexion axis in each IMU frame which is optimized in the least-squares sense using the Levenberg-Marquardt algorithm. Finally, the position vector of the knee joint center with respect to the thigh- and shank-fixed IMUs (constant) is determined using a nonlinear least-squares method [198], [385]. This approach exploits a mechanical constraint imposed by non-translating joints for which the position of the knee joint center with respect to either IMU is constant, namely that the magnitude of the knee joint center specific force computed using IMU data from either segment should be equivalent [385]. This equality constraint is nonlinear in the unknown coordinates of the position vector of the knee joint center in the IMU frame which is optimized in the least-squares sense using the Levenberg-Marquardt algorithm. Data recorded during the hip and knee joint movements of the star calibration task were used for both calibrations (knee joint flexion axis and knee joint center location) in addition to straight, level walking trials for the knee joint flexion axis calibration. The static and functional calibration trials would be performed each day when sensors are placed on the person.

6.5.2. Inverse kinematics: inertial motion capture

This section describes the computation of all 28 generalized coordinates describing the rigid body system configuration during the stance phase of gait using only data from the thigh- and shank-worn IMUs. This analysis is henceforth referred to as inertial motion capture (IMC). Thigh and shank IMU data are expressed relative to their respective segment coordinate systems (those that coincide with the musculoskeletal model) based on the sensor-to-segment alignment described previously. The medio-lateral axis of the shank gyroscope signal is used to identify foot contact and foot off events as described by Mansour et al. (2015) [17]. The shank-worn accelerometer data is used to identify the stillest quarter of the identified stance phase. The average accelerometer output during this interval is used to estimate the shank orientation ($\mathbf{q}_s$) at the middle of this interval (assuming zero heading angle) [26]. Then, the shank orientation before and after this mid-stance instant (for the remainder of the stance phase) is obtained by integrating eq. (6.24). To this end, the angular rate is assumed constant between time instant t_k and t_{k+1} and equal to the average value of the gyroscope signal between these two time instants [386]. Then, the linear differential equation of the quaternion kinematics in eq. (6.24) has the analytic solution [154], [368]

$$\mathbf{q}_{s,k+1} = \mathbf{q}_{s,k} \otimes \exp\left(\boldsymbol{\omega}_{s,k}^{B} \frac{\Delta t}{2}\right) \tag{6.43}$$

where $\Delta t = t_{k+1} - t_k$. The exponential map of the pure quaternion $\boldsymbol{\omega}_{s,k}^{B} \frac{\Delta t}{2}$ can be shown by expansion [368] to have scalar part (see Appendix C)

$$\left[\exp\left(\boldsymbol{\omega}_{s,k}^{B} \frac{\Delta t}{2}\right)\right]_4 = \cos\left(\left\|\boldsymbol{\omega}_{s,k}^{B}\right\| \frac{\Delta t}{2}\right) \tag{6.44}$$

and vector part

$$\left[\exp\left(\boldsymbol{\omega}_{s,k}^{B} \frac{\Delta t}{2}\right)\right]_{1:3} = \left\|\boldsymbol{\omega}_{s,k}^{B}\right\|^{-1} \boldsymbol{\omega}_{s,k}^{B} \sin\left(\left\|\boldsymbol{\omega}_{s,k}^{B}\right\| \frac{\Delta t}{2}\right). \tag{6.45}$$

Next, the knee joint angle is estimated using the method described by Seel et al. (2014) [198]. Briefly, the difference between the thigh and shank angular rates (gyroscope signals) about the knee flexion axis were integrated yielding a drift-prone estimate of knee joint angle. This estimate is fused with a noisy,

accelerometer-based estimate utilizing the fact that the specific force of the knee joint center computed using the shank- and thigh-worn IMU data along with the position vector of the knee joint center relative to the respective sensor frame (determined from the sensor-to-segment alignment) [387], [388] should differ only according to a single rotation about the knee flexion axis through an angle equal to the knee flexion angle [198]. The fusion was performed using a complementary filter (gain = 0.01) as done by Seel et al. (2014) [198].

Thigh orientation can be determined just from the shank orientation and the knee flexion angle since the knee is modeled as a hinge joint. The pelvis orientation was assumed null (i.e., the identity quaternion) except that the heading angle was constant and equal to the average heading angle of the shank during the stance phase. The ankle joint center has a known (local) position relative to the knee joint center based on the musculoskeletal geometry. Thus, the acceleration of both the knee and ankle joint centers was computed from the shank-worn accelerometer (after removing gravity) along with the segment angular rate (gyroscope signal), and the known joint center position vector relative to the shank sensor frame (from the sensor-to-segment alignment) as per standard rigid body dynamics analysis [387], [388]. The ankle joint center position is computed by double integration of the ankle joint center acceleration using the trapezoidal method. The foot orientation was determined by assuming the heading angle was equivalent to the shank heading angle through the stance phase, the roll angle was null, and the pitch angle was computed based on a simple foot-ground contact model as shown in Figure 29.

Thus, given all segment orientations and the ankle joint center position throughout the stance phase, the remaining generalized coordinates (the position of each segment coordinate system origin) were given completely by the musculoskeletal geometry model and because the joint center positions relative to each segment coordinate system were known. MTU length and moment arm were computed from the 28 IMC-estimated generalized coordinates using the same methods as for the OMC estimates described previously.

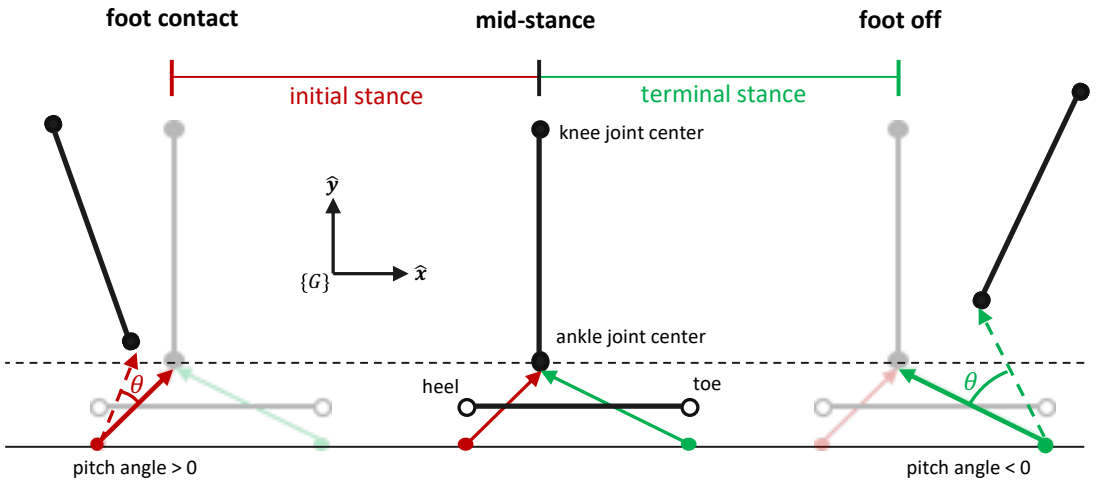

Figure 29: Simple foot-ground contact model for estimating foot pitch angle in the inertial motion capture inverse kinematics analysis. The ankle joint center throughout stance is available via direct integration as described in the main text. This foot-ground contact model is planar and thus only the vertical *y* and horizontal *x* position of the joint center in the global frame {*G*} is needed. The ankle joint center height at mid-stance is set equal to the height (black dashed line) in the reference configuration (middle configuration) from which the positions of the initial stance rotation point (red dot, directly inferior to the heel) and terminal stance rotation point (green dot, directly inferior to the toe) are computed (also available from the reference configuration). Initial stance is defined as the interval between foot contact and mid-stance (left configuration) and terminal stance is between mid-stance and foot off (right configuration). Rotation of the foot during stance is assumed to occur about an axis (*z*, out of the page) through these points for their respective intervals (initial or terminal stance) and thus the magnitude of the red and green vectors (i.e., from the rotation point to the ankle joint center) should be close to constant. Then the angle between these vectors at each time instant during initial stance (red dashed arrow) or terminal stance (green dashed arrow) and the same vectors in the reference configuration (solid red and green arrows at mid-stance and thus also the reference configuration) is the foot pitch angle (θ). Since the axis of rotation is out of the page, the pitch angle is positive in initial stance and negative in terminal stance.

6.5.2. Simulating muscle contraction dynamics

The four measured muscle excitations were used as inputs to the GP synergy functions trained during the model calibration step yielding a complete set of 10 muscle excitation time series. These signals along with the IMC-based MTU length were used to simulate the muscle contraction dynamics as described previously along with the IMC-based moment arm estimates to estimate KFM and AFM as per eqs. (6.1) and (6.2).

6.6. Experimental validation

6.6.1. Data collection

The proposed technique was validated on a healthy 20 year-old female (height: 1.75 m, mass: 65.89 kg). Analysis was for the right leg only. The subject performed 10 overground walking trials at a self-selected normal speed (stride time: 1.08 $\pm$ 0.02 m/s, stride length: 1.59 $\pm$ 0.05 m, stride velocity: 1.48 $\pm$ 0.05 m/s) for which the right foot completely contacted the force plate for a single contact. Thus, one stance phase was analyzed per trial. Marker position data were captured at 100 Hz using a 19-camera OMC system (Vicon Motion Systems, Oxford, UK). Force plate data (AMTI, Watertown, MA, USA) and raw EMG data (BioStamp, MC10, Inc., Cambridge, MA, USA) were collected at 1000 Hz. Force plate data were downsampled to 100 Hz for synchronization with marker data as were the EMG data after excitations were computed as described previously. Shank and thigh IMUs (BioStamp, MC10, Inc., Cambridge, MA, USA, gyroscope range: $\pm$ 2000°/s, accelerometer range: $\pm$ 16g) were placed over the distal lateral shank and anterior thigh, respectively. IMU data were recorded at 250 Hz, downsampled to 100 Hz, and synchronized with marker position data.

The subject performed the static and functional calibration trials as described previously for calibrating the musculoskeletal geometry. The first seven overground walking trials were set apart for the global optimization of the MTU parameters. The last three overground walking trials, now referred to as test walking trials, were used for validating the proposed technique. The sensor-to-segment alignment described previously requires data captured during a static calibration trial, a functional calibration trial, and walking trials. Only the test walking trials were used for the sensor-to-segment alignment while the same static and functional calibration trials that were used for calibrating the musculoskeletal geometry were also used for the sensor-to-segment alignment. To train the GP synergy function models, the subject walked on a treadmill (h/p/cosmos quasar, Nussdorf-Traunstein, Germany) at a self-selected slow, normal, and fast speed. The training set consisted of 20 seconds of data from each of the three treadmill walking trials.

6.6.2. Statistical analysis

Errors in estimating the biomechanical variables of interest using the proposed technique will generally be due to inaccurate MTU kinematics (MTU length and moment arm) and/or inaccurate estimation of the unmeasured muscle excitations from the GP synergy function model. Thus, each of these and their effects on the final estimation of the biomechancial variables of interest were analyzed separately only for the three test walking trials. The IMC estimates of MTU length as well as knee and ankle flexion moment arm for each MTU were compared to the ground truth OMC estimates. The GP synergy function estimates of muscle excitation and activation for the six unmeasured muscles (SOL, TA, VL, RF, ST, BFL) were compared to the measured data (ground truth). Estimates of muscle fiber length, force, power, and cumulative concentric and eccentric work were computed for four analyses: (1) OMC-based kinematics with a full set of EMG (OMC-Full, ground truth for simulating muscle contraction dynamics), (2) OMC-based kinematics with the four-EMG subset and GP synergy functions (OMC-GP, to assess the effect of the inaccuracies in the GP synergy functions), (3) IMC-based kinematics with a full set of EMG (IMC-Full, to assess the effect of inaccuracies in IMC-based kinematics), and (4) IMC-based kinematics with the four-EMG subset and GP synergy functions (IMC-GP, to evaluate the estimation error in using the proposed technique). Analyses (2) – (3) were compared to OMC-Full (ground truth) for evaluation of muscle fiber length, force, power, and cumulative concentric and eccentric work estimates. Finally, KFM and AFM were estimated using analyses (1) – (4) and were compared to the inverse dynamics-based estimate (ground truth) for evaluation.

Estimation error of all time-series relative to the ground truth data specified for each comparison was quantified using the average Pearson correlation coefficient (r) and the average percentage variance accounted for (VAF) across all three test walking trials. Percentage variance accounted for was computed as per

$$\text{VAF} = \left(1 - \frac{(\boldsymbol{y} - \hat{\boldsymbol{y}})^T(\boldsymbol{y} - \hat{\boldsymbol{y}})}{\boldsymbol{y}^T\boldsymbol{y}}\right)100 \tag{6.46}$$

where $\boldsymbol{y}$ is a column vector of ground truth values and $\hat{\boldsymbol{y}}$ is the linear regression of $\boldsymbol{y}$ (with no intercept) using the estimated values as the predictor. The correlation coefficient captures similarity in the shape of two curves

without regard for magnitude whereas VAF (a.k.a. the uncentered coefficient of determination) considers both shape and magnitude [389]. The average root mean squared error (RMSE) across all three test walking trials was also used to quantify errors in the proposed technique only (IMC-GP) to provide context for the error in physical units of measurement. For comparison to previous work, the RMSE is also reported as a percentage of the product BW*H [24], [25] (where BW is the subject body weight in Newtons and H is the subject height in meters) and as a percentage of the range of the joint moment during stance (denoted M_{range}) [222], [390]. All trial-averaged correlation coefficients were corrected using Fisher's z transformation [322] and interpreted qualitatively as weak ($r \leq 0.35$), moderate ($0.35 < r \leq 0.67$), strong ($0.67 < r \leq 0.90$), and very strong ($r > 0.90$). All trial-averaged VAF were rounded to the nearest percentage. The estimation error of cumulative concentric and eccentric work as well as the peak knee extension moment (during the loading phase of initial stance) and peak ankle plantarflexion moment (toward terminal stance) was quantified by the mean absolute percent error (MAPE) and the mean absolute error (MAE) to provide context of the error in physical units of measurement.

6.7. Results

6.7.1. Muscle-tendon unit parameter identification

The MTU parameters identified via the Bayesian optimization as well as the optimal fiber length and tendon slack length computed via eq. (6.36) are tabulated in Table 7. Across all seven calibration walking trials, the average correlation between inverse dynamics and OMC-Full estimates of KFM and AFM was 0.89 and 0.97, respectively, and the average RMSE of the OMC-Full estimate (training error) was 13.50 Nm (1.19% BW*H) for KFM and 11.12 Nm (0.98% BW*H) for AFM. The strength scalar was 1.54 for the knee extensor group, 1.23 for the knee flexor group, 0.71 for the gastrocnemii group, 0.77 for the uniarticular plantarflexor group, and 1.83 for the dorsiflexor group. All activation dynamics and activation nonlinearity functions were used for at least one activation group except for the N_1T_2 activation model. The range of the activation time constant was 25 – 58 ms and the range of the activation to deactivation ratio was 0.39 – 0.98. The length of each MTU in the reference configuration was 38.19 cm for the TA, 36.28 cm for the PL, 35.53

Table 7: Optimization of MTU parameters. Dashed lines separate activation groups. Bolded variables were tuned via Bayesian optimization and all others were computed from eq. (6.36).

Muscle	ℓ_0 (cm)	ℓ_S (cm)	$\boldsymbol{F_0}$ (N)	$\dot{\boldsymbol{\alpha}}$	$\boldsymbol{t_{act}}$ (ms)	$\boldsymbol{\zeta}$	$\boldsymbol{f_A}$	$\boldsymbol{A}$
TA	9.98	29.75	1461.45	L_2T_1	39.65	0.85	Ac	-1.77
PL	6.53	29.94	549.75	L_1T_1	25.01	0.97	Ac	-1.32
SOL	8.63	30.15	4145.00					
MG	17.36	38.93	927.07	L_2T_2	58.23	0.98	A	-1.61
LG	13.81	41.06	507.98					
VM	9.09	18.67	2759.90	B_1T_2	49.65	0.39	Aexp	-2.34
VI	8.89	14.70	1755.46					
VL	9.15	18.05	3211.43					
RF	7.12	37.46	1331.57					
BFL	10.18	34.61	992.43	L_2T_1	38.99	0.94	Ac	-2.98
BFS	8.41	14.71	430.54					
ST	25.77	24.57	536.35	L_2T_2	25.66	0.88	Ac	-0.70
SM	11.70	34.43	623.92					

ℓ_0: optimal fiber length, ℓ_S: tendon slack length, F_0: maximal isometric force, $\dot{\alpha}$: activation dynamics function, t_{act}: activation time constant, ζ: activation to deactivation ratio where $\zeta = t_{act}/t_{deact}$; f_A: activation nonlinearity function; A: the parameter of the activation nonlinearity function.

cm for the SOL, 55.68 cm for the MG, 53.60 cm for the LG, 25.74 cm for the VM, 21.47 cm for the VI, 25.17 cm for the VL, 44.35 cm for the RF, 42.65 cm for the BFL, 24.95 cm for the BFS, 51.92 cm for the ST, and 43.60 cm for the SM. The optimal fiber length and tendon slack length were all within the range of previously published data [209], [379], [391].

6.7.2. Inverse kinematics

The error statistics of the IMC-estimated MTU kinematics are tabulated in Table 8. IMC-estimated knee flexion angle was very strongly correlated (r = 0.99) with the OMC estimate and with low RMSE (1.81°) whereas only a moderate correlation (r = 0.39) was observed for the IMC-estimated ankle flexion angle and with larger errors (8.85° RMSE) which appears mostly due to an overestimated dorsiflexion angle in terminal stance (Figure 30). This was reflected in the estimation of flexion DOF moment arms for the respective joints (Figures 31 and 32) wherein moderate correlations (r = 0.40 – 0.62) were observed for the ankle joint but very strong correlations (r = 0.99) were observed for the knee joint. Likewise, RMSE in the IMC-estimated knee flexion moment arm was less than 0.15 cm but was between 0.22 and 0.82 cm for ankle flexion moment

arm. A similar observation was made for MTU length wherein the IMC estimate for all MTUs crossing the knee joint (Figure 33) were strongly to very strongly correlated with OMC estimates (r = 0.83 – 1.00) while moderate correlations (r = 0.35 – 0.37) were observed for MTUs crossing only the ankle joint. The RMSE of the IMC-estimated MTU length was less than 1.00 cm for all MTUs and less than 0.50 cm for all MTUs crossing only the knee joint. For all MTUs, the IMC-estimate explained 100% VAF in the OMC-estimate for MTU length and both knee and ankle flexion moment arm except for the ankle flexion moment arm of all plantarflexor MTUs (PL, SOL, MG, LG) for which VAF was between 93 – 98%.

Table 8: IMC vs. OMC estimated MTU kinematics across the three test walking trials.

Muscle	MTU Length			Knee Flexion Moment Arm			Ankle Flexion Moment Arm		
	r	VAF (%)	RMSE (cm)	*r*	VAF (%)	RMSE (cm)	*r*	VAF (%)	RMSE (cm)
TA	0.37	100	0.65	-	-	-	0.62	100	0.24
PL	0.43	100	0.13	-	-	-	0.45	93	0.22
SOL	0.35	100	0.69	-	-	-	0.40	98	0.75
MG	0.87	100	0.71	0.99	100	0.06	0.44	98	0.82
LG	0.83	100	0.71	0.99	100	0.06	0.44	98	0.73
VM	0.99	100	0.10	0.99	100	0.09	-	-	-
VI	0.99	100	0.10	0.99	100	0.10	-	-	-
VL	0.99	100	0.10	0.99	100	0.09	-	-	-
RF	1.00	100	0.29	0.99	100	0.13	-	-	-
BFL	0.99	100	0.26	0.99	100	0.10	-	-	-
BFS	0.99	100	0.13	0.99	100	0.08	-	-	-
ST	0.98	100	0.41	0.99	100	0.13	-	-	-
SM	0.97	100	0.26	0.99	100	0.14	-	-	-

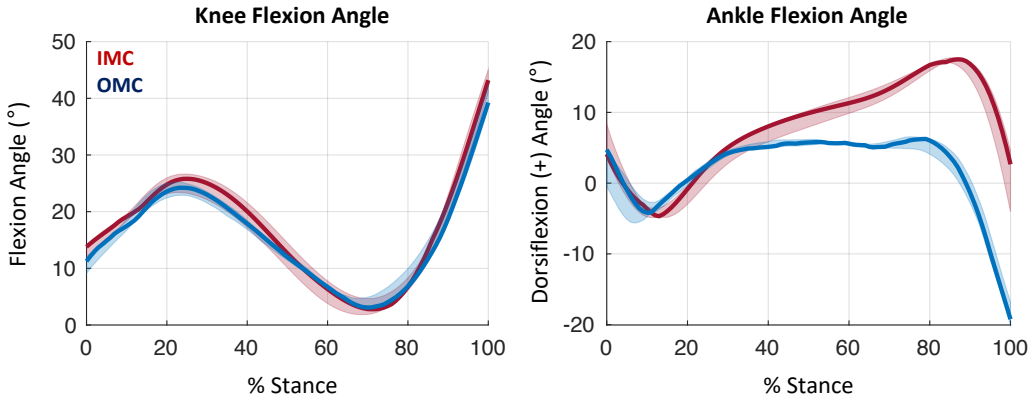

Figure 30: Visual comparison of knee flexion angle (left) and ankle flexion angle (right) in degrees during the stance phase of gait for IMC (red) and OMC (blue) estimates. Solid lines indicate the median and the shaded area indicates the range across the three test walking trials. Positive values on the ankle flexion plot indicate dorsiflexion angle whereas negative values indicate plantarflexion.

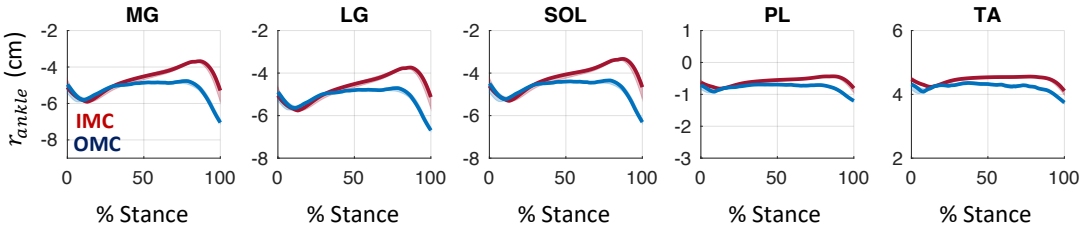

Figure 31: Visual comparison of ankle flexion moment arm in cm during the stance phase of gait for IMC (red) and OMC (blue) estimates. Solid lines indicate the median and the shaded area indicates the range across the three test walking trials. Negative moment arms correspond to the generation of a plantarflexion moment. Positive moment arms correspond to the generation of a dorsiflexion moment.

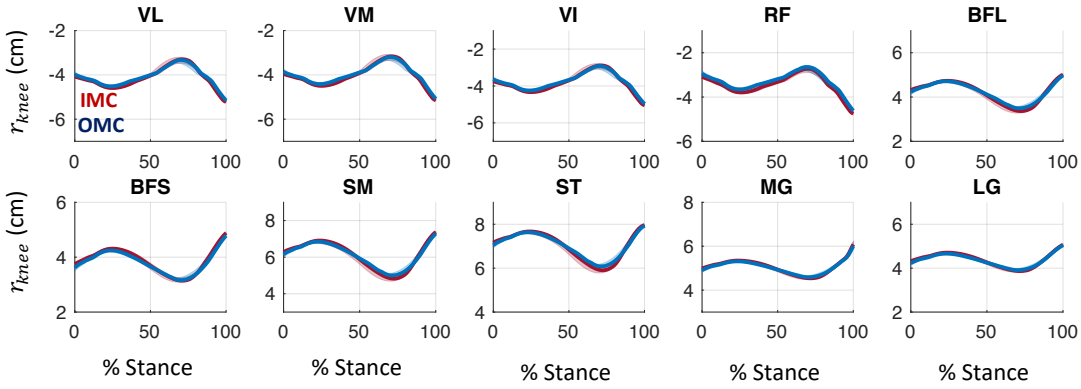

Figure 32: Visual comparison of knee flexion moment arm in cm during the stance phase of gait for IMC (red) and OMC (blue) estimates. Solid lines indicate the median and the shaded area indicates the range across the three test walking trials. Negative moment arms correspond to the generation of an extension moment. Positive values correspond to the generation of a flexion moment.

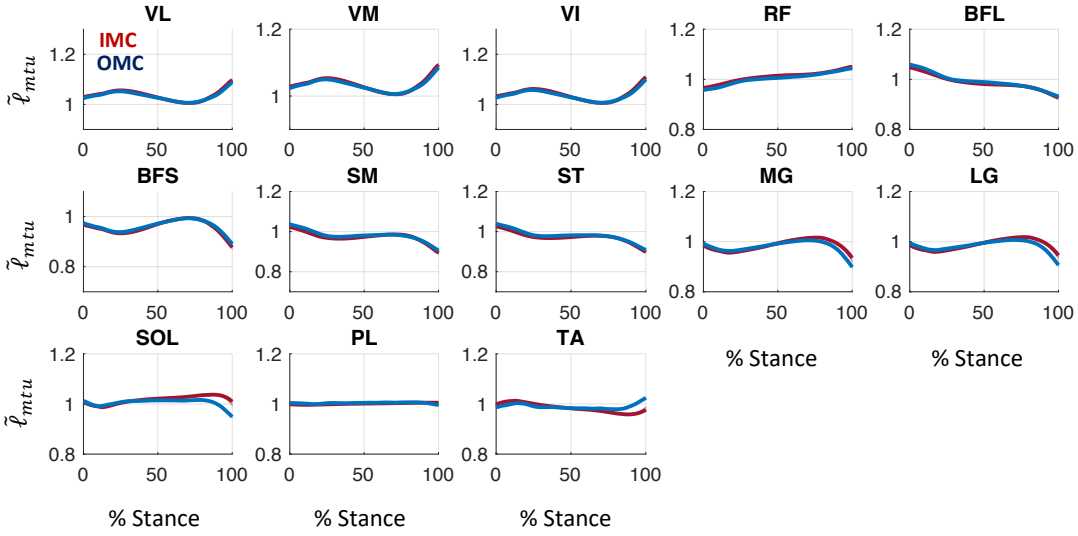

Figure 33: Visual comparison of normalized MTU length (normalized by MTU length in the reference configuration) during the stance phase of gait for IMC (red) and OMC (blue) estimates. Solid lines indicate the median and the shaded area indicates the range across the three test walking trials.

6.7.3. Muscle excitation and activation

The error statistics of the estimated excitation and activation for all unmeasured muscles from the GP synergy function models are tabulated in Table 9 and a graphical comparison of muscle activation is displayed in Figure 34. Estimated excitations were strongly to very strongly correlated ($r = 0.73 – 0.98$) with measured excitations and explained 83 – 98% VAF with RMSE less than 3% MVC for all muscles except for the BFL (9.36% MVC). Muscle activations driven by the estimated excitations were very strongly correlated with those driven by the measured excitations ($r \geq 0.93$) and explained between 93 and 99% VAF with RMSE less than 3% MVC for all muscles except the BFL (6.91% MVC).

Table 9: Estimation of muscle excitation and activation for all GP synergy function output muscles compared to measured EMG data across the three test walking trials.

Muscle	Excitation			Activation		
	r	VAF (%)	RMSE (%MVC)	*r*	VAF (%)	RMSE (%MVC)
TA	0.92	94	2.16	0.98	99	1.94
SOL	0.98	98	2.67	0.98	99	2.19
VL	0.96	95	1.77	0.96	98	1.10
RF	0.73	85	1.97	0.96	98	0.85
BFL	0.95	90	9.36	0.96	94	6.91
ST	0.80	83	2.06	0.93	93	1.81

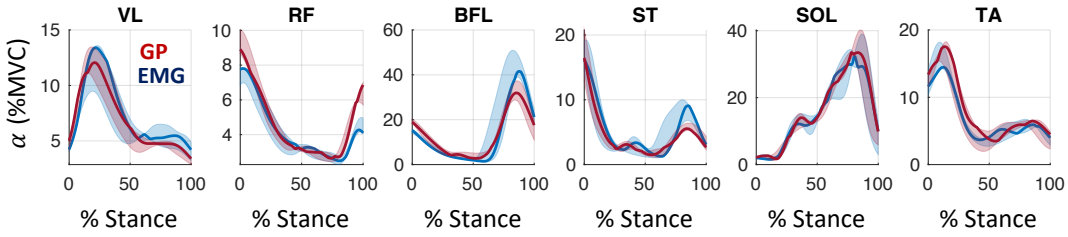

Figure 34: Visual comparison of muscle activation expressed as a percentage of MVC for all GP synergy function output muscles during the stance phase of gait driven by measured excitations (blue line, EMG) and estimated excitations from the GP synergy functions (red line, GP). Solid lines indicate the median and the shaded area indicates the range across the three test walking trials.

6.7.4. Muscle contraction dynamics

The error statistics characterizing the OMC-GP, IMC-Full, and IMC-GP simulation of contraction dynamics relative to the ground truth OMC-Full analysis are tabulated in Table 10 (time-series variables) and Table 11 (concentric and eccentric work) and graphically compared in Figures 35-37.

Muscle fiber length

For the IMC-GP analysis, estimated fiber length explained 100% VAF in the OMC-Full analysis for all muscles and with RMSE less than 0.50 cm for all muscles crossing only the knee joint (or less than 3.50% of the optimal fiber length) and between 0.11 cm (PL) and 0.63 cm (MG) RMSE for all muscles crossing the ankle joint (or between 1.72% and 5.63% of the optimal fiber length). Correlation coefficients were very strong (r = 0.97 – 0.99) for all muscles crossing only the knee joint and were strong (r = 0.71 – 0.83) for all muscles crossing the ankle joint except for the SOL (r = -0.07) and TA (r = 0.15). These low correlations for the SOL and TA were reflected in the IMC-Full analysis (r = -0.08 and 0.15, respectively), but not in the OMC-GP analysis (r > 0.99 for both muscles) suggesting errors in the IMC-based kinematics may have contributed more to these weak correlations than did inaccuracies in the GP synergy functions.

Muscle force

For the IMC-GP analysis, estimated muscle force explained greater than 90% VAF for all muscles except for the SM (88% VAF) and was very strongly correlated with OMC-Full estimates except for all knee flexors wherein strong correlations were observed (r = 0.82 – 0.88). For all muscles, the estimation performance (r and VAF) of the OMC-GP and IMC-Full analyses were comparable or better than the IMC-GP analysis. For only those muscles crossing the knee joint, the estimation performance of the IMC-Full analysis was comparable or better than the OMC-GP analysis. However, the opposite was observed for TA and SOL (the only synergy function output muscles crossing the ankle joint) wherein the estimation performance of the OMC-GP analysis was comparable or better than the IMC-Full analysis. The RMSE in estimating muscle force was between 9.41 N for PL and 178.53 N for SOL and as a percentage of each muscle's maximum isometric force (F_0 in Table 7) was 4.32% for TA, 1.71% for PL, 4.31% for SOL, 2.54%

for MG, 2.12% for LG, 0.91% for VM, 0.95% for VI, 1.91% for VL, 2.39% for RF, 6.17% for BFL, 10.24% for BFS, 4.04% for ST, and 2.68% for SM.

Muscle power

For the IMC-GP analysis, estimated muscle power for MTUs crossing the knee joint was strongly to very strongly correlated (r = 0.80 – 0.97) with estimates from the OMC-Full analysis and with VAF between 83 and 95%. However, moderate correlations (r = 0.56 – 0.68) were observed for uniarticular MTUs crossing the ankle joint (TA, PL, SOL) and with VAF between 16 and 37%. For all muscles, estimation performance (r and VAF) of the IMC-Full analysis was comparable or better than for the IMC-GP analysis, and the OMC-GP analysis was comparable or better than for the IMC-Full analysis. The RMSE in estimating muscle power was between 1.60 W for SM to 37.81 W for SOL.

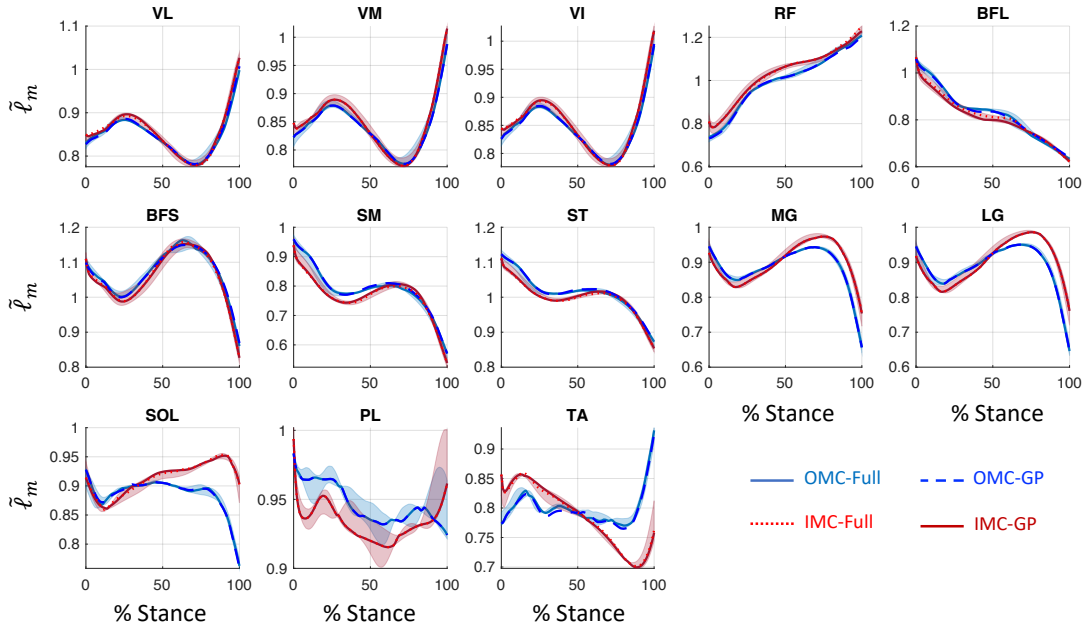

Figure 35: Visual comparison of normalized fiber length (normalized by the optimal fiber length) computed using OMC-Full (solid soft blue, ground truth), OMC-GP (dashed blue), IMC-Full (dotted red), and IMC-GP (solid maroon, proposed technique) during the stance phase of gait. Lines indicate the median and the shaded area indicates the range across the three test walking trials (shaded area only shown for OMC-Full and IMC-GP)

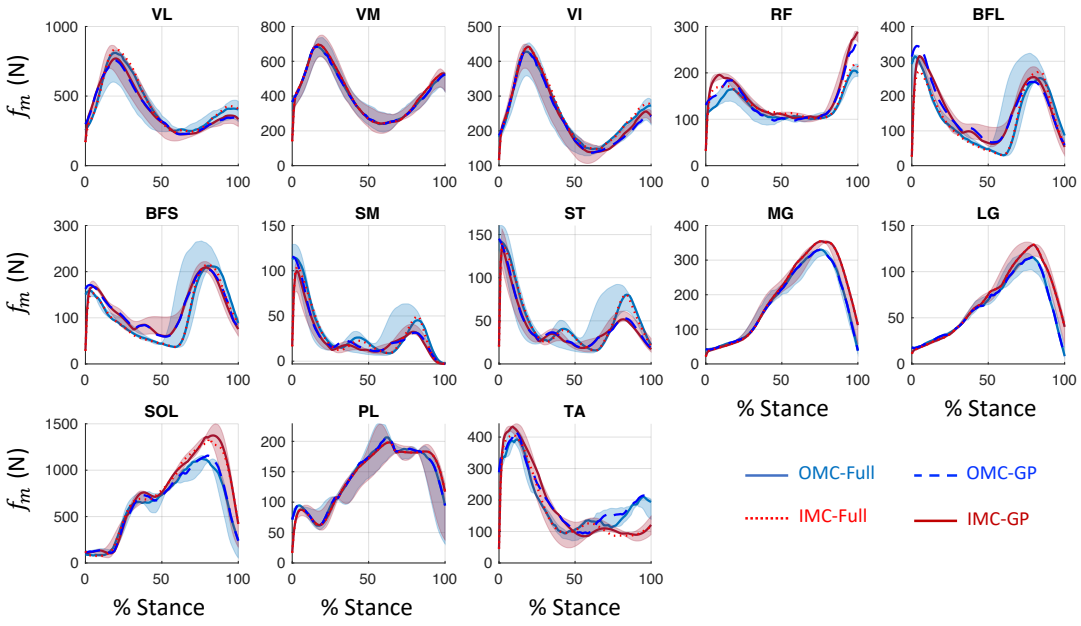

Figure 36: Visual comparison of muscle force in Newtons computed using OMC-Full (solid soft blue, ground truth), OMC-GP (dashed blue), IMC-Full (dotted red), and IMC-GP (solid maroon, proposed technique) during the stance phase of gait. Lines indicate the median and the shaded area indicates the range across the three test walking trials (shaded area only shown for OMC-Full and IMC-GP).

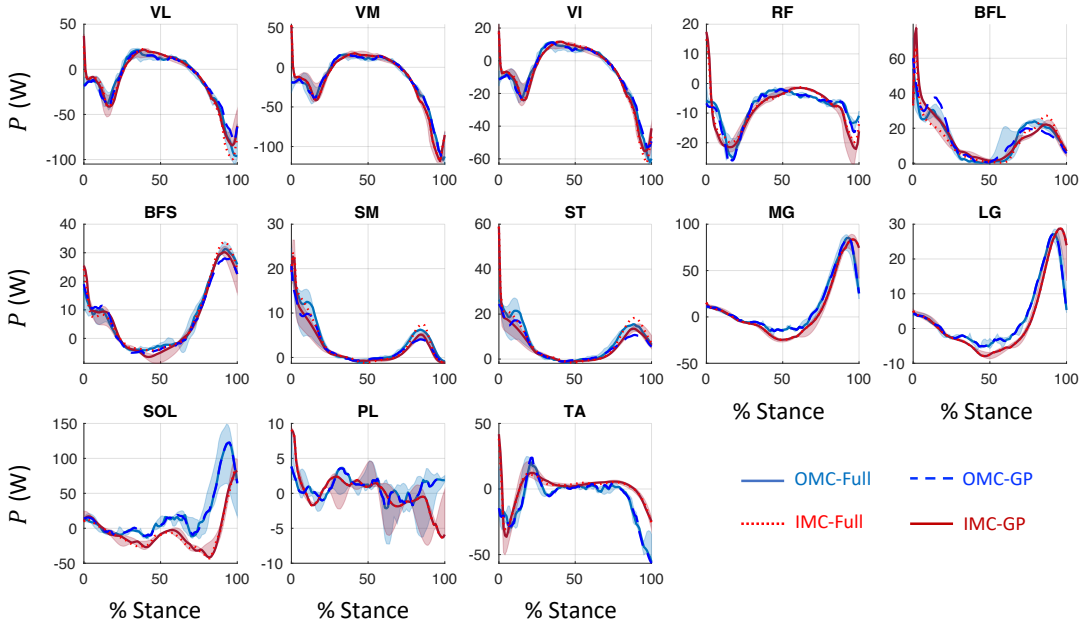

Figure 37: Visual comparison of muscle power in Watts computed using OMC-Full (solid soft blue, ground truth), OMC-GP (dashed blue), IMC-Full (dotted red), and IMC-GP (solid maroon, proposed technique) during the stance phase of gait. Lines indicate the median and the shaded area indicates the range across the three test walking trials (shaded area only shown for OMC-Full and IMC-GP).

Table 10: Estimation of muscle fiber length, force, and power for the IMC-GP, OMC-GP, and IMC-Full analyses compared to the OMC-Full analysis (ground truth) across the three test walking trials.

		IMC-GP			OMC-GP		IMC-Full	
Muscle	Variable	*r*	VAF (%)	RMSE	*r*	VAF (%)	*r*	VAF (%)
TA	Fiber Length (cm)	0.15	100	0.56	1.00	100	0.15	100
	Force (N)	0.91	93	63.11	0.99	99	0.92	94
	Power (W)	0.68	37	13.85	1.00	99	0.62	39
PL	Fiber Length (cm)	0.71	100	0.11	-	-	-	-
	Force (N)	0.98	100	9.41	-	-	-	-
	Power (W)	0.62	36	2.47	-	-	-	-
SOL	Fiber Length (cm)	-0.07	100	0.42	1.00	100	-0.08	100
	Force (N)	0.96	98	178.53	0.99	99	0.97	98
	Power (W)	0.56	16	37.81	0.99	98	0.60	20
MG	Fiber Length (cm)	0.83	100	0.63	-	-	-	-
	Force (N)	0.99	99	23.54	-	-	-	-
	Power (W)	0.97	92	9.62	-	-	-	-
LG	Fiber Length (cm)	0.80	100	0.59	-	-	-	-
	Force (N)	0.98	99	10.79	-	-	-	-
	Power (W)	0.95	89	3.60	-	-	-	-
VM	Fiber Length (cm)	0.99	100	0.10	-	-	-	-
	Force (N)	0.99	100	25.00	-	-	-	-
	Power (W)	0.96	93	10.51	-	-	-	-
VI	Fiber Length (cm)	0.99	100	0.10	1.00	100	0.99	100
	Force (N)	0.99	100	16.73	0.99	100	1.00	100
	Power (W)	0.97	95	4.75	1.00	100	0.97	95
VL	Fiber Length (cm)	0.99	100	0.11	1.00	100	0.99	100
	Force (N)	0.97	98	61.19	0.96	98	1.00	100
	Power (W)	0.96	93	9.44	0.99	98	0.97	95
RF	Fiber Length (cm)	0.99	100	0.24	1.00	100	1.00	100
	Force (N)	0.93	98	31.86	0.96	99	0.95	99
	Power (W)	0.80	83	5.11	0.99	99	0.81	86
BFL	Fiber Length (cm)	0.99	100	0.27	1.00	100	0.99	100
	Force (N)	0.82	91	61.21	0.89	94	0.94	97
	Power (W)	0.83	86	7.95	0.95	95	0.88	91
BFS	Fiber Length (cm)	0.99	100	0.16	1.00	100	0.99	100
	Force (N)	0.82	92	44.07	0.89	94	0.97	99
	Power (W)	0.97	95	3.17	0.99	98	0.99	98
ST	Fiber Length (cm)	0.98	100	0.39	1.00	100	0.98	100
	Force (N)	0.84	90	21.68	0.92	93	0.93	96
	Power (W)	0.88	85	4.05	0.99	97	0.93	91
SM	Fiber Length (cm)	0.97	100	0.30	1.00	100	0.97	100
	Force (N)	0.88	88	16.70	0.94	92	0.93	94
	Power (W)	0.96	93	1.60	0.99	98	0.97	95

Cumulative muscle work

For the OMC-Full analysis (ground truth), all posterior musculature (plantarflexors and knee flexors) did more concentric than eccentric work whereas all anterior musculature (dorsiflexor and knee extensors) did more eccentric than concentric work during stance. This was reflected in the power-time curves (Figure 37) where the posterior musculature produces mostly positive power, and the anterior musculature produces mostly negative power. The same observation was manifest in the IMC-GP analysis except for the PL and SOL. Estimation error was worst for PL eccentric work (121% MAPE), SOL eccentric work (385% MAPE), and RF concentric work (220% MAPE) and for all other muscles varied between 0% for BFL eccentric work and 77% for SM eccentric work in terms of MAPE. However, the largest percentage errors were observed for the work estimates corresponding to the type of work (concentric or eccentric) which was *least* for each muscle except for the uniarticular knee extensors (3-10% MAPE for concentric work) and for the BFL (0% MAPE for eccentric work). When considering only the type of work which was *greatest* for each muscle, MAPE varied between 4% for BFS concentric work and 42% for SOL concentric work. Across all muscles, estimation performance was comparable (within 4% MAPE) or superior for the OMC-GP analysis when compared to IMC-GP and IMC-Full (except for the BFS eccentric work for which the IMC-Full analysis was superior) whereas the superiority in estimation performance of the IMC-GP vs. the IMC-Full analyses varied between muscles and work type.

Table 11: Estimation of cumulative concentric (Con.) and eccentric (Ecc.) muscle work during the stance phase of gait for the IMC-GP, OMC-GP, and IMC-Full analyses compared to the OMC-Full analysis (ground truth) across the three test walking trials.

		OMC-Full	IMC-GP			OMC-GP	IMC-Full
Muscle	Work	Mean (J)	Mean (J)	MAE (J)	MAPE (%)	MAPE (%)	MAPE (%)
TA	Con.	1.74	2.93	1.20	68	21	56
	Ecc.	5.32	4.17	1.15	22	11	23
PL	Con.	0.85	0.65	0.20	22	-	-
	Ecc.	0.39	0.81	0.42	121	-	-
SOL	Con.	12.39	6.99	5.41	42	7	49
	Ecc.	1.77	8.12	6.34	385	24	387
MG	Con.	9.81	10.34	0.53	6	-	-
	Ecc.	2.84	4.84	2.00	70	-	-
LG	Con.	3.15	3.38	0.23	7	-	-
	Ecc.	0.94	1.62	0.68	73	-	-
VM	Con.	3.08	3.39	0.31	10	-	-
	Ecc.	11.96	15.90	3.93	33	-	-
VI	Con.	1.86	1.91	0.05	3	3	5
	Ecc.	6.42	8.06	1.64	26	6	32
VL	Con.	3.42	3.42	0.13	4	7	4
	Ecc.	10.73	12.49	2.01	19	14	30
RF	Con.	0.07	0.21	0.14	220	62	126
	Ecc.	5.05	6.19	1.13	23	8	12
BFL	Con.	10.46	9.53	0.93	9	13	13
	Ecc.	0.00	0.00	0.00	0	0	0
BFS	Con.	5.59	5.72	0.20	4	5	10
	Ecc.	0.75	1.10	0.34	47	38	4
ST	Con.	5.19	3.94	1.24	24	12	11
	Ecc.	0.10	0.13	0.04	67	16	49
SM	Con.	2.60	1.75	0.86	32	11	20
	Ecc.	0.08	0.11	0.04	77	28	57

6.7.5. Muscle moment

Across all three test walking trials, the average KFM estimation error was 13.56 Nm (1.20% BW*H, 15.02% M_{range}) for the proposed IMC-GP analysis when compared to inverse dynamics (Table 12). Most of the KFM error appears attributable to an overestimated extension moment toward terminal stance (Figure 38). Estimation error was similar for AFM (15.18 Nm RMSE, 1.34% BW*H, 14.06% M_{range}) but the estimation error of the peak plantarflexion moment in terminal stance (31.32 Nm MAE, generally underestimated) was larger than that observed for the peak knee extension moment in initial stance (2.78 Nm MAE). The RMSE in Nm and as a percentage of BW*H for all other analyses are shown in Table 12. The RMSE in estimating KFM as a percentage of M_{range} was 15.19% for OMC-Full, 14.15% for OMC-GP, and 15.90% for IMC-Full while for AFM it was 12.62% for OMC-Full, 12.00% for OMC-GP, and 14.58% for IMC-Full. The correlation between joint moment estimates from the inverse dynamics analysis and all four EMG-driven analyses was between 0.94 and 0.97 for the ankle (r = 0.95 for IMC-GP) and between 0.89 and 0.90 for the knee (r = 0.90 for IMC-GP). Likewise, across all four EMG-driven analyses, VAF varied between 81 and 84% for KFM (83% VAF for IMC-GP) and between 93 and 96% for AFM (94% VAF for IMC-GP).

Table 12: Estimation of knee and ankle flexion moment during the stance phase of gait for the IMC-GP (proposed technique), OMC-Full, OMC-GP, and IMC-Full analyses compared to the estimate from inverse dynamics (ID, ground truth) across the three test walking trials.

		Peak			Time-Series			
Method	Joint	Mean (Nm)	MAPE (%)	MAE (Nm)	r	VAF (%)	RMSE (Nm)	RMSE (%BW*H)
ID	Knee	64.47	-	-	-		-	-
	Ankle	93.49	-	-	-		-	-
IMC-GP	Knee	67.25	4	2.78	0.90	83	13.56	1.20
	Ankle	62.17	34	31.32	0.95	94	15.18	1.34
OMC-Full	Knee	65.43	5	3.05	0.90	82	13.78	1.22
	Ankle	66.29	29	27.20	0.97	95	13.63	1.20
OMC-GP	Knee	64.73	2	1.46	0.90	84	12.49	1.10
	Ankle	66.77	29	26.72	0.97	96	12.96	1.14
IMC-Full	Knee	68.32	8	5.52	0.89	81	15.13	1.34
	Ankle	61.97	34	31.52	0.94	93	15.74	1.39

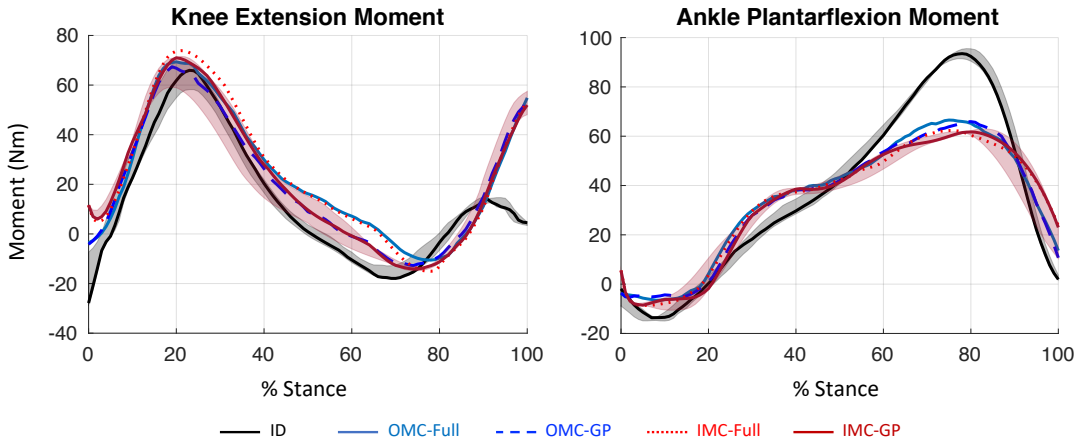

Figure 38: Visual comparison of knee extension moment (left) and ankle plantarflexion moment (right) computed using inverse dynamics (ID, solid black line, ground truth), OMC-Full (solid soft blue, ground truth for EMG-driven), OMC-GP (dashed blue), IMC-Full (dotted red), and IMC-GP (solid maroon, proposed technique) during the stance phase of gait. Lines indicate the median and the shaded area indicates the range across the three test walking trials (shaded area only shown for ID and IMC-GP). Positive values indicate an extension moment for the knee and a plantarflexion moment for the ankle and negative values indicate a flexion moment for the knee and a dorsiflexion moment for the ankle.

For individual muscle moments, very strong correlations (r = 0.91 – 0.99) were observed between estimates from the IMC-GP and OMC-Full analyses except for strong correlations (r = 0.80 – 0.90) for the PL ankle flexion muscle moment and the knee flexion muscle moment for all knee flexors (Table 13). The IMC-GP estimates explained between 89 and 100% VAF in the OMC-Full estimate. Across all muscles and for both the knee and ankle flexion moment, the estimation performance of the IMC-Full analysis was superior or comparable to both the OMC-GP and IMC-GP analyses except that the OMC-GP analysis outperformed IMC-Full in estimating TA ankle flexion muscle moment. Further, the estimation performance of the OMC-GP analysis was superior or comparable to the IMC-GP analysis for all muscles and DOFs. Figures 39 and 40 depict a graphical comparison of individual muscle moment for both the knee and ankle flexion DOF, respectively.

Table 13: Estimation of individual muscle moment for the knee and ankle flexion DOF during the stance phase of gait for the IMC-GP (proposed technique), OMC-GP, and IMC-Full analyses compared to the OMC-Full estimate (ground truth) across the three test walking trials.

Muscle	Joint	IMC-GP			OMC-GP		IMC-Full	
		r	VAF (%)	RMSE (Nm)	*r*	VAF (%)	*r*	VAF (%)
TA	Ankle	0.91	94	2.63	0.99	99	0.92	95
PL	Ankle	0.85	97	0.34	-	-	-	-
SOL	Ankle	0.98	99	3.52	0.98	99	0.99	100
MG	Ankle	0.99	99	1.11	-	-	-	-
	Knee	0.99	99	1.16	-	-	-	-
LG	Ankle	0.99	99	0.31	-	-	-	-
	Knee	0.97	99	0.47	-	-	-	-
VM	Knee	0.99	100	1.18	-	-	-	-
VI	Knee	0.99	100	0.66	0.99	100	1.00	100
VL	Knee	0.98	98	2.57	0.97	98	1.00	100
RF	Knee	0.97	98	1.38	0.98	99	0.98	99
BFL	Knee	0.82	92	2.43	0.90	95	0.94	97
BFS	Knee	0.80	92	1.56	0.90	95	0.97	99
ST	Knee	0.85	90	1.47	0.93	94	0.93	96
SM	Knee	0.90	89	0.97	0.95	93	0.94	95

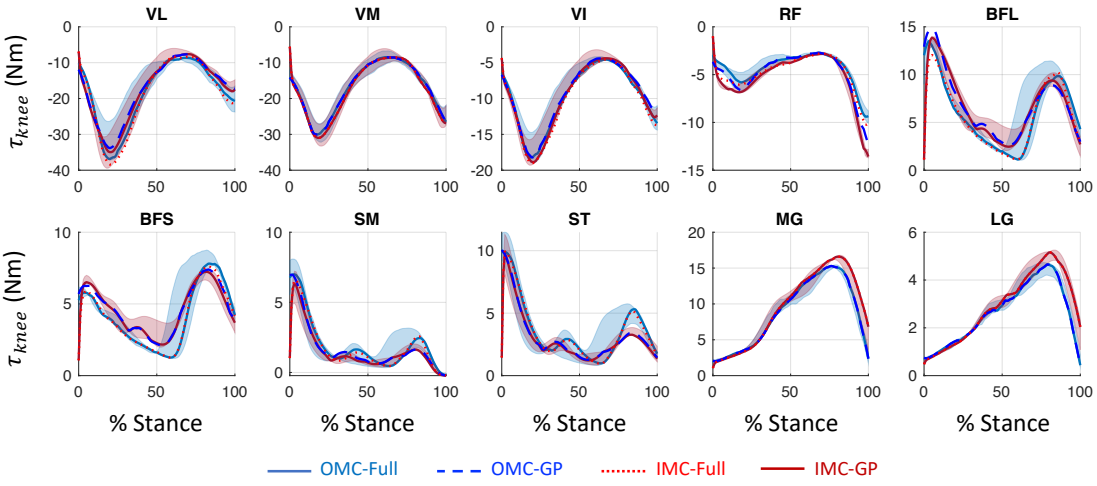

Figure 39: Visual comparison of individual muscle moment for the knee flexion DOF computed using OMC-Full (solid soft blue, ground truth), OMC-GP (dashed blue), IMC-Full (dotted red), and IMC-GP (solid maroon, proposed technique) during the stance phase of gait. Lines indicate the median and the shaded area indicates the range across the three test walking trials (shaded area only shown for OMC-Full and IMC-GP). Negative values indicate a knee extension moment. Positive values indicate a knee flexion moment.

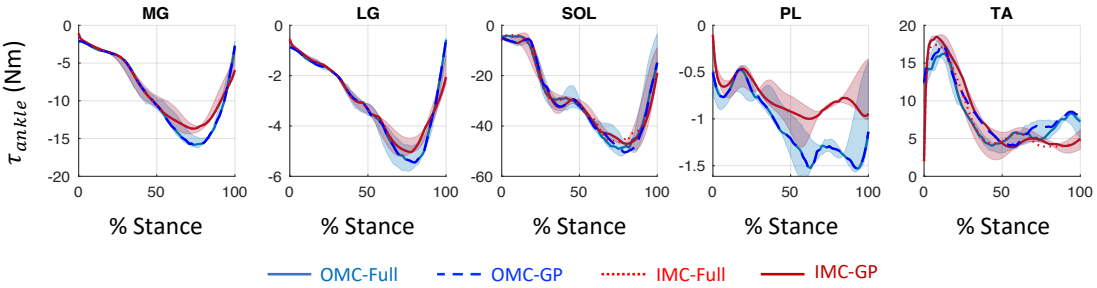

Figure 40: Visual comparison of individual muscle moment for the ankle flexion DOF computed using OMC-Full (solid soft blue, ground truth), OMC-GP (dashed blue), IMC-Full (dotted red), and IMC-GP (solid maroon, proposed technique) during the stance phase of gait. Lines indicate the median and the shaded area indicates the range across the three test walking trials (shaded area only shown for OMC-Full and IMC-GP). Negative values indicate a plantarflexion moment. Positive values indicate a dorsiflexion moment.

6.8. Discussion

6.8.1. On the results of the validation study

Perhaps the most promising result from the current validation study is the estimation of KFM with strong correlations (r = 0.90) and relatively low errors (13.56 Nm RMSE, 1.20% BW*H nRMSE) using the proposed IMC-GP technique. Likewise, the peak knee extension moment during the loading phase of initial stance was estimated to within 2.78 Nm MAE. This amounts to 0.25% BW*H which is well below previously observed inter-limb differences for patients post-ACLR (e.g., 1.08% BW*H [329]) and differences between patients post-ACLR and healthy controls (e.g., 1.72% BW*H [329], 1.10% BW*H for patellar tendon graft [332]). As a percentage of body mass, the peak knee extension moment error (4.21% BM) is 87% less than the gender differences observed for patients 12 months post-ACLR (33.50% BM) reported by Asaeda et al. (2017) [333]. Further, the 4.21% BM error is 58% and 75% less than the differences observed by Teng et al. (2017) between patients six months post-ACLR compared to pre-surgery (10% BM reduction) and healthy controls (17% BM), respectively [331]. In the context of osteoarthritis, Chehab et al. (2014) found a 1%

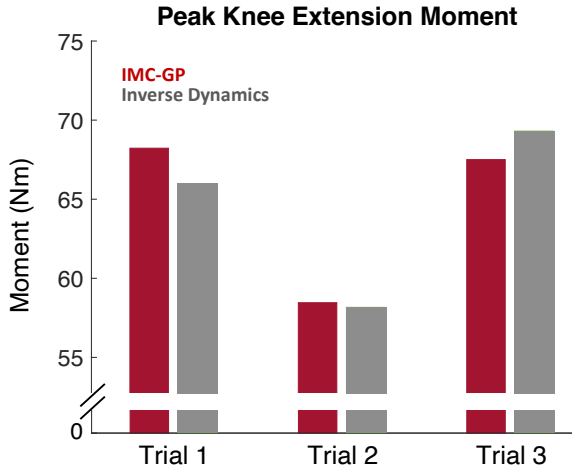

Figure 41: Visual comparison of peak knee extension moment estimated from the IMC-GP analysis (maroon, proposed technique) and the inverse dynamics analysis (grey, ground truth) across all three test walking trials.

BW*H increase in baseline peak knee extension moment (four times larger than the error in the proposed technique) was associated with an average loss of 0.15 mm medial tibial cartilage thickness over 5 years [51]. Therefore, the absolute errors appear low enough to detect clinically meaningful differences. However, in this context, it is arguably more important that estimates correlate well with ground truth data. This validation study consisted of only three test walking trials, all for a normal walking speed, which is too few and too homogenous to appropriately evaluate correlation. Nonetheless, the proposed technique preliminarily appears able to track differences in the peak knee extension moment between the three test walking trials (Figure 41). Future work should investigate this further across multiple walking conditions (speed, load) and subjects.

The proposed technique (IMC-GP) generally compared well to the gold standard OMC-Full analysis (OMC-based kinematics with a full set of EMG data) in the simulation of muscle contraction dynamics, especially for the muscles crossing the knee joint. The most apparent discrepancies were observed in the mean absolute percent errors (121 to 385%) for the PL and SOL cumulative muscle eccentric work and RF cumulative muscle concentric work. These large percent errors were driven by small work magnitudes associated with the type of work which was least for each muscle. For example, the SOL did 86% less

eccentric work than concentric work and the VM did 74% less concentric work than eccentric work during the stance phase. When considering the estimation of the cumulative muscle work associated with the type of work which was greatest for each muscle (e.g., concentric work for SOL, eccentric work for VM), the percent errors were much less (4 to 42% MAPE). Thus, the proposed technique performed better in estimating the power requirements of each muscle which characterize its dominant function during the stance phase of gait (e.g., propulsion in terminal stance for the SOL, absorbing load in initial stance for VM). A strong correlation (r = 0.87) was observed between estimates from the proposed technique and OMC-Full of the average work (across the three test trials) done by each muscle (again, for the type of work which was greatest for each muscle). Thus, the proposed technique was sensitive to variability in muscle work across muscles. As for the peak knee extension moments, further investigation is needed across more non-uniform walking conditions to appropriately evaluate correlation in estimating muscle work within the same muscle.

The superiority in simulating muscle contraction for muscles crossing the knee joint when compared to those crossing the ankle joint was manifest in the estimation of muscle power. Strong correlations between IMC-GP and OMC-Full estimates of muscle power were observed for muscles crossing the knee joint and with 83 – 95% VAF as opposed to moderate correlations and only 16 – 37% VAF for uniarticular ankle muscles. This discrepancy in estimating muscle power appears mostly due to inaccuracies in estimating fiber length trajectories (Figure 35) as opposed to muscle force (Figure 36) as correlations between IMC-GP and OMC-Full estimates of muscle force were strongly to very strongly correlated for all muscles and likewise for fiber length except for weak correlations observed for SOL (r = -0.07) and TA (r = 0.15). Further, the results suggest the inaccuracies in IMC-estimated MTU kinematics may have contributed more to the error in simulating uniarticular ankle muscle contractions as opposed to inaccuracies in the GP synergy functions. The opposite was true for MTUs crossing the knee joint. These observations may be due to the fact that (1) three of the four input muscles to the GP synergy functions were plantarflexors and (2) estimated MTU kinematics compared very well to OMC estimates for those crossing the knee joint (more so than ankle MTUs).

The greater estimation error in ankle MTU kinematics is likely due to greater errors in estimating ankle dorsiflexion angle (especially in terminal stance) relative to that observed for knee flexion angle (Figure 30). For example, the IMC-estimated ankle flexion moment arm (Figure 31) deviates from the OMC estimate in a temporal fashion similar to the dorsiflexion angle error (Figure 30). This phenomenon was observed to a lesser degree in the SOL and TA MTU length estimates (Figure 33). This may be expected as the dorsiflexion angle error is influenced by both the single-IMU, integration-based estimate of shank orientation in addition to the estimated foot kinematics from the simple foot-ground contact model. This foot-ground contact model was proposed in order to avoid having to place an additional IMU on the foot. Future work should investigate additional techniques to improve on this estimation including, for example, forward dynamic estimates of segment kinematics based on estimated joint moments. Nonetheless, these inaccuracies had a negligible effect in estimating individual muscle moments as all estimates from the IMC-GP analysis were strongly to very strongly correlated with OMC-Full estimates and with only 0.32 to 3.52 Nm RMSE.

The error in estimating KFM for both OMC-Full (ground truth for EMG-driven) and IMC-GP (proposed technique) was primarily driven by an overestimated knee extension moment towards foot off (Figure 38). It is not clear what underlies this error. At the instant of foot off the knee is flexing (Figure 30) and thus the uniarticular knee extensor MTUs are lengthening (Figure 33) as are the muscle fibers (Figure 35). Thus, these muscles are operating on the eccentric portion of the force-velocity curve (Figure 26) for which force production is greater. It may be that tuning of some force-velocity properties of these muscles would result in a better fit. For example, increasing the maximal shortening velocity would diminish the effects of increased force development for a lengthening fiber. However, the maximal shortening velocity v_0 was set to 15 optimal fiber lengths per second as done by Arnold et al. (2013) [373], which is already on the high end of what is typically used [223]. Given that the muscles are lengthening, one may also reason that the passive force-length properties of the muscle are contributing to this error. However, the RF is the only knee extensor with fiber lengths well above the optimum (Figure 35) wherein passive forces are developed (Figure 27). The knee flexion angle was about 40° at foot off and the knee extension moment arm was about 5 cm at the same instant which is within the range ($\pm$ 1.0 cm) of previous literature [364], [365], [392]. A reduction in the knee extensor moment arm would yield better results at foot off, but it may result in an

underestimate of the peak knee extension moment if the adjusted geometry affects moment arm in early stance. This and other explanations should be investigated further in future research.

6.8.2. Comparison to other techniques

Several techniques using only data from wearable sensors to estimate joint dynamics have previously been proposed to which our results may be compared. Concerning techniques based solely on machine learning models, Hahne and O'Keefe (2008) used data from seven EMG sensors as inputs to a neural network to estimate KFM and AFM with coefficients of determination (r^2) equal to 0.54 and 0.84, respectively, compared to 0.81 and 0.90, respectively, for the proposed technique. Howell et al. (2013) used data from an instrumented insole with 12 force sensitive resistors as inputs to a linear model to estimate KFM and AFM with correlations of 0.89 and 0.97, respectively, which is comparable to the current study. Similarly, Jacobs and Ferris (2015) used data from an eight-sensor instrumented insole and a load cell placed over the Achilles' tendon as inputs to a neural network to estimate AFM during walking at speeds of 1.0 and 1.5 m/s with RMSE equal to 1.17 and 1.30% BW*L (where the leg length L was the height of the trochanter marker in the standing calibration trial) compared to 2.41% BW*L in the current study. The downside to these machine learning techniques is that they involve no simulation of muscle contraction dynamics and thus no insight into the function of individual muscles. Likewise, they are arguably less generalizable than physics-based techniques and two of these studies used sensor arrays that are, to date, not very common for remote monitoring (e.g., instrumented insole, load cell).

Concerning physics-based techniques for comparison to the proposed technique, there are generally two approaches that have been proposed. One is to utilize techniques requiring only estimated segment kinematics that have been developed for OMC. Given segment kinematics, joint moment estimation is then based on inverse dynamics [215] or on estimates of muscle force (via optimization, not EMG-driven) with an underlying musculoskeletal model [393]. Karatsidis et al. (2016) implemented a version of the former using wearable sensor data only (17 IMUs) for estimating ground reaction forces and moments, but they did not report estimation of joint moment [394]. A version of the latter (driven by optimization-based muscle

force estimates) was implemented by Karatsidis et al. (2019) with wearable sensor data (17 IMUs placed on 17 different segments) wherein joint moment was estimated for 11 healthy males across three walking speeds [24]. Knee and ankle flexion moment were estimated with correlation coefficients of 0.86 and 0.96, respectively, and with RMSE of 0.9% BW*H (16.7% M_{range}) for the knee and 1.0% BW*H (10.1% M_{range}) for the ankle. These results are comparable to the current study, but with very different sensor array complexity (sensors placed on 17 segments compared to two in the proposed technique). A second approach, proposed by Dorschky et al. (2019), is based on optimal control of a musculoskeletal model wherein the states of the model were optimized so as to track measured sensor signals (seven IMUs on seven different segments) via trajectory optimization [25]. Knee and ankle flexion moment were estimated for 10 healthy males across three walking speeds with correlation coefficients of 0.81 and 0.95, respectively, and with RMSE of 1.5% BW*H (27.1% M_{range}) for the knee and 1.6% BW*H (14.4% M_{range}) for the ankle (although estimation was for the full gait cycle and not just the stance phase of gait). Thus, the proposed technique presents improvements in estimation of KFM and with comparable performance for estimating AFM compared to the trajectory optimization approach, but with reduced sensor array complexity (sensors placed on 7 segments compared to two in the proposed technique).

To the author's knowledge, there is only one study (a recent conference paper [390]) using a hybrid machine learning- and physics-based technique similar to the proposed approach. Their method used machine learning (Gaussian mixture models) to inform both the mapping from a subset of EMG to a full set as well as the MTU kinematics. Only KFM was estimated with RMSE equal to 26% M_{range} for slow walking, 30% M_{range} for normal walking, and 20% M_{range} for fast walking compared to 15% M_{range} in the current study (although their estimates were for the full gait cycle as opposed to just the stance phase of gait). The GP synergy functions of this study estimated excitations with superior or comparable performance compared to their Gaussian mixture model for VL (r = 0.82 vs. 0.96 in the current study), BFL (r = 0.71 vs. 0.95 in the current study), ST (r = 0.81 vs. 0.80 in the current study), and plantaflexor musculature (r = 0.24 for the gastrocnemii vs. 0.98 for SOL in the current study), but not for the RF (r = 0.89 vs. 0.73 in the current study).

6.8.3. Verification of the musculoskeletal model and EMG-driven simulation

It is important to compare the results of the EMG-driven simulation from the current study to previous work in order to verify the construct validity of the muscle model and of the OMC-Full analysis in general as an appropriate ground truth for validation. Falisse et al. (2016) estimated KFM with 12.84 Nm RMSE and with r^2 equal to 0.71 compared to 13.78 Nm RMSE and r^2 equal to 0.81 in the current study. Besier et al. (2009) also reported r^2 equal to 0.81 for estimating KFM and their model included the same muscles crossing the knee joint as in the current study. Likewise, Buchanan et al. (2005) estimated AFM with 7.1 Nm RMSE and r^2 equal to 0.94 compared to 13.63 Nm RMSE and r^2 equal to 0.94 in the current study. The 7.1 Nm RMSE is close to half the observed error in the current study and could be explained by the fact that the objective function of the MTU parameter global optimization included only AFM whereas the objective in the current study sought to minimize both KFM and AFM simultaneously. Meyer et al. (2017) also report slightly lesser MAE (4.22 – 6.43 Nm MAE for KFM and 5.93 – 8.48 Nm MAE for AFM) for a walking speed of 0.8 m/s compared to the current study 10.20 Nm MAE for KFM and 10.98 Nm MAE for AFM). This may be due in part to the difference in walking speed (0.8 m/s vs. 1.48 m/s in the current study) which would explain the differences in joint moment magnitudes between studies. For example, Meyer et al. (2017) observed peak knee extension moment well below 50 Nm compared to 65 Nm in the current study.

The simulated fiber length trajectories (Figure 35) are comparable to previously published data [373], [380]. For example, the BFL fiber length was monotone decreasing (constantly shortening) throughout stance which has been observed previously [380] and explains the null eccentric work observed for this muscle (Table 11). The muscle force trajectories (Figure 36) are also comparable to previous observations and appear to scale similarly as well [353]. For example, in the current study, the maximal muscle force throughout stance as a percentage of F_0 was 25% for VM and 23% for VL near the instant of peak knee extension moment, 35% for MG and 22% for LG near the instant of peak ankle plantarflexion moment, and was 32% for BFL and 27% for ST near the instant of foot contact; and these all appear to be within 1 SD of the data reported by Besier et al. (2009) [353]. Honert and Zelik (2016) [395] reported plantarflexor MTU push-off work (note that MTU work is the sum of the tendon work and muscle work) equal to 21.2 J (walking

at 1.25 m/s) which is comparable to the 26.2 J plantarflexor muscle work observed in the current study (computed as the sum of the concentric work of the SOL, MG, LG, and PL). Further, Bogey et al. (2010) [396] report peak power of the LG and SOL equal to 26 and 108 W, respectively, which is comparable to the 27 and 111 W computed for the OMC-Full analysis in the current study. However, the OMC-Full estimate of peak power for MG in the current study (82 W) was greater than their estimate (50 W).

6.8.4. On the results of the Bayesian optimization

This study also differs from previous work in the use of Bayesian optimization for tuning MTU parameters. Several activation dynamics [321], [377], [382], [383] and activation nonlinearity functions [209], [374], [384] have been proposed in previous research and it was not clear which model was most appropriate. The approach in previous work has been to choose a model for activation dynamics and activation-force nonlinearity and assign it to every muscle. The parameters of those models are then optimized via global optimization (e.g., simulated annealing [209], [397]), often in addition to the optimal fiber length and tendon slack length. However, empirical evidence suggests activation dynamics may be muscle specific and related to fiber type distribution [348], which informed the activation muscle groupings in the current study. Further uncertainty was introduced surrounding the activation dynamics by using GP synergy functions to estimate some of the excitation signals. Thus, the decision was made to include these functions as tunable (categorical) parameters in the global optimization for which Bayesian optimization is suitable. This is a novel development and motivates future work. For example, the results of the optimization suggest activation dynamics and the nonlinearity functions may be muscle specific as all models were ascribed to at least one muscle except for the N_1T_2 activation dynamics model. However, the extent to which the optimization of the functions $\dot{\alpha}$ and f_A is superior to an arbitrary choice of those functions was not tested and should be investigated further.

6.8.5. Limitations

This study has several limitations that should be considered when interpreting these results. This validation was only for one healthy female across three normal walking speeds. Future work should

investigate the estimation error of the proposed technique across a larger sample size, multiple walking conditions (e.g., multi-speed, multi-load), and in impaired populations for which the proposed technique would be deployed. It is important to note that the GP synergy functions were trained on multi-speed, treadmill walking data and preliminary results have suggested these models may be able to interpolate and extrapolate between and outside of gait speeds used for model training [398]. Further, while neural control may be different between overground and treadmill gait [399], the results of this study suggest GP synergy function models based on treadmill walking data can extrapolate for estimation in overground gait (Table 9). The EMG-driven simulation of muscle contraction requires excitations be normalized by the MVC value which may vary throughout the day due to changes in the properties of the skin-electrode interface [400]. Thus, compensatory methods must be developed that are robust to these variations. The knee was modeled as a non-translational joint with a single rotational DOF. More complex knee joint models with translational DOFs have been proposed, however, this translation has been shown to be small during walking gait [401]. Moreover, by assuming negligible translation of the knee joint center in the sagittal plane, the distance between the knee joint center and the ankle joint center should be a constant value. Indeed, in this work, the range of this distance during the full range of motion knee flexion and extension movements of the functional calibration trial was less than 1.00 cm (0.62 cm). Joint moments were estimated for the sagittal plane only and muscles with negligible flexion moment were ignored as in previous studies [324], [353]. Future work should consider additional musculature so as to enable the estimation of frontal plane joint moment and joint contact forces which are especially relevant in an orthopedic context [32], [120], [326]. Finally, while the muscle contraction dynamics and inverse kinematics analysis are generally applicable, the foot-ground contact and GP synergy function models assume walking gait. This is not a problem for remote monitoring as bouts of walking activity are identified first in the processing pipeline [70]. However, it may be desirable to characterize the musculoskeletal system dynamics for other tasks in which case other task-specific models must be developed. The potential to develop task-general and person-general GP synergy functions was suggested in their original development (Chapter 5) [162] and may enable more general deployment of the proposed technique.

6.9. Conclusion

This study presents a comprehensive validation of a novel, hybrid machine learning- and physics-based technique for simulating muscle contraction and characterizing joint dynamics during the stance phase of gait using only wearable sensor data. Gaussian process synergy functions were used to reduce the number of required EMG sensors for EMG-driven simulation. Data from two IMUs were used to inform the musculoskeletal kinematics via physics-based techniques and a simple foot-ground contact model. Importantly, the proposed technique requires sensor placement near the knee joint such that they could be seamlessly integrated into a knee brace for practical deployment. Peak knee extension moment was estimated to within 0.25% BW*H MAE and continuous knee and ankle flexion moment estimates were strongly correlated with ground truth inverse dynamics estimates. Joint moment estimation performance was comparable to gold standard EMG-driven techniques (i.e., marker-based motion capture, full set of EMG data) as well as other wearable sensor-based techniques with more complex sensor arrays. Finally, a novel Bayesian optimization approach was introduced that enables tuning MTU-specific functions related to the muscle contraction dynamics in addition to other continuous MTU parameters. These preliminary results motivate future development including validation on a larger sample size and across multiple walking conditions.

Chapter 7: Conclusion

7.1. Summary of developments

The aim of this project has been to lay the foundation for practical deployment of remote gait analysis techniques. The literature review in Chapter 1 demonstrated that despite a plethora of research dedicated to algorithm development for wearables-based human motion analysis, these techniques have not translated to practical deployment for remote monitoring. Several barriers to translation were discussed and in particular, methods that have been developed for estimation of the most clinically relevant biomechanics require complex sensor arrays with multiple sensors placed on multiple body segments. These complex sensor arrays discourage use and thus, the primary aim of this research was to develop algorithms that are capable of estimating clinically relevant biomechanics but with a reduced sensor array.

Chapter 2 described the validation of an algorithm for detecting gait events using a single, thigh-worn accelerometer. The major contributions from that work were a slight modification to the algorithm proposed by Aminian et al. (1999) [172] that enabled algorithm parameters to adapt with varying gait speed, the source code was made publicly available, and an analysis of the error in estimating the actual gait events (i.e., foot contact and foot off) rather than just temporal descriptors of gait quantified from those events (e.g., stride and stance time). The latter is an important distinction as it is often neglected in gait event detection validation studies but is important for techniques that use gait events to apply simplifying assumptions (e.g., the foot-ground contact model in Chapter 6).

Chapter 3 described a general analytical framework for remote biomechanical analysis: (1) activity identification, (2) event detection, and (3) analysis. The major contribution from that work was an open-source platform demonstrating how this approach could be applied for monitoring patients following knee surgery. To that end, a novel asymmetry measure was proposed that considered temporal descriptors of gait (e.g., duty factor), phase-specific mean muscle excitation, and between-leg similarity of like time-series (i.e., acceleration and excitation). This asymmetry measure was more sensitive to recovery time than was step count or time spent walking and better distinguished between patients at different stages of recovery.

Following the development of the general analytical framework in Chapter 3, the remaining chapters focused on how to further improve step (3) of that process (biomechanical analysis), namely, to estimate other clinically relevant biomechanical variables that augment the aforementioned asymmetry analysis. Specifically, the aim was to characterize joint moment and muscle contraction dynamics with the caveat of using a reduced sensor array.

Chapter 4 reviewed machine learning techniques that have been proposed for estimating biomechanical time-series with a reduced number of sensors. The major findings from that work were that EMG data were the most popular inputs, models for estimating muscle contraction dynamics were non-existent, most algorithms are not open-source and not validated on impaired populations, non-parametric regression may be better suited for small datasets, and incorporating domain knowledge into the structure of the model may improve performance.

The latter finding concerning incorporating domain knowledge motivated the pursuit of a hybrid technique combining physics and probabilistic models. In this approach, machine learning would be used only where the physics are least well understood or insufficiently informed. For the estimation of human joint dynamics, this approach may be implemented by using a probabilistic model to estimate a complete set of muscle excitations from a measured subset (reduced sensor array) which could then drive the muscle contraction dynamics using inertial sensor-based estimates of the system kinematics. This hybrid technique was developed and validated in Chapter 6 where the probabilistic model describing the synergistic relationship between muscles was developed and validated in Chapter 5.

The major contributions of the work described in Chapter 5 were the development of a Gaussian process (GP) model of muscle synergy functions, validation of the model for estimating unmeasured muscle excitations and activations from a measured subset during gait, a comparison to an NNMF-based technique for estimating excitations, and a comprehensive analysis investigating the effect of different modeling choices (e.g., input/output muscles, different covariance functions) on estimation performance. Moreover, an open-source platform was published that streamlines the training of GP synergy function models.

Chapter 6 describes the validation of a hybrid technique for estimating joint moment and simulating muscle contraction dynamics. The major contribution of that work was the demonstration of the first wearables-only EMG-driven simulation of muscle contraction dynamics where machine learning was used only in the GP synergy model and that requires only four EMG and two IMU sensors located near the knee joint. Further, a novel Bayesian optimization approach was developed that enables optimizing categorical muscle-tendon unit parameters related to the muscle contraction dynamics (i.e., functions describing the activation dynamics and nonlinear activation-force relationship). Previous studies only optimize continuous, scalar parameters. Other contributions include a detailed analysis of the estimation performance of the approach including the separate effects of the IMU-based inverse-kinematics and the GP synergy models on the estimation error as well as for estimating different biomechancial variables: joint angle, muscle-tendon unit length, muscle excitation and activation, muscle fiber length and velocity, muscle force, muscle power, cumulative concentric and eccentric muscle work, as well as individual and net muscle moment.

7.2. Implications for future work

This work lays a foundation for the computational methods that might enable longitudinal tracking of joint and tissue loading. These techniques must undergo further validation across a larger sample size and in impaired populations for which they would be deployed. The GP muscle synergy function models present an exciting new research area that may have implications for probabilistic theories of motor control and that may enable novel clinical insight currently absent in remote patient monitoring. A line of inquiry of particular interest concerns the person- and task-generalizability of the model. If muscle synergies generalize across tasks and these phenomena are manifest in a broad enough range of activities, then it may be that given an equally broad enough training set, the GP synergy function models could capture those generalizations enabling estimation for tasks not represented in the training set. These should be explored in future research as well as sub-task generalization (e.g., across multiple gait speeds and inclines).

The GP synergy models require EMG data be normalized by the excitation value during a maximal voluntary contraction. This is further complicated in remote environments as the normalization constant obtained at one instant during a day may be different than if observed at another time in the day since the properties of the skin-electrode interface varies. One potential solution may be to train the GP synergy function models using input data that are normalized by the average value during the activity of interest (e.g., gait) and that estimate output muscle excitations that are normalized by the maximal voluntary contraction. This may also be necessary for exploring person-general models or for application on impaired persons who cannot perform maximal voluntary contractions.

The largest source of error in the hybrid technique proposed in Chapter 6 appears to be related to estimating the foot kinematics. No sensor was placed on the foot and thus foot kinematics were informed by a simple foot-ground contact model. A future approach may be to estimate the foot kinematics via forward-dynamics simulation (since the net ankle muscle moment can be characterized) wherein the foot segment generalized coordinates would augment the fiber length and muscle activation states in the system dynamics formulation. This is sufficient for estimation during the swing phase of gait as the foot distal contact forces are negligible. However, during stance, they are not negligible and thus the ground reaction force, ground reaction moment, and center of pressure would need to be modeled in this approach.

Importantly, the hybrid technique in Chapter 6 required only four EMG and two IMUs that were located very near the knee joint. Thus, these sensors could seamlessly be integrated into a knee brace as an unobtrusive and convenient system for monitoring patients who may be prescribed such a device anyway (e.g., following surgery) and for whom these techniques would be especially relevant. To this end, work has begun to develop a prototype (Figure 42). This brace is being developed in collaboration with Dr. Ryan McGinnis and five senior engineering students at the University of Vermont as a part of their senior experience in engineering design: Nicole Donahue, James Doherty, Cole Garabed, Curtis Ianni, and Tori Weissman.

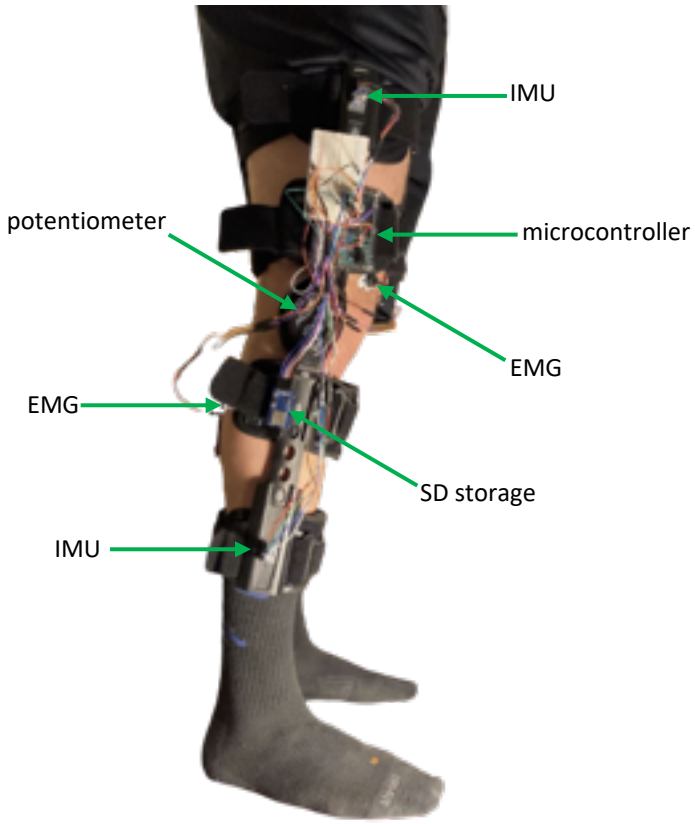

Figure 42: Instrumented knee brace prototype. All included sensors are sufficient to implement the hybrid estimation technique described in Chapter 6.

References

[1] T. Vos *et al.*, "Global burden of 369 diseases and injuries in 204 countries and territories, 1990–2019: a systematic analysis for the Global Burden of Disease Study 2019," *The Lancet*, vol. 396, no. 10258, pp. 1204–1222, Oct. 2020, doi: 10.1016/S0140-6736(20)30925-9.

[2] S. L. James *et al.*, "Global, regional, and national incidence, prevalence, and years lived with disability for 354 diseases and injuries for 195 countries and territories, 1990–2017: a systematic analysis for the Global Burden of Disease Study 2017," *The Lancet*, vol. 392, no. 10159, pp. 1789–1858, Nov. 2018, doi: 10.1016/S0140-6736(18)32279-7.

[3] M. Cross *et al.*, "The global burden of hip and knee osteoarthritis: estimates from the Global Burden of Disease 2010 study," *Ann Rheum Dis*, vol. 73, no. 7, pp. 1323–1330, Jul. 2014, doi: 10.1136/annrheumdis-2013-204763.

[4] K. R. Fingar and A. J. Weiss, "Most Frequent Operating Room Procedures Performed in U.S. Hospitals, 2003–2012," p. 15.

[5] J. L. Dieleman *et al.*, "US Health Care Spending by Payer and Health Condition, 1996-2016," *JAMA*, vol. 323, no. 9, p. 863, Mar. 2020, doi: 10.1001/jama.2020.0734.

[6] C. J. L. Murray *et al.*, "Five insights from the Global Burden of Disease Study 2019," *The Lancet*, vol. 396, no. 10258, pp. 1135–1159, Oct. 2020, doi: 10.1016/S0140-6736(20)31404-5.

[7] A. J. Espay *et al.*, "Technology in Parkinson's disease: Challenges and opportunities: Technology in PD," *Movement Disorders*, vol. 31, no. 9, pp. 1272–1282, Sep. 2016, doi: 10.1002/mds.26642.

[8] M. L. Frechette, B. M. Meyer, L. J. Tulipani, R. D. Gurchiek, R. S. McGinnis, and J. J. Sosnoff, "Next Steps in Wearable Technology and Community Ambulation in Multiple Sclerosis," *Curr Neurol Neurosci Rep*, vol. 19, no. 10, p. 80, Sep. 2019, doi: 10.1007/s11910-019-0997-9.

[9] E. W. McGinnis *et al.*, "Movements indicate threat response phases in children at-risk for anxiety," *IEEE J Biomed Health Inform*, vol. 21, no. 5, pp. 1460–1465, Sep. 2017, doi: 10.1109/JBHI.2016.2603159.

[10] A. Coravos, S. Khozin, and K. D. Mandl, "Developing and adopting safe and effective digital biomarkers to improve patient outcomes," *npj Digital Medicine*, vol. 2, no. 1, Dec. 2019, doi: 10.1038/s41746-019-0090-4.

[11] T. Loncar-Turukalo, E. Zdravevski, J. Machado da Silva, I. Chouvarda, and V. Trajkovik, "Literature on Wearable Technology for Connected Health: Scoping Review of Research Trends, Advances, and Barriers," *J Med Internet Res*, vol. 21, no. 9, p. e14017, Sep. 2019, doi: 10.2196/14017.

[12] R. D. Gurchiek, N. Cheney, and R. S. McGinnis, "Estimating Biomechanical Time-Series with Wearable Sensors: A Systematic Review of Machine Learning Techniques," *Sensors*, vol. 19, no. 23, p. 5227, Jan. 2019, doi: 10.3390/s19235227.

[13] D. Kobsar *et al.*, "Validity and reliability of wearable inertial sensors in healthy adult walking: a systematic review and meta-analysis," *J NeuroEngineering Rehabil*, vol. 17, no. 1, p. 62, Dec. 2020, doi: 10.1186/s12984-020-00685-3.

[14] A. Ancillao, S. Tedesco, J. Barton, and B. O'Flynn, "Indirect Measurement of Ground Reaction Forces and Moments by Means of Wearable Inertial Sensors: A Systematic Review," *Sensors*, vol. 18, no. 8, p. 2564, Aug. 2018, doi: 10.3390/s18082564.

[15] I. Weygers, M. Kok, M. Konings, H. Hallez, H. De Vroey, and K. Claeys, "Inertial Sensor-Based Lower Limb Joint Kinematics: A Methodological Systematic Review," *Sensors*, vol. 20, no. 3, p. 673, Jan. 2020, doi: 10.3390/s20030673.

[16] P. Picerno, "25 years of lower limb joint kinematics by using inertial and magnetic sensors: A review of methodological approaches," *Gait & Posture*, vol. 51, pp. 239–246, Jan. 2017, doi: 10.1016/j.gaitpost.2016.11.008.

[17] K. Ben Mansour, N. Rezzoug, and P. Gorce, "Analysis of several methods and inertial sensors locations to assess gait parameters in able-bodied subjects," *Gait & Posture*, vol. 42, no. 4, pp. 409–414, Oct. 2015, doi: 10.1016/j.gaitpost.2015.05.020.

[18] R. D. Gurchiek, R. S. McGinnis, A. R. Needle, J. M. McBride, and H. van Werkhoven, “An adaptive filtering algorithm to estimate sprint velocity using a single inertial sensor,” *Sports Engineering*, vol. 21, no. 4, pp. 389–399, Aug. 2018, doi: 10.1007/s12283-018-0285-y.
[19] R. D. Gurchiek *et al.*, “Sprint Assessment Using Machine Learning and a Wearable Accelerometer,” *J Appl Biomech*, pp. 1–6, Feb. 2019, doi: 10.1123/jab.2018-0107.
[20] R. S. McGinnis *et al.*, “A machine learning approach for gait speed estimation using skin-mounted wearable sensors: From healthy controls to individuals with multiple sclerosis,” *PLOS ONE*, vol. 12, no. 6, pp. 1–16, Jun. 2017, doi: 10.1371/journal.pone.0178366.
[21] I. Weygers *et al.*, “Drift-Free Inertial Sensor-Based Joint Kinematics for Long-Term Arbitrary Movements,” *IEEE Sensors J.*, vol. 20, no. 14, pp. 7969–7979, Jul. 2020, doi: 10.1109/JSEN.2020.2982459.
[22] R. V. Vitali, R. S. McGinnis, and N. C. Perkins, “Robust Error-State Kalman Filter for Estimating IMU Orientation,” *IEEE Sensors*, p. 9.
[23] L. Adamowicz, R. Gurchiek, J. Ferri, A. Ursiny, N. Fiorentino, and R. McGinnis, “Validation of Novel Relative Orientation and Inertial Sensor-to-Segment Alignment Algorithms for Estimating 3D Hip Joint Angles,” *Sensors*, vol. 19, no. 23, p. 5143, Nov. 2019, doi: 10.3390/s19235143.
[24] A. Karatsidis *et al.*, “Musculoskeletal model-based inverse dynamic analysis under ambulatory conditions using inertial motion capture,” *Medical Engineering & Physics*, vol. 65, pp. 68–77, Mar. 2019, doi: 10.1016/j.medengphy.2018.12.021.
[25] E. Dorschky, M. Nitschke, A.-K. Seifer, A. J. van den Bogert, and B. M. Eskofier, “Estimation of gait kinematics and kinetics from inertial sensor data using optimal control of musculoskeletal models,” *Journal of Biomechanics*, vol. 95, p. 109278, Oct. 2019, doi: 10.1016/j.jbiomech.2019.07.022.
[26] R. D. Gurchiek, R. S. McGinnis, A. R. Needle, J. M. McBride, and H. van Werkhoven, “The use of a single inertial sensor to estimate 3-dimensional ground reaction force during accelerative running tasks,” *Journal of Biomechanics*, vol. 61, pp. 263–268, Aug. 2017, doi: 10.1016/j.jbiomech.2017.07.035.
[27] R. S. McGinnis, J. Hough, and N. C. Perkins, “Accuracy of Wearable Sensors for Estimating Joint Reactions,” *J. Comput. Nonlinear Dynam*, vol. 12, no. 4, pp. 041010-041010–10, Jan. 2017, doi: 10.1115/1.4035667.
[28] K. M. Steele, A. Rozumalski, and M. H. Schwartz, “Muscle synergies and complexity of neuromuscular control during gait in cerebral palsy,” *Dev Med Child Neurol*, vol. 57, no. 12, pp. 1176–1182, Dec. 2015, doi: 10.1111/dmcn.12826.
[29] R. D. Gurchiek *et al.*, “Remote Gait Analysis Using Wearable Sensors Detects Asymmetric Gait Patterns in Patients Recovering from ACL Reconstruction,” in *2019 IEEE 16th International Conference on Wearable and Implantable Body Sensor Networks (BSN)*, Chicago, IL, USA, May 2019, pp. 1–4, doi: 10.1109/BSN.2019.8771038.
[30] C. A. Emery *et al.*, “Establishing outcome measures in early knee osteoarthritis,” *Nat Rev Rheumatol*, vol. 15, no. 7, pp. 438–448, Jul. 2019, doi: 10.1038/s41584-019-0237-3.
[31] T. P. Andriacchi and A. Mündermann, “The role of ambulatory mechanics in the initiation and progression of knee osteoarthritis:,” *Current Opinion in Rheumatology*, vol. 18, no. 5, pp. 514–518, Sep. 2006, doi: 10.1097/01.bor.0000240365.16842.4e.
[32] T. P. Andriacchi, A. Mündermann, R. L. Smith, E. J. Alexander, C. O. Dyrby, and S. Koo, “A Framework for the in Vivo Pathomechanics of Osteoarthritis at the Knee,” *Annals of Biomedical Engineering*, vol. 32, no. 3, pp. 447–457, Mar. 2004, doi: 10.1023/B:ABME.0000017541.82498.37.
[33] N. Takayanagi *et al.*, “Relationship between Daily and In-laboratory Gait Speed among Healthy Community-dwelling Older Adults,” *Sci Rep*, vol. 9, no. 1, p. 3496, Dec. 2019, doi: 10.1038/s41598-019-39695-0.
[34] K. C. Foucher, L. E. Thorp, D. Orozco, M. Hildebrand, and M. A. Wimmer, “Differences in Preferred Walking Speeds in a Gait Laboratory Compared With the Real World After Total Hip Replacement,” *Archives of Physical Medicine and Rehabilitation*, vol. 91, no. 9, pp. 1390–1395, Sep. 2010, doi: 10.1016/j.apmr.2010.06.015.

[35] M. D. Czech *et al.*, "Age and environment-related differences in gait in healthy adults using wearables," *npj Digital Medicine*, vol. 3, no. 1, Art. no. 1, Sep. 2020, doi: 10.1038/s41746-020-00334-y.
[36] J. Sanchez-Adams, H. A. Leddy, A. L. McNulty, C. J. O'Conor, and F. Guilak, "The Mechanobiology of Articular Cartilage: Bearing the Burden of Osteoarthritis," *Curr Rheumatol Rep*, vol. 16, no. 10, p. 451, Oct. 2014, doi: 10.1007/s11926-014-0451-6.
[37] M. A. Hunt, J. M. Charlton, and J.-F. Esculier, "Osteoarthritis year in review 2019: mechanics," *Osteoarthritis and Cartilage*, vol. 28, no. 3, pp. 267–274, Mar. 2020, doi: 10.1016/j.joca.2019.12.003.
[38] S. N. Edd, P. Omoumi, T. P. Andriacchi, B. M. Jolles, and J. Favre, "Modeling knee osteoarthritis pathophysiology using an integrated joint system (IJS): a systematic review of relationships among cartilage thickness, gait mechanics, and subchondral bone mineral density," *Osteoarthritis and Cartilage*, vol. 26, no. 11, pp. 1425–1437, Nov. 2018, doi: 10.1016/j.joca.2018.06.017.
[39] H. Khajehsaeid and Z. Abdollahpour, "Progressive deformation-induced degradation of knee articular cartilage and osteoarthritis," *Journal of Biomechanics*, vol. 111, p. 109995, Oct. 2020, doi: 10.1016/j.jbiomech.2020.109995.
[40] A. Jamshidi, J.-P. Pelletier, and J. Martel-Pelletier, "Machine-learning-based patient-specific prediction models for knee osteoarthritis," *Nat Rev Rheumatol*, vol. 15, no. 1, pp. 49–60, 2019, doi: 10.1038/s41584-018-0130-5.
[41] M. J. Long, E. Papi, L. D. Duffell, and A. H. McGregor, "Predicting knee osteoarthritis risk in injured populations," *Clin Biomech*, vol. 47, pp. 87–95, Aug. 2017, doi: 10.1016/j.clinbiomech.2017.06.001.
[42] L.-J. Wang, N. Zeng, Z.-P. Yan, J.-T. Li, and G.-X. Ni, "Post-traumatic osteoarthritis following ACL injury," *Arthritis Res Ther*, vol. 22, no. 1, p. 57, Dec. 2020, doi: 10.1186/s13075-020-02156-5.
[43] E. Wellsandt, E. S. Gardinier, K. Manal, M. J. Axe, T. S. Buchanan, and L. Snyder-Mackler, "Decreased Knee Joint Loading Associated With Early Knee Osteoarthritis After Anterior Cruciate Ligament Injury," *Am J Sports Med*, vol. 44, no. 1, pp. 143–151, Jan. 2016, doi: 10.1177/0363546515608475.
[44] B. Pietrosimone *et al.*, "Walking gait asymmetries 6 months following anterior cruciate ligament reconstruction predict 12-month patient-reported outcomes," *J. Orthop. Res.*, vol. 36, no. 11, pp. 2932–2940, Nov. 2018, doi: 10.1002/jor.24056.
[45] M. J. Decker, M. R. Torry, T. J. Noonan, W. I. Sterett, and J. R. Steadman, "Gait retraining after anterior cruciate ligament reconstruction," *Arch Phys Med Rehabil*, vol. 85, no. 5, pp. 848–856, May 2004.
[46] B. J. Fregly, J. A. Reinbolt, K. L. Rooney, K. H. Mitchell, and T. L. Chmielewski, "Design of patient-specific gait modifications for knee osteoarthritis rehabilitation," *IEEE Trans. Biomed. Eng.*, vol. 54, no. 9, pp. 1687–1695, Sep. 2007, doi: 10.1109/TBME.2007.891934.
[47] T. Kernozek, M. Torry, K. Shelburne, C. J. Durall, and J. Willson, "From the Gait Laboratory to the Rehabilitation Clinic: Translation of Motion Analysis and Modeling Data to Interventions That Impact Anterior Cruciate Ligament Loads in Gait and Drop Landing," *Critical Reviews in Biomedical Engineering*, vol. 41, no. 3, pp. 243–258, 2013, doi: 10.1615/CritRevBiomedEng.2014010676.
[48] R. R. Bannuru *et al.*, "OARSI guidelines for the non-surgical management of knee, hip, and polyarticular osteoarthritis," *Osteoarthritis and Cartilage*, vol. 27, no. 11, pp. 1578–1589, Nov. 2019, doi: 10.1016/j.joca.2019.06.011.
[49] P. B. Shull, "Toe-in gait reduces the first peak knee adduction moment in patients with medial compartment knee osteoarthritis," *J Biomech*, vol. 46, no. 1, p. 7, 2013.
[50] J. C. Erhart-Hledik, J. Favre, and T. P. Andriacchi, "New insight in the relationship between regional patterns of knee cartilage thickness, osteoarthritis disease severity, and gait mechanics," *Journal of Biomechanics*, vol. 48, no. 14, pp. 3868–3875, Nov. 2015, doi: 10.1016/j.jbiomech.2015.09.033.

[51] E. F. Chehab, J. Favre, J. C. Erhart-Hledik, and T. P. Andriacchi, “Baseline knee adduction and flexion moments during walking are both associated with 5 year cartilage changes in patients with medial knee osteoarthritis,” *Osteoarthritis and Cartilage*, vol. 22, no. 11, pp. 1833–1839, Nov. 2014, doi: 10.1016/j.joca.2014.08.009.

[52] B. M. Meyer *et al.*, “Wearables and Deep Learning Classify Fall Risk from Gait in Multiple Sclerosis,” *IEEE Journal of Biomedical and Health Informatics*, pp. 1–1, 2020, doi: 10.1109/JBHI.2020.3025049.

[53] E. Halilaj, T. J. Hastie, G. E. Gold, and S. L. Delp, “Physical activity is associated with changes in knee cartilage microstructure,” *Osteoarthritis and Cartilage*, vol. 26, no. 6, pp. 770–774, Jun. 2018, doi: 10.1016/j.joca.2018.03.009.

[54] J. F. Hafer and R. F. Zernicke, “Propulsive joint powers track with sensor-derived angular velocity: A potential tool for lab-less gait retraining,” *Journal of Biomechanics*, vol. 106, p. 109821, Jun. 2020, doi: 10.1016/j.jbiomech.2020.109821.

[55] K. A. Pratt and S. M. Sigward, “Inertial Sensor Angular Velocities Reflect Dynamic Knee Loading during Single Limb Loading in Individuals Following Anterior Cruciate Ligament Reconstruction,” *Sensors*, vol. 18, no. 10, p. 3460, Oct. 2018, doi: 10.3390/s18103460.

[56] S. Jung *et al.*, “The Use of Inertial Measurement Units for the Study of Free Living Environment Activity Assessment: A Literature Review,” *Sensors*, vol. 20, no. 19, p. 5625, Oct. 2020, doi: 10.3390/s20195625.

[57] C.-C. Yang and Y.-L. Hsu, “A Review of Accelerometry-Based Wearable Motion Detectors for Physical Activity Monitoring,” *Sensors*, vol. 10, no. 8, pp. 7772–7788, Aug. 2010, doi: 10.3390/s100807772.

[58] I. T. G. de Oliveira Gondim, C. de C. B. de Souza, M. A. B. Rodrigues, I. M. Azevedo, M. das G. W. de Sales Coriolano, and O. G. Lins, “Portable accelerometers for the evaluation of spatio-temporal gait parameters in people with Parkinson’s disease: an integrative review,” *Archives of Gerontology and Geriatrics*, vol. 90, p. 104097, Sep. 2020, doi: 10.1016/j.archger.2020.104097.

[59] J. B. Arnold, J. L. Walters, and K. E. Ferrar, “Does Physical Activity Increase After Total Hip or Knee Arthroplasty for Osteoarthritis? A Systematic Review,” *J Orthop Sports Phys Ther*, vol. 46, no. 6, pp. 431–442, Jun. 2016, doi: 10.2519/jospt.2016.6449.

[60] T. M. Withers, S. Lister, C. Sackley, A. Clark, and T. O. Smith, “Is there a difference in physical activity levels in patients before and up to one year after unilateral total hip replacement? A systematic review and meta-analysis,” *Clin Rehabil*, vol. 31, no. 5, pp. 639–650, May 2017, doi: 10.1177/0269215516673884.

[61] W. L. Johns *et al.*, “Return to Sports and Activity After Total Ankle Arthroplasty and Arthrodesis: A Systematic Review,” *Foot Ankle Int.*, vol. 41, no. 8, pp. 916–929, Aug. 2020, doi: 10.1177/1071100720927706.

[62] S. R. Small, G. S. Bullock, S. Khalid, K. Barker, M. Trivella, and A. J. Price, “Current clinical utilisation of wearable motion sensors for the assessment of outcome following knee arthroplasty: a scoping review,” *BMJ Open*, vol. 9, no. 12, p. e033832, Dec. 2019, doi: 10.1136/bmjopen-2019-033832.

[63] P. M. Dall, P. R. W. McCrorie, M. H. Granat, and B. W. Stansfield, “Step accumulation per minute epoch is not the same as cadence for free-living adults,” *Med Sci Sports Exerc*, vol. 45, no. 10, pp. 1995–2001, Oct. 2013, doi: 10.1249/MSS.0b013e3182955780.

[64] J. Jelsma, M. G. M. Schotanus, I. T. A. F. Buil, S. M. J. van Kuijk, I. C. Heyligers, and B. Grimm, “Patients with hip resurfacing arthroplasty are not physically more active than those with a stemmed total hip,” *Acta Orthop*, pp. 1–5, Jun. 2020, doi: 10.1080/17453674.2020.1771652.

[65] J. Jelsma, M. G. M. Schotanus, S. M. J. van Kuijk, I. T. A. F. Buil, I. C. Heyligers, and B. Grimm, “Quality, but not quantity of physical activity is associated with metal ion concentrations in unilateral hip resurfacing,” *J. Orthop. Res.*, vol. 38, no. 10, pp. 2206–2212, Oct. 2020, doi: 10.1002/jor.24637.

[66] M. Lipperts, S. van Laarhoven, R. Senden, I. Heyligers, and B. Grimm, “Clinical validation of a body-fixed 3D accelerometer and algorithm for activity monitoring in orthopaedic patients,” *Journal of Orthopaedic Translation*, vol. 11, pp. 19–29, Oct. 2017, doi: 10.1016/j.jot.2017.02.003.

[67] S. Saporito *et al.*, “Remote timed up and go evaluation from activities of daily living reveals changing mobility after surgery,” *Physiol Meas*, vol. 40, no. 3, p. 035004, 03 2019, doi: 10.1088/1361-6579/ab0d3e.

[68] L. Verlaan *et al.*, “Accelerometer-based Physical Activity Monitoring in Patients with Knee Osteoarthritis: Objective and Ambulatory Assessment of Actual Physical Activity During Daily Life Circumstances,” *Open Biomed Eng J*, vol. 9, pp. 157–163, 2015, doi: 10.2174/1874120701509010157.

[69] M. G. M. Schotanus, Y. F. L. Bemelmans, B. Grimm, I. C. Heyligers, and N. P. Kort, “Physical activity after outpatient surgery and enhanced recovery for total knee arthroplasty,” *Knee Surg Sports Traumatol Arthrosc*, vol. 25, no. 11, pp. 3366–3371, Nov. 2017, doi: 10.1007/s00167-016-4256-1.

[70] R. D. Gurchiek *et al.*, “Open-Source Remote Gait Analysis: A Post-Surgery Patient Monitoring Application,” *Sci Rep*, vol. 9, no. 1, p. 17966, Dec. 2019, doi: 10.1038/s41598-019-54399-1.

[71] M. H. Hjorth, I. Mechlenburg, K. Soballe, L. Roemer, and M. Stilling, “The correlation between activity level, serum-ion concentrations and pseudotumours in patients with metal-on-metal hip articulations and metal-on-polyethylene total hip articulations,” *Journal of Orthopaedic Translation*, vol. 18, pp. 74–83, Jul. 2019, doi: 10.1016/j.jot.2018.11.001.

[72] J. Vangeneugden *et al.*, “Signatures of knee osteoarthritis in women in the temporal and fractal dynamics of human gait,” *Clin Biomech (Bristol, Avon)*, vol. 76, p. 105016, Jun. 2020, doi: 10.1016/j.clinbiomech.2020.105016.

[73] M. M. Vissers, J. B. J. Bussmann, I. B. de Groot, J. a. N. Verhaar, and M. Reijman, “Walking and chair rising performed in the daily life situation before and after total hip arthroplasty,” *Osteoarthr. Cartil.*, vol. 19, no. 9, pp. 1102–1107, Sep. 2011, doi: 10.1016/j.joca.2011.06.004.

[74] M. M. Vissers, J. B. Bussmann, I. B. de Groot, J. A. N. Verhaar, and M. Reijman, “Physical functioning four years after total hip and knee arthroplasty,” *Gait & Posture*, vol. 38, no. 2, pp. 310–315, Jun. 2013, doi: 10.1016/j.gaitpost.2012.12.007.

[75] R. M. Chapman, W. E. Moschetti, and D. W. Van Citters, “Stance and swing phase knee flexion recover at different rates following total knee arthroplasty: An inertial measurement unit study,” *Journal of Biomechanics*, vol. 84, pp. 129–137, 2019, doi: 10.1016/j.jbiomech.2018.12.027.

[76] JA Oldham and T. Howe, “Electromyographic assessment of daily quadriceps activity in young subjects and elderly osteoarthritic subjects,” *Clinical Effectiveness in Nursing*, vol. 2, pp. 41–43, 1998.

[77] D. J. Walker, “Measured ambulation and self-reported health status following total joint replacement for the osteoarthritic knee,” *Rheumatology*, vol. 41, no. 7, pp. 755–758, Jul. 2002, doi: 10.1093/rheumatology/41.7.755.

[78] L. A. Talbot, J. M. Gaines, T. N. Huynh, and E. J. Metter, “A home-based pedometer-driven walking program to increase physical activity in older adults with osteoarthritis of the knee: a preliminary study,” *J Am Geriatr Soc*, vol. 51, no. 3, pp. 387–392, Mar. 2003, doi: 10.1046/j.1532-5415.2003.51113.x.

[79] P. D. Franklin, J. McLaughlin, C. B. Boisvert, W. Li, and D. C. Ayers, “Pilot Study of Methods to Document Quantity and Variation of Independent Patient Exercise and Activity After Total Knee Arthroplasty,” *The Journal of Arthroplasty*, vol. 21, no. 6, pp. 157–163, Sep. 2006, doi: 10.1016/j.arth.2006.05.007.

[80] M. Brandes, R. Schomaker, G. Möllenhoff, and D. Rosenbaum, “Quantity versus quality of gait and quality of life in patients with osteoarthritis,” *Gait Posture*, vol. 28, no. 1, pp. 74–79, Jul. 2008, doi: 10.1016/j.gaitpost.2007.10.004.

[81] I. B. de Groot, H. J. Bussmann, H. J. Stam, and J. A. Verhaar, “Small Increase of Actual Physical Activity 6 Months After Total Hip or Knee Arthroplasty,” *Clin Orthop Relat Res*, vol. 466, no. 9, pp. 2201–2208, Sep. 2008, doi: 10.1007/s11999-008-0315-3.

[82] T. E. Howe and D. Rafferty, “Quadriceps activity and physical activity profiles over long durations in patients with osteoarthritis of the knee and controls,” *J Electromyogr Kinesiol*, vol. 19, no. 2, pp. e78-83, Apr. 2009, doi: 10.1016/j.jelekin.2007.10.005.

[83] T. L. Schulte *et al.*, “Step activity monitoring in lumbar stenosis patients undergoing decompressive surgery,” *Eur Spine J*, vol. 19, no. 11, pp. 1855–1864, Nov. 2010, doi: 10.1007/s00586-010-1324-y.

[84] S. Tsuji, T. Tomita, M. Fujii, R. S. Laskin, H. Yoshikawa, and K. Sugamoto, “Is Minimally Invasive Surgery–Total Knee Arthroplasty Truly Less Invasive Than Standard Total Knee Arthroplasty?,” *The Journal of Arthroplasty*, vol. 25, no. 6, pp. 970–976, Sep. 2010, doi: 10.1016/j.arth.2009.06.016.

[85] M. M. Vissers, I. B. de Groot, M. Reijman, J. B. Bussmann, H. J. Stam, and J. A. Verhaar, “Functional capacity and actual daily activity do not contribute to patient satisfaction after total knee arthroplasty,” *BMC Musculoskelet Disord*, vol. 11, p. 121, Jun. 2010, doi: 10.1186/1471-2474-11-121.

[86] C. C. Winter *et al.*, “Walking ability during daily life in patients with osteoarthritis of the knee or the hip and lumbar spinal stenosis: a cross sectional study,” *BMC Musculoskelet Disord*, vol. 11, p. 233, Oct. 2010, doi: 10.1186/1471-2474-11-233.

[87] M. Assal, A. C. Ahmad, A. Lacraz, D. S. Courvoisier, R. Stern, and X. Crevoisier, “Step activity monitoring to assess ambulation before and after total ankle arthroplasty,” *Foot and Ankle Surgery*, vol. 17, no. 3, pp. 136–139, Sep. 2011, doi: 10.1016/j.fas.2010.03.006.

[88] M. Brandes, M. Ringling, C. Winter, A. Hillmann, and D. Rosenbaum, “Changes in physical activity and health-related quality of life during the first year after total knee arthroplasty,” *Arthritis Care Res*, vol. 63, no. 3, pp. 328–334, 2011, doi: 10.1002/acr.20384.

[89] D. A. Hayes, M. C. Watts, L. J. Anderson, and W. R. Walsh, “Knee arthroplasty: a cross-sectional study assessing energy expenditure and activity: TKA: assessing energy expenditure & activity,” *ANZ Journal of Surgery*, vol. 81, no. 5, pp. 371–374, May 2011, doi: 10.1111/j.1445-2197.2010.05570.x.

[90] S. M. Robbins, T. B. Birmingham, J. P. Callaghan, G. R. Jones, B. M. Chesworth, and M. R. Maly, “Association of pain with frequency and magnitude of knee loading in knee osteoarthritis,” *Arthritis Care & Research*, vol. 63, no. 7, pp. 991–997, 2011, doi: https://doi.org/10.1002/acr.20476.

[91] S. M. Tonelli, B. A. Rakel, N. A. Cooper, W. L. Angstom, and K. A. Sluka, “Women with knee osteoarthritis have more pain and poorer function than men, but similar physical activity prior to total knee replacement,” *Biol Sex Differ*, vol. 2, p. 12, Nov. 2011, doi: 10.1186/2042-6410-2-12.

[92] A. Holsgaard-Larsen and E. M. Roos, “Objectively measured physical activity in patients with end stage knee or hip osteoarthritis,” *Eur J Phys Rehabil Med*, vol. 48, no. 4, pp. 577–585, Dec. 2012.

[93] E. Chmelo, B. Nicklas, C. Davis, G. D. Miller, C. Legault, and S. Messier, “Physical Activity and Physical Function in Older Adults With Knee Osteoarthritis,” *Journal of Physical Activity and Health*, vol. 10, no. 6, pp. 777–783, Aug. 2013, doi: 10.1123/jpah.10.6.777.

[94] D. A. Doré *et al.*, “The association between objectively measured physical activity and knee structural change using MRI,” *Ann. Rheum. Dis.*, vol. 72, no. 7, pp. 1170–1175, Jul. 2013, doi: 10.1136/annrheumdis-2012-201691.

[95] K. Fujita, K. Makimoto, R. Tanaka, M. Mawatari, and T. Hotokebuchi, “Prospective study of physical activity and quality of life in Japanese women undergoing total hip arthroplasty,” *Journal of Orthopaedic Science*, vol. 18, no. 1, pp. 45–53, Jan. 2013, doi: 10.1007/s00776-012-0318-5.

[96] B. A. Lin, P. Thomas, F. Spiezia, M. Loppini, and N. Maffulli, “Changes in daily physical activity before and after total hip arthroplasty. A pilot study using accelerometry,” *The Surgeon*, vol. 11, no. 2, pp. 87–91, Apr. 2013, doi: 10.1016/j.surge.2012.04.006.

[97] M. R. Maly, S. M. Robbins, P. W. Stratford, T. B. Birmingham, and J. P. Callaghan, “Cumulative knee adductor load distinguishes between healthy and osteoarthritic knees–A proof of principle study,” *Gait & Posture*, vol. 37, no. 3, pp. 397–401, Mar. 2013, doi: 10.1016/j.gaitpost.2012.08.013.

[98] S. Bolszak, N. C. Casartelli, F. M. Impellizzeri, and N. A. Maffiuletti, “Validity and reproducibility of the Physical Activity Scale for the Elderly (PASE) questionnaire for the measurement of the physical activity level in patients after total knee arthroplasty,” *BMC Musculoskelet Disord*, vol. 15, no. 1, p. 46, Dec. 2014, doi: 10.1186/1471-2474-15-46.

[99] Y. Dessery, É. L. Belzile, S. Turmel, J. Doré, B. Diallo, and P. Corbeil, "Modulation of physical activity to optimize pain sensation following an intra-articular corticosteroid injection in patients with knee osteoarthritis," *ScientificWorldJournal*, vol. 2014, p. 209165, 2014, doi: 10.1155/2014/209165.
[100] P. Harding, A. E. Holland, C. Delany, and R. S. Hinman, "Do activity levels increase after total hip and knee arthroplasty?," *Clin. Orthop. Relat. Res.*, vol. 472, no. 5, pp. 1502–1511, May 2014, doi: 10.1007/s11999-013-3427-3.
[101] C. Lützner, S. Kirschner, and J. Lützner, "Patient Activity After TKA Depends on Patient-specific Parameters," *Clin Orthop Relat Res*, vol. 472, no. 12, pp. 3933–3940, Dec. 2014, doi: 10.1007/s11999-014-3813-5.
[102] D. K. White *et al.*, "Daily Walking and the Risk of Incident Functional Limitation in Knee Osteoarthritis: An Observational Study: Walking and Risk of Functional Limitation Over 2 Years in Knee OA," *Arthritis Care & Research*, vol. 66, no. 9, pp. 1328–1336, Sep. 2014, doi: 10.1002/acr.22362.
[103] S. J. Davenport, M. Arnold, C. Hua, A. Schenck, S. Batten, and N. F. Taylor, "Physical Activity Levels During Acute Inpatient Admission After Hip Fracture are Very Low," *Physiother Res Int*, vol. 20, no. 3, pp. 174–181, Sep. 2015, doi: 10.1002/pri.1616.
[104] T. L. Kahn and R. Schwarzkopf, "Does Total Knee Arthroplasty Affect Physical Activity Levels? Data from the Osteoarthritis Initiative," *The Journal of Arthroplasty*, vol. 30, no. 9, pp. 1521–1525, Sep. 2015, doi: 10.1016/j.arth.2015.03.016.
[105] M. Kretzschmar *et al.*, "Association of Physical Activity Measured by Accelerometer, Knee Joint Abnormalities, and Cartilage T2 Measurements Obtained From 3T Magnetic Resonance Imaging: Data From the Osteoarthritis Initiative," *Arthritis Care & Research*, vol. 67, no. 9, pp. 1272–1280, Sep. 2015, doi: 10.1002/acr.22586.
[106] J. Lee *et al.*, "Sedentary behavior and physical function: objective evidence from the Osteoarthritis Initiative," *Arthritis Care Res (Hoboken)*, vol. 67, no. 3, pp. 366–373, Mar. 2015, doi: 10.1002/acr.22432.
[107] G. H. Lo *et al.*, "Symptom Assessment in Knee Osteoarthritis Needs to Account for Physical Activity Level," *Arthritis & Rheumatology*, vol. 67, no. 11, pp. 2897–2904, Nov. 2015, doi: 10.1002/art.39271.
[108] M. R. Maly *et al.*, "Knee adduction moment relates to medial femoral and tibial cartilage morphology in clinical knee osteoarthritis," *Journal of Biomechanics*, vol. 48, no. 12, pp. 3495–3501, Sep. 2015, doi: 10.1016/j.jbiomech.2015.04.039.
[109] B. E. Øiestad *et al.*, "No Association between Daily Walking and Knee Structural Changes in People at Risk of or with Mild Knee Osteoarthritis. Prospective Data from the Multicenter Osteoarthritis Study," *J. Rheumatol.*, vol. 42, no. 9, pp. 1685–1693, Sep. 2015, doi: 10.3899/jrheum.150071.
[110] J. Song *et al.*, "Sedentary Behavior as a Risk Factor for Physical Frailty Independent of Moderate Activity: Results From the Osteoarthritis Initiative," *Am J Public Health*, vol. 105, no. 7, pp. 1439–1445, Jul. 2015, doi: 10.2105/AJPH.2014.302540.
[111] N. Fukutani *et al.*, "Knee pain during activities of daily living and its relationship with physical activity in patients with early and severe knee osteoarthritis," *Clin Rheumatol*, vol. 35, no. 9, pp. 2307–2316, Sep. 2016, doi: 10.1007/s10067-016-3251-8.
[112] T. L. Kahn and R. Schwarzkopf, "Do Total Knee Arthroplasty Patients Have a Higher Activity Level Compared to Patients With Osteoarthritis?," *Geriatr Orthop Surg Rehabil*, vol. 7, no. 3, pp. 142–147, Sep. 2016, doi: 10.1177/2151458516654518.
[113] S.-H. Liu, J. B. Driban, C. B. Eaton, T. E. McAlindon, L. R. Harrold, and K. L. Lapane, "Objectively Measured Physical Activity and Symptoms Change in Knee Osteoarthritis," *The American Journal of Medicine*, vol. 129, no. 5, pp. 497-505.e1, May 2016, doi: 10.1016/j.amjmed.2015.12.029.
[114] C. Lützner, F. Beyer, S. Kirschner, and J. Lützner, "How Much Improvement in Patient Activity Can Be Expected After TKA?," *Orthopedics*, vol. 39, no. 3 Suppl, pp. S18-23, May 2016, doi: 10.3928/01477447-20160509-15.

[115] R. J. Mobbs, K. Phan, M. Maharaj, and P. J. Rao, “Physical Activity Measured with Accelerometer and Self-Rated Disability in Lumbar Spine Surgery: A Prospective Study,” *Global Spine Journal*, vol. 6, no. 5, pp. 459–464, Aug. 2016, doi: 10.1055/s-0035-1565259.
[116] M. Taniguchi, S. Sawano, M. Kugo, S. Maegawa, T. Kawasaki, and N. Ichihashi, “Physical Activity Promotes Gait Improvement in Patients With Total Knee Arthroplasty,” *The Journal of Arthroplasty*, vol. 31, no. 5, pp. 984–988, May 2016, doi: 10.1016/j.arth.2015.11.012.
[117] P. A. Toogood, M. P. Abdel, J. A. Spear, S. M. Cook, D. J. Cook, and M. J. Taunton, “The monitoring of activity at home after total hip arthroplasty,” *The Bone & Joint Journal*, vol. 98-B, no. 11, pp. 1450–1454, Nov. 2016, doi: 10.1302/0301-620X.98B11.BJJ-2016-0194.R1.
[118] D. K. White *et al.*, “Prospective change in daily walking over 2 years in older adults with or at risk of knee osteoarthritis: the MOST study,” *Osteoarthritis and Cartilage*, vol. 24, no. 2, pp. 246–253, Feb. 2016, doi: 10.1016/j.joca.2015.08.004.
[119] D. R. Bell *et al.*, “Objectively Measured Physical Activity in Patients After Anterior Cruciate Ligament Reconstruction,” *The American Journal of Sports Medicine*, vol. 45, no. 8, pp. 1893–1900, Jul. 2017, doi: 10.1177/0363546517698940.
[120] N. M. Brisson *et al.*, “Baseline knee adduction moment interacts with body mass index to predict loss of medial tibial cartilage volume over 2.5 years in knee osteoarthritis,” *J. Orthop. Res.*, vol. 35, no. 11, pp. 2476–2483, Nov. 2017, doi: 10.1002/jor.23564.
[121] N. A. Cooper *et al.*, “Predictors of multidimensional functional outcomes after total knee arthroplasty,” *J. Orthop. Res.*, vol. 35, no. 12, pp. 2790–2798, 2017, doi: 10.1002/jor.23596.
[122] M. Engdal, O. A. Foss, K. Taraldsen, V. S. Husby, and S. B. Winther, “Daily Physical Activity in Total Hip Arthroplasty Patients Undergoing Different Surgical Approaches: A Cohort Study,” *Am J Phys Med Rehabil*, vol. 96, no. 7, pp. 473–478, Jul. 2017, doi: 10.1097/PHM.0000000000000657.
[123] N. Mehta, C. Steiner, K. G. Fields, D. H. Nawabi, and S. L. Lyman, “Using Mobile Tracking Technology to Visualize the Trajectory of Recovery After Hip Arthroscopy: a Case Report,” *HSS Jrnl*, vol. 13, no. 2, pp. 194–200, Jul. 2017, doi: 10.1007/s11420-017-9544-x.
[124] V. Agarwal, M. Smuck, C. Tomkins-Lane, and N. H. Shah, “Inferring Physical Function From Wearable Activity Monitors: Analysis of Free-Living Activity Data From Patients With Knee Osteoarthritis,” *JMIR Mhealth Uhealth*, vol. 6, no. 12, p. e11315, Dec. 2018, doi: 10.2196/11315.
[125] R. Daugaard, M. Tjur, M. Sliepen, M. Lipperts, B. Grimm, and I. Mechlenburg, “Are patients with knee osteoarthritis and patients with knee joint replacement as physically active as healthy persons?,” *J Orthop Translat*, vol. 14, pp. 8–15, Jul. 2018, doi: 10.1016/j.jot.2018.03.001.
[126] M. G. E. Fenten, S. M. K. Bakker, G. J. Scheffer, A. B. Wymenga, R. Stienstra, and P. J. C. Heesterbeek, “Femoral nerve catheter vs local infiltration for analgesia in fast track total knee arthroplasty: short-term and long-term outcomes,” *British Journal of Anaesthesia*, vol. 121, no. 4, pp. 850–858, Oct. 2018, doi: 10.1016/j.bja.2018.05.069.
[127] S. a. M. Fenton *et al.*, “Does the intensity of daily walking matter for protecting against the development of a slow gait speed in people with or at high risk of knee osteoarthritis? An observational study,” *Osteoarthr. Cartil.*, vol. 26, no. 9, pp. 1181–1189, 2018, doi: 10.1016/j.joca.2018.04.015.
[128] K. Hayashi *et al.*, “Impact of variation in physical activity after total joint replacement,” *J Pain Res*, vol. 2018, no. 11, pp. 2399–2406, Oct. 2018, doi: 10.2147/JPR.S178853.
[129] M. H. Hjorth, I. Mechlenburg, K. Soballe, S. S. Jakobsen, L. Roemer, and M. Stilling, “Physical Activity Is Associated With the Level of Chromium but Not With Changes in Pseudotumor Size in Patients With Metal-on-Metal Hip Arthroplasty,” *The Journal of Arthroplasty*, vol. 33, no. 9, pp. 2932–2939, Sep. 2018, doi: 10.1016/j.arth.2018.04.039.
[130] E. Losina *et al.*, “Financial Incentives and Health Coaching to Improve Physical Activity Following Total Knee Replacement: A Randomized Controlled Trial,” *Arthritis Care Res*, vol. 70, no. 5, pp. 732–740, May 2018, doi: 10.1002/acr.23324.
[131] H. Master, L. M. Thoma, M. B. Christiansen, E. Polakowski, L. A. Schmitt, and D. K. White, “Minimum Performance on Clinical Tests of Physical Function to Predict Walking 6,000 Steps/Day in Knee Osteoarthritis: An Observational Study,” *Arthritis Care Res (Hoboken)*, vol. 70, no. 7, pp. 1005–1011, 2018, doi: 10.1002/acr.23448.

[132] C. A. Pellegrini *et al.*, “Comparison of a Patient-Centered Weight Loss Program starting before versus after knee replacement: A pilot study,” *Obesity Research & Clinical Practice*, vol. 12, no. 5, pp. 472–478, Sep. 2018, doi: 10.1016/j.orcp.2018.06.009.
[133] M. Sliepen, E. Mauricio, M. Lipperts, B. Grimm, and D. Rosenbaum, “Objective assessment of physical activity and sedentary behaviour in knee osteoarthritis patients - beyond daily steps and total sedentary time,” *BMC Musculoskelet Disord*, vol. 19, no. 1, p. 64, 23 2018, doi: 10.1186/s12891-018-1980-3.
[134] J. Twiggs, L. Salmon, E. Kolos, E. Bogue, B. Miles, and J. Roe, “Measurement of physical activity in the pre- and early post-operative period after total knee arthroplasty for Osteoarthritis using a Fitbit Flex device,” *Medical Engineering & Physics*, vol. 51, pp. 31–40, Jan. 2018, doi: 10.1016/j.medengphy.2017.10.007.
[135] K. D. Allen *et al.*, “Composite measures of physical activity and pain associate better with functional assessments than pain alone in knee osteoarthritis,” *Clin. Rheumatol.*, vol. 38, no. 8, pp. 2241–2247, Aug. 2019, doi: 10.1007/s10067-019-04530-4.
[136] E. Frimpong *et al.*, “Light intensity physical activity increases and sedentary behavior decreases following total knee arthroplasty in patients with osteoarthritis,” *Knee Surg Sports Traumatol Arthrosc*, vol. 27, no. 7, pp. 2196–2205, Jul. 2019, doi: 10.1007/s00167-018-4987-2.
[137] S. J. Gilmore, A. J. Hahne, M. Davidson, and J. A. McClelland, “Physical activity patterns of patients immediately after lumbar surgery,” *Disabil Rehabil*, pp. 1–7, May 2019, doi: 10.1080/09638288.2019.1610512.
[138] J.-N. Jeong, S.-H. Kim, and K.-N. Park, “Relationship between objectively measured lifestyle factors and health factors in patients with knee osteoarthritis: The STROBE Study,” *Medicine (Baltimore)*, vol. 98, no. 26, p. e16060, Jun. 2019, doi: 10.1097/MD.0000000000016060.
[139] C. Kuenze *et al.*, “Relationship Between Physical Activity and Clinical Outcomes After ACL Reconstruction,” *Journal of Sport Rehabilitation*, vol. 28, no. 2, pp. 180–187, Feb. 2019, doi: 10.1123/jsr.2017-0186.
[140] C. Kuenze *et al.*, “Sex differences in physical activity engagement after ACL reconstruction,” *Physical Therapy in Sport*, vol. 35, pp. 12–17, Jan. 2019, doi: 10.1016/j.ptsp.2018.10.016.
[141] I. E. Luna, H. Kehlet, H. R. Wede, S. J. Hoevsgaard, and E. K. Aasvang, “Objectively measured early physical activity after total hip or knee arthroplasty,” *J Clin Monit Comput*, vol. 33, no. 3, pp. 509–522, Jun. 2019, doi: 10.1007/s10877-018-0185-5.
[142] P. N. Ramkumar, “Remote Patient Monitoring Using Mobile Health for Total Knee Arthroplasty: Validation of a Wearable and Machine Learning-Based Surveillance Platform,” *The Journal of Arthroplasty*, p. 7, 2019.
[143] J. B. Shofer *et al.*, “Step Activity After Surgical Treatment of Ankle Arthritis:,” *The Journal of Bone and Joint Surgery*, vol. 101, no. 13, pp. 1177–1184, Jul. 2019, doi: 10.2106/JBJS.18.00511.
[144] N. H. Vaughn, M. F. Dunklebarger, and M. W. Mason, “Individual Patient-reported Activity Levels Before and After Joint Arthroplasty Are Neither Accurate nor Reproducible,” *Clin. Orthop. Relat. Res.*, vol. 477, no. 3, pp. 536–544, 2019, doi: 10.1097/CORR.0000000000000591.
[145] S. E. Baez, M. C. Hoch, and J. M. Hoch, “Psychological factors are associated with return to pre-injury levels of sport and physical activity after ACL reconstruction,” *Knee Surg Sports Traumatol Arthrosc*, vol. 28, no. 2, pp. 495–501, Feb. 2020, doi: 10.1007/s00167-019-05696-9.
[146] N. M. Brisson, A. A. Gatti, and M. R. Maly, “Association of Pain and Steps Per Day in Persons With Mild-to-Moderate, Symptomatic Knee Osteoarthritis: A Mixed-Effects Models Analysis of Multiple Measurements Over Three Years,” *Arthritis Care Res (Hoboken)*, vol. 72, no. 1, pp. 114–121, 2020, doi: 10.1002/acr.23842.
[147] M. B. Christiansen *et al.*, “Feasibility and Preliminary Outcomes of a Physical Therapist–Administered Physical Activity Intervention After Total Knee Replacement,” *Arthritis Care Res*, vol. 72, no. 5, pp. 661–668, May 2020, doi: 10.1002/acr.23882.
[148] A. M. Keppler *et al.*, “Postoperative physical activity in orthogeriatric patients - new insights with continuous monitoring,” *Injury*, vol. 51, no. 3, pp. 628–632, Mar. 2020, doi: 10.1016/j.injury.2020.01.041.

[149] C. M. Lisee, A. H. K. Montoye, N. F. Lewallen, M. Hernandez, D. R. Bell, and C. M. Kuenze, "Assessment of Free-Living Cadence Using ActiGraph Accelerometers Between Individuals With and Without Anterior Cruciate Ligament Reconstruction," *J Athl Train*, Aug. 2020, doi: 10.4085/1062-6050-425-19.
[150] H. Sakakima, S. Takada, K. Norimatsu, S. Otsuka, K. Nakanishi, and A. Tani, "Diurnal Profiles of Locomotive and Household Activities Using an Accelerometer in Community-Dwelling Older Adults with Musculoskeletal Disorders: A Cross-Sectional Survey," *Int J Environ Res Public Health*, vol. 17, no. 15, Jul. 2020, doi: 10.3390/ijerph17155337.
[151] N. F. Taylor *et al.*, "Association between physical activity and short-term physical function changes after hip fracture: An observational study," *Physiother Res Int*, p. e1876, Sep. 2020, doi: 10.1002/pri.1876.
[152] D. Voinier *et al.*, "Using Cumulative Load to Explain How Body Mass Index and Daily Walking Relate to Worsening Knee Cartilage Damage Over Two Years: The MOST Study," *Arthritis & Rheumatology (Hoboken, N.J.)*, vol. 72, no. 6, pp. 957–965, 2020, doi: 10.1002/art.41181.
[153] R. S. McGinnis *et al.*, "Skin mounted accelerometer system for measuring knee range of motion," in *Engineering in Medicine and Biology Society (EMBC), 2016 IEEE 38th Annual International Conference of the*, Orlando, FL, USA, Aug. 2016, pp. 5298–5302, Accessed: Jan. 31, 2017. [Online]. Available: http://ieeexplore.ieee.org/abstract/document/7591923/.
[154] A. M. Sabatini, "Estimating Three-Dimensional Orientation of Human Body Parts by Inertial/Magnetic Sensing," *Sensors*, vol. 11, no. 12, pp. 1489–1525, Jan. 2011, doi: 10.3390/s110201489.
[155] S. Yusuf *et al.*, "Effect of potentially modifiable risk factors associated with myocardial infarction in 52 countries (the INTERHEART study): case-control study," *Lancet*, vol. 364, no. 9438, pp. 937–952, Sep. 2004, doi: 10.1016/S0140-6736(04)17018-9.
[156] J. M. Jakicic *et al.*, "Objective Physical Activity and Weight Loss in Adults: The Step-Up Randomized Clinical Trial," *Obesity (Silver Spring, Md.)*, vol. 22, no. 11, p. 2284, Nov. 2014, doi: 10.1002/oby.20830.
[157] O. Klets *et al.*, "Estimation of the effect of body weight on the development of osteoarthritis based on cumulative stresses in cartilage: Data from the Osteoarthritis Initiative," *Annals of biomedical engineering*, vol. 46, no. 2, p. 334, Feb. 2018, doi: 10.1007/s10439-017-1974-6.
[158] K. Blazek, J. Favre, J. Asay, J. Erhart-Hledik, and T. Andriacchi, "Age and obesity alter the relationship between femoral articular cartilage thickness and ambulatory loads in individuals without osteoarthritis," *J Orthop Res*, vol. 32, no. 3, pp. 394–402, Mar. 2014, doi: 10.1002/jor.22530.
[159] S. R. Goldberg and S. J. Stanhope, "Sensitivity of joint moments to changes in walking speed and body-weight-support are interdependent and vary across joints," *J Biomech*, vol. 46, no. 6, pp. 1176–1183, Apr. 2013, doi: 10.1016/j.jbiomech.2013.01.001.
[160] J. E. Thorp, P. G. Adamczyk, H.-L. Ploeg, and K. A. Pickett, "Monitoring Motor Symptoms During Activities of Daily Living in Individuals With Parkinson's Disease," *Front. Neurol.*, vol. 9, p. 1036, Dec. 2018, doi: 10.3389/fneur.2018.01036.
[161] D. Bothun and M. Lieberman, "The Wearable Life 2.0: Connected living in a wearable world," PwC, Consumer Intelligence Series, 2016. Accessed: Oct. 27, 2020. [Online]. Available: pwc.com/CISwearables.
[162] R. D. Gurchiek, A. T. Ursiny, and R. S. McGinnis, "A Gaussian Process Model of Muscle Synergy Functions for Estimating Unmeasured Muscle Excitations Using a Measured Subset," *IEEE Transactions on Neural Systems and Rehabilitation Engineering*, vol. 28, no. 11, pp. 2478–2487, Nov. 2020, doi: 10.1109/TNSRE.2020.3028052.
[163] M. Czech *et al.*, "The Impact of Reducing the Number of Wearable Devices on Measuring Gait in Parkinson Disease: Noninterventional Exploratory Study," *JMIR Rehabilitation and Assistive Technologies*, vol. 7, no. 2, p. e17986, 2020, doi: 10.2196/17986.
[164] B. M. Eskofier *et al.*, "An Overview of Smart Shoes in the Internet of Health Things: Gait and Mobility Assessment in Health Promotion and Disease Monitoring," *Applied Sciences*, vol. 7, no. 10, Art. no. 10, Oct. 2017, doi: 10.3390/app7100986.

[165] J. L. Riskowski, “Gait and neuromuscular adaptations after using a feedback-based gait monitoring knee brace,” *Gait & Posture*, vol. 32, no. 2, pp. 242–247, Jun. 2010, doi: 10.1016/j.gaitpost.2010.05.002.
[166] N. J. Collins, H. F. Hart, and K. A. G. Mills, “Osteoarthritis year in review 2018: rehabilitation and outcomes,” *Osteoarthritis and Cartilage*, vol. 27, no. 3, pp. 378–391, Mar. 2019, doi: 10.1016/j.joca.2018.11.010.
[167] J. L. Whittaker, L. K. Truong, K. Dhiman, and C. Beck, “Osteoarthritis year in review 2020: Rehabilitation and outcomes,” *Osteoarthritis and Cartilage*, Nov. 2020, doi: 10.1016/j.joca.2020.10.005.
[168] S. Del Din, A. Godfrey, B. Galna, S. Lord, and L. Rochester, “Free-living gait characteristics in ageing and Parkinson’s disease: impact of environment and ambulatory bout length,” *J Neuroeng Rehabil*, vol. 13, no. 1, p. 46, 12 2016, doi: 10.1186/s12984-016-0154-5.
[169] M. Ullrich *et al.*, “Detection of Gait From Continuous Inertial Sensor Data Using Harmonic Frequencies,” *IEEE Journal of Biomedical and Health Informatics*, pp. 1–1, 2020, doi: 10.1109/JBHI.2020.2975361.
[170] C. Fischer, P. Talkad Sukumar, and M. Hazas, “Tutorial: Implementing a Pedestrian Tracker Using Inertial Sensors,” *IEEE Pervasive Comput.*, vol. 12, no. 2, pp. 17–27, Apr. 2013, doi: 10.1109/MPRV.2012.16.
[171] J. Rueterbories, E. G. Spaich, B. Larsen, and O. K. Andersen, “Methods for gait event detection and analysis in ambulatory systems,” *Medical Engineering & Physics*, vol. 32, no. 6, pp. 545–552, Jul. 2010, doi: 10.1016/j.medengphy.2010.03.007.
[172] K. Aminian, K. Rezakhanlou, E. De Andres, C. Fritsch, P. F. Leyvraz, and P. Robert, “Temporal feature estimation during walking using miniature accelerometers: an analysis of gait improvement after hip arthroplasty,” *Med Biol Eng Comput*, vol. 37, no. 6, pp. 686–691, Nov. 1999.
[173] Y. Shimada *et al.*, “Clinical Application of Acceleration Sensor to Detect the Swing Phase of Stroke Gait in Functional Electrical Stimulation,” *Tohoku J. Exp. Med.*, vol. 207, no. 3, pp. 197–202, 2005, doi: 10.1620/tjem.207.197.
[174] S. Khandelwal and N. Wickström, “Novel methodology for estimating Initial Contact events from accelerometers positioned at different body locations,” *Gait & Posture*, vol. 59, pp. 278–285, Jan. 2018, doi: 10.1016/j.gaitpost.2017.07.030.
[175] D. Sun, G. Fekete, Q. Mei, and Y. Gu, “The effect of walking speed on the foot inter-segment kinematics, ground reaction forces and lower limb joint moments,” *PeerJ*, vol. 6, p. e5517, Aug. 2018, doi: 10.7717/peerj.5517.
[176] F. Hug, “Can muscle coordination be precisely studied by surface electromyography?,” *J Electromyogr Kinesiol*, vol. 21, no. 1, pp. 1–12, Feb. 2011, doi: 10.1016/j.jelekin.2010.08.009.
[177] J. M. Bland and D. G. Altman, “Statistical methods for assessing agreement between two methods of clinical measurement,” *Lancet*, vol. 1, no. 8476, pp. 307–310, Feb. 1986.
[178] J. M. Bland and D. G. Altman, “Agreement between methods of measurement with multiple observations per individual,” *Journal of biopharmaceutical statistics*, vol. 17, no. 4, pp. 571–582, 2007.
[179] E. S. Fisher *et al.*, “Evaluating Efficiency Across Patient-Focused Episodes of Care,” 2009, Accessed: Mar. 31, 2019. [Online]. Available: https://www.scholars.northwestern.edu/en/publications/evaluating-efficiency-across-patient-focused-episodes-of-care-2.
[180] M. D. Naylor, L. H. Aiken, E. T. Kurtzman, D. M. Olds, and K. B. Hirschman, “The care span: The importance of transitional care in achieving health reform,” *Health Aff (Millwood)*, vol. 30, no. 4, pp. 746–754, Apr. 2011, doi: 10.1377/hlthaff.2011.0041.
[181] R. T. Konetzka, W. Spector, and M. R. Limcangco, “Reducing hospitalizations from long-term care settings,” *Med Care Res Rev*, vol. 65, no. 1, pp. 40–66, Feb. 2008, doi: 10.1177/1077558707307569.
[182] B. D. Stauffer *et al.*, “Effectiveness and Cost of a Transitional Care Program for Heart Failure: A Prospective Study With Concurrent Controls,” *Arch Intern Med*, vol. 171, no. 14, pp. 1238–1243, Jul. 2011, doi: 10.1001/archinternmed.2011.274.

[183] L. C. Kourtis, O. B. Regele, J. M. Wright, and G. B. Jones, “Digital biomarkers for Alzheimer’s disease: the mobile/wearable devices opportunity,” *npj Digital Medicine*, vol. 2, no. 1, Dec. 2019, doi: 10.1038/s41746-019-0084-2.
[184] C. Tomkins-Lane, J. Norden, A. Sinha, R. Hu, and M. Smuck, “Digital biomarkers of spine and musculoskeletal disease from accelerometers: Defining phenotypes of free-living physical activity in knee osteoarthritis and lumbar spinal stenosis,” *The Spine Journal*, vol. 19, no. 1, pp. 15–23, Jan. 2019, doi: 10.1016/j.spinee.2018.07.007.
[185] R. S. McGinnis *et al.*, “Rapid detection of internalizing diagnosis in young children enabled by wearable sensors and machine learning,” *PLOS ONE*, vol. 14, no. 1, p. e0210267, Jan. 2019, doi: 10.1371/journal.pone.0210267.
[186] M. Sparaco, L. Lavorgna, R. Conforti, G. Tedeschi, and S. Bonavita, “The Role of Wearable Devices in Multiple Sclerosis,” *Multiple Sclerosis International*, vol. 2018, pp. 1–7, Oct. 2018, doi: 10.1155/2018/7627643.
[187] J. T. Blackburn, B. Pietrosimone, M. S. Harkey, B. A. Luc, and D. N. Pamukoff, “Quadriceps Function and Gait Kinetics after Anterior Cruciate Ligament Reconstruction:,” *Medicine & Science in Sports & Exercise*, vol. 48, no. 9, pp. 1664–1670, Sep. 2016, doi: 10.1249/MSS.0000000000000963.
[188] H. F. Hart *et al.*, “Knee kinematics and joint moments during gait following anterior cruciate ligament reconstruction: a systematic review and meta-analysis,” *Br J Sports Med*, vol. 50, no. 10, pp. 597–612, May 2016, doi: 10.1136/bjsports-2015-094797.
[189] A. Samà *et al.*, “Estimating bradykinesia severity in Parkinson’s disease by analysing gait through a waist-worn sensor,” *Computers in Biology and Medicine*, vol. 84, pp. 114–123, May 2017, doi: 10.1016/j.compbiomed.2017.03.020.
[190] A. Rodríguez-Molinero *et al.*, “Validation of a Portable Device for Mapping Motor and Gait Disturbances in Parkinson’s Disease,” *JMIR mHealth uHealth*, vol. 3, no. 1, p. e9, Feb. 2015, doi: 10.2196/mhealth.3321.
[191] A. Rodríguez-Molinero *et al.*, “A Kinematic Sensor and Algorithm to Detect Motor Fluctuations in Parkinson Disease: Validation Study Under Real Conditions of Use,” *JMIR Rehabil Assist Technol*, vol. 5, no. 1, p. e8, Apr. 2018, doi: 10.2196/rehab.8335.
[192] S. K. Prajapati, W. H. Gage, D. Brooks, S. E. Black, and W. E. McIlroy, “A Novel Approach to Ambulatory Monitoring: Investigation Into the Quantity and Control of Everyday Walking in Patients With Subacute Stroke,” *Neurorehabil Neural Repair*, vol. 25, no. 1, pp. 6–14, Jan. 2011, doi: 10.1177/1545968310374189.
[193] R. S. McGinnis, J. R. Slauterbeck, T. W. Tourville, and M. J. Toth, “Wearable Sensors Capture Differences in Muscle Activity and Gait Patterns During Daily Activity in Patients Recovering from ACL Reconstruction,” in *Proceedings of the 15th International Conference on Wearable and Implantable Body Sensor Networks*, Las Vegas, Nevada, USA, Mar. 2018, pp. 38–41.
[194] K. Lee, “Physical activity classification in free-living conditions using smartphone accelerometer data and exploration of predicted results,” *Comp Env Urb Sys*, vol. 67, pp. 124–131, 2018.
[195] N. Haji Ghassemi *et al.*, “Segmentation of Gait Sequences in Sensor-Based Movement Analysis: A Comparison of Methods in Parkinson’s Disease,” *Sensors (Basel)*, vol. 18, no. 1, Jan. 2018, doi: 10.3390/s18010145.
[196] R. S. McGinnis *et al.*, “Accuracy of Femur Angles Estimated by IMUs During Clinical Procedures Used to Diagnose Femoroacetabular Impingement,” *IEEE Transactions on Biomedical Engineering*, vol. 62, no. 6, pp. 1503–1513, Jun. 2015, doi: 10.1109/TBME.2015.2392758.
[197] Y. Moon *et al.*, “Monitoring gait in multiple sclerosis with novel wearable motion sensors,” *PLOS ONE*, vol. 12, no. 2, p. e0171346, Feb. 2017, doi: 10.1371/journal.pone.0171346.
[198] T. Seel, J. Raisch, and T. Schauer, “IMU-Based Joint Angle Measurement for Gait Analysis,” *Sensors*, vol. 14, no. 4, pp. 6891–6909, Apr. 2014, doi: 10.3390/s140406891.
[199] R. C. Mather *et al.*, “Societal and Economic Impact of Anterior Cruciate Ligament Tears:,” *The Journal of Bone and Joint Surgery-American Volume*, vol. 95, no. 19, pp. 1751–1759, Oct. 2013, doi: 10.2106/JBJS.L.01705.

[200] A. Carbone and S. Rodeo, “Review of current understanding of post-traumatic osteoarthritis resulting from sports injuries,” *Journal of Orthopaedic Research*, vol. 35, no. 3, pp. 397–405, Mar. 2017, doi: 10.1002/jor.23341.
[201] S. M. Sigward, P. Lin, and K. Pratt, “Knee loading asymmetries during gait and running in early rehabilitation following anterior cruciate ligament reconstruction: A longitudinal study,” *Clinical Biomechanics*, vol. 32, pp. 249–254, Feb. 2016, doi: 10.1016/j.clinbiomech.2015.11.003.
[202] P. Devita *et al.*, “Gait adaptations before and after anterior cruciate ligament reconstruction surgery,” *Med Sci Sports Exerc*, vol. 29, no. 7, pp. 853–859, Jul. 1997.
[203] C. Lisee, “Quadriceps Strength and Volitional Activation After Anterior Cruciate Ligament Reconstruction: A Systematic Review and Meta-analysis,” *SPORTS HEALTH*, vol. 11, no. 2, pp. 163–179, 2019.
[204] S. Farrokhi, C. A. Voycheck, J. A. Gustafson, G. K. Fitzgerald, and S. Tashman, “Knee joint contact mechanics during downhill gait and its relationship with varus/valgus motion and muscle strength in patients with knee osteoarthritis,” *Knee*, vol. 23, no. 1, pp. 49–56, Jan. 2016, doi: 10.1016/j.knee.2015.07.011.
[205] L. V. Slater, J. M. Hart, A. R. Kelly, and C. M. Kuenze, “Progressive Changes in Walking Kinematics and Kinetics After Anterior Cruciate Ligament Injury and Reconstruction: A Review and Meta-Analysis,” *Journal of Athletic Training*, vol. 52, no. 9, pp. 847–860, Sep. 2017, doi: 10.4085/1062-6050-52.6.06.
[206] A. S. Lepley, P. A. Gribble, A. C. Thomas, M. A. Tevald, D. H. Sohn, and B. G. Pietrosimone, “Quadriceps neural alterations in anterior cruciate ligament reconstructed patients: A 6-month longitudinal investigation: ACLr neural alterations,” *Scandinavian Journal of Medicine & Science in Sports*, vol. 25, no. 6, pp. 828–839, Dec. 2015, doi: 10.1111/sms.12435.
[207] R. M. Palmieri-Smith and L. K. Lepley, “Quadriceps Strength Asymmetry After Anterior Cruciate Ligament Reconstruction Alters Knee Joint Biomechanics and Functional Performance at Time of Return to Activity,” *The American Journal of Sports Medicine*, vol. 43, no. 7, pp. 1662–1669, Jul. 2015, doi: 10.1177/0363546515578252.
[208] D. L. Davies and D. W. Bouldin, “A Cluster Separation Measure,” *IEEE Transactions on Pattern Analysis and Machine Intelligence*, vol. PAMI-1, no. 2, pp. 224–227, Apr. 1979, doi: 10.1109/TPAMI.1979.4766909.
[209] D. G. Lloyd and T. F. Besier, “An EMG-driven musculoskeletal model to estimate muscle forces and knee joint moments in vivo,” *Journal of Biomechanics*, vol. 36, no. 6, pp. 765–776, Jun. 2003, doi: 10.1016/S0021-9290(03)00010-1.
[210] J. Cohen, “The statistical power of abnormal-social psychological research: A review,” *The Journal of Abnormal and Social Psychology*, vol. 65, no. 3, pp. 145–153, Sep. 1962, doi: http://dx.doi.org/10.1037/h0045186.
[211] A. Hobson, “The Etiology of Persistent Quadriceps Weakness Following Anterior Cruciate Ligament Reconstruction:,” *JBJS Journal of Orthopaedics for Physician Assistants*, vol. 6, no. 3, p. e24, Jul. 2018, doi: 10.2106/JBJS.JOPA.18.00001.
[212] S. Pfeiffer *et al.*, “Associations Between Slower Walking Speed and T1ρ Magnetic Resonance Imaging of Femoral Cartilage Following Anterior Cruciate Ligament Reconstruction,” *Arthritis Care & Research*, vol. 70, no. 8, pp. 1132–1140, 2018, doi: 10.1002/acr.23477.
[213] S. M. Sigward, M.-S. M. Chan, and P. E. Lin, “Characterizing knee loading asymmetry in individuals following anterior cruciate ligament reconstruction using inertial sensors,” *Gait & Posture*, vol. 49, pp. 114–119, Sep. 2016, doi: 10.1016/j.gaitpost.2016.06.021.
[214] R. van der Straaten, L. De Baets, I. Jonkers, and A. Timmermans, “Mobile assessment of the lower limb kinematics in healthy persons and in persons with degenerative knee disorders: A systematic review,” *Gait & Posture*, vol. 59, pp. 229–241, Jan. 2018, doi: 10.1016/j.gaitpost.2017.10.005.
[215] L. Ren, R. K. Jones, and D. Howard, “Whole body inverse dynamics over a complete gait cycle based only on measured kinematics,” *Journal of Biomechanics*, vol. 41, no. 12, pp. 2750–2759, Aug. 2008, doi: 10.1016/j.jbiomech.2008.06.001.
[216] R. E. Richards, J. C. van den Noort, M. van der Esch, M. J. Booij, and J. Harlaar, “Effect of real-time biofeedback on peak knee adduction moment in patients with medial knee osteoarthritis: Is

direct feedback effective?," *Clinical Biomechanics*, vol. 57, pp. 150–158, Aug. 2018, doi: 10.1016/j.clinbiomech.2017.07.004.
[217] S. L. Delp, J. P. Loan, M. G. Hoy, F. E. Zajac, E. L. Topp, and J. M. Rosen, "An interactive graphics-based model of the lower extremity to study orthopaedic surgical procedures," *IEEE Trans. Biomed. Eng.*, vol. 37, no. 8, pp. 757–767, Aug. 1990, doi: 10.1109/10.102791.
[218] L. E. Cofré Lizama, F. Khan, P. V. Lee, and M. P. Galea, "The use of laboratory gait analysis for understanding gait deterioration in people with multiple sclerosis," *Mult. Scler.*, vol. 22, no. 14, pp. 1768–1776, 2016, doi: 10.1177/1352458516658137.
[219] B. van Veen, E. Montefiori, L. Modenese, C. Mazzà, and M. Viceconti, "Muscle recruitment strategies can reduce joint loading during level walking," *Journal of Biomechanics*, p. 109368, Sep. 2019, doi: 10.1016/j.jbiomech.2019.109368.
[220] C. A. Myers *et al.*, "Simulated hip abductor strengthening reduces peak joint contact forces in patients with total hip arthroplasty," *Journal of Biomechanics*, vol. 93, pp. 18–27, Aug. 2019, doi: 10.1016/j.jbiomech.2019.06.003.
[221] E. Bergamini, G. Ligorio, A. Summa, G. Vannozzi, A. Cappozzo, and A. Sabatini, "Estimating Orientation Using Magnetic and Inertial Sensors and Different Sensor Fusion Approaches: Accuracy Assessment in Manual and Locomotion Tasks," *Sensors*, vol. 14, no. 10, pp. 18625–18649, Oct. 2014, doi: 10.3390/s141018625.
[222] M. Sartori, M. Reggiani, D. Farina, and D. G. Lloyd, "EMG-Driven Forward-Dynamic Estimation of Muscle Force and Joint Moment about Multiple Degrees of Freedom in the Human Lower Extremity," *PLoS ONE*, vol. 7, no. 12, p. e52618, Dec. 2012, doi: 10.1371/journal.pone.0052618.
[223] J. M. Winters, "Hill-Based Muscle Models: A Systems Engineering Perspective," in *Multiple Muscle Systems: Biomechanics and Movement Organization*, J. M. Winters and S. L.-Y. Woo, Eds. New York, NY: Springer New York, 1990, pp. 69–93.
[224] J. J. Dowling, "The Use of Electromyography for the Noninvasive Prediction of Muscle Forces: Current Issues," *Sports Medicine*, vol. 24, no. 2, pp. 82–96, Aug. 1997, doi: 10.2165/00007256-199724020-00002.
[225] S. S. Blemker, P. M. Pinsky, and S. L. Delp, "A 3D model of muscle reveals the causes of nonuniform strains in the biceps brachii," *J Biomech*, vol. 38, no. 4, pp. 657–665, Apr. 2005, doi: 10.1016/j.jbiomech.2004.04.009.
[226] J. W. Fernandez, M. L. Buist, D. P. Nickerson, and P. J. Hunter, "Modelling the passive and nerve activated response of the rectus femoris muscle to a flexion loading: A finite element framework," *Medical Engineering & Physics*, vol. 27, no. 10, pp. 862–870, Dec. 2005, doi: 10.1016/j.medengphy.2005.03.009.
[227] O. Röhrle, M. Sprenger, and S. Schmitt, "A two-muscle, continuum-mechanical forward simulation of the upper limb," *Biomechanics and Modeling in Mechanobiology*, vol. 16, no. 3, pp. 743–762, Jun. 2017, doi: 10.1007/s10237-016-0850-x.
[228] D. Staudenmann, K. Roeleveld, D. F. Stegeman, and J. H. van Dieën, "Methodological aspects of SEMG recordings for force estimation – A tutorial and review," *Journal of Electromyography and Kinesiology*, vol. 20, no. 3, pp. 375–387, Jun. 2010, doi: 10.1016/j.jelekin.2009.08.005.
[229] R. Dumas, A. Barré, F. Moissenet, and R. Aissaoui, "Can a reduction approach predict reliable joint contact and musculo-tendon forces?," *Journal of Biomechanics*, vol. 95, p. 109329, Oct. 2019, doi: 10.1016/j.jbiomech.2019.109329.
[230] E. A. Clancy, O. Bida, and D. Rancourt, "Influence of advanced electromyogram (EMG) amplitude processors on EMG-to-torque estimation during constant-posture, force-varying contractions," *Journal of Biomechanics*, vol. 39, no. 14, pp. 2690–2698, Jan. 2006, doi: 10.1016/j.jbiomech.2005.08.007.
[231] C. E. Rasmussen and K. I. Williams, *Gaussian Processes for Machine Learning*. Cambridge, MA: The MIT Press, 2006.
[232] B. J. Stetter, S. Ringhof, F. C. Krafft, S. Sell, and T. Stein, "Estimation of Knee Joint Forces in Sport Movements Using Wearable Sensors and Machine Learning," *Sensors*, vol. 19, no. 17, p. 3690, Aug. 2019, doi: 10.3390/s19173690.

[233] A. I. Faisal, S. Majumder, T. Mondal, D. Cowan, S. Naseh, and M. J. Deen, “Monitoring Methods of Human Body Joints: State-of-the-Art and Research Challenges,” *Sensors (Basel)*, vol. 19, no. 11, Jun. 2019, doi: 10.3390/s19112629.
[234] U. Trinler, K. Hollands, R. Jones, and R. Baker, “A systematic review of approaches to modelling lower limb muscle forces during gait: Applicability to clinical gait analyses,” *Gait & Posture*, vol. 61, pp. 353–361, Mar. 2018, doi: 10.1016/j.gaitpost.2018.02.005.
[235] W. I. Schöllhorn, “Applications of artificial neural nets in clinical biomechanics,” *Clinical Biomechanics*, vol. 19, no. 9, pp. 876–898, Nov. 2004, doi: 10.1016/j.clinbiomech.2004.04.005.
[236] P. B. Shull, W. Jirattigalachote, M. A. Hunt, M. R. Cutkosky, and S. L. Delp, “Quantified self and human movement: A review on the clinical impact of wearable sensing and feedback for gait analysis and intervention,” *Gait & Posture*, vol. 40, no. 1, pp. 11–19, May 2014, doi: 10.1016/j.gaitpost.2014.03.189.
[237] R. Caldas, M. Mundt, W. Potthast, F. Buarque de Lima Neto, and B. Markert, “A systematic review of gait analysis methods based on inertial sensors and adaptive algorithms,” *Gait & Posture*, vol. 57, pp. 204–210, Sep. 2017, doi: 10.1016/j.gaitpost.2017.06.019.
[238] S. Suryanarayanan, N. P. Reddy, and V. Gupta, “An intelligent system with EMG-based joint angle estimation for telemanipulation,” *Stud Health Technol Inform*, vol. 29, pp. 546–552, 1996.
[239] E. A. Clancy, L. Liu, Pu Liu, and D. V. Z. Moyer, “Identification of Constant-Posture EMG–Torque Relationship About the Elbow Using Nonlinear Dynamic Models,” *IEEE Trans. Biomed. Eng.*, vol. 59, no. 1, pp. 205–212, Jan. 2012, doi: 10.1109/TBME.2011.2170423.
[240] R. Song and K. Y. Tong, “Using recurrent artificial neural network model to estimate voluntary elbow torque in dynamic situations,” *Med. Biol. Eng. Comput.*, vol. 43, no. 4, pp. 473–480, Aug. 2005, doi: 10.1007/BF02344728.
[241] W. Youn and J. Kim, “Estimation of elbow flexion force during isometric muscle contraction from mechanomyography and electromyography,” *Med Biol Eng Comput*, vol. 48, no. 11, pp. 1149–1157, Nov. 2010, doi: 10.1007/s11517-010-0641-y.
[242] M. Xiloyannis, C. Gavriel, A. A. C. Thomik, and A. A. Faisal, “Gaussian Process Autoregression for Simultaneous Proportional Multi-Modal Prosthetic Control With Natural Hand Kinematics,” *IEEE Trans. Neural Syst. Rehabil. Eng.*, vol. 25, no. 10, pp. 1785–1801, Oct. 2017, doi: 10.1109/TNSRE.2017.2699598.
[243] A. M. Howell, T. Kobayashi, H. A. Hayes, K. B. Foreman, and S. J. M. Bamberg, “Kinetic Gait Analysis Using a Low-Cost Insole,” *IEEE Trans. Biomed. Eng.*, vol. 60, no. 12, pp. 3284–3290, Dec. 2013, doi: 10.1109/TBME.2013.2250972.
[244] D. A. Jacobs and D. P. Ferris, “Estimation of ground reaction forces and ankle moment with multiple, low-cost sensors,” *J NeuroEngineering Rehabil*, vol. 12, no. 1, p. 90, Dec. 2015, doi: 10.1186/s12984-015-0081-x.
[245] J. Wang, L. Wang, S. M. Miran, X. Xi, and A. Xue, “Surface Electromyography Based Estimation of Knee Joint Angle by Using Correlation Dimension of Wavelet Coefficient,” *IEEE Access*, vol. 7, pp. 60522–60531, 2019, doi: 10.1109/ACCESS.2019.2913959.
[246] P. Xia, J. Hu, and Y. Peng, “EMG-Based Estimation of Limb Movement Using Deep Learning With Recurrent Convolutional Neural Networks,” *Artificial Organs*, vol. 42, no. 5, pp. E67–E77, May 2018, doi: 10.1111/aor.13004.
[247] L. Xu, X. Chen, S. Cao, X. Zhang, and X. Chen, “Feasibility Study of Advanced Neural Networks Applied to sEMG-Based Force Estimation,” *Sensors*, vol. 18, no. 10, p. 3226, Sep. 2018, doi: 10.3390/s18103226.
[248] S. Farmer, B. Silver-Thorn, P. Voglewede, and S. A. Beardsley, “Within-socket myoelectric prediction of continuous ankle kinematics for control of a powered transtibial prosthesis,” *J. Neural Eng.*, vol. 11, no. 5, p. 056027, Oct. 2014, doi: 10.1088/1741-2560/11/5/056027.
[249] F. Stulp and O. Sigaud, “Many regression algorithms, one unified model: A review,” *Neural Networks*, vol. 69, pp. 60–79, Sep. 2015, doi: 10.1016/j.neunet.2015.05.005.
[250] S. Michieletto *et al.*, “GMM-Based Single-Joint Angle Estimation Using EMG Signals,” in *Intelligent Autonomous Systems 13*, vol. 302, E. Menegatti, N. Michael, K. Berns, and H. Yamaguchi, Eds. Cham, Switzerland: Springer International Publishing, 2016, pp. 1173–1184.

[251] A. Ziai and C. Menon, “Comparison of regression models for estimation of isometric wrist joint torques using surface electromyography,” *J NeuroEngineering Rehabil*, vol. 8, no. 1, p. 56, 2011, doi: 10.1186/1743-0003-8-56.
[252] J. M. Hahne *et al.*, “Linear and Nonlinear Regression Techniques for Simultaneous and Proportional Myoelectric Control,” *IEEE Trans. Neural Syst. Rehabil. Eng.*, vol. 22, no. 2, pp. 269–279, Mar. 2014, doi: 10.1109/TNSRE.2014.2305520.
[253] B. Mijovic, M. B. Popovic, and D. B. Popovic, “Synergistic control of forearm based on accelerometer data and artificial neural networks,” *Braz J Med Biol Res*, vol. 41, no. 5, pp. 389–397, Apr. 2008, doi: 10.1590/S0100-879X2008005000019.
[254] Y. Koike and M. Kawato, “Estimation of dynamic joint torques and trajectory formation from surface electromyography signals using a neural network model,” *Biol Cybern*, vol. 73, no. 4, pp. 291–300, 1995.
[255] T. Hastie, R. Tibshirani, and J. Friedman, *The Elements of Statistical Learning: Data Mining, Inference, and Prediction*, 2nd ed. New York, NY, USA: Springer, 2009.
[256] J. G. Ngeo, T. Tamei, and T. Shibata, “Continuous and simultaneous estimation of finger kinematics using inputs from an EMG-to-muscle activation model,” *J NeuroEngineering Rehabil*, vol. 11, no. 1, p. 122, 2014, doi: 10.1186/1743-0003-11-122.
[257] A. Findlow, J. Y. Goulermas, C. Nester, D. Howard, and L. P. J. Kenney, “Predicting lower limb joint kinematics using wearable motion sensors,” *Gait & Posture*, vol. 28, no. 1, pp. 120–126, Jul. 2008, doi: 10.1016/j.gaitpost.2007.11.001.
[258] J. Y. Goulermas *et al.*, “An Instance-Based Algorithm With Auxiliary Similarity Information for the Estimation of Gait Kinematics From Wearable Sensors,” *IEEE Trans. Neural Netw.*, vol. 19, no. 9, pp. 1574–1582, Sep. 2008, doi: 10.1109/TNN.2008.2000808.
[259] F. Wouda, M. Giuberti, G. Bellusci, and P. Veltink, “Estimation of Full-Body Poses Using Only Five Inertial Sensors: An Eager or Lazy Learning Approach?,” *Sensors*, vol. 16, no. 12, p. 2138, Dec. 2016, doi: 10.3390/s16122138.
[260] W. Sun, J. Zhu, Y. Jiang, H. Yokoi, and Q. Huang, “One-Channel Surface Electromyography Decomposition for Muscle Force Estimation,” *Front. Neurorobot.*, vol. 12, p. 20, May 2018, doi: 10.3389/fnbot.2018.00020.
[261] P.-S. Shih and P. E. Patterson, “Predicting Joint Moments and Angles from EMG Signals,” *Biomedical Sciences Instrumentation*, vol. 33, pp. 191–196, 1997.
[262] J. H. van Dieën and B. Visser, “Estimating net lumbar sagittal plane moments from EMG data. The validity of calibration procedures,” *Journal of Electromyography and Kinesiology*, vol. 9, no. 5, pp. 309–315, Oct. 1999, doi: 10.1016/S1050-6411(99)00004-8.
[263] A. T. C. Au and R. F. Kirsch, “EMG-based prediction of shoulder and elbow kinematics in able-bodied and spinal cord injured individuals,” *IEEE Trans. Rehab. Eng.*, vol. 8, no. 4, pp. 471–480, Dec. 2000, doi: 10.1109/86.895950.
[264] L. Dipietro, A. M. Sabatini, and P. Dario, “Artificial neural network model of the mapping between electromyographic activation and trajectory patterns in free-arm movements,” *Med. Biol. Eng. Comput.*, vol. 41, no. 2, pp. 124–132, Mar. 2003, doi: 10.1007/BF02344879.
[265] S. Dosen and D. B. Popovic, “Accelerometers and Force Sensing Resistors for Optimal Control of Walking of a Hemiplegic,” *IEEE Trans. Biomed. Eng.*, vol. 55, no. 8, pp. 1973–1984, Aug. 2008, doi: 10.1109/TBME.2008.919715.
[266] M. E. Hahn and K. B. O’Keefe, “A NEURAL NETWORK MODEL FOR ESTIMATION OF NET JOINT MOMENTS DURING NORMAL GAIT,” *J. Musculoskelet. Res.*, vol. 11, no. 03, pp. 117–126, Sep. 2008, doi: 10.1142/S0218957708002036.
[267] A. L. Delis, J. L. A. Carvalho, A. F. da Rocha, R. U. Ferreira, S. S. Rodrigues, and G. A. Borges, “Estimation of the knee joint angle from surface electromyographic signals for active control of leg prostheses,” *Physiol. Meas.*, vol. 30, no. 9, pp. 931–946, Sep. 2009, doi: 10.1088/0967-3334/30/9/005.
[268] N. Jiang, K. B. Englehart, and P. A. Parker, “Extracting Simultaneous and Proportional Neural Control Information for Multiple-DOF Prostheses From the Surface Electromyographic Signal,”

IEEE Trans. Biomed. Eng., vol. 56, no. 4, pp. 1070–1080, Apr. 2009, doi: 10.1109/TBME.2008.2007967.

[269] J. L. G. Nielsen, S. Holmgaard, Ning Jiang, K. B. Englehart, D. Farina, and P. A. Parker, "Simultaneous and Proportional Force Estimation for Multifunction Myoelectric Prostheses Using Mirrored Bilateral Training," *IEEE Trans. Biomed. Eng.*, vol. 58, no. 3, pp. 681–688, Mar. 2011, doi: 10.1109/TBME.2010.2068298.

[270] W. H. K. de Vries, H. E. J. Veeger, C. T. M. Baten, and F. C. T. van der Helm, "Determining a long term ambulatory load profile of the shoulder joint: Neural networks predicting input for a musculoskeletal model," *Human Movement Science*, vol. 31, no. 2, pp. 419–428, Apr. 2012, doi: 10.1016/j.humov.2011.07.010.

[271] N. Jiang, J. L. Vest-Nielsen, S. Muceli, and D. Farina, "EMG-based simultaneous and proportional estimation of wrist/hand kinematics in uni-lateral trans-radial amputees," *J NeuroEngineering Rehabil*, vol. 9, no. 1, p. 42, 2012, doi: 10.1186/1743-0003-9-42.

[272] S. Muceli and D. Farina, "Simultaneous and Proportional Estimation of Hand Kinematics From EMG During Mirrored Movements at Multiple Degrees-of-Freedom," *IEEE Trans. Neural Syst. Rehabil. Eng.*, vol. 20, no. 3, pp. 371–378, May 2012, doi: 10.1109/TNSRE.2011.2178039.

[273] E. N. Kamavuako, E. J. Scheme, and K. B. Englehart, "Wrist torque estimation during simultaneous and continuously changing movements: surface vs. untargeted intramuscular EMG," *Journal of Neurophysiology*, vol. 109, no. 11, pp. 2658–2665, Jun. 2013, doi: 10.1152/jn.00086.2013.

[274] N. Jiang, S. Muceli, B. Graimann, and D. Farina, "Effect of arm position on the prediction of kinematics from EMG in amputees," *Med Biol Eng Comput*, vol. 51, no. 1–2, pp. 143–151, Feb. 2013, doi: 10.1007/s11517-012-0979-4.

[275] W. H. K. de Vries, H. E. J. Veeger, C. T. M. Baten, and F. C. T. van der Helm, "Can shoulder joint reaction forces be estimated by neural networks?," *Journal of Biomechanics*, vol. 49, no. 1, pp. 73–79, Jan. 2016, doi: 10.1016/j.jbiomech.2015.11.019.

[276] Q. Zhang, R. Liu, W. Chen, and C. Xiong, "Simultaneous and Continuous Estimation of Shoulder and Elbow Kinematics from Surface EMG Signals," *Front. Neurosci.*, vol. 11, p. 280, May 2017, doi: 10.3389/fnins.2017.00280.

[277] Q. Ding, J. Han, and X. Zhao, "Continuous Estimation of Human Multi-Joint Angles From sEMG Using a State-Space Model," *IEEE Trans. Neural Syst. Rehabil. Eng.*, vol. 25, no. 9, pp. 1518–1528, Sep. 2017, doi: 10.1109/TNSRE.2016.2639527.

[278] E. A. Clancy, C. Martinez-Luna, M. Wartenberg, C. Dai, and T. R. Farrell, "Two degrees of freedom quasi-static EMG-force at the wrist using a minimum number of electrodes," *Journal of Electromyography and Kinesiology*, vol. 34, pp. 24–36, Jun. 2017, doi: 10.1016/j.jelekin.2017.03.004.

[279] F. J. Wouda *et al.*, "Estimation of Vertical Ground Reaction Forces and Sagittal Knee Kinematics During Running Using Three Inertial Sensors," *Front. Physiol.*, vol. 9, p. 218, Mar. 2018, doi: 10.3389/fphys.2018.00218.

[280] J. Chen, X. Zhang, Y. Cheng, and N. Xi, "Surface EMG based continuous estimation of human lower limb joint angles by using deep belief networks," *Biomedical Signal Processing and Control*, vol. 40, pp. 335–342, Feb. 2018, doi: 10.1016/j.bspc.2017.10.002.

[281] C. Dai and X. Hu, "Finger Joint Angle Estimation Based on Motoneuron Discharge Activities," *IEEE J. Biomed. Health Inform.*, Jul. 2019, doi: 10.1109/JBHI.2019.2926307.

[282] C. Dai, Z. Zhu, C. Martinez-Luna, T. R. Hunt, T. R. Farrell, and E. A. Clancy, "Two degrees of freedom, dynamic, hand-wrist EMG-force using a minimum number of electrodes," *Journal of Electromyography and Kinesiology*, vol. 47, pp. 10–18, Aug. 2019, doi: 10.1016/j.jelekin.2019.04.003.

[283] T. Kapelner *et al.*, "Predicting wrist kinematics from motor unit discharge timings for the control of active prostheses," *J NeuroEngineering Rehabil*, vol. 16, no. 1, p. 47, Dec. 2019, doi: 10.1186/s12984-019-0516-x.

[284] W. Tang and E. S. Sazonov, "Highly Accurate Recognition of Human Postures and Activities Through Classification With Rejection," *IEEE Journal of Biomedical and Health Informatics*, vol. 18, no. 1, pp. 309–315, Jan. 2014, doi: 10.1109/JBHI.2013.2287400.

[285] D. S. Kern, J. G. Semmler, and R. M. Enoka, “Long-term activity in upper- and lower-limb muscles of humans,” *Journal of Applied Physiology*, vol. 91, no. 5, pp. 2224–2232, Nov. 2001, doi: 10.1152/jappl.2001.91.5.2224.
[286] O. Tikkanen *et al.*, “Muscle Activity and Inactivity Periods during Normal Daily Life,” *PLoS ONE*, vol. 8, no. 1, p. e52228, Jan. 2013, doi: 10.1371/journal.pone.0052228.
[287] T. Finni, P. Haakana, A. J. Pesola, and T. Pullinen, “Exercise for fitness does not decrease the muscular inactivity time during normal daily life: Inactivity time is independent of exercise,” *Scand J Med Sci Sports*, vol. 24, no. 1, pp. 211–219, Feb. 2014, doi: 10.1111/j.1600-0838.2012.01456.x.
[288] Y. Gao *et al.*, “Children’s physical activity and sedentary time compared using assessments of accelerometry counts and muscle activity level,” *PeerJ*, vol. 6, p. e5437, Aug. 2018, doi: 10.7717/peerj.5437.
[289] E. A. Clancy, E. L. Morin, and R. Merletti, “Sampling, noise-reduction and amplitude estimation issues in surface electromyography,” *Journal of Electromyography and Kinesiology*, vol. 12, pp. 1–16, 2002.
[290] T. S. Buchanan, D. G. Lloyd, K. Manal, and T. F. Besier, “Neuromusculoskeletal Modeling: Estimation of Muscle Forces and Joint Moments and Movements from Measurements of Neural Command,” *Journal of Applied Biomechanics*, vol. 20, no. 4, pp. 367–395, Nov. 2004, doi: 10.1123/jab.20.4.367.
[291] R. R. Neptune, D. J. Clark, and S. A. Kautz, “Modular control of human walking: A simulation study,” *Journal of Biomechanics*, vol. 42, no. 9, pp. 1282–1287, Jun. 2009, doi: 10.1016/j.jbiomech.2009.03.009.
[292] M. C. Tresch and A. Jarc, “The case for and against muscle synergies,” *Current Opinion in Neurobiology*, vol. 19, no. 6, pp. 601–607, Dec. 2009, doi: 10.1016/j.conb.2009.09.002.
[293] M. C. Tresch, V. C. K. Cheung, and A. d’Avella, “Matrix Factorization Algorithms for the Identification of Muscle Synergies: Evaluation on Simulated and Experimental Data Sets,” *Journal of Neurophysiology*, vol. 95, no. 4, pp. 2199–2212, Apr. 2006, doi: 10.1152/jn.00222.2005.
[294] N. A. Bianco, C. Patten, and B. J. Fregly, “Can Measured Synergy Excitations Accurately Construct Unmeasured Muscle Excitations?,” *Journal of Biomechanical Engineering*, vol. 140, no. 1, p. 011011, Jan. 2018, doi: 10.1115/1.4038199.
[295] Lin Wang and T. S. Buchanan, “Prediction of joint moments using a neural network model of muscle activations from EMG signals,” *IEEE Trans. Neural Syst. Rehabil. Eng.*, vol. 10, no. 1, pp. 30–37, Mar. 2002, doi: 10.1109/TNSRE.2002.1021584.
[296] M. Reichstein *et al.*, “Deep learning and process understanding for data-driven Earth system science,” *Nature*, vol. 566, no. 7743, pp. 195–204, Feb. 2019, doi: 10.1038/s41586-019-0912-1.
[297] Y. Xiong *et al.*, “Seamless global positioning system/inertial navigation system navigation method based on square-root cubature Kalman filter and random forest regression,” *Review of Scientific Instruments*, vol. 90, no. 1, p. 015101, Jan. 2019, doi: 10.1063/1.5079889.
[298] J. Pathak *et al.*, “Hybrid forecasting of chaotic processes: Using machine learning in conjunction with a knowledge-based model,” *Chaos*, vol. 28, no. 4, p. 041101, Apr. 2018, doi: 10.1063/1.5028373.
[299] “Artificial intelligence alone won’t solve the complexity of Earth sciences,” *Nature*, vol. 566, pp. 153–153, Feb. 2019, doi: 10.1038/d41586-019-00556-5.
[300] K. Gui, H. Liu, and D. Zhang, “A Practical and Adaptive Method to Achieve EMG-Based Torque Estimation for a Robotic Exoskeleton,” *IEEE/ASME Trans. Mechatron.*, vol. 24, no. 2, pp. 483–494, Apr. 2019, doi: 10.1109/TMECH.2019.2893055.
[301] D. Jarchi, B. Lo, C. Wong, E. Ieong, D. Nathwani, and G.-Z. Yang, “Gait Analysis From a Single Ear-Worn Sensor: Reliability and Clinical Evaluation for Orthopaedic Patients,” *IEEE Trans. Neural Syst. Rehabil. Eng.*, vol. 24, no. 8, pp. 882–892, Aug. 2016, doi: 10.1109/TNSRE.2015.2477720.
[302] E. A. Clancy, S. Bouchard, and D. Rancourt, “Estimation and application of EMG amplitude during dynamic contractions,” *IEEE Eng. Med. Biol. Mag.*, vol. 20, no. 6, pp. 47–54, Dec. 2001, doi: 10.1109/51.982275.

[303] A. F. Huxley, “Muscular contraction.,” *The Journal of Physiology*, vol. 243, no. 1, pp. 1–43, 1974, doi: 10.1113/jphysiol.1974.sp010740.
[304] K. L. Rodriguez, R. T. Roemmich, B. Cam, B. J. Fregly, and C. J. Hass, “Persons with Parkinson’s disease exhibit decreased neuromuscular complexity during gait,” *Clinical Neurophysiology*, vol. 124, no. 7, pp. 1390–1397, Jul. 2013, doi: 10.1016/j.clinph.2013.02.006.
[305] A. L. Goldberg, “PROTEIN SYNTHESIS DURING WORK-INDUCED GROWTH OF SKELETAL MUSCLE,” *J Cell Biol*, vol. 36, no. 3, pp. 653–658, Mar. 1968.
[306] B. W. Heller, P. H. Veltink, N. J. M. Rijkhoff, W. L. C. Rutten, and B. J. Andrews, “Reconstructing muscle activation during normal walking: a comparison of symbolic and connectionist machine learning techniques,” *Biol. Cybern.*, vol. 69, no. 4, pp. 327–335, Aug. 1993, doi: 10.1007/BF00203129.
[307] M. A. Nussbaum, D. B. Chaffin, and B. J. Martin, “A back-propagation neural network model of lumbar muscle recruitment during moderate static exertions,” *J Biomech*, vol. 28, no. 9, pp. 1015–1024, Sep. 1995, doi: 10.1016/0021-9290(94)00171-Y.
[308] S. D. Prentice, A. E. Patla, and D. A. Stacey, “Artificial neural network model for the generation of muscle activation patterns for human locomotion,” *Journal of Electromyography and Kinesiology*, vol. 11, no. 1, pp. 19–30, Feb. 2001, doi: 10.1016/S1050-6411(00)00038-9.
[309] L. A. Johnson and A. J. Fuglevand, “Evaluation of probabilistic methods to predict muscle activity: implications for neuroprosthetics,” *J. Neural Eng.*, vol. 6, no. 5, p. 055008, Oct. 2009, doi: 10.1088/1741-2560/6/5/055008.
[310] A. Erdemir, S. McLean, W. Herzog, and A. J. van den Bogert, “Model-based estimation of muscle forces exerted during movements,” *Clinical Biomechanics*, vol. 22, no. 2, pp. 131–154, Feb. 2007, doi: 10.1016/j.clinbiomech.2006.09.005.
[311] J. Konrath, A. Karatsidis, H. Schepers, G. Bellusci, M. de Zee, and M. Andersen, “Estimation of the Knee Adduction Moment and Joint Contact Force during Daily Living Activities Using Inertial Motion Capture,” *Sensors*, vol. 19, no. 7, p. 1681, Apr. 2019, doi: 10.3390/s19071681.
[312] K. P. Körding and D. M. Wolpert, “Bayesian integration in sensorimotor learning,” *Nature*, vol. 427, no. 6971, pp. 244–247, Jan. 2004, doi: 10.1038/nature02169.
[313] R. Gurchiek, A. Ursiny, and R. McGinnis, “Modeling muscle synergies as a Gaussian process: Estimating unmeasured muscle excitations using a measured subset,” presented at the 42nd Annual International Conferences of the IEEE Engineering in Medicine and Biology Society, Jul. 2020.
[314] A. Papoulis, *Probability, Random Variables, and Stochastic Processes*, 3rd ed. New York, NY, USA: McGraw-Hill, Inc., 1991.
[315] Richard A. Johnson and Dean W. Wichern, *Applied Multivariate Statistical Analysis*, 2nd ed. Englewood Cliffs, NJ, USA: Prentice-Hall, Inc., 1988.
[316] C. E. Rasmussen and H. Nickisch, “Gaussian Processes for Machine Learning (GPML) Toolbox,” *Journal of Machine Learning Research*, vol. 11, no. 100, pp. 3011–3015, 2010.
[317] Carl E. Rasmussen and Hannes Nickisch, *Gaussian Processes for Machine Learning (GPML) Toolbox version 4.2*. 2018.
[318] H. J. Hermens, B. Freriks, C. Disselhorst-Klug, and G. Rau, “Development of recommendations for SEMG sensors and sensor placement procedures,” *Journal of Electromyography and Kinesiology*, vol. 10, no. 5, pp. 361–374, Oct. 2000, doi: 10.1016/S1050-6411(00)00027-4.
[319] S. R. Ward, C. M. Eng, L. H. Smallwood, and R. L. Lieber, “Are Current Measurements of Lower Extremity Muscle Architecture Accurate?,” *Clin Orthop Relat Res*, vol. 467, no. 4, pp. 1074–1082, Apr. 2009, doi: 10.1007/s11999-008-0594-8.
[320] C. K. I. Williams, “Computation with Infinite Neural Networks,” *Neural Computation*, vol. 10, no. 5, pp. 1203–1216, Jul. 1998, doi: 10.1162/089976698300017412.
[321] H. S. Milner-Brown, R. B. Stein, and R. Yemm, “The contractile properties of human motor units during voluntary isometric contractions,” *The Journal of Physiology*, vol. 228, no. 2, pp. 285–306, Jan. 1973, doi: 10.1113/jphysiol.1973.sp010087.
[322] N. C. Silver and W. P. Dunlap, “Averaging correlation coefficients: Should Fisher’s z transformation be used?,” *Journal of Applied Psychology*, vol. 72, no. 1, pp. 146–148, 1987, doi: 10.1037/0021-9010.72.1.146.

[323] R. Taylor, “Interpretation of the Correlation Coefficient: A Basic Review:,” *Journal of Diagnostic Medical Sonography*, Jul. 2016, doi: 10.1177/875647939000600106.
[324] K. Manal, K. Gravare-Silbernagel, and T. S. Buchanan, “A real-time EMG-driven musculoskeletal model of the ankle,” *Multibody Syst Dyn*, vol. 28, no. 1–2, pp. 169–180, Aug. 2012, doi: 10.1007/s11044-011-9285-4.
[325] D. Rimini, V. Agostini, and M. Knaflitz, “Intra-Subject Consistency during Locomotion: Similarity in Shared and Subject-Specific Muscle Synergies,” *Front. Hum. Neurosci.*, vol. 11, p. 586, Dec. 2017, doi: 10.3389/fnhum.2017.00586.
[326] A. J. Baliunas *et al.*, “Increased knee joint loads during walking are present in subjects with knee osteoarthritis,” *Osteoarthritis and Cartilage*, vol. 10, no. 7, pp. 573–579, Jul. 2002, doi: 10.1053/joca.2002.0797.
[327] K. R. Kaufman, C. Hughes, B. F. Morrey, M. Morrey, and K.-N. An, “Gait characteristics of patients with knee osteoarthritis,” *Journal of Biomechanics*, vol. 34, no. 7, pp. 907–915, Jul. 2001, doi: 10.1016/S0021-9290(01)00036-7.
[328] M. W. Creaby, “It’s not all about the knee adduction moment: the role of the knee flexion moment in medial knee joint loading,” *Osteoarthritis and Cartilage*, vol. 23, no. 7, pp. 1038–1040, Jul. 2015, doi: 10.1016/j.joca.2015.03.032.
[329] J. M. Timoney *et al.*, “Return of normal gait patterns after anterior cruciate ligament reconstruction,” *Am J Sports Med*, vol. 21, no. 6, pp. 887–889, Nov. 1993, doi: 10.1177/036354659302100623.
[330] J. M. Moore *et al.*, “Lower limb biomechanics before and after anterior cruciate ligament reconstruction: A systematic review,” *Journal of Biomechanics*, vol. 106, p. 109828, Jun. 2020, doi: 10.1016/j.jbiomech.2020.109828.
[331] H.-L. Teng *et al.*, “Gait Characteristics Associated With a Greater Increase in Medial Knee Cartilage T1ρ and T2 Relaxation Times in Patients Undergoing Anterior Cruciate Ligament Reconstruction,” *Am J Sports Med*, vol. 45, no. 14, pp. 3262–3271, Dec. 2017, doi: 10.1177/0363546517723007.
[332] K. E. Webster, J. E. Wittwer, J. O’Brien, and J. A. Feller, “Gait Patterns after Anterior Cruciate Ligament Reconstruction are Related to Graft Type,” *Am J Sports Med*, vol. 33, no. 2, pp. 247–254, Feb. 2005, doi: 10.1177/0363546504266483.
[333] M. Asaeda *et al.*, “Gender differences in the restoration of knee joint biomechanics during gait after anterior cruciate ligament reconstruction,” *The Knee*, vol. 24, no. 2, pp. 280–288, Mar. 2017, doi: 10.1016/j.knee.2017.01.001.
[334] K. F. Reid and R. A. Fielding, “Skeletal muscle power: a critical determinant of physical functioning in older adults,” *Exerc Sport Sci Rev*, vol. 40, no. 1, pp. 4–12, Jan. 2012, doi: 10.1097/JES.0b013e31823b5f13.
[335] G. R. Marcotte, D. W. D. West, and K. Baar, “The Molecular Basis for Load-Induced Skeletal Muscle Hypertrophy,” *Calcif Tissue Int*, vol. 96, no. 3, pp. 196–210, Mar. 2015, doi: 10.1007/s00223-014-9925-9.
[336] R. S. Husted, “The relationship between prescribed pre-operative knee-extensor exercise dosage and effect on knee-extensor strength prior to and following total knee arthroplasty: a systematic review and meta-regression analysis of randomized controlled trials,” *Osteoarthr. Cartil.*, vol. 28, no. 1, pp. 1412–1426, 2020.
[337] J. L. Nielsen, K. Arp, M. L. Villadsen, S. S. Christensen, and P. Aagaard, “Rate of Force Development Remains Reduced in the Knee Flexors 3 to 9 Months After Anterior Cruciate Ligament Reconstruction Using Medial Hamstring Autografts: A Cross-Sectional Study,” *Am J Sports Med*, vol. 48, no. 13, pp. 3214–3223, Nov. 2020, doi: 10.1177/0363546520960108.
[338] A. C. Thomas, E. M. Wojtys, C. Brandon, and R. M. Palmieri-Smith, “Muscle atrophy contributes to quadriceps weakness after anterior cruciate ligament reconstruction,” *Journal of Science and Medicine in Sport*, vol. 19, no. 1, pp. 7–11, Jan. 2016, doi: 10.1016/j.jsams.2014.12.009.
[339] M. J. Toth *et al.*, “Utility of Neuromuscular Electrical Stimulation to Preserve Quadriceps Muscle Fiber Size and Contractility After Anterior Cruciate Ligament Injuries and Reconstruction: A

Randomized, Sham-Controlled, Blinded Trial," *Am J Sports Med*, vol. 48, no. 10, pp. 2429–2437, Aug. 2020, doi: 10.1177/0363546520933622.
[340] J. M. Hart, B. Pietrosimone, J. Hertel, and C. D. Ingersoll, "Quadriceps Activation Following Knee Injuries: A Systematic Review," *Journal of Athletic Training*, vol. 45, no. 1, pp. 87–97, Jan. 2010, doi: 10.4085/1062-6050-45.1.87.
[341] S. D. Uhlrich, A. Silder, G. S. Beaupre, P. B. Shull, and S. L. Delp, "Subject-specific toe-in or toe-out gait modifications reduce the larger knee adduction moment peak more than a non-personalized approach," *Journal of Biomechanics*, vol. 66, pp. 103–110, Jan. 2018, doi: 10.1016/j.jbiomech.2017.11.003.
[342] F. Routhier *et al.*, "Clinicians' perspectives on inertial measurement units in clinical practice," *PLOS ONE*, vol. 15, no. 11, p. e0241922, Nov. 2020, doi: 10.1371/journal.pone.0241922.
[343] F. E. Zajac, R. R. Neptune, and S. A. Kautz, "Biomechanics and muscle coordination of human walking: Part I: Introduction to concepts, power transfer, dynamics and simulations," *Gait & posture*, vol. 16, no. 3, pp. 215–232, 2002.
[344] M. Millard, T. Uchida, A. Seth, and S. L. Delp, "Flexing Computational Muscle: Modeling and Simulation of Musculotendon Dynamics," *Journal of Biomechanical Engineering*, vol. 135, no. 2, p. 021005, Feb. 2013, doi: 10.1115/1.4023390.
[345] A. V. Hill, "The heat of shortening and the dynamic constants of muscle," *Proceedings of the Royal Society of London B: Biological Sciences*, vol. 126, no. 843, pp. 136–195, 1938.
[346] A. M. Gordon, A. F. Huxley, and F. J. Julian, "The variation in isometric tension with sarcomere length in vertebrate muscle fibres," *The Journal of Physiology*, vol. 184, no. 1, pp. 170–192, May 1966, doi: 10.1113/jphysiol.1966.sp007909.
[347] J. R. Potvin, R. W. Norman, and S. M. McGill, "Mechanically corrected EMG for the continuous estimation of erector spinae muscle loading during repetitive lifting," *Europ. J. Appl. Physiol.*, vol. 74, no. 1–2, pp. 119–132, Aug. 1996, doi: 10.1007/BF00376504.
[348] J. J. Woods and B. Bigland-Ritchie, "Linear and non-linear surface EMG/force relationships in human muscles. An anatomical/functional argument for the existence of both," *Am J Phys Med*, vol. 62, no. 6, pp. 287–299, Dec. 1983.
[349] F. E. Zajac, "Muscle and tendon: properties, models, scaling, and application to biomechanics and motor control," *Crit Rev Biomed Eng*, vol. 17, no. 4, pp. 359–411, 1989.
[350] L. Schutte, "Using musculoskeletal models to explore strategies for improving performance in electrical stimulation-induced leg cycle ergometry," PhD Dissertation, Stanford University, 1993.
[351] A. C. Guimaraes, W. Herzog, M. Hulliger, Y. T. Zhang, and S. Day, "Effects of muscle length on the EMG-force relationship of the cat soleus muscle studied using non-periodic stimulation of ventral root filaments.," *Journal of Experimental Biology*, vol. 193, no. 1, pp. 49–64, Aug. 1994.
[352] A. J. van den Bogert, D. Blana, and D. Heinrich, "Implicit methods for efficient musculoskeletal simulation and optimal control," *Procedia IUTAM*, vol. 2, pp. 297–316, 2011, doi: 10.1016/j.piutam.2011.04.027.
[353] T. F. Besier, M. Fredericson, G. E. Gold, G. S. Beaupré, and S. L. Delp, "Knee muscle forces during walking and running in patellofemoral pain patients and pain-free controls," *Journal of Biomechanics*, vol. 42, no. 7, pp. 898–905, May 2009, doi: 10.1016/j.jbiomech.2009.01.032.
[354] T. S. Buchanan, D. G. Lloyd, K. Manal, and T. F. Besier, "Estimation of Muscle Forces and Joint Moments Using a Forward-Inverse Dynamics Model:," *Medicine & Science in Sports & Exercise*, vol. 37, no. 11, pp. 1911–1916, Nov. 2005, doi: 10.1249/01.mss.0000176684.24008.6f.
[355] M. D. Klein Horsman, H. F. J. M. Koopman, F. C. T. van der Helm, L. P. Prosé, and H. E. J. Veeger, "Morphological muscle and joint parameters for musculoskeletal modelling of the lower extremity," *Clinical Biomechanics*, vol. 22, no. 2, pp. 239–247, Feb. 2007, doi: 10.1016/j.clinbiomech.2006.10.003.
[356] F. L. Markley and D. Mortari, "Quaternion Attitude Estimation Using Vector Observations," *J of Astronaut Sci*, vol. 48, no. 2–3, pp. 359–380, Jun. 2000, doi: 10.1007/BF03546284.
[357] M. D. Shuster and S. D. Oh, "Three-axis attitude determination from vector observations," *Journal of Guidance and Control*, vol. 4, no. 1, pp. 70–77, 1981, doi: 10.2514/3.19717.

[358] C. W. Spoor and F. E. Veldpaus, “Rigid body motion calculated from spatial co-ordinates of markers,” *Journal of Biomechanics*, vol. 13, no. 4, pp. 391–393, Jan. 1980, doi: 10.1016/0021-9290(80)90020-2.
[359] R. A. Siston and S. L. Delp, “Evaluation of a new algorithm to determine the hip joint center,” *Journal of Biomechanics*, vol. 39, no. 1, pp. 125–130, Jan. 2006, doi: 10.1016/j.jbiomech.2004.10.032.
[360] R. M. Ehrig, W. R. Taylor, G. N. Duda, and M. O. Heller, “A survey of formal methods for determining the centre of rotation of ball joints,” *Journal of Biomechanics*, vol. 39, no. 15, pp. 2798–2809, Jan. 2006, doi: 10.1016/j.jbiomech.2005.10.002.
[361] R. M. Ehrig, W. R. Taylor, G. N. Duda, and M. O. Heller, “A survey of formal methods for determining functional joint axes,” *Journal of Biomechanics*, vol. 40, no. 10, pp. 2150–2157, Jan. 2007, doi: 10.1016/j.jbiomech.2006.10.026.
[362] P. de Leva, “Adjustments to Zatsiorsky-Seluyanov’s segment inertia parameters,” *Journal of Biomechanics*, vol. 29, no. 9, pp. 1223–1230, Sep. 1996, doi: 10.1016/0021-9290(95)00178-6.
[363] G. Wu *et al.*, “ISB recommendation on definitions of joint coordinate system of various joints for the reporting of human joint motion—part I: ankle, hip, and spine,” *Journal of biomechanics*, vol. 35, no. 4, pp. 543–548, 2002.
[364] W. Herzog and L. J. Read, “Lines of action and moment arms of the major force-carrying structures crossing the human knee joint.,” *J Anat*, vol. 182, no. Pt 2, pp. 213–230, Apr. 1993.
[365] N. M. Fiorentino, J. S. Lin, K. B. Ridder, M. A. Guttman, E. R. McVeigh, and S. S. Blemker, “Rectus Femoris Knee Muscle Moment Arms Measured in Vivo During Dynamic Motion With Real-Time Magnetic Resonance Imaging,” *Journal of Biomechanical Engineering*, vol. 135, no. 4, p. 044501, Apr. 2013, doi: 10.1115/1.4023523.
[366] A. J. van den Bogert, G. D. Smith, and B. M. Nigg, “In vivo determination of the anatomical axes of the ankle joint complex: An optimization approach,” *Journal of Biomechanics*, vol. 27, no. 12, pp. 1477–1488, Dec. 1994, doi: 10.1016/0021-9290(94)90197-X.
[367] M. Shuster, “A Survey of Attitude Representations,” *The Journal of the Astronautical Sciences*, vol. 41, no. 4, pp. 439–517, 1993.
[368] P. Betsch and R. Siebert, “Rigid body dynamics in terms of quaternions: Hamiltonian formulation and conserving numerical integration,” *International Journal for Numerical Methods in Engineering*, vol. 79, no. 4, pp. 444–473, Jul. 2009, doi: 10.1002/nme.2586.
[369] M. S. Andersen, M. Damsgaard, and J. Rasmussen, “Kinematic analysis of over-determinate biomechanical systems,” *Computer Methods in Biomechanics and Biomedical Engineering*, vol. 12, no. 4, pp. 371–384, Aug. 2009, doi: 10.1080/10255840802459412.
[370] T. M. G. J. van Eijden, W. de Boer, and W. A. Weijs, “The orientation of the distal part of the quadriceps femoris muscle as a function of the knee flexion-extension angle,” *Journal of Biomechanics*, vol. 18, no. 10, pp. 803–809, Jan. 1985, doi: 10.1016/0021-9290(85)90055-7.
[371] J. B. Kuipers, *Quaternions and Rotation Sequences*. Princeton, NJ: Princeton University Press, 1999.
[372] D. G. E. Robertson and J. J. Dowling, “Design and responses of Butterworth and critically damped digital filters,” *Journal of Electromyography and Kinesiology*, vol. 13, no. 6, pp. 569–573, Dec. 2003, doi: 10.1016/S1050-6411(03)00080-4.
[373] E. M. Arnold, S. R. Hamner, A. Seth, M. Millard, and S. L. Delp, “How muscle fiber lengths and velocities affect muscle force generation as humans walk and run at different speeds,” *Journal of Experimental Biology*, vol. 216, no. 11, pp. 2150–2160, Jun. 2013, doi: 10.1242/jeb.075697.
[374] A. J. Meyer, C. Patten, and B. J. Fregly, “Lower extremity EMG-driven modeling of walking with automated adjustment of musculoskeletal geometry,” *PLoS ONE*, vol. 12, no. 7, p. e0179698, Jul. 2017, doi: 10.1371/journal.pone.0179698.
[375] B. Shahriari, K. Swersky, Z. Wang, R. P. Adams, and N. de Freitas, “Taking the Human Out of the Loop: A Review of Bayesian Optimization,” *Proc. IEEE*, vol. 104, no. 1, pp. 148–175, Jan. 2016, doi: 10.1109/JPROC.2015.2494218.

[376] E. C. Garrido-Merchán and D. Hernández-Lobato, “Dealing with categorical and integer-valued variables in Bayesian Optimization with Gaussian processes,” *Neurocomputing*, vol. 380, pp. 20–35, Mar. 2020, doi: 10.1016/j.neucom.2019.11.004.
[377] F. De Groote, A. L. Kinney, A. V. Rao, and B. J. Fregly, “Evaluation of Direct Collocation Optimal Control Problem Formulations for Solving the Muscle Redundancy Problem,” *Ann Biomed Eng*, vol. 44, no. 10, pp. 2922–2936, 2016, doi: 10.1007/s10439-016-1591-9.
[378] D. G. Thelen, “Adjustment of Muscle Mechanics Model Parameters to Simulate Dynamic Contractions in Older Adults,” *Journal of Biomechanical Engineering*, vol. 125, no. 1, pp. 70–77, Feb. 2003, doi: 10.1115/1.1531112.
[379] L. Modenese, E. Ceseracciu, M. Reggiani, and D. G. Lloyd, “Estimation of musculotendon parameters for scaled and subject specific musculoskeletal models using an optimization technique,” *Journal of Biomechanics*, vol. 49, no. 2, pp. 141–148, Jan. 2016, doi: 10.1016/j.jbiomech.2015.11.006.
[380] E. M. Arnold and S. L. Delp, “Fibre operating lengths of human lower limb muscles during walking,” *Phil. Trans. R. Soc. B*, vol. 366, no. 1570, pp. 1530–1539, May 2011, doi: 10.1098/rstb.2010.0345.
[381] G. Yamaguchi, A. Sawa, D. Moran, M. Fessler, and J. Winters, “A Survey of Human Musculotendon Actuator Parameters,” in *Multiple Muscle Systems: Biomechanics and Movement Organization*, J. Winters and S. L.-Y. Woo, Eds. New York, NY: Springer New York, 1990, pp. 69–93.
[382] J. M. Winters and L. Stark, “Estimated mechanical properties of synergistic muscles involved in movements of a variety of human joints,” *Journal of Biomechanics*, vol. 21, no. 12, pp. 1027–1041, Jan. 1988, doi: 10.1016/0021-9290(88)90249-7.
[383] J. He, W. S. Levine, and G. E. Loeb, “Feedback gains for correcting small perturbations to standing posture,” *IEEE Trans. Automat. Contr.*, vol. 36, no. 3, pp. 322–332, Mar. 1991, doi: 10.1109/9.73565.
[384] K. Manal and T. S. Buchanan, “A one-parameter neural activation to muscle activation model: estimating isometric joint moments from electromyograms,” *Journal of Biomechanics*, vol. 36, no. 8, pp. 1197–1202, Aug. 2003, doi: 10.1016/S0021-9290(03)00152-0.
[385] T. Seel, T. Schauer, and J. Raisch, “Joint axis and position estimation from inertial measurement data by exploiting kinematic constraints,” Oct. 2012, pp. 45–49, doi: 10.1109/CCA.2012.6402423.
[386] R. McGinnis and N. Perkins, “A Highly Miniaturized, Wireless Inertial Measurement Unit for Characterizing the Dynamics of Pitched Baseballs and Softballs,” *SENSORS*, vol. 12, no. 9, pp. 11933–11945, Sep. 2012.
[387] R. McGinnis, N. C. Perkins, and K. King, “Reconstructing Free-Flight Angular Velocity from a Miniaturized Wireless Accelerometer,” *J. Appl. Mech*, vol. 79, no. 4, Jul. 2012, doi: 10.1115/1.4006162.
[388] R. S. McGinnis and N. C. Perkins, “Inertial sensor based method for identifying spherical joint center of rotation,” *Journal of Biomechanics*, vol. 46, no. 14, pp. 2546–2549, Sep. 2013, doi: 10.1016/j.jbiomech.2013.07.017.
[389] G. Torres-Oviedo, J. M. Macpherson, and L. H. Ting, “Muscle Synergy Organization Is Robust Across a Variety of Postural Perturbations,” *Journal of Neurophysiology*, vol. 96, no. 3, pp. 1530–1546, Sep. 2006, doi: 10.1152/jn.00810.2005.
[390] A. Cimolato, G. Milandri, L. S. Mattos, E. De Momi, M. Laffranchi, and L. De Michieli, “Hybrid Machine Learning-Neuromusculoskeletal Modeling for Control of Lower Limb Prosthetics,” in *2020 8th IEEE RAS/EMBS International Conference for Biomedical Robotics and Biomechatronics (BioRob)*, New York City, NY, USA, Nov. 2020, pp. 557–563, doi: 10.1109/BioRob49111.2020.9224448.
[391] A. Falisse, S. Van Rossom, I. Jonkers, and F. De Groote, “EMG-Driven Optimal Estimation of Subject-SPECIFIC Hill Model Muscle–Tendon Parameters of the Knee Joint Actuators,” *IEEE Transactions on Biomedical Engineering*, vol. 64, no. 9, pp. 2253–2262, Sep. 2017, doi: 10.1109/TBME.2016.2630009.

[392] J. L. Krevolin, M. G. Pandy, and J. C. Pearce, “Moment arm of the patellar tendon in the human knee,” *Journal of Biomechanics*, vol. 37, no. 5, pp. 785–788, May 2004, doi: 10.1016/j.jbiomech.2003.09.010.
[393] S. Skals, M. K. Jung, M. Damsgaard, and M. S. Andersen, “Prediction of ground reaction forces and moments during sports-related movements,” *Multibody Syst Dyn*, vol. 39, no. 3, pp. 175–195, Mar. 2017, doi: 10.1007/s11044-016-9537-4.
[394] A. Karatsidis, G. Bellusci, H. Schepers, M. de Zee, M. Andersen, and P. Veltink, “Estimation of Ground Reaction Forces and Moments During Gait Using Only Inertial Motion Capture,” *Sensors*, vol. 17, no. 1, p. 75, Dec. 2016, doi: 10.3390/s17010075.
[395] E. C. Honert and K. E. Zelik, “Inferring Muscle-Tendon Unit Power from Ankle Joint Power during the Push-Off Phase of Human Walking: Insights from a Multiarticular EMG-Driven Model,” *PLOS ONE*, vol. 11, no. 10, p. e0163169, Oct. 2016, doi: 10.1371/journal.pone.0163169.
[396] R. A. Bogey, A. J. Gitter, and L. A. Barnes, “Determination of ankle muscle power in normal gait using an EMG-to-force processing approach,” *J Electromyogr Kinesiol*, vol. 20, no. 1, pp. 46–54, Feb. 2010, doi: 10.1016/j.jelekin.2008.09.013.
[397] M. Sartori, M. Reggiani, E. Pagello, and D. G. Lloyd, “Modeling the human knee for assistive technologies,” *IEEE Trans Biomed Eng*, vol. 59, no. 9, pp. 2642–2649, Sep. 2012, doi: 10.1109/TBME.2012.2208746.
[398] R. Gurchiek, A. Ursiny, and R. McGinnis, “Estimating muscle excitations using a reduced sEMG array across a range of walking speeds,” presented at the Dynamic Walking, May 2020, [Online]. Available: https://www.seas.upenn.edu/~posa/DynamicWalking2020/596-863-1-RV.pdf.
[399] I. Mileti *et al.*, “Muscle Activation Patterns Are More Constrained and Regular in Treadmill Than in Overground Human Locomotion,” *Front Bioeng Biotechnol*, vol. 8, p. 581619, 2020, doi: 10.3389/fbioe.2020.581619.
[400] D. Farina, “Interpretation of the Surface Electromyogram in Dynamic Contractions:,” *Exercise and Sport Sciences Reviews*, vol. 34, no. 3, pp. 121–127, Jul. 2006, doi: 10.1249/00003677-200607000-00006.
[401] T. Gale and W. Anderst, “Tibiofemoral helical axis of motion during the full gait cycle measured using biplane radiography,” *Medical Engineering & Physics*, vol. 86, pp. 65–70, Dec. 2020, doi: 10.1016/j.medengphy.2020.10.014.

Appendix A: Quaternion Algebra

Let $\mathrm{q} \in \mathbb{H}$ be a *quaternion* (denoted by lower-case roman font) defined as the sum of a vector part, $\boldsymbol{q} \in \mathbb{R}^3$ (denoted by lower-case, bolded, and italic font), and a scalar part, $q_4 \in \mathbb{R}$ (denoted by lower-case italic font), as per

$$\mathrm{q} = \boldsymbol{q} + q_4 \tag{A.1}$$

or equivalently

$$\mathrm{q} = q_1\boldsymbol{e_1} + q_2\boldsymbol{e_2} + q_3\boldsymbol{e_3} + q_4 \tag{A.2}$$

where $\boldsymbol{q} = q_1\boldsymbol{e_1} + q_2\boldsymbol{e_2} + q_3\boldsymbol{e_3}$ and $\{\boldsymbol{e_1}, \boldsymbol{e_2}, \boldsymbol{e_3}\}$ is the natural basis for $\mathbb{R}^3$ (orthonormal and right-handed). An arbitrary *Cartesian* or *spatial* vector, $\boldsymbol{v} \in \mathbb{R}^3$, has a corresponding quaternion representation, $\mathrm{v} \in \mathbb{H}$ (where correspondence is denoted by using the same letter), called a *pure quaternion*, where the scalar part of v is zero so that $\mathrm{v} = \boldsymbol{v} + 0$. An arbitrary scalar, $\alpha \in \mathbb{R}$, has a corresponding quaternion representation, $\alpha \in \mathbb{H}$, wherein the vector part of α is the zero vector, $\boldsymbol{0} = 0\boldsymbol{e_1} + 0\boldsymbol{e_2} + 0\boldsymbol{e_3}$, so that $\alpha = \boldsymbol{0} + \alpha$. In addition to the linear combinations A.1 and A.2, it is common to represent the quaternion q equivalently as the column vector of coefficients

$$\mathrm{q} = [q_1 \quad q_2 \quad q_3 \quad q_4]^T \tag{A.3}$$

or likewise

$$\mathrm{q} = \begin{bmatrix}\boldsymbol{q}^T & q_4\end{bmatrix}^T \tag{A.4}$$

where the superscript T denotes the matrix transpose operation. In this work, the representation of q or $\boldsymbol{q}$ as the linear combination in eqs. A.1 and A.2 or as the column vector of coefficients in eqs. A.3 and A.4 will be used interchangeably, will be clear from the context, and will be of no consequence except for matrix operations; namely, matrix multiplication and transposition will imply the column vector representation. The sum of two quaternions, $\mathrm{p} + \mathrm{q}$, is computed as the sum of like terms via

$$\mathrm{p} + \mathrm{q} = (p_1 + q_1)\boldsymbol{e_1} + (p_2 + q_2)\boldsymbol{e_2} + (p_3 + q_3)\boldsymbol{e_3} + (p_4 + q_4). \tag{A.5}$$

Thus, the zero element of $\mathbb{H}$ or *null quaternion*, 0 such that $\mathrm{q} + 0 = \mathrm{q}$, is the scalar quaternion

$$0 = \mathbf{0} + 0. \tag{A.6}$$

The *quaternion product* is based on the following relation:

$$\boldsymbol{e_i e_j} = \begin{cases} -\boldsymbol{e_i} \cdot \boldsymbol{e_j} & for\ i = j \\ \boldsymbol{e_i} \times \boldsymbol{e_j} & for\ i \neq j \end{cases} \tag{A.7}$$

where $\cdot$ denotes the dot product and $\times$ denotes the right-handed vector cross product. The product pq may be written

$$\mathrm{pq} = (p_1\boldsymbol{e_1} + p_2\boldsymbol{e_2} + p_3\boldsymbol{e_3} + p_4)(q_1\boldsymbol{e_1} + q_2\boldsymbol{e_2} + q_3\boldsymbol{e_3} + q_4) \tag{A.8}$$

and by the distributive property

$$\begin{aligned} \mathrm{pq} = {} & p_1q_1\boldsymbol{e_1 e_1} + p_1q_2\boldsymbol{e_1 e_2} + p_1q_3\boldsymbol{e_1 e_3} + p_1q_4\boldsymbol{e_1} + \\ & p_2q_1\boldsymbol{e_2 e_1} + p_2q_2\boldsymbol{e_2 e_2} + p_2q_3\boldsymbol{e_2 e_3} + p_2q_4\boldsymbol{e_2} + \\ & p_3q_1\boldsymbol{e_3 e_1} + p_3q_2\boldsymbol{e_3 e_2} + p_3q_3\boldsymbol{e_3 e_3} + p_3q_4\boldsymbol{e_3} + \\ & p_4q_1\boldsymbol{e_1} + p_4q_2\boldsymbol{e_2} + p_4q_3\boldsymbol{e_3} + p_4q_4. \end{aligned} \tag{A.9}$$

Substituting eq. A.7 into eq. A.9 and combining like terms yields

$$\begin{aligned} \mathrm{pq} = {} & (p_2q_3 - p_3q_2 + p_4q_1 + p_1q_4)\boldsymbol{e_1} + \\ & (p_3q_1 - p_1q_3 + p_4q_2 + p_2q_4)\boldsymbol{e_2} + \\ & (p_1q_2 - p_2q_1 + p_4q_3 + p_3q_4)\boldsymbol{e_3} + \\ & p_4q_4 - p_1q_1 - p_2q_2 - p_3q_3. \end{aligned} \tag{A.10}$$

which can be written

$$\mathrm{pq} = p_4\boldsymbol{q} + q_4\boldsymbol{p} + \boldsymbol{p} \times \boldsymbol{q} + p_4q_4 - \boldsymbol{p} \cdot \boldsymbol{q} \tag{A.11}$$

and thus if $\mathrm{r} = \mathrm{pq}$ then $\boldsymbol{r} = p_4\boldsymbol{q} + q_4\boldsymbol{p} + \boldsymbol{p} \times \boldsymbol{q}$ and $r_4 = p_4q_4 - \boldsymbol{p} \cdot \boldsymbol{q}$. Note that the quaternion product is associative but is not commutative due to the cross product in eq. A.11. Further, note that the product of a scalar quaternion, $\alpha = \mathbf{0} + \alpha_4$, and an arbitrary quaternion, $\mathrm{q} = \boldsymbol{q} + q_4$, results in the expected scalar multiplication $\alpha\mathrm{q} = \alpha_4\boldsymbol{q} + \alpha_4q_4$. For this reason, scalar quaternions will henceforth be referred to simply as

scalars and no distinction will be made between the two. The *identity quaternion*, 1 such that $1\mathrm{q} = \mathrm{q}$, is the scalar

$$1 = \mathbf{0} + 1. \tag{A.12}$$

Let $\widetilde{\boldsymbol{v}} \in \mathbb{R}^{3\times3}$ be the skew-symmetric matrix (i.e., $\widetilde{\boldsymbol{v}}^T = -\widetilde{\boldsymbol{v}}$) associated with the Cartesian vector $\boldsymbol{v} \in \mathbb{R}^3$ as per

$$\widetilde{\boldsymbol{v}} = \begin{bmatrix} 0 & -v_3 & v_2 \\ v_3 & 0 & -v_1 \\ -v_2 & v_1 & 0 \end{bmatrix} \tag{A.13}$$

such that $\boldsymbol{p} \times \boldsymbol{q} = \widetilde{\boldsymbol{p}}\boldsymbol{q}$. Then, with $\boldsymbol{p} \cdot \boldsymbol{q} = \boldsymbol{p}^T\boldsymbol{q}$, eq. A.11 can be written

$$\mathrm{pq} = \begin{bmatrix} \widetilde{\boldsymbol{p}} + p_4\boldsymbol{I}_3 & \boldsymbol{p} \\ -\boldsymbol{p}^T & p_4 \end{bmatrix} \mathrm{q} = \mathrm{P_L q} \tag{A.14}$$

where $\boldsymbol{I}_N \in \mathbb{R}^{N\times N}$ is the $N \times N$ identity matrix and the definition of $\mathrm{P_L} \in \mathbb{R}^{4\times4}$ is clear from eq. A.14. Equivalently, since $\widetilde{\boldsymbol{p}}\boldsymbol{q} = -\widetilde{\boldsymbol{q}}\boldsymbol{p}$, one has

$$\mathrm{pq} = \begin{bmatrix} -\widetilde{\boldsymbol{q}} + q_4\boldsymbol{I}_3 & \boldsymbol{q} \\ -\boldsymbol{q}^T & q_4 \end{bmatrix} \mathrm{p} = \mathrm{Q_R p}. \tag{A.15}$$

The real 4×4 matrices $\mathrm{P_L}$ and $\mathrm{Q_R}$ are called the left and right *quaternion product matrices* corresponding to the quaternions p and q, respectively. Thus, for clarity, $\mathrm{qp} = \mathrm{Q_L p}$ and $\mathrm{qp} = \mathrm{P_R q}$. The *magnitude* or *length* of the quaternion q, denoted $|\mathrm{q}|$, is a scalar computed as per

$$|\mathrm{q}|^2 = q_1^2 + q_2^2 + q_3^2 + q_4^2 \tag{A.16}$$

or equivalently

$$|\mathrm{q}|^2 = \mathrm{q}^T\mathrm{q}. \tag{A.17}$$

The *conjugate* of q, denoted $\bar{\mathrm{q}}$, is computed by negating the vector part:

$$\bar{\mathrm{q}} = [\, -\boldsymbol{q}^T \quad q_4 \,]^T. \tag{A.18}$$

By eqs. A.11 and A.18, one can show

$$\mathrm{q}\bar{\mathrm{q}} = \bar{\mathrm{q}}\mathrm{q} = |\mathrm{q}|^2. \qquad \text{A. 19}$$

Thus, if q is pure then $\bar{\mathrm{q}} = -\mathrm{q}$. Since, for $|\mathrm{q}|^2 \neq 0$,

$$1 = \frac{|\mathrm{q}|^2}{|\mathrm{q}|^2}$$

$$= \frac{\mathrm{q}\bar{\mathrm{q}}}{|\mathrm{q}|^2} = \frac{\bar{\mathrm{q}}\mathrm{q}}{|\mathrm{q}|^2} \qquad \text{A. 20}$$

and with 1 being the identity quaternion, the multiplicative inverse of q, q^{-1} where $1 = \mathrm{q}\mathrm{q}^{-1} = \mathrm{q}^{-1}\mathrm{q}$, is

$$\mathrm{q}^{-1} = \frac{\bar{\mathrm{q}}}{|\mathrm{q}|^2}. \qquad \text{A. 21}$$

Therefore,

$$\mathrm{q}^{-1} = \bar{\mathrm{q}} \quad for \quad |\mathrm{q}|^2 = 1 \qquad \text{A. 22}$$

in which case q is called a *unit quaternion*. As for eqs. A.14 and A.15, we use $\overline{\mathrm{P}}_{\mathrm{L}}$ and $\overline{\mathrm{Q}}_{\mathrm{R}}$ to denote the left and right quaternion product matrices corresponding to $\bar{\mathrm{p}}$ and $\bar{\mathrm{q}}$, respectively, so that

$$\bar{\mathrm{p}}\bar{\mathrm{q}} = \overline{\mathrm{P}}_{\mathrm{L}}\bar{\mathrm{q}} = \overline{\mathrm{Q}}_{\mathrm{R}}\bar{\mathrm{p}} \qquad \text{A. 23}$$

and from eqs. A.14, A.15, and A.18

$$\overline{\mathrm{P}}_{\mathrm{L}} = \mathrm{P}_{\mathrm{L}}^{T} \qquad \text{A. 24}$$

and

$$\overline{\mathrm{Q}}_{\mathrm{R}} = \mathrm{Q}_{\mathrm{R}}^{T}. \qquad \text{A. 25}$$

That is, conjugation and transposition are equivalent operations on a quaternion and its corresponding product matrix, respectively. Thus, if q is unit length, then by eqs. A.22 – A.25, one has

$$\mathrm{Q}_{\mathrm{R}}^{T} = \mathrm{Q}_{\mathrm{R}}^{-1} \quad and \quad \mathrm{Q}_{\mathrm{L}}^{T} = \mathrm{Q}_{\mathrm{L}}^{-1}. \qquad \text{A. 26}$$

From eqs. A.11 and A.18, the conjugate of the quaternion product pq is the product of the conjugates in reverse order since

$$\begin{aligned}\overline{\mathrm{pq}} &= -p_4\boldsymbol{q} - q_4\boldsymbol{p} - \boldsymbol{p}\times\boldsymbol{q} + p_4q_4 - \boldsymbol{p}\cdot\boldsymbol{q}\\ &= -p_4\boldsymbol{q} - q_4\boldsymbol{p} + \boldsymbol{q}\times\boldsymbol{p} + p_4q_4 - \boldsymbol{p}\cdot\boldsymbol{q}\\ &= p_4(-\boldsymbol{q}) + q_4(-\boldsymbol{p}) + (-\boldsymbol{q})\times(-\boldsymbol{p}) + p_4q_4 - (-\boldsymbol{p})\cdot(-\boldsymbol{q})\\ &= \bar{\mathrm{q}}\bar{\mathrm{p}}. \end{aligned} \quad \text{A. 27}$$

Thus, the magnitude of the quaternion product pq is the product of the magnitudes |p| and |q| since

$$\begin{aligned}|\mathrm{pq}| &= (\mathrm{pq})(\overline{\mathrm{pq}})\\ &= \mathrm{pq}\bar{\mathrm{q}}\bar{\mathrm{p}}\\ &= |\mathrm{q}|\mathrm{p}\bar{\mathrm{p}}\\ &= |\mathrm{q}||\mathrm{p}|. \end{aligned} \quad \text{A. 28}$$

Finally, we develop quaternion operations that are analogous to the vector cross product and dot product. Let $\mathrm{v}, \mathrm{w} \in \mathbb{H}$ be the pure quaternions corresponding to the Cartesian vectors $\boldsymbol{v}, \boldsymbol{w} \in \mathbb{R}^3$, respectively. The quaternion product of the pure quaternions v and w is given from eq. A.11 where, since $v_4 = w_4 = 0$,

$$\mathrm{vw} = \boldsymbol{v}\times\boldsymbol{w} - \boldsymbol{v}\cdot\boldsymbol{w} \quad \text{A. 29}$$

and also

$$\mathrm{wv} = -\boldsymbol{v}\times\boldsymbol{w} - \boldsymbol{v}\cdot\boldsymbol{w}. \quad \text{A. 30}$$

Thus,

$$\frac{1}{2}(\mathrm{vw} - \mathrm{wv}) = \boldsymbol{v}\times\boldsymbol{w} \quad \text{A. 31}$$

and

$$-\frac{1}{2}(\mathrm{vw} + \mathrm{wv}) = \boldsymbol{v}\cdot\boldsymbol{w}. \quad \text{A. 32}$$

Appendix B: Quaternion Parametrization of Attitude

Let $\boldsymbol{n} \in \mathbb{R}^3$ be a unit length Cartesian vector ($\boldsymbol{n}^T\boldsymbol{n} = 1$) and $\mathrm{q} \in \mathbb{H}$ be parametrized as per

$$\mathrm{q} = [\, s\boldsymbol{n}^T \quad c\,]^T \tag{B.1}$$

where

$$c = \cos\frac{\theta}{2} \tag{B.2}$$

and

$$s = \sin\frac{\theta}{2}. \tag{B.3}$$

Notice, q is a unit quaternion ($\mathrm{q}^T\mathrm{q} = 1$) and thus $\mathrm{q}^{-1} = \bar{\mathrm{q}}$ by eq. A.22. Let $\mathrm{v} \in \mathbb{H}$ be the pure quaternion corresponding to an arbitrary Cartesian vector $\boldsymbol{v} \in \mathbb{R}^3$ with $\boldsymbol{v} \neq \boldsymbol{0}$. In the following, the triple product $\mathrm{q}\mathrm{v}\bar{\mathrm{q}}$ will be shown to correspond to a rotation of $\boldsymbol{v}$ about the axis $\boldsymbol{n}$ through an angle θ. By eq. A.11,

$$\begin{aligned} \mathrm{v}\bar{\mathrm{q}} &= (\boldsymbol{v} + 0)(-s\boldsymbol{n} + c) \\ &= c\boldsymbol{v} + s\tilde{\boldsymbol{n}}\boldsymbol{v} + s\boldsymbol{n}^T\boldsymbol{v} \end{aligned} \tag{B.4}$$

and thus

$$\begin{aligned} \mathrm{q}\mathrm{v}\bar{\mathrm{q}} &= (s\boldsymbol{n} + c)(c\boldsymbol{v} + s\tilde{\boldsymbol{n}}\boldsymbol{v} + s\boldsymbol{n}^T\boldsymbol{v}) \\ &= c^2\boldsymbol{v} + s^2\boldsymbol{n}\boldsymbol{n}^T\boldsymbol{v} + s^2\tilde{\boldsymbol{n}}^2\boldsymbol{v} + 2cs\tilde{\boldsymbol{n}}\boldsymbol{v} + cs\boldsymbol{n}^T\boldsymbol{v} - cs\boldsymbol{n}^T\boldsymbol{v} - s^2\boldsymbol{n}^T\tilde{\boldsymbol{n}}\boldsymbol{v}. \end{aligned} \tag{B.5}$$

Let $\mathrm{v}' = \mathrm{q}\mathrm{v}\bar{\mathrm{q}}$ in eq. B.5. Then, the scalar part of v' is

$$\begin{aligned} \mathrm{v}'_4 &= cs\boldsymbol{n}^T\boldsymbol{v} - cs\boldsymbol{n}^T\boldsymbol{v} - s^2\boldsymbol{n}^T\tilde{\boldsymbol{n}}\boldsymbol{v} \\ &= 0 \end{aligned} \tag{B.6}$$

since $\boldsymbol{n}^T\tilde{\boldsymbol{n}} = \boldsymbol{0}^T$. Therefore, v' is pure and corresponds to the quaternion representation of the Cartesian vector $\boldsymbol{v}' \in \mathbb{R}^3$. Per eq. B.5, the vector part of v' is

$$\boldsymbol{v}' = c^2\boldsymbol{v} + s^2(\boldsymbol{n}\boldsymbol{n}^T + \tilde{\boldsymbol{n}}^2)\boldsymbol{v} + 2cs\tilde{\boldsymbol{n}}\boldsymbol{v}. \tag{B.7}$$

or equivalently

$$\boldsymbol{v}' = c^2\boldsymbol{v} + s^2\boldsymbol{v} + 2s^2\tilde{\boldsymbol{n}}^2\boldsymbol{v} + 2cs\tilde{\boldsymbol{n}}\boldsymbol{v} \tag{B.8}$$

since $\boldsymbol{n}\boldsymbol{n}^T = \tilde{\boldsymbol{n}}^2 + \boldsymbol{I}_3$ when $\boldsymbol{n}^T\boldsymbol{n} = 1$. Using the trigonometric relations

$$c^2 + s^2 = 1, \tag{B.9}$$

$$2s^2 = 1 - c_\theta, \tag{B.10}$$

and

$$2cs = s_\theta, \tag{B.11}$$

where $s_\theta = \sin\theta$ and $c_\theta = \cos\theta$, then eq. B.8 becomes

$$\boldsymbol{v}' = [\boldsymbol{I}_3 + s_\theta\tilde{\boldsymbol{n}} + (1 - c_\theta)\tilde{\boldsymbol{n}}^2]\boldsymbol{v} \tag{B.12}$$

which is the well-known Euler-Rodrigues rotation formula. We use $\boldsymbol{R}$ to denote the 3×3 rotation matrix in eq. B.12 as per

$$\boldsymbol{R} = \boldsymbol{I}_3 + s_\theta\tilde{\boldsymbol{n}} + (1 - c_\theta)\tilde{\boldsymbol{n}}^2 \tag{B.13}$$

which is an element of the special orthogonal group, $SO(3)$, since $\boldsymbol{R}^{-1} = \boldsymbol{R}^T$ and $\det\boldsymbol{R} = 1$. Thus, combining eqs. B.6, B.12, and B.13, we have

$$\mathrm{q}\mathrm{v}\bar{\mathrm{q}} = \begin{bmatrix} \boldsymbol{R}\boldsymbol{v} \\ 0 \end{bmatrix} = \begin{bmatrix} \boldsymbol{v}' \\ 0 \end{bmatrix} = \mathrm{v}' \tag{B.14}$$

and, with $\mathrm{q}^{-1} = \bar{\mathrm{q}}$, the inverse rotation is

$$\bar{\mathrm{q}}\mathrm{v}'\mathrm{q} = \begin{bmatrix} \boldsymbol{R}^T\boldsymbol{v}' \\ 0 \end{bmatrix} = \mathrm{v}. \tag{B.15}$$

Further, by eqs. A.14, A.15, A.23, and A.25,

$$\mathrm{q}\mathrm{v}\bar{\mathrm{q}} = \mathrm{Q}_\mathrm{L}\mathrm{Q}_\mathrm{R}^T \begin{bmatrix} \boldsymbol{v} \\ 0 \end{bmatrix} \tag{B.16}$$

where the 4×4 matrix $\mathrm{Q_L Q_R^T}$ has the form

$$\mathrm{Q_L Q_R^T} = \begin{bmatrix} \boldsymbol{M} & \boldsymbol{0} \\ \boldsymbol{0}^T & 1 \end{bmatrix}. \tag{B.17}$$

with $\boldsymbol{M} \in \mathbb{R}^{3\times3}$. Combining eqs. B.14, B.16, and B.17, we find $\boldsymbol{M} = \boldsymbol{R}$ which is parametrized by q as per

$$\boldsymbol{R} = \begin{bmatrix} q_1^2 - q_2^2 - q_3^2 + q_4^2 & 2(q_1q_2 - q_3q_4) & 2(q_1q_3 + q_2q_4) \\ 2(q_1q_2 + q_3q_4) & -q_1^2 + q_2^2 - q_3^2 + q_4^2 & 2(q_2q_3 - q_1q_4) \\ 2(q_1q_3 - q_2q_4) & 2(q_2q_3 + q_1q_4) & -q_1^2 - q_2^2 + q_3^2 + q_4^2 \end{bmatrix}. \tag{B.18}$$

To be clear about the perspective of $\boldsymbol{n}$ and $\boldsymbol{R}$, note that if $\{B\} = \{\boldsymbol{b}_1^W, \boldsymbol{b}_2^W, \boldsymbol{b}_3^W\}$ is a right-handed, orthonormal basis fixed to a rigid body where $\boldsymbol{b}_i^W$ is the representation of the i^{th} basis vector with respect to the world frame $\{W\}$ then

$$\boldsymbol{R} = [\, \boldsymbol{b}_1^W \quad \boldsymbol{b}_2^W \quad \boldsymbol{b}_3^W \,] \tag{B.19}$$

so that

$$\boldsymbol{v}^W = \boldsymbol{R}\boldsymbol{v}^B \tag{B.20}$$

where $\boldsymbol{v}^A$ denotes the representation of the Cartesian vector $\boldsymbol{v} \in \mathbb{R}^3$ with respect to the basis $\{A\}$, and one would imagine aligning $\{W\}$ with $\{B\}$ by rotating $\{W\}$ about the axis $\boldsymbol{n}$ (expressed with respect to $\{W\}$) through the angle θ.

To explain rotation composition, consider a body frame $\{B\}$ initially aligned with the world frame $\{W\}$ and that is rotated first about $\boldsymbol{n}_1^W$ through θ_1 and second about $\boldsymbol{n}_2^W$ through θ_2 where both $\boldsymbol{n}_1^W$ and $\boldsymbol{n}_2^W$ are expressed with respect to the (fixed) world frame $\{W\}$. Then $\mathrm{q}_i = [\, s_i(\boldsymbol{n}_i^W)^T \quad c_i \,]^T$ is the unit quaternion associated with the i^{th} rotation where $s_i = \sin\frac{\theta_i}{2}$ and $c_i = \cos\frac{\theta_i}{2}$. Let $\mathrm{v}^B \in \mathbb{H}$ be the pure quaternion associated with $\boldsymbol{v}^B$ which is the representation of an arbitrary, non-zero Cartesian vector $\boldsymbol{v} \in \mathbb{R}^3$ with respect to $\{B\}$ and that is fixed in $\{B\}$ (i.e., $\boldsymbol{v}^B$ is constant). Since $\{B\}$ and $\{W\}$ are initially aligned, then also $\boldsymbol{v}^W = \boldsymbol{v}^B$ initially. The representation of $\boldsymbol{v}^B$ with respect to $\{W\}$ after the first rotation, denoted $\boldsymbol{v}_1^W$ which is the vector part of the pure quaternion v_1^W, is computed using eq. B.14 as per

$$\mathrm{v}_1^W = \mathrm{q}_1 \mathrm{v}^B \bar{\mathrm{q}}_1 \tag{B.21}$$

and after the second rotation

$$\begin{aligned} \mathrm{v}_2^W &= \mathrm{q}_2 \mathrm{v}_1^W \bar{\mathrm{q}}_2 \\ &= \mathrm{q}_2 \mathrm{q}_1 \mathrm{v}^B \bar{\mathrm{q}}_1 \bar{\mathrm{q}}_2. \end{aligned} \tag{B.22}$$

By eq. A.28, the quaternion $\mathrm{q} = \mathrm{q}_2 \mathrm{q}_1$ and its conjugate $\bar{\mathrm{q}} = \bar{\mathrm{q}}_1 \bar{\mathrm{q}}_2$ are also unit length. Therefore, q may be constructed using $\mathrm{q} = [s(\boldsymbol{n}^W)^T \quad c]^T$ where $s^2 = \boldsymbol{q}^T \boldsymbol{q}$, $\boldsymbol{n}^W = s^{-1}\boldsymbol{q}$, and $c = q_4$ in which case $\mathrm{q}\mathrm{v}^B\bar{\mathrm{q}}$ in eq. B.22 corresponds to the single rotation of $\boldsymbol{v}^B$ about the axis $\boldsymbol{n}^W$ through the angle θ where $s = \sin\frac{\theta}{2}$ and $c = \cos\frac{\theta}{2}$. Now consider the same two successive rotations but with $\boldsymbol{n}_1^W$ and $\boldsymbol{n}_2^W$ expressed instantaneously with respect to $\{B\}$, denoted $\boldsymbol{n}_i^B$. Let q_i^B be the quaternion associated with the rotation about $\boldsymbol{n}_i^B$ through θ_i as per eq. B.14 and with $\mathrm{q}_i^B = [s_i(\boldsymbol{n}_i^B)^T \quad c_i]^T$. Since $\{B\}$ and $\{W\}$ are initially aligned, $\boldsymbol{n}_1^W = \boldsymbol{n}_1^B$ and thus $\mathrm{q}_1 = \mathrm{q}_1^B$. Then

$$\boldsymbol{n}_2^W = \boldsymbol{R}_1 \boldsymbol{n}_2^B \tag{B.23}$$

where $\boldsymbol{R}_1$ is parametrized by q_1 (or equivalently q_1^B) as in eq. B.18. Notice, from eqs. B.15 – B.17 and B.23, we can relate

$$\mathrm{q}_2 = \mathrm{q}_1^B \mathrm{q}_2^B \bar{\mathrm{q}}_1^B \tag{B.24}$$

in which case the product $\mathrm{q}_2\mathrm{q}_1$ in eq. B.22 becomes

$$\mathrm{q}_2 \mathrm{q}_1 = \mathrm{q}_1^B \mathrm{q}_2^B. \tag{B.25}$$

In summary, if a unit quaternion is constructed as in eq. B.1 with the rotation axis $\boldsymbol{n}$ expressed with respect to the (non-rotating) world frame $\{W\}$, then N successive rotations compose as per $\mathrm{q}_N \mathrm{q}_{N-1} \cdots \mathrm{q}_2 \mathrm{q}_1$ whereas if the rotation axis is expressed instantaneously with respect to the (rotating) body frame $\{B\}$, then N successive rotations compose in the reverse order as per $\mathrm{q}_1^B \mathrm{q}_2^B \cdots \mathrm{q}_{N-1}^B \mathrm{q}_N^B$.

Appendix C: Quaternion Kinematics

Let $\mathrm{v}^A \in \mathbb{H}$ be the pure quaternion corresponding to $\boldsymbol{v}^A$ which is the representation of the Cartesian vector $\boldsymbol{v} \in \mathbb{R}^3$ with respect to the basis $\{A\}$ and let $\mathrm{q} \in \mathbb{H}$ be the unit quaternion such that

$$\mathrm{v}^W = \mathrm{q}\mathrm{v}^B\bar{\mathrm{q}} \tag{C.1}$$

where $\{W\}$ is the non-rotating world frame and $\{B\}$ is a rotating, but non-translating, body frame. Further, let v^B be constant such that $\boldsymbol{v}^W$ rotates with $\{B\}$. Differentiating eq. C.1 with respect to time yields

$$\dot{\mathrm{v}}^W = \dot{\mathrm{q}}\mathrm{v}^B\bar{\mathrm{q}} + \mathrm{q}\dot{\mathrm{v}}^B\bar{\mathrm{q}} + \mathrm{q}\mathrm{v}^B\dot{\bar{\mathrm{q}}} \tag{C.2}$$

and since v^B is constant

$$\dot{\mathrm{v}}^W = \dot{\mathrm{q}}\mathrm{v}^B\bar{\mathrm{q}} + \mathrm{q}\mathrm{v}^B\dot{\bar{\mathrm{q}}}. \tag{C.3}$$

Left multiplication by $\bar{\mathrm{q}}$ and right multiplication by q in eq. C.3 gives

$$\bar{\mathrm{q}}\dot{\mathrm{v}}^W\mathrm{q} = \bar{\mathrm{q}}\dot{\mathrm{q}}\mathrm{v}^B + \mathrm{v}^B\dot{\bar{\mathrm{q}}}\mathrm{q}. \tag{C.4}$$

Since $|\mathrm{q}|^2 = 1$ is constant, then

$$\dot{\bar{\mathrm{q}}}\mathrm{q} = -\bar{\mathrm{q}}\dot{\mathrm{q}} \tag{C.5}$$

by differentiating eq. A.19 with respect to time. Notice, eq. C.5 indicates that $\dot{\bar{\mathrm{q}}}\mathrm{q}$ is equal to the negative of its conjugate. Therefore, $\dot{\bar{\mathrm{q}}}\mathrm{q}$ must be pure in which case the equation for the scalar part of $\dot{\bar{\mathrm{q}}}\mathrm{q}$ yields the kinematic equality constraint equation

$$\mathrm{q}^T\dot{\mathrm{q}} = 0. \tag{C.6}$$

Since $\boldsymbol{v}^W$ only rotates, the velocity $\dot{\boldsymbol{v}}^W$ is given by

$$\dot{\boldsymbol{v}}^W = \boldsymbol{\omega}^W \times \boldsymbol{v}^W \tag{C.7}$$

where $\boldsymbol{\omega} \in \mathbb{R}^3$ is the Cartesian vector corresponding to the angular velocity of $\{B\}$ and $\boldsymbol{\omega}^W$ is the representation of $\boldsymbol{\omega}$ with respect to $\{W\}$. Using eq. A.31, we have the equivalent quaternion operation corresponding to the cross product $\boldsymbol{\omega}^W \times \boldsymbol{v}^W$ in eq. C.7 as per

$$\dot{\mathrm{v}}^W = \frac{1}{2}(\omega^W \mathrm{v}^W - \mathrm{v}^W \omega^W). \tag{C.8}$$

Subsituting eqs. C.5 and C.8 into eq. C.4 yields

$$\frac{1}{2}\bar{\mathrm{q}}\omega^W \mathrm{v}^W \mathrm{q} - \frac{1}{2}\bar{\mathrm{q}}\mathrm{v}^W \omega^W \mathrm{q} = \bar{\mathrm{q}}\dot{\mathrm{q}}\mathrm{v}^B - \mathrm{v}^B \bar{\mathrm{q}}\dot{\mathrm{q}} \tag{C.9}$$

Using $\mathrm{q}\bar{\mathrm{q}} = 1$ and eq. C.1, the left side of eq. C.9 can be written

$$\frac{1}{2}\bar{\mathrm{q}}\omega^W \mathrm{v}^W \mathrm{q} - \frac{1}{2}\bar{\mathrm{q}}\mathrm{v}^W \omega^W \mathrm{q} = \frac{1}{2}\bar{\mathrm{q}}\omega^W \mathrm{q}\bar{\mathrm{q}}\mathrm{v}^W \mathrm{q} - \frac{1}{2}\bar{\mathrm{q}}\mathrm{v}^W \mathrm{q}\bar{\mathrm{q}}\omega^W \mathrm{q}$$

$$= \frac{1}{2}\omega^B \mathrm{v}^B - \frac{1}{2}\mathrm{v}^B \omega^B. \tag{C.10}$$

Equating eqs. C.9 and C.10, we relate

$$\frac{1}{2}\omega^B = \bar{\mathrm{q}}\dot{\mathrm{q}}. \tag{C.11}$$

Equivalently, using the left quaternion product matrix in eq. A.14 and accounting for the conjugation as in eq. A.24, we have

$$\omega^B = 2\mathrm{Q}_{\mathrm{L}}^T \dot{\mathrm{q}} \tag{C.12}$$

so that the first three rows of $2\mathrm{Q}_{\mathrm{L}}^T$ form the 3×4 matrix, denoted $\mathcal{J}_\omega$, that maps the quaternion velocity to the Cartesian angular velocity as per

$$\boldsymbol{\omega}^B = \mathcal{J}_\omega \dot{\mathrm{q}} \tag{C.13}$$

with

$$\mathcal{J}_\omega = 2[-\tilde{\boldsymbol{q}} + p_4 \boldsymbol{I}_3 \quad -\boldsymbol{q}^T]. \tag{C.14}$$

Left multiplication by q in eq. C.11 yields the quaternion kinematic equation given by

$$\dot{\mathrm{q}} = \frac{1}{2}\mathrm{q}\omega^B \qquad \text{C. 15}$$

or equivalently using the right quaternion product matrix for ω^B, denoted Ω_{R}^B, from eq. A.15

$$\dot{\mathrm{q}} = \frac{1}{2}\Omega_{\mathrm{R}}^B\mathrm{q}. \qquad \text{C. 16}$$

Let the subscript t in q_t denote the unit quaternion q in eq. C.1 representing the orientation of the rotating body frame $\{B\}$ at the time instant t. Assume the angular velocity is constant with respect to $\{B\}$ during the time interval $t \to t + \Delta t$ with $\Delta t > 0$ such that ω^B in eq. C.15 is constant during the same time interval. Further, let $\boldsymbol{n}$ and $\dot{\theta}$ denote the direction and magnitude of $\boldsymbol{\omega}^B$, respectively, such that

$$\boldsymbol{\omega}^B = \boldsymbol{n}\dot{\theta} \qquad \text{C. 17}$$

and with $\boldsymbol{n}^T\boldsymbol{n} = 1$. Then, the solution to eq. C.15 is

$$\mathrm{q}_{t+\delta t} = \mathrm{q}_t \exp\left(\frac{\delta t}{2}\omega^B\right) \qquad \text{C. 18}$$

where $0 < \delta t \leq \Delta t$. Since the square of ω^B is the negative of its magnitude squared per eqs. A.17 and A.29, we have

$$(\omega^B)^2 = -\dot{\theta}^2 \qquad \text{C. 19}$$

and thus,

$$\begin{aligned}(\omega^B)^3 &= -\dot{\theta}^2\boldsymbol{\omega}^B \\ &= -\dot{\theta}^3\boldsymbol{n}.\end{aligned} \qquad \text{C. 20}$$

For higher powers,

$$(\omega^B)^4 = \dot{\theta}^4 \qquad \text{C. 21}$$

$$(\omega^B)^5 = \dot{\theta}^5\boldsymbol{n} \qquad \text{C. 22}$$

$$(\omega^B)^6 = -\dot{\theta}^6 \qquad \text{C. 23}$$

$$(\omega^B)^7 = -\dot{\theta}^7\boldsymbol{n} \qquad \text{C. 24}$$

and so on, so that

$$\exp\left(\frac{\delta t}{2}\omega^B\right) = 1 + \frac{\delta t}{2}\omega^B + \frac{1}{2}\left(\frac{\delta t}{2}\omega^B\right)^2 + \frac{1}{3!}\left(\frac{\delta t}{2}\omega^B\right)^3 + \frac{1}{4!}\left(\frac{\delta t}{2}\omega^B\right)^4 + \frac{1}{5!}\left(\frac{\delta t}{2}\omega^B\right)^5 + \cdots$$

$$= 1 + \frac{\delta t\dot{\theta}}{2}\boldsymbol{n} - \frac{1}{2}\left(\frac{\delta t\dot{\theta}}{2}\right)^2 - \frac{1}{3!}\left(\frac{\delta t\dot{\theta}}{2}\right)^3\boldsymbol{n} + \frac{1}{4!}\left(\frac{\delta t\dot{\theta}}{2}\right)^4 + \frac{1}{5!}\left(\frac{\delta t\dot{\theta}}{2}\right)^5\boldsymbol{n} - \cdots$$

$$= \left[\left(\frac{\delta t\dot{\theta}}{2}\right) - \frac{1}{3!}\left(\frac{\delta t\dot{\theta}}{2}\right)^3 + \frac{1}{5!}\left(\frac{\delta t\dot{\theta}}{2}\right)^5 - \cdots\right]\boldsymbol{n} + \left[1 - \frac{1}{2}\left(\frac{\delta t\dot{\theta}}{2}\right)^2 + \frac{1}{4!}\left(\frac{\delta t\dot{\theta}}{2}\right)^4 - \cdots\right]$$

$$= \sin\left(\frac{\delta t\dot{\theta}}{2}\right)\boldsymbol{n} + \cos\left(\frac{\delta t\dot{\theta}}{2}\right). \qquad \text{C. 25}$$

Thus, $\exp\left(\frac{\delta t}{2}\omega^B\right)$ in eq. C.18 is a unit quaternion corresponding to the rotation about $\boldsymbol{n}$ (expressed with respect to $\{B\}$) through the angle $\delta t\dot{\theta}$ via the operation eq. B.14. Finally, note that for an infinitesimal δt, we have the asymptotic approximation

$$\exp\left(\frac{\delta t}{2}\omega^B\right) \sim \frac{\delta t\dot{\theta}}{2}\boldsymbol{n} + 1 \qquad for \qquad \delta t \ll 1. \qquad \text{C. 26}$$

Appendix D: Optimization-Based Optical Motion Capture

D.1. Optimization problem

Let $\boldsymbol{p}_i \in \mathbb{R}^3$ be the Cartesian vector describing the position of the center of mass of segment i and let $\mathrm{q}_i \in \mathbb{H}$ with $|\mathrm{q}_i| = 1$ be the unit quaternion describing the orientation of segment i relative to the inertial world frame $\{W\}$ such that

$$\boldsymbol{v}^W = \boldsymbol{R}_i \boldsymbol{v}^{B_i} \tag{D.1}$$

where $\boldsymbol{R}_i \in SO(3)$ is the rotation matrix parametrized by q_i as in eq. B.18, B_i denotes the frame $\{B_i\}$ fixed to segment i (coincident with the segment's principal axes of inertia), and $\boldsymbol{v}^A$ is the representation of the Cartesian vector $\boldsymbol{v} \in \mathbb{R}^3$ with respect to the basis $\{A\}$. Thus, $\boldsymbol{p}_i$ and q_i comprise the seven generalized coordinates corresponding to segment i as described in section 6.4.2. Further, let $\boldsymbol{\mu}_n^{B_i}$ be the constant (due to the rigid body assumption) 3×1 vector describing the position of marker n with respect to the segment frame $\{B_i\}$, in which it is fixed, such that

$$\widehat{\boldsymbol{m}}_n^W = \boldsymbol{p}_i^W + \boldsymbol{R}_i \boldsymbol{\mu}_n^{B_i} \tag{D.2}$$

where $\widehat{\boldsymbol{m}}_n^W$ is the position of marker n with respect to the basis $\{W\}$ as in eq. 6.21. The problem of estimating the generalized coordinates based on measured marker positions was formulated as an optimization problem in eq. 6.22 and is restated here in a slightly different form:

$$\min_{\boldsymbol{x}} \frac{1}{2} \boldsymbol{\Phi}^T \boldsymbol{W} \boldsymbol{\Phi} \tag{D.3}$$

subject to 16 equality constraints

$$\boldsymbol{c}(\boldsymbol{x}) = \begin{bmatrix} c_1(\boldsymbol{x}) \\ \vdots \\ c_{16}(\boldsymbol{x}) \end{bmatrix} = \boldsymbol{0}_{16\times 1} \tag{D.4}$$

where $\boldsymbol{W}$ is block diagonal with the 3×3 marker-specific weighting matrices W_n from eq. 6.22 on the diagonal, $\boldsymbol{x}$ is the 28×1 column vector of generalized coordinates for the four-segment system described in section 6.4 organized as per

$$\boldsymbol{x} = \begin{bmatrix} \boldsymbol{p}_1 \\ \mathrm{q}_1 \\ \vdots \\ \boldsymbol{p}_4 \\ \mathrm{q}_4 \end{bmatrix}. \tag{D.5}$$

As a clarifying example, note that $x_8 = p_{2_1}$ is the first positional coordinate of segment 2 and $x_{21} = q_{3_4}$ is the fourth rotational coordinate of segment 3 (the scalar part of q_3). In the objective function of eq. D.3, $\boldsymbol{\Phi}$ is the $3N \times 1$ column vector of errors

$$\boldsymbol{\Phi} = \begin{bmatrix} \boldsymbol{\phi}_1 \\ \vdots \\ \boldsymbol{\phi}_N \end{bmatrix} \tag{D.6}$$

where N is the number of markers and $\boldsymbol{\phi}_n$ is the difference between the marker position based on the generalized coordinates ($\widehat{\boldsymbol{m}}_n^W$ from eq. D.2) and the measured marker position $\boldsymbol{m}_n^W$ from the optical motion capture system:

$$\boldsymbol{\phi}_n = \widehat{\boldsymbol{m}}_n^W - \boldsymbol{m}_n^W. \tag{D.7}$$

D.2. Objective function

As described in section 6.4.2, eq. D.3 is solved using the fmincon function in MATLAB R2019b with the interior-point algorithm and analytic Jacobian and Hessian matrices of the objective and constraint equations with respect to $\boldsymbol{x}$. Presented here are analytic expressions for those Jacobian and Hessian matrices. For the Jacobian of the objective, we have

$$\frac{\partial}{\partial \boldsymbol{x}}\left(\frac{1}{2}\boldsymbol{\Phi}^T\boldsymbol{W}\boldsymbol{\Phi}\right) = \boldsymbol{\Phi}^T\boldsymbol{W}\frac{\partial \boldsymbol{\Phi}}{\partial \boldsymbol{x}} \tag{D.8}$$

where $\frac{\partial \boldsymbol{\Phi}}{\partial \boldsymbol{x}}$ is an $N \times 28$ matrix structured as per

$$\frac{\partial \boldsymbol{\Phi}}{\partial \boldsymbol{x}} = \begin{bmatrix} \frac{\partial \boldsymbol{\phi}_1}{\partial \boldsymbol{x}} \\ \vdots \\ \frac{\partial \boldsymbol{\phi}_N}{\partial \boldsymbol{x}} \end{bmatrix}. \tag{D.9}$$

Let i index the segment to which marker n is fixed. Then, from eqs. D.2 and D.7, the 3×28 matrix $\frac{\partial \boldsymbol{\phi}_n}{\partial \boldsymbol{x}}$ in eq. D.9 has the form

$$\frac{\partial \boldsymbol{\phi}_n}{\partial \boldsymbol{x}} = \begin{bmatrix} \frac{\partial \boldsymbol{\phi}_n}{\partial \boldsymbol{p}_1} & \frac{\partial \boldsymbol{\phi}_n}{\partial \mathrm{q}_1} & \cdots & \frac{\partial \boldsymbol{\phi}_n}{\partial \boldsymbol{p}_4} & \frac{\partial \boldsymbol{\phi}_n}{\partial \mathrm{q}_4} \end{bmatrix} \tag{D.10}$$

and, since $\boldsymbol{\phi}_n$ depends only on the coordinates corresponding to segment i, we have

$$\frac{\partial \boldsymbol{\phi}_n}{\partial \boldsymbol{x}} = \begin{bmatrix} \mathbf{0}_{3\times3} & \mathbf{0}_{3\times4} & \cdots & \frac{\partial \boldsymbol{\phi}_n}{\partial \boldsymbol{p}_i} & \frac{\partial \boldsymbol{\phi}_n}{\partial \mathrm{q}_i} & \cdots & \mathbf{0}_{3\times3} & \mathbf{0}_{3\times4} \end{bmatrix}. \tag{D.11}$$

From eq. D.7

$$\frac{\partial \boldsymbol{\phi}_n}{\partial \boldsymbol{p}_i} = \boldsymbol{I}_3. \tag{D.12}$$

The 3×4 matrix $\frac{\partial \boldsymbol{\phi}_n}{\partial \mathrm{q}_i}$ in eq. D.11 has the form

$$\frac{\partial \boldsymbol{\phi}_n}{\partial \mathrm{q}_i} = \begin{bmatrix} \frac{\partial \boldsymbol{\phi}_n}{\partial q_{i_1}} & \frac{\partial \boldsymbol{\phi}_n}{\partial q_{i_2}} & \frac{\partial \boldsymbol{\phi}_n}{\partial q_{i_3}} & \frac{\partial \boldsymbol{\phi}_n}{\partial q_{i_4}} \end{bmatrix} \tag{D.13}$$

and from eqs. D.2 and D.7

$$\frac{\partial \boldsymbol{\phi}_n}{\partial \mathrm{q}_i} = \begin{bmatrix} \frac{\partial \boldsymbol{R}_i}{\partial q_{i_1}} \boldsymbol{\mu}_n^{B_i} & \frac{\partial \boldsymbol{R}_i}{\partial q_{i_2}} \boldsymbol{\mu}_n^{B_i} & \frac{\partial \boldsymbol{R}_i}{\partial q_{i_3}} \boldsymbol{\mu}_n^{B_i} & \frac{\partial \boldsymbol{R}_i}{\partial q_{i_4}} \boldsymbol{\mu}_n^{B_i} \end{bmatrix} \tag{D.14}$$

where, by eq. B.18,

$$\frac{\partial \boldsymbol{R}_i}{\partial q_{i_1}} = 2 \begin{bmatrix} q_{i_1} & q_{i_2} & q_{i_3} \\ q_{i_2} & -q_{i_1} & -q_{i_4} \\ q_{i_3} & q_{i_4} & -q_{i_1} \end{bmatrix}, \tag{D.15}$$

$$\frac{\partial \boldsymbol{R}_i}{\partial q_{i_2}} = 2\begin{bmatrix} -q_{i_2} & q_{i_1} & q_{i_4} \\ q_{i_1} & q_{i_2} & q_{i_3} \\ -q_{i_4} & q_{i_3} & -q_{i_2} \end{bmatrix}, \tag{D.16}$$

$$\frac{\partial \boldsymbol{R}_i}{\partial q_{i_3}} = 2\begin{bmatrix} -q_{i_3} & -q_{i_4} & q_{i_1} \\ q_{i_4} & -q_{i_3} & q_{i_2} \\ q_{i_1} & q_{i_2} & q_{i_3} \end{bmatrix}, \tag{D.17}$$

and

$$\frac{\partial \boldsymbol{R}_i}{\partial q_{i_4}} = 2\begin{bmatrix} q_{i_4} & -q_{i_3} & q_{i_1} \\ q_{i_3} & q_{i_4} & -q_{i_1} \\ -q_{i_2} & q_{i_1} & q_{i_4} \end{bmatrix}. \tag{D.18}$$

Let $\boldsymbol{H}_o$ be the 28×28 symmetric Hessian of the objective function, i.e., $\frac{\partial}{\partial \boldsymbol{x}}\left(\boldsymbol{\Phi}^T \boldsymbol{W} \frac{\partial \boldsymbol{\Phi}}{\partial \boldsymbol{x}} \right)$:

$$\boldsymbol{H}_o = \frac{\partial \boldsymbol{\Phi}^T}{\partial \boldsymbol{x}} \boldsymbol{W} \frac{\partial \boldsymbol{\Phi}}{\partial \boldsymbol{x}} + \boldsymbol{\Phi}^T \boldsymbol{W} \frac{\partial}{\partial \boldsymbol{x}}\left(\frac{\partial \boldsymbol{\Phi}}{\partial \boldsymbol{x}} \right). \tag{D.19}$$

The first term in eq. D.14 is given from eqs. D.9 – D.18. The element in row j and column k of the second term is given by

$$\left[\boldsymbol{\Phi}^T \boldsymbol{W} \frac{\partial}{\partial \boldsymbol{x}}\left(\frac{\partial \boldsymbol{\Phi}}{\partial \boldsymbol{x}} \right) \right]_{j,k} = \boldsymbol{\Phi}^T \boldsymbol{W} \frac{\partial}{\partial x_j}\left(\frac{\partial \boldsymbol{\Phi}}{\partial x_k} \right). \tag{D.20}$$

The vector $\frac{\partial \boldsymbol{\Phi}}{\partial x_k}$ in eq. D.20 is column k of the matrix $\frac{\partial \boldsymbol{\Phi}}{\partial \boldsymbol{x}}$ in eq. D.9. Thus, note that because $\frac{\partial}{\partial x_j}\left(\frac{\partial \boldsymbol{\phi}_n}{\partial x_k} \right) = \boldsymbol{0}_{3\times 1}$ for all k indexing positional coordinates (since the 3×1 vector $\frac{\partial \boldsymbol{\phi}_n}{\partial x_k}$ is constant and contains only zeros or ones per eq. D.12) as well as for all j indexing positional coordinates (since q_i is independent of $\boldsymbol{p}_i$), elements of $\frac{\partial}{\partial x_j}\left(\frac{\partial \boldsymbol{\Phi}}{\partial x_k} \right)$ may be non-zero only for j and k indexing rotational coordinates for the same segment i and only for rows of $\frac{\partial \boldsymbol{\Phi}}{\partial x_k}$ corresponding to $\frac{\partial \boldsymbol{\phi}_n}{\partial x_k}$ for all n indexing markers attached to the same segment i.

Therefore, it will suffice to specify $\frac{\partial}{\partial q_{i_a}}\left(\frac{\partial \boldsymbol{\phi}_n}{\partial q_{i_b}}\right)$ for all combinations of a and b for $a = b = \{1,2,3,4\}$, which from eq. D.14 reduces to $\frac{\partial}{\partial q_{i_a}}\left(\frac{\partial \boldsymbol{R}_i}{\partial q_{i_b}}\right)\boldsymbol{\mu}_n^{B_i}$. Let $\boldsymbol{e}_i$ be the i^{th} natural basis (e.g., $\boldsymbol{e}_2 = [0 \quad 1 \quad 0]^T$) and let $\text{diag}(u, v, w)$ be the diagonal matrix with u, v, and w on the diagonal (following MATLAB notation) as per

$$\text{diag}(u, v, w) = \begin{bmatrix} u & 0 & 0 \\ 0 & v & 0 \\ 0 & 0 & w \end{bmatrix}. \tag{D.21}$$

Then, from eqs. D.15 – D.18, we have

$$\frac{\partial}{\partial q_{i_1}}\left(\frac{\partial \boldsymbol{R}_i}{\partial q_{i_1}}\right) = \text{diag}(2, -2, -2), \tag{D.22}$$

$$\frac{\partial}{\partial q_{i_2}}\left(\frac{\partial \boldsymbol{R}_i}{\partial q_{i_2}}\right) = \text{diag}(-2, 2, -2), \tag{D.23}$$

$$\frac{\partial}{\partial q_{i_3}}\left(\frac{\partial \boldsymbol{R}_i}{\partial q_{i_3}}\right) = \text{diag}(-2, -2, 2), \tag{D.24}$$

$$\frac{\partial}{\partial q_{i_4}}\left(\frac{\partial \boldsymbol{R}_i}{\partial q_{i_4}}\right) = 2\boldsymbol{I}_3, \tag{D.25}$$

$$\frac{\partial}{\partial q_{i_2}}\left(\frac{\partial \boldsymbol{R}_i}{\partial q_{i_1}}\right) = \begin{bmatrix} 0 & 2 & 0 \\ 2 & 0 & 0 \\ 0 & 0 & 0 \end{bmatrix}, \tag{D.26}$$

$$\frac{\partial}{\partial q_{i_3}}\left(\frac{\partial \boldsymbol{R}_i}{\partial q_{i_1}}\right) = \begin{bmatrix} 0 & 0 & 2 \\ 0 & 0 & 0 \\ 2 & 0 & 0 \end{bmatrix}, \tag{D.27}$$

$$\frac{\partial}{\partial q_{i_3}}\left(\frac{\partial \boldsymbol{R}_i}{\partial q_{i_2}}\right) = \begin{bmatrix} 0 & 0 & 0 \\ 0 & 0 & 2 \\ 0 & 2 & 0 \end{bmatrix}, \tag{D.28}$$

and

$$\frac{\partial}{\partial q_{i_j}}\left(\frac{\partial \boldsymbol{R}_i}{\partial q_{i_4}}\right) = 2\tilde{\boldsymbol{e}}_j \quad for \quad j = 1, 2, 3. \tag{D.29}$$

The remaining second partial derivatives are given due to the symmetry

$$\frac{\partial}{\partial q_{i_j}}\left(\frac{\partial \boldsymbol{\phi}_n}{\partial q_{i_k}}\right) = \frac{\partial}{\partial q_{i_k}}\left(\frac{\partial \boldsymbol{\phi}_n}{\partial q_{i_j}}\right). \tag{D.30}$$

D.3. Constraints

The following provides analytic expressions for the 16 constraint equations, the Jacobian matrix of the constraints with respect to the generalized coordinates, and the Hessian matrix of the constraints in the Lagrangian ($\mathcal{L}$) for its use in the interior-point algorithm as a part of the fmincon function in MATLAB. The Lagrangian is given by

$$\mathcal{L} = \frac{1}{2}\boldsymbol{\Phi}^T \boldsymbol{W} \boldsymbol{\Phi} + \boldsymbol{\lambda}^T \boldsymbol{c} \tag{D.31}$$

where $\boldsymbol{\lambda}$ is the 16×1 column vector of Lagrange multipliers. The element in row j and column k of the 16×28 Jacobian matrix $\frac{\partial \boldsymbol{c}}{\partial \boldsymbol{x}}$ is given by

$$\left[\ \frac{\partial \boldsymbol{c}}{\partial \boldsymbol{x}}\ \right]_{j,k} = \frac{\partial c_j}{\partial x_k}. \tag{D.32}$$

The 28×28 Hessian matrix of the Lagrangian $\mathcal{L}$ is given by

$$\frac{\partial}{\partial \boldsymbol{x}}\left(\frac{\partial \mathcal{L}}{\partial \boldsymbol{x}}\right) = \boldsymbol{H}_o + \boldsymbol{H}_c \tag{D.33}$$

where $\boldsymbol{H}_o$ was given in eq. D.19 and the matrix $\boldsymbol{H}_c$ may be written

$$\boldsymbol{H}_c = \sum_{j=1}^{16} \lambda_j \frac{\partial}{\partial \boldsymbol{x}}\left(\frac{\partial c_j}{\partial \boldsymbol{x}}\right). \tag{D.34}$$

Note that $\frac{\partial c_j}{\partial \boldsymbol{x}}$ is row j of the Jacobian matrix $\frac{\partial \boldsymbol{c}}{\partial \boldsymbol{x}}$ and the element in row j and column k of $\boldsymbol{H}_c$ is given by

$$[\ \boldsymbol{H}_c\ ]_{j,k} = \boldsymbol{\lambda}^T \frac{\partial}{\partial x_j}\left(\frac{\partial \boldsymbol{c}}{\partial x_k}\right). \tag{D.35}$$

D.3.1. Unit-length quaternion constraints

Four of the constraint equations enforce the unit length constraint for the quaternion parameters for each of the four segments. Let L (for length) index the element of $\boldsymbol{c}$ associated with this constraint for segment i. Then,

$$c_L = \mathrm{q}_i^T \mathrm{q}_i - 1 \qquad \text{D.36}$$

in which case all elements of $\frac{\partial c_L}{\partial \boldsymbol{x}}$ are zero except for those indexing elements of q_i where

$$\frac{\partial c_L}{\partial \mathrm{q}_i} = 2\mathrm{q}_i^T. \qquad \text{D.37}$$

Likewise, $\frac{\partial}{\partial x_j}\left(\frac{\partial c_L}{\partial x_k}\right) = 0$ for all j and k except for those indexing elements of q_i where

$$\frac{\partial}{\partial \mathrm{q}_i}\left(\frac{\partial c_L}{\partial \mathrm{q}_i}\right) = 2\boldsymbol{I}_4. \qquad \text{D.38}$$

D.3.2. Non-translational joint constraints

Nine of the constraint equations (three for each joint) enforce the non-translational constraint of the joints (i.e., joints are not allowed to dislocate). Thus, if $\boldsymbol{\rho}_i^{B_i}$ and $\boldsymbol{\rho}_j^{B_j}$ are the constant 3×1 vectors pointing from $\boldsymbol{p}_i$ and $\boldsymbol{p}_j$, respectively, to the joint center of joint j which articulates the segments indexed by i and j (expressed with respect to their respective body-fixed coordinate systems), then

$$\boldsymbol{c}_{NT} = \boldsymbol{p}_i^W + \boldsymbol{R}_i\boldsymbol{\rho}_i^{B_i} - \boldsymbol{p}_j^W - \boldsymbol{R}_j\boldsymbol{\rho}_j^{B_j} \qquad \text{D.39}$$

where the subscript NT (for non-translational) indexes the 3×1 component of $\boldsymbol{c}$ corresponding to constraint eq. D.39 for joint j. The first and second partial derivatives of $\boldsymbol{c}_{NT}$ are found similarly as for $\boldsymbol{\phi}_n$ in eq. D.10 – D.18.

D.3.3. Revolute and universal joint constraints

Three of the constraint equations enforce rotational constraints for one DOF revolute joints (e.g., the knee, two constraint equations) and two DOF universal joints (e.g., the ankle, one constraint equation).

For this development, let joint j articulate segments A and B with corresponding segment-fixed bases $\{A\}$ and $\{B\}$, respectively. Let $\{Z\} = \{\boldsymbol{z}_1, \boldsymbol{z}_2, \boldsymbol{z}_3\}$ be an orthonormal basis defining the joint coordinate system in a reference configuration where $\boldsymbol{z}_i$ is the rotation axis for the i^{th} rotational DOF expressed with respect to the inertial frame $\{W\}$. Thus, for a revolute joint, $\boldsymbol{z}_1$ is the single joint axis and $\boldsymbol{z}_2$ and $\boldsymbol{z}_3$ are unit length and mutually orthogonal to each other and to $\boldsymbol{z}_1$, but otherwise arbitrary. Likewise, for a universal joint, $\boldsymbol{z}_1$ and $\boldsymbol{z}_2$ are joint axes for the first and second rotational DOFs while $\boldsymbol{z}_3 = \boldsymbol{z}_1 \times \boldsymbol{z}_2$. Assume we have available the orientations of $\{A\}$, $\{B\}$, and $\{Z\}$ for a reference configuration and those orientations are parametrized by the quaternion q_i as per

$$\mathrm{v}^W = \mathrm{q}_i \mathrm{v}^i \bar{\mathrm{q}}_i \qquad \text{D.40}$$

for $i = A, B, Z$ and where $\mathrm{v} \in \mathbb{H}$ is the pure quaternion associated with the Cartesian vector $\boldsymbol{v} \in \mathbb{R}^3$. We will use the primed quaternion q'_i to denote the orientation of frame i in a displaced configuration relative to the reference configuration. Note that we may consider the basis $\{Z\}$ (from the reference configuration) as fixed in segment A and B such that it rotates with the segment in the same way as for frames $\{A\}$ and $\{B\}$. We introduce Z_A and Z_B, respectively, to denote these bases which is necessary because the joint constraints are enforced on the *joint quaternion* q_j that maps the representation of $\boldsymbol{v}$ with respect to $\{Z_A\}$, $\boldsymbol{v}^{Z_A}$, to its representation with respect to $\{Z_B\}$, $\boldsymbol{v}^{Z_B}$, via

$$\mathrm{v}^{Z_B} = \mathrm{q}_j \mathrm{v}^{Z_A} \bar{\mathrm{q}}_j. \qquad \text{D.41}$$

Note that in this case, the *perspective* of the joint would be "B to A" since the relation in eq. D.41 indicates that we would imagine aligning frame $\{Z_B\}$ onto $\{Z_A\}$ by rotating $\{Z_B\}$ about the axis $\boldsymbol{n}$ (expressed with respect to $\{W\}$) through the angle θ that parametrizes q_j as in eq. B.1 (see discussion following eq. B.18). To be clear, the bases $\{Z_A\}$, $\{Z_B\}$, and $\{Z\}$ all coincide in the reference configuration, but $\{Z_A\}$ and $\{Z_B\}$ may not be aligned for an arbitrary configuration. Further, for an arbitrary configuration, the orientation of $\{Z_A\}$ relative to $\{A\}$ and likewise $\{Z_B\}$ relative to $\{B\}$ is constant and parametrized by the constant quaternions q_{c_A} and q_{c_B}, respectively, such that

$$\mathrm{v}^i = \mathrm{q}_{c_i} \mathrm{v}^{Z_i} \bar{\mathrm{q}}_{c_i} \qquad \text{D.42}$$

where

$$\mathrm{q}_{c_i} = \bar{\mathrm{q}}'_i \mathrm{q}'_{Z_i} \tag{D.43}$$

and since eq. D.42 holds for an arbitrary configuration, q_{c_i} may be computed from the reference configuration as per

$$\mathrm{q}_{c_i} = \bar{\mathrm{q}}_i \mathrm{q}_{Z_i}. \tag{D.44}$$

Now, for an arbitrary displaced configuration, we have

$$\mathrm{v}^{Z_B} = \bar{\mathrm{q}}_{c_B} \bar{\mathrm{q}}'_B \mathrm{q}'_A \mathrm{q}_{c_A} \mathrm{v}^{Z_A} \bar{\mathrm{q}}_{c_A} \bar{\mathrm{q}}'_A \mathrm{q}'_B \mathrm{q}_{c_B} \tag{D.45}$$

and by equating eqs. D.41 and D.45, clearly

$$\mathrm{q}_{\not\jmath} = \bar{\mathrm{q}}_{c_B} \bar{\mathrm{q}}'_B \mathrm{q}'_A \mathrm{q}_{c_A}. \tag{D.46}$$

Using the left and right quaternion product matrices, eq. D.46 can be written

$$\mathrm{q}_{\not\jmath} = \mathrm{P} \mathrm{Q}^{\mathrm{T}}_{B'_L} \mathrm{q}'_A \tag{D.47}$$

where $\mathrm{Q}^{\mathrm{T}}_{B'_L}$ is the left quaternion product matrix associated with $\bar{\mathrm{q}}'_B$ and the 4×4 matrix P is constant and given by

$$\mathrm{P} = \mathrm{Q}^{T}_{c_{B_L}} \mathrm{Q}_{c_{A_R}}. \tag{D.48}$$

That is, $\mathrm{Q}^{T}_{c_{B_L}}$ is the left quaternion product matrix associated with $\bar{\mathrm{q}}_{c_B}$ and $\mathrm{Q}_{c_{A_R}}$ is the right quaternion product matrix associated with q_{c_A}. Equivalently, the joint quaternion may be expressed as per

$$\mathrm{q}_{\not\jmath} = \mathrm{P} \underline{\mathrm{Q}}_{A'_R} \mathrm{q}'_B \tag{D.49}$$

where $\mathrm{Q}_{A'_R}$ is the right quaternion product matrix associated with q'_A and the underline in $\underline{\mathrm{Q}}_{A'_R}$ is to denote the same product $\mathrm{Q}_{A'_R} \bar{\mathrm{q}}'_B$ but in terms of q'_B instead of its conjugate so that

$$\underline{\mathrm{Q}}_{A'_R} \mathrm{q}'_B = \mathrm{Q}_{A'_R} \bar{\mathrm{q}}'_B \tag{D.50}$$

and

$$\underline{\mathrm{Q}}_{A'_R} = \begin{bmatrix} -q'_{A_4} & -q'_{A_3} & q'_{A_2} & q'_{A_1} \\ q'_{A_3} & -q'_{A_4} & -q'_{A_1} & q'_{A_2} \\ -q'_{A_2} & q'_{A_1} & -q'_{A_4} & q'_{A_3} \\ q'_{A_1} & q'_{A_2} & q'_{A_3} & q'_{A_4} \end{bmatrix}. \qquad \text{D.51}$$

The joint quaternion q_j is expressed as in eqs. D.47 and D.49 in order to develop the partial derivatives of the constraints with respect to the generalized coordinates q'_A and q'_B, respectively.

Revolute joints

If joint j is a one DOF revolute joint, then q_j has the form

$$\mathrm{q}_j = \begin{bmatrix} \sin\frac{\theta_1}{2} \\ 0 \\ 0 \\ \cos\frac{\theta_1}{2} \end{bmatrix}. \qquad \text{D.52}$$

Thus, the two constraint equations for revolute joints are the second $\left(q_{j_2}\right)$ and third $\left(q_{j_3}\right)$ components of q_j in eq. D.52. Let r_2 and r_3 (r for revolute) index the components of $\boldsymbol{c}$ corresponding to q_{j_2} and q_{j_3}, respectively, so that

$$c_{r_2} = q_{j_2} \qquad \text{D.53}$$

and

$$c_{r_3} = q_{j_3}. \qquad \text{D.54}$$

Then,

$$c_{r_i} = \left[\, \mathrm{PQ}^{\mathrm{T}}_{B'_L} \,\right]_{i,:} \mathrm{q}'_A \qquad \text{D.55}$$

$$= \left[\, \mathrm{P}\underline{\mathrm{Q}}_{A'_R} \,\right]_{i,:} \mathrm{q}'_B \qquad \text{D.56}$$

where the subscript $i,:$ indicates row i of the bracketed matrix (following MATLAB notation). Then all elements (columns) of the row vector $\frac{\partial c_{r_i}}{\partial \boldsymbol{x}}$ are zero except for those corresponding to elements of q'_A and q'_B in which case

$$\frac{\partial c_{r_i}}{\partial \mathrm{q}'_A} = \left[\mathrm{P}\mathrm{Q}^{\mathrm{T}}_{B'_L}\right]_{i,:} \tag{D.57}$$

and

$$\frac{\partial c_{r_i}}{\partial \mathrm{q}'_B} = \left[\mathrm{P}\underline{\mathrm{Q}}_{A'_R}\right]_{i,:}. \tag{D.58}$$

Likewise, $\frac{\partial}{\partial x_j}\left(\frac{\partial c_{r_i}}{\partial x_k}\right) = 0$ for all j and k not indexing elements of q'_A and q'_B. For j and k indexing elements of q'_A and q'_B, we have

$$\frac{\partial}{\partial \mathrm{q}'_{A_a}}\left(\frac{\partial c_{r_i}}{\partial \mathrm{q}'_A}\right) = \mathbf{0}_{1\times 4}, \tag{D.59}$$

$$\frac{\partial}{\partial \mathrm{q}'_{B_a}}\left(\frac{\partial c_{r_i}}{\partial \mathrm{q}'_B}\right) = \mathbf{0}_{1\times 4}, \tag{D.60}$$

$$\frac{\partial}{\partial \mathrm{q}'_{B_a}}\left(\frac{\partial c_{r_i}}{\partial \mathrm{q}'_A}\right) = \left[\mathrm{P}\frac{\partial \mathrm{Q}^{\mathrm{T}}_{B'_L}}{\partial \mathrm{q}'_{B_a}}\right]_{i,:}, \tag{D.61}$$

and

$$\frac{\partial}{\partial \mathrm{q}'_{A_a}}\left(\frac{\partial c_{r_i}}{\partial \mathrm{q}'_B}\right) = \left[\mathrm{P}\frac{\partial \underline{\mathrm{Q}}_{A'_R}}{\partial \mathrm{q}'_{A_a}}\right]_{i,:} \tag{D.62}$$

where

$$\frac{\partial \mathrm{Q}^{\mathrm{T}}_{B'_L}}{\partial \mathrm{q}'_{B_4}} = \boldsymbol{I}_4, \tag{D.63}$$

$$\frac{\partial \underline{\mathrm{Q}}_{A'_R}}{\partial \mathrm{q}'_{A_4}} = \mathrm{diag}(-1,-1,-1,1), \tag{D.64}$$

$$\frac{\partial \mathrm{Q}_{B_L'}^{\mathrm{T}}}{\partial \mathrm{q}_{B_a}'} = \begin{bmatrix} -\tilde{\boldsymbol{e}}_a & -\boldsymbol{e}_a \\ \boldsymbol{e}_a^T & 0 \end{bmatrix} \quad for \quad a = 1,2,3, \tag{D.65}$$

and

$$\frac{\partial \mathrm{Q}_{A_R'}}{\partial \mathrm{q}_{A_a}'} = \begin{bmatrix} \tilde{\boldsymbol{e}}_a & \boldsymbol{e}_a \\ \boldsymbol{e}_a^T & 0 \end{bmatrix} \quad for \quad a = 1,2,3. \tag{D.66}$$

Universal joints

If joint j is modeled as a two DOF universal joint, then q_j has the form

$$\mathrm{q}_j = \mathrm{q}_1 \mathrm{q}_2 \tag{D.67}$$

where

$$\mathrm{q}_1 = \begin{bmatrix} \sin\frac{\theta_1}{2} \\ 0 \\ 0 \\ \cos\frac{\theta_1}{2} \end{bmatrix} \tag{D.68}$$

and

$$\mathrm{q}_2 = \begin{bmatrix} 0 \\ \sin\frac{\theta_2}{2} \\ 0 \\ \cos\frac{\theta_2}{2} \end{bmatrix} \tag{D.69}$$

so that

$$\mathrm{q}_{\jmath} = \begin{bmatrix} \sin\frac{\theta_1}{2}\cos\frac{\theta_2}{2} \\ \sin\frac{\theta_2}{2}\cos\frac{\theta_1}{2} \\ \sin\frac{\theta_1}{2}\sin\frac{\theta_2}{2} \\ \cos\frac{\theta_1}{2}\cos\frac{\theta_2}{2} \end{bmatrix}. \tag{D.70}$$

Thus, for a universal joint, we have

$$q_{\jmath_1} + q_{\jmath_2} = \sin\left(\frac{\theta_1}{2} + \frac{\theta_2}{2}\right) \tag{D.71}$$

and

$$q_{\jmath_4} - q_{\jmath_3} = \cos\left(\frac{\theta_1}{2} + \frac{\theta_2}{2}\right) \tag{D.72}$$

yielding the constraint equation

$$c_u = \left(q_{\jmath_1} + q_{\jmath_2}\right)^2 + \left(q_{\jmath_4} - q_{\jmath_3}\right)^2 - 1$$

$$c_u = q_{\jmath_1} q_{\jmath_2} - q_{\jmath_3} q_{\jmath_4} \tag{D.73}$$

which is clear from eq. D.70 and where u (for universal) indexes the element of $\boldsymbol{c}$ corresponding to constraint eq. D.73. Then, $\frac{\partial c_u}{\partial x_k} = 0$ for all k not indexing elements of q'_A and q'_B, but for k indexing elements of q'_A and q'_B, we have

$$\frac{\partial c_u}{\partial \mathrm{q}'_i} = \frac{\partial q_{\jmath_1}}{\partial \mathrm{q}'_i} q_{\jmath_2} + \frac{\partial q_{\jmath_2}}{\partial \mathrm{q}'_i} q_{\jmath_1} - \frac{\partial q_{\jmath_3}}{\partial \mathrm{q}'_i} q_{\jmath_4} - \frac{\partial q_{\jmath_4}}{\partial \mathrm{q}'_i} q_{\jmath_3} \tag{D.74}$$

where, as in eq. D.57 and D.58,

$$\frac{\partial q_{\jmath_i}}{\partial \mathrm{q}'_A} = \left[\mathrm{P}\mathrm{Q}_{B'_L}^{\mathrm{T}}\right]_{i,:}, \tag{D.75}$$

and

$$\frac{\partial q_{j_i}}{\partial \mathrm{q}'_B} = \left[\mathrm{PQ}_{\underline{A}'_R}\right]_{i,:}. \tag{D.76}$$

Likewise, $\frac{\partial}{\partial x_j}\left(\frac{\partial c_u}{\partial x_k}\right) = 0$ for all j and k not indexing elements of q'_A and q'_B. For j and k indexing elements of q'_A and q'_B, since $\frac{\partial}{\partial q'_{i_a}}\left(\frac{\partial c_u}{\partial \mathrm{q}'_i}\right) = \mathbf{0}_{1\times 4}$, we have

$$\frac{\partial}{\partial q'_{i_a}}\left(\frac{\partial c_u}{\partial \mathrm{q}'_i}\right) = \frac{\partial q_{j_1}}{\partial \mathrm{q}'_i}\frac{\partial q_{j_2}}{\partial q'_{i_a}} + \frac{\partial q_{j_2}}{\partial \mathrm{q}'_i}\frac{\partial q_{j_1}}{\partial q'_{i_a}} - \frac{\partial q_{j_3}}{\partial \mathrm{q}'_i}\frac{\partial q_{j_4}}{\partial q'_{i_a}} - \frac{\partial q_{j_4}}{\partial \mathrm{q}'_i}\frac{\partial q_{j_3}}{\partial q'_{i_a}} \tag{D.77}$$

where $\frac{\partial q_{j_i}}{\partial q'_{i_a}}$ is column a of $\frac{\partial q_{j_i}}{\partial \mathrm{q}'_i}$ in eqs. D.75 and D.76. Finally,

$$\begin{aligned}\frac{\partial}{\partial q'_{B_a}}\left(\frac{\partial c_u}{\partial q'_{A_b}}\right) = {} & \frac{\partial}{\partial q'_{B_a}}\left(\frac{\partial q_{j_1}}{\partial q'_{A_b}}\right)\partial q_{j_2} + \frac{\partial q_{j_1}}{\partial q'_{A_b}}\frac{\partial q_{j_2}}{\partial q'_{B_a}} + \\ & \frac{\partial}{\partial q'_{B_a}}\left(\frac{\partial q_{j_2}}{\partial q'_{A_b}}\right)\partial q_{j_1} + \frac{\partial q_{j_2}}{\partial q'_{A_b}}\frac{\partial q_{j_1}}{\partial q'_{B_a}} + \\ & -\frac{\partial}{\partial q'_{B_a}}\left(\frac{\partial q_{j_3}}{\partial q'_{A_b}}\right)\partial q_{j_4} - \frac{\partial q_{j_3}}{\partial q'_{A_b}}\frac{\partial q_{j_4}}{\partial q'_{B_a}} + \\ & -\frac{\partial}{\partial q'_{B_a}}\left(\frac{\partial q_{j_4}}{\partial q'_{A_b}}\right)\partial q_{j_3} - \frac{\partial q_{j_4}}{\partial q'_{A_b}}\frac{\partial q_{j_3}}{\partial q'_{B_a}}\end{aligned} \tag{D.78}$$

where $\frac{\partial}{\partial q'_{B_a}}\left(\frac{\partial q_{j_i}}{\partial q'_{A_b}}\right)$ is column b of $\frac{\partial}{\partial q'_{B_a}}\left(\frac{\partial q_{j_i}}{\partial \mathrm{q}'_A}\right)$ in eq. D.61 and vice versa for $\frac{\partial}{\partial q'_{A_a}}\left(\frac{\partial c_u}{\partial q'_{B_b}}\right)$.